Characterising Filaments in Cosmological Simulations

Marius Ramsøy

St Hugh's College

University of Oxford

A thesis submitted for the degree of

Doctor of Philosophy

Trinity 2020

Acknowledgements

First of all I have to thank my supervisors Julien Devriendt and Adrianne Slyz for their patience, guidance and for believing in me over the course of the project. I could not have done this without you and I can't thank you enough. To my collaborators, Clotilde Laigle, Harley Katz, Yohan Dubois for your help and support and fascinating discussions during the DPhil. I would also like especially thank Ryan Jackson and Sugata Kaviraj for never being too serious.

I would also like to thank Thomas Caton Harrison, Alexander Edward Stronell, Anna Senkiw, Ewan Miller, Rachael Sproule, Vivan Nguyen, Sergio Martín Álvarez and Joe Bright for making my time in Oxford some of the best times in my life.

My housemates past and present for putting up with me for all these years: Hayyu Imanda, Cristian Trovato, Vivian van Weperen and Scott Marquis for making Oxford a place to call home.

For the friendships I gained at the Kavli Summer School I would like to thank Rachel Cochrane, Tyler Parsotan, Lydia Elias, Aditi Vijayan. I loved every moment of our time together.

I also could not have done pursued the DPhil without the support of my parents, Linda and Harald Ramsøy and my sisters Camilla and Sophie. I owe a special thanks to my brother, Andreas, for coming to rescue me from the then impending pandemic.

Lexi, for always having been there for me.

I would also like to thank Jonathan Patterson and Stephane Rouberol for maintaining GLAMDRING and HORIZON in spite of my dangerous programming skills.

Last of all I would like to thank the my teachers who set me on this course to begin with, Mr Peter Darmady and the late Dr Kevin Costello.

Abstract

At high redshift, the cosmic web is widely expected to have a significant impact on the morphologies, dynamics and star formation rates of the galaxies embedded within it, underscoring the need for a comprehensive study of the properties of such a filamentary network. With this goal in mind, we perform an analysis of high-z gas and dark matter (DM) filaments around a Milky Way-like progenitor simulated with the RAMSES adaptive mesh refinement (AMR) code from cosmic scales ($\sim$1 Mpc) down to the virial radius of its DM halo host ($\sim$20 kpc at $z = 4$). Radial density profiles of both gas and DM filaments are found to have the same functional form, namely a plummer-like profile modified to take into account the wall within which these filaments are embedded. Measurements of the typical filament core radius r_0 from the simulation are consistent with that of isothermal cylinders in hydrostatic equilibrium. Such an analytic model also predicts a redshift evolution for the core radius of filaments in fair agreement with the measured value for DM ($r_0 \propto (1+z)^{-3.18\pm0.28}$). Gas filament cores grow as $r_0 \propto (1+z)^{-2.72\pm0.26}$. In both gas and DM, temperature and vorticity sharply drop at the edge of filaments, providing an excellent way to constrain the outer filament radius. When feedback is included the gas temperature and vorticity fields are strongly perturbed, hindering such a measurement in the vicinity of the galaxy. However, the core radius of the filaments as measured from the gas density field is largely unaffected by feedback, and the median central density is only reduced by about 20%.

Extending the analysis to a larger cosmological sample of filaments feeding tens of galaxies with halo masses between $10^{10}\mathrm{M}_\odot$ and $10^{12.6}\mathrm{M}_\odot$, the median filament density profiles are found to be consistent at all redshifts. This is highly suggestive of the existence of a universal filament density profile. Gas and DM filaments that feed higher mass halos and galaxies are typically higher density and hotter, with the central gas temperature rising faster than the peak temperature. This confirms that cold accretion from filaments disappears at low redshifts. Galaxies are found to be rapidly accreted into the filamentary network, with halos that reside in the network typically having a higher galaxy

formation efficiency. However, the density of the nearest filament, a proxy of the local density, has little effect on the galaxy properties we considered. Gas filaments exhibit the tendency to evolve away from a state where they are confined within the DM counterpart as time goes by and final galaxy properties do not correlate well with filament densities, suggesting that other processes are more important in shaping the low redshift properties of galaxies.

The thesis also explored the impact of reionisation on the accretion of gas onto cosmic filaments, and the effect of this on the embedded galaxies using a set of large scale cosmological radiative transfer simulations. Reionisation is able to heat the IGM filaments to the point where the gas no longer sees the shallow potential well of the lower mass filaments. While the DM is unaffected by this, the filament gas density is reduced by 60-80% by $z = 6$, driven by proximity to the galaxies they feed. Filaments with shock temperatures higher than the post-reionisation IGM gas temperature continue to accrete efficiently in spite of reionisation, and feed high mass galaxies. Meanwhile halos with $\mathrm{M_{vir}} \lesssim 10^8 \mathrm{M_\odot}$ see their gas accretion rates reduced by an order of magnitude. For even lower mass halos, with $\mathrm{M_{vir}} \lesssim 3 \times 10^7 \mathrm{M_\odot}$, gas outflow rates are enhanced due to photoevaporation, however, the reduction in inflow is even greater and thus starvation is more important in quenching the star formation in low mass halos at early epochs.

Statement of Originality

I hereby declare that that no part of this thesis has been accepted, or is currently being submitted, for any degree or diploma or certificate or any other qualification at the University of Oxford or elsewhere. Except where otherwise stated the work within this thesis is entirely my own and has been carried out under the supervision of Professor Julien Devriendt and Professor Adrianne Slyz.

The work presented in this thesis used the DiRAC Data Centric system at Durham University, operated by the Institute for Computational Cosmology on behalf of the STFC DiRAC HPC Facility (www.dirac.ac.uk). This equipment was funded by a BIS National E-infrastructure capital grant ST/K00042X/1, STFC capital grant ST/K00087X/1, DiRAC Operations grant ST/K003267/1 and Durham University. DiRAC is part of the National E-Infrastructure.

Chapter 3 has been submitted to The Monthly Notices of the Astronomical Society on 24/6/20 under the title: **"Rivers of Gas I.: Unveiling The Properties of High Redshift Filaments"**, Marius Ramsøy, Adrianne Slyz, Julien Devriendt, Clotilde Laigle and Yohan Dubois

Chapter 5 has been published in The Monthly Notices of the Royal Astronomical Society under the title: **"How to Quench a Dwarf Galaxy: The Impact of Inhomogeneous Reionization on Dwarf Galaxies and Cosmic Filaments"**, Harley Katz, Marius Ramsoy, Joakim Rosdahl, Taysun Kimm, Jérémy Blaizot, Martin G. Haehnelt, Léo Michel-Dansac, Thibault Garel, Clotilde Laigle, Julien Devriendt and Adrianne Slyz. I performed the analysis of the cosmic filaments for this paper and have reproduced plots that visualise this data and any necessary to draw conclusions on the importance of cosmic filaments. The chapter has been extensively rewritten.

Marius Ramsøy, *August 2020*

Contents

List of Figures

Chapter 1

Introduction

This chapter summarises the state of the field in observations and the theory of filamentary accretion, together with its impact on galaxies and the cosmic web. Chapter 2 will give an overview of the implementation of the hydrodynamics code RAMSES , as well as the methods used to analyse these simulations such as the filament finder DISPERSE . Chapter 3 is a pilot study of the filaments of a single Milky Way (MW) like galaxy, intended to refine the techniques used in Chapter 4, which extends the analysis to a larger sample of galaxies. Chapter 5 explores the effects of reionisation on filaments and the galaxies they feed. Finally, in Chapter 6 the thesis is summarised and gives perspectives for future work.

1.1 Cosmology and Dark Matter

The most fundamental assumptions in cosmology are the principles of homogeneity and isotropy (e.g. Hanson and Lewis, 2009). These principles together extend the view that our place in the Universe, as when Copernicus moved the cosmos from an Earth centric to a sun centred model, is not special. Continuing on in this tradition, arguments on the nature of spiral nebulae, were eventually resolved using distance measurements by Hubble (1926) showing that these spiral nebulae were not objects within our own galaxy, but were in fact galaxies in their own right. Our galaxy, like our Sun before it, was relegated to one of billions of its own kind. Looking out into the Universe in any direction the cosmos appears more or less the same, while on large enough scales ($\sim$ Gpc) the density is more or less constant. We may feed these assumptions into the Einstein Field Equations to obtain the Friedmann equations(Eqs. 1.1 and 1.2) by allowing a, the scale factor of the Universe, as well as densities and pressures to evolve only in time and not as a function of position:

$$H^2 = \left(\frac{\dot{a}}{a}\right)^2 = \frac{8\pi G}{3}\bar{\rho} - \frac{kc^2}{a^2} + \frac{\Lambda}{3}\,; \tag{1.1}$$

$$\frac{\ddot{a}}{a} = -\frac{4\pi G}{3}\left(\bar{P} + \frac{3\bar{\rho}}{c^2}\right) + \frac{\Lambda}{3}\,. \tag{1.2}$$

The evolution of the largest scales in cosmology is given by the Hubble parameter H[1] in terms of the mean density of the Universe $\bar{\rho}$ (which includes the density of all matter, radiation or other exotic gravitating matter), and k determines the Universe's geometry (+1,-1,0 for closed, open and flat Universes respectively). Λ is the dark energy density and finally $\bar{P}$ is the pressure contribution of all the matter in the Universe (including radiation). These equations describe an evolution in the size of the Universe, which was also observed by Hubble (1926). Prior to this, the Universe had been assumed to be static, unchanging and eternal. Strangely the homogeneity in time was traded for one in space instead. Another consequence of this expansion is that the Universe started at some finite time in the past. The first evidence for this (Penzias and Wilson, 1965) was microwave background, emanating from every part of the sky, with perfect uniformity within the precision of their instrument, though this is revised up to 1 part in 10^5 in subsequent measurements e.g. COBE (Mather et al., 1990), WMAP (Dunkley et al., 2009), PLANCK (Planck Collaboration et al., 2018). This is the cosmic microwave background (CMB), the afterglow of the Big Bang made up of radiation released 370 thousand years after the Big Bang when the Universe had cooled enough for atomic nuclei to capture electrons, in an event known as recombination. For the intervening 13.7 billion years this radiation has travelled unimpeded across the cosmos, being stretched as the Universe expanded, cooling to 2.7 K. The big bang also accurately predicts the primordial composition of matter (e.g. Schramm and Turner, 1998). Extensions to the theory include inflation (e.g. Guth, 1981), a short period of extremely rapid expansion required to generate homogeneity and isotropy on scales much larger than the observable Universe. Regions on opposite sides of the sky have the same CMB temperature, despite them being causally disconnected from each other.

In order to make progress in describing our cosmos with the Friedmann equations it is necessary to study its composition. We take the limit $k = 0, \Lambda = 0, \rho_r = 0$ to define the critical density:

$$\rho_C = \frac{3H^2}{8\pi G}\,, \tag{1.3}$$

which allows us to separate the different components of the Universe in terms of various quantities of interest:

$$\Omega_m = \Omega_b + \Omega_{\rm DM} = \frac{\rho_b + \rho_{\rm DM}}{\rho_C}\,, \quad \Omega_k = \frac{1}{a^2}\frac{kc^2}{\rho_C}, \quad \Omega_r = \frac{\rho_r}{\rho_C}, \quad \Omega_\Lambda = \frac{1}{3}\frac{\Lambda}{\rho_C}\,, \tag{1.4}$$

[1] In this work the quantity $\dot{x} \equiv \frac{dx}{dt}$

where $\rho_b, \rho_{\rm DM}, \rho_r$ are the densities for the baryonic matter, dark matter and radiation (which includes relativistic particles such as neutrinos) respectively.

Eq. 1.1 may now be rewritten as

$$H^2 = \left(\frac{\dot{a}}{a}\right)^2 = H_0^2 \left[\Omega_{\rm k,0}(1+z)^2 + \Omega_{\rm r,0}(1+z)^4 + \Omega_{\rm m,0}(1+z)^3 + \Omega_{\Lambda,0}\right] , \tag{1.5}$$

where the 0-subscript signifies that the quantity has been evaluated at $z = 0$. In this form the relative importance of the different terms can be seen and how they evolve with redshift, z. Redshift is a directly observable quantity

$$z = \frac{1}{a} - 1 , \tag{1.6}$$

ranging from $z \to \infty$ at the beginning of time, $z = 0$ at the present and $z \to -1$ as the Universe expands into the far future. As well as defining the past history of our Universe, the Friedmann equation also tells us how it will end, though this is dependant on the exact nature of dark energy. If it remains unchanged from its current state then the cosmos is destined to expand forever at an exponentially increasing pace. Objects which are not gravitationally bound will eventually be torn apart.

1.1.1 The Λ Cold Dark Matter Cosmology

Observations of the kinematics of galaxies within clusters reveal a disparity in the visible mass and the dynamical mass of clusters (e.g. Zwicky, 1937). Similarly, observations of hot, x-ray emitting galaxy clusters show that these structures contain a hidden form of matter, which contributes to the gravitational mass, but does not show up as stars or gas (e.g. Allen et al., 2002). In addition galaxy rotation curves do not follow the expected Keplerian $1/\sqrt{r}$ curve out to large radii, instead they flatten (e.g. Rubin and Ford, 1971). This is indicative of their mass growing roughly linearly with radius. These problems are resolved by adding a dark matter component to the Universe. This is matter only seen through its gravitational effects. It is otherwise non-interacting with ordinary matter. An additional problem solved is that of structure formation. With temperature fluctuations in the CMB having an amplitude of 10^{-5} without DM there is insufficient time to form the structures we see today. In addition without DM, Silk damping (Silk, 1968), causes radiation to diffuse out of overdensities and would smooth out fluctuations of structures with masses less than $10^{11}{\rm M}_\odot$. This is ruled out by observations of dwarf galaxies with much smaller masses than this. As it dominates the mass budget of the Universe, DM

allows the collapse of structures on much smaller scales and for gas to be pulled into them at later times.

Following recombination, a new regime begins where the evolution of the cosmos is dominated first by dark matter and later by dark energy.This is an as yet unexplained component of the universe making up approximately 70% (Planck Collaboration et al., 2018) of the energy density which exerts a negative pressure on the Universe and accelerates the rate of expansion. Statistically the best fit to the data is the ΛCDM model. The dark matter is termed 'cold' as it has a negligible thermal velocity initially. 'Hotter' models of dark matter smooth out small scale fluctuations, resulting in fewer low mass galaxies.

1.1.1.1 Large Scale Structure

While homogeneity holds in the Universe on extremely large scales it does break down; on smaller scales we observe galaxies, clusters of galaxies and the ordering of these structures into filaments and voids. Primordial quantum fluctuations during inflation result in small scale inhomogeneities in the density field with a power spectrum of the form

$$\mathcal{P}_{\rm prim}(k) = Ak^{n_s}\,, \tag{1.7}$$

where k is the spatial wavenumber, and n_s is the spectral index. These inhomogeneities tend to grow under the action of gravity. Ignoring the pressure exerted by baryonic matter, the equations we have to solve are the continuity, Euler and Poisson equations:

$$\frac{d\rho}{dt} + \nabla\cdot(\rho\mathbf{u}) = 0\,; \tag{1.8}$$

$$\rho\frac{d(\rho\mathbf{u})}{dt} = -\rho\nabla\phi\,; \tag{1.9}$$

$$\nabla^2\phi = 4\pi G\rho\,. \tag{1.10}$$

Linearising these equations, expressing in comoving coordinates and taking the Fourier transform yields:

$$\frac{d^2\delta(\mathbf{k},t)}{dt^2} + 2\frac{\dot{a}}{a}\frac{d\delta(\mathbf{k},t)}{dt} - 4\pi G\bar{\rho}\delta(\mathbf{k},t) = 0\,, \tag{1.11}$$

where δ is the density contrast, $(\rho-\bar{\rho})/\bar{\rho}$. Note that the equation has no scale dependence, which means that these fluctuations can readily be followed up until the density contrast $\delta \lesssim 1$ beyond which point the non-linear effects become important. In all but the simplest cases the evolution of matter can be followed into this regime without significant computational resources. A useful example of when the collapse can be followed analytically is the spherical collapse model (Gunn and Gott, 1972). In this model a spherical overdensity is followed in an otherwise homogeneous, expanding Universe. The overdensity initially

expands with the Universe, before a point of maximum expansion and then collapses to a singularity. In reality the spherical symmetry is imperfect, resulting in different parts of the collapsing object reaching the centre at different times. The fluctuating potential allows the exchange of energy between collapsing shells, preventing the complete collapse, in a process known as virialisation. Despite the observed structures not forming under such an idealised set up, the DM halo mass function of the Universe can be derived reasonably well by applying spherical collapse to the initial density field (Press-Schechter formalism, Press and Schechter, 1974). However, in order to understand the fundamental physics at play in more complex and interacting environments, and especially the behaviour of baryons it is necessary to turn to computational modelling.

1.1.1.2 The Origins of Galaxies

Dark matter clusters hierarchically, forming halos with masses down to around $1M_{\oplus}$ for cold DM, with the exact cut off mass being dependant on the nature of the dark matter particle (Loeb and Zaldarriaga, 2005). These halos merge to form larger halos as time progresses, as described by (Press and Schechter, 1974). The formation of galaxies therefore is a two stage process (White and Rees, 1978), with the galaxy forming later in the potential of the DM halo. Due to thermal pressure in the baryonic component, the potential of low mass DM halos is largely ignored by the gas. However once halos reach a sufficient mass, the virial temperature rises to be greater than the atomic cooling limit temperature of the gas, causing it to be trapped in the DM potential and radiatively cool. This reduces the gas pressure, causing collapse, increased density and therefore even greater cooling. The collapse is eventually halted by rotational support from the angular momentum intrinsic to the collapsing cloud, followed by the fragmentation of the resulting disk. This leads to the birth of the first stars, termed Population III. These stars have proved to be extremely elusive, with most evidence for their existence being indirect (e.g. Audouze and Silk, 1995) suggests that the variation in the metallicity of metal poor stars is due to the poorly mixed remnants of this generation from a small number of very large stars. These stars are likely to be too faint (Schaerer, 2002) to detect even with the next generation of instruments, such as JWST (Gardner et al., 2006), Euclid (Laureijs et al., 2011) or the Extremely Large Telescope (Tamai and Spyromilio, 2014), though the SN of these stars should be visible (Hummel et al., 2012).

As the first stars explode in supernovae, the cosmos is polluted with metals (any element heavier than Helium is labelled a metal in the context of astronomy) and black holes, which are thought to be the seeds of today's supermassive black holes, are left behind. A galaxy is the sum of all these components, i.e. a gravitationally bound collection of stars, dust, gas,

black holes of various types, all residing within a DM halo. A galaxy's stellar mass can be anywhere from $M_* \approx 10^{12} M_\odot$ in the largest galaxies in the centres of clusters, down to only a few hundred thousand stars in ultra-faint dwarf galaxies.

1.1.1.3 Galaxy Evolution

The holy grail of galaxy evolution is to reproduce the vast diversity in galactic morphology observed in the Universe using the initial conditions imposed by the spectrum of the CMB and our knowledge of fluid dynamics, general relativity and stellar physics. The ΛCDM halo mass function does not have the same shape as the local galaxy stellar mass function (GSMF), tending to produce too many high and low mass galaxies. To counter this inconsistency, stellar feedback to suppress the low mass galaxies and AGN feedback to suppress the high mass end are invoked. Simulations which include both these modes of feedback are now able to reproduce the shape of the GSMF e.g. Puchwein and Springel (2013); Dubois et al. (2014a); Davé et al. (2016, 2019), see Fig. 1.1.

Galaxies with stellar masses below approximately $10^{10} \mathrm{M}_\odot$ are suppressed by supernova feedback (Dekel and Silk, 1986), which can drive outflows at a similar rate to star formation. Above this mass supernova feedback becomes insufficient, and cannot drive fast enough outflows to overcome the potential of the halo (Dekel and Silk, 1986; Somerville and Primack, 1999) and are therefore not efficient at suppressing star formation. However, these larger galaxies also host supermassive black holes which are capable of driving outflows and heating the galactic and circumgalactic gas (Beckmann et al., 2017).

While mass is the primary characteristic of a galaxy, morphology comes a close second. Morphology can be separated into two broad classes, ellipticals and disks. Massive galaxies tend to be redder, spheroidal and quenched, as opposed to the less massive and star forming blue disks (Kauffmann et al., 2003). Observationally galaxies are also separated by colour (Strateva et al., 2001; Baldry et al., 2004; Balogh et al., 2004). At low redshift this occurs as a result of quenching. Galaxies are in some way prevented from forming stars, resulting in a redder, and older galaxy population. While galaxies in general can be separated into these two populations, there also exist red disk galaxies (e.g. Davidge et al., 2012) and blue ellipticals (e.g. George, 2017) which our models of galaxy formation must also be able to explain.

1.1.2 Disk Galaxies

Disk galaxies are rotationally supported, though they may also have a dispersion dominated central bulge or pseudo bulge component. Bulges have more in common with elliptical

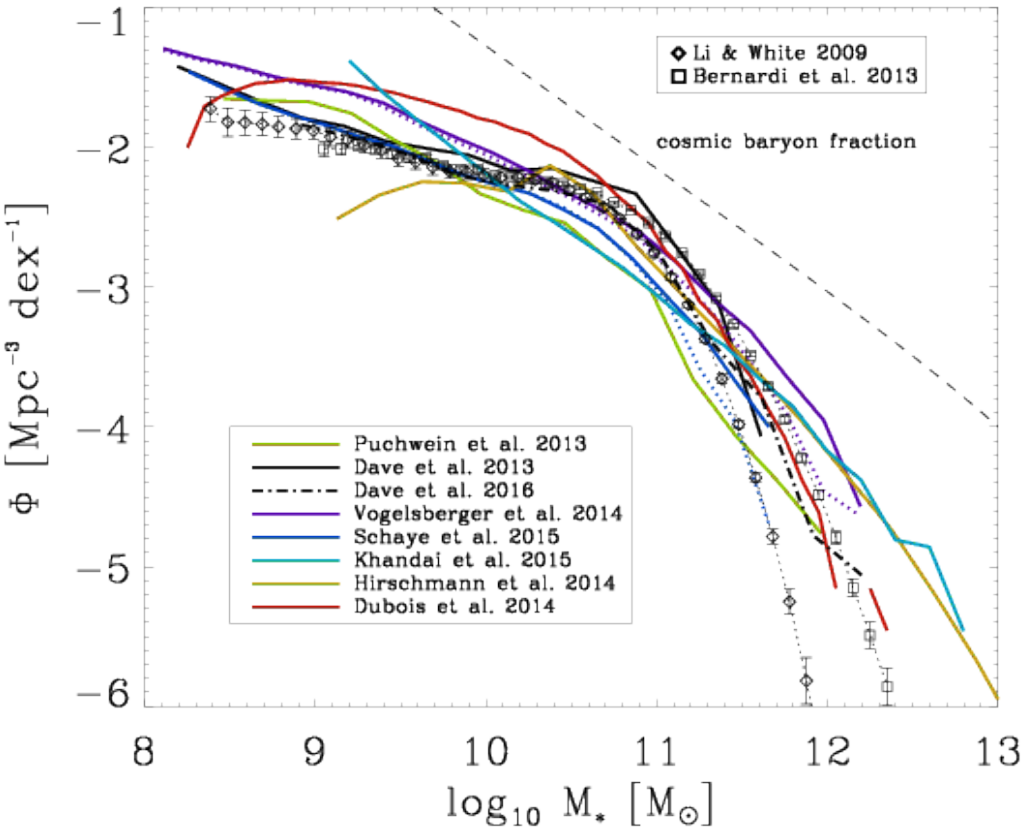

Figure 1.1: Comparison of the stellar mass functions from a range of range of simulations using SPH, moving mesh and grid based codes (*coloured* lines). Observations are marked with symbols. The dashed line marked as the cosmic baryon function is the halo mass function scaled to 15%. Modern simulations tend to reproduce the stellar mass function seen in observations. Reproduced from Naab and Ostriker (2017).

galaxies than with the disk component. Disk galaxies tend to have higher star formation rates and high gas fractions. Though disks exist at high redshifts (e.g. Labbé et al., 2003; Förster Schreiber et al., 2009; Kriek et al., 2009), high merger rates work to destroy these ordered structures. As a result it is believed that, modern day spirals emerge around $z = 1$, the so-called epoch of disk settling (Kassin et al., 2012). Disk galaxies show a number of features derived from instabilities such as bars and spiral arms, which can lead to enhancements in star formation and the channelling of gas into the galactic core. Metallicity gradients in disk galaxies lend support to them forming inside out, with progressively younger stars found at larger radii (e.g. MacArthur et al., 2004).

Gas is recycled within these systems with a galactic fountain, where pre-enriched gas cast out by feedback rains back down on the disk at later times, potentially causing the condensation of halo gas (e.g. Fraternali and Binney, 2008).

1.1.3 Elliptical Galaxies

Elliptical galaxies are dispersion dominated, typically have higher mass, lower star formation rates and are composed of an older stellar population than spiral galaxies. In large halos, gas should cool efficiently onto them, triggering star formation rates of $\sim 100 \mathrm{M}_{\odot} \mathrm{yr}^{-1}$. However, this is not observed, suggesting that the gas must be kept hot to prevent these 'cold flows' from forming. The source of this heating is thought to be the central super massive black hole powering an AGN. This also keeps gas within the galaxy hot, further suppressing star formation. These galaxies lie off the star formation main sequence and are said to be quenched. Elliptical galaxies first grow their stellar component in situ, while later growth occurs by accreting other galaxies (e.g. Naab et al., 2007).

Interactions can transform galaxies between the two types, e.g. ellipticals into spirals by merging with a gas rich galaxy. The fresh gas is able to cool to form a new, rotationally supported gas disk and slowly transform this into stars. The reverse can occur where a merger disrupts the disk of a spiral and removes the ordered motion of the disk. As well as mergers, less dramatic environmental influences can also drastically alter the fate of a galaxy. In group environments harassment (close encounters with neighbours), strangulation (gas accretion cut off by entering a hot halo) and ram pressure stripping (orbital motion through the hot intracluster gas removes gas from the galaxy) play a role in determining the evolution of galaxies. This summary only briefly covers the general properties and effects relevant to galaxy evolution in order to provide context for the effect of gas accretion on halos from the cosmic web.

1.2 The Cosmic Web

The cosmic web is apparent in large scale surveys (e.g. Geller and Huchra, 1989; Gott et al., 2005; Hwang et al., 2016) as a density enhancement which can easily be picked out by eye, traced by the distribution of galaxies themselves. Early cosmological simulations showed signs of filamentary structure similar to those seen in large scale surveys, see Fig. 1.2. By computing the eigenvectors of the tidal field and following the particle trajectories Zel'Dovich (1970) was able to show that arbitrary perturbations of an otherwise homogeneous medium collapse to form a flattened ellipsoid. Subsequently Bond et al. (1996) realised that the filamentary structure was encoded in the initial conditions of the Universe, bridging the gap between the peak density regions containing clusters and the voids which contain considerably fewer galaxies, and that the so-called 'Zel'dovich' pancakes were further able to collapse to form filaments which finally collapsed into halos.

1.3 Cosmic Filaments

When forming a protohalo the angular momentum of a region grows until the region decouples from the expansion of the Universe and begins its collapse. After this point the angular momentum is fixed, resulting from a a misalignment of the tidal tensor and the inertia of the protohalo. This is Tidal Torque Theory (Hoyle, 1951; Peebles, 1969; Doroshkevich, 1970; White, 1984). While TTT does fairly well at predicting the amount of angular momentum of halos, it does not explain how halos are found to have preferential alignments with the large scale structure, filaments on Mpc scales, with a mass dependence. Aragón-Calvo et al. (2007b); Codis et al. (2012); Welker et al. (2014); Codis et al. (2015); Kang and Wang (2015); Laigle et al. (2015); Wang and Kang (2017, 2018) find that galaxies below a redshift dependent threshold mass are aligned with the cosmic web, whereas larger galaxies are perpendicular to it.

Laigle et al. (2015) proposed a toy model where the vorticity quadrupole of the filament (see Fig. 1.3) determines the spin of the gas accreted onto the galaxy and thereby the direction of its angular momentum. Halos which are small enough to fit into a single quadrant are able to coherently build up angular momentum and align with its local quadrant. However, as the halo the galaxy resides in grows, it can cross into other quadrants, with differing angular momentum, which will tend to decrease the alignment. Since these galaxies are formed primarily from mergers along the filament, orbital angular momentum during the merger is transformed into halo spin, realigning the spin direction to be perpendicular to the large scale filament direction. However, these effects are weak, only resulting

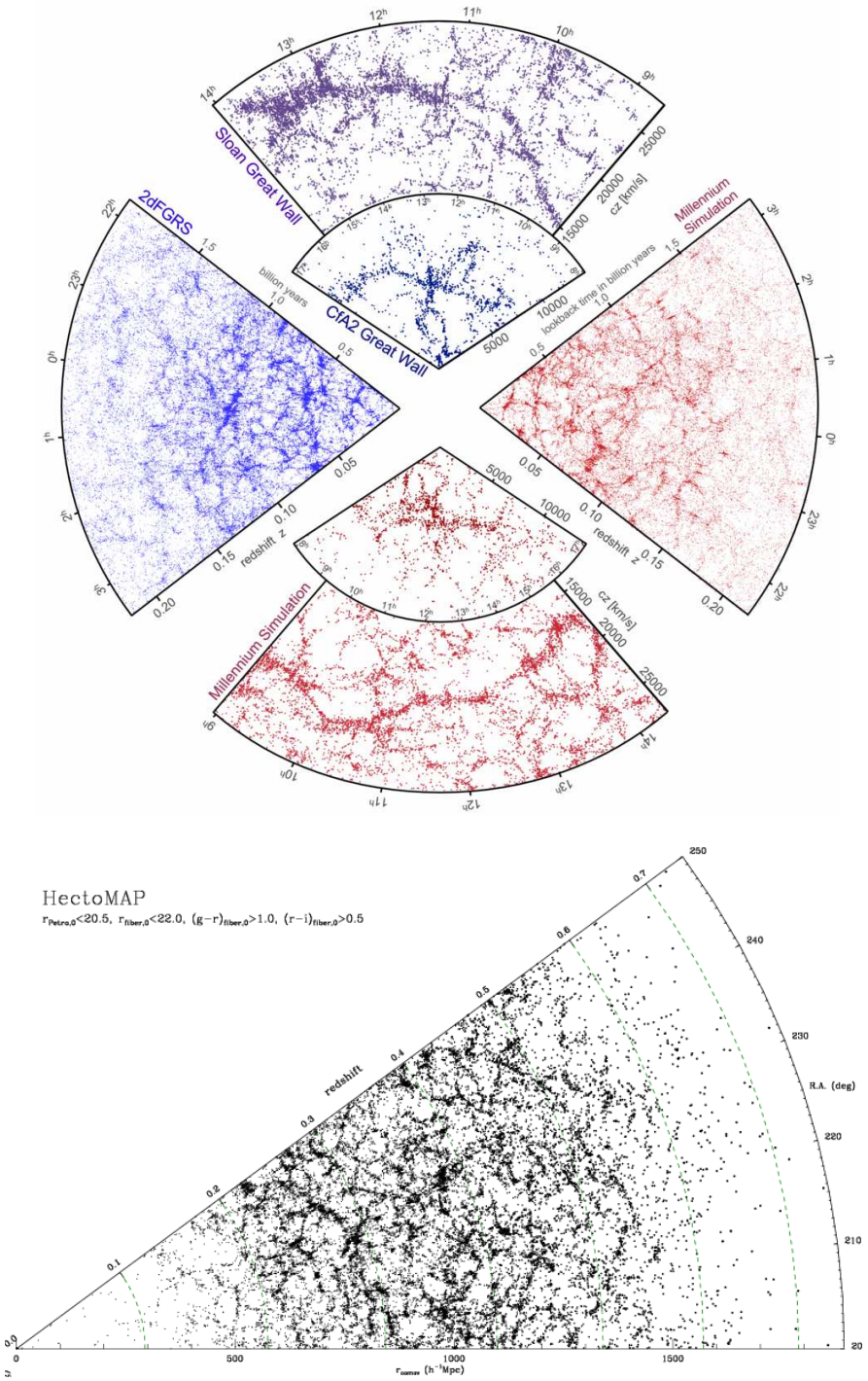

Figure 1.2: *Top* figure shows the distribution of galaxies across the Universe in *blue*. *Red* shows the distribution of halos in the MILLENIUM simulation (Springel et al., 2005) of comparably sized regions, reproduced from Springel et al. (2006). In the *bottom* plot, the Cosmic Web is revealed by the spectroscopic survey HECTOMAP, reproduced from Hwang et al. (2016). The filamentary arrangement of galaxies, and their connections at nodes can clearly be seen in all cases, in both the real and simulated versions of the cosmos.

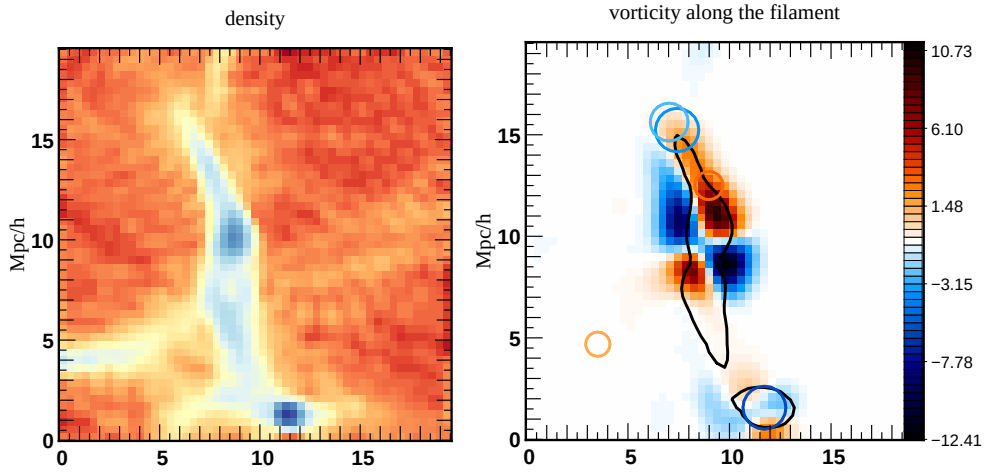

Figure 1.3: *Left* shows the density field of a filament looking along the filament axis. The filament is flattened in the direction of the wall it is embedded in. *Right* shows the same region in vorticity instead, with the isodensity contour. Vorticity oriented towards the observer in red. Similarly circles with spins oriented towards the observer are red, and circle size is proportional to the virial radius. The large scale filaments show a vorticity quadrupole. Reproduced from Laigle et al. (2015)

in a slight excess in probability of alignment or misalignment. The tidal forces exerted by filaments are considerably smaller than those acting within a halo itself, and as a result do not have a strong influence on the properties of the central galaxy. Smaller scale filaments however, can act as a bridge between the scales of the cosmic web and the halos residing within.

Conditional TTT (Codis et al., 2015) is an extension to the TTT model of angular momentum acquisition which predicts this transition mass between alignment and non-alignment based on proximity to filaments, explaining results found in cosmological simulations (Aragón-Calvo et al., 2007b; Hahn et al., 2007; Codis et al., 2012; Trowland et al., 2013; Wang and Kang, 2017), performed with a diverse range of techniques (SPH, AMR and moving mesh).

1.4 Cold Mode Accretion

As well as existing on Mpc scales, filaments of much smaller scales also feed halos and galaxies. These connections are much more direct and could be, at least partially, responsible for the present day bimodality in the galaxy population is (e.g. Baldry et al., 2014). Dekel and Birnboim (2006) suggested that the ability to accrete cold gas directly into a galaxy, could drive differences in star formation, stellar age, colour and morphology.

Birnboim and Dekel (2003) explored the stability of gas which experiences cooling after shocking as it is accreted. In order to achieve this a generalised shock stability criterion was developed

$$\gamma_{\rm eff} \equiv \left(\frac{d\log P}{d\log\rho}\right)_S = \frac{\dot{P}}{P}\frac{\rho}{\dot{\rho}} > \frac{2\gamma}{\gamma + 2/3}\,, \tag{1.12}$$

where $\gamma_{\rm eff}$ is the effective adiabatic index, P and ρ are the pressure and density, and γ is the adiabatic index of the gas.

Using idealised simulations with spherical symmetry, the authors found that halos with masses below a few $10^{11}{\rm M}_\odot$ cannot sustain a stable shock at the virial radius at any redshift, showing that the halos will always accrete via the cold mode. It was also found that for higher masses there exists a critical redshift after which the virial shock stabilises and prevents direct accretion into the halo (see Fig. 1.4). Intuitively this cut-off makes sense as the ratio of dynamical time to cooling time determines whether accreted gas is able to acquire pressure support against collapse before it reaches the galaxy. If the accretion shock is unstable, a hot halo is not formed (e.g. Kereš et al., 2005; Ocvirk et al., 2008a; Brooks et al., 2009; Dekel et al., 2009). This transition mass which separates stable and unstable shocks lies suspiciously close to the observed bimodality mass scale.

The simulations considered by Birnboim and Dekel (2003) are spherically symmetric, while the accretion flow from the cosmic web they are attempting to model is filamentary and anisotropic. While these methods provide approximate limits on when cold mode accretion can occur, only detailed three dimensional simulations can realistically probe this accretion mechanism for fuelling high redshift star formation. Nevertheless, Mandelker et al. (2016) used perturbation theory to explore the stability of perturbations to a dense cylinder of gas moving with respect to a rarefied background medium in the linear regime. Padnos et al. (2018); Mandelker et al. (2019); Berlok and Pfrommer (2019a) extended this to the non-linear regime. It was found that filaments are stable against disintegration by Kelvin-Helmholtz instability provided the filament is sufficiently wide, and fast flowing. The minimum thickness for a stream to survive for a virial crossing time was between $0.005R_{\rm vir}$ and $0.05R_{\rm vir}$. Various extensions to this work have been done, e.g. Pfrommer et al. (2017); Berlok and Pfrommer (2019b) added a magnetic field to stabilise the magnetic filament and found that this tends to extend the lifetime of the filament by preventing hot and cold gas from mixing. Aung et al. (2019) added self gravity, finding that the filaments can be more than 3 times thinner than in the case of Mandelker et al. (2019). Mandelker et al. (2019) added radiative cooling, and find that this also stabilises the filament, even causing them to grow in some astrophysically important parts of the parameter space, by condensing hot gas onto the filament stream. This could potentially be a driver of Ly-α

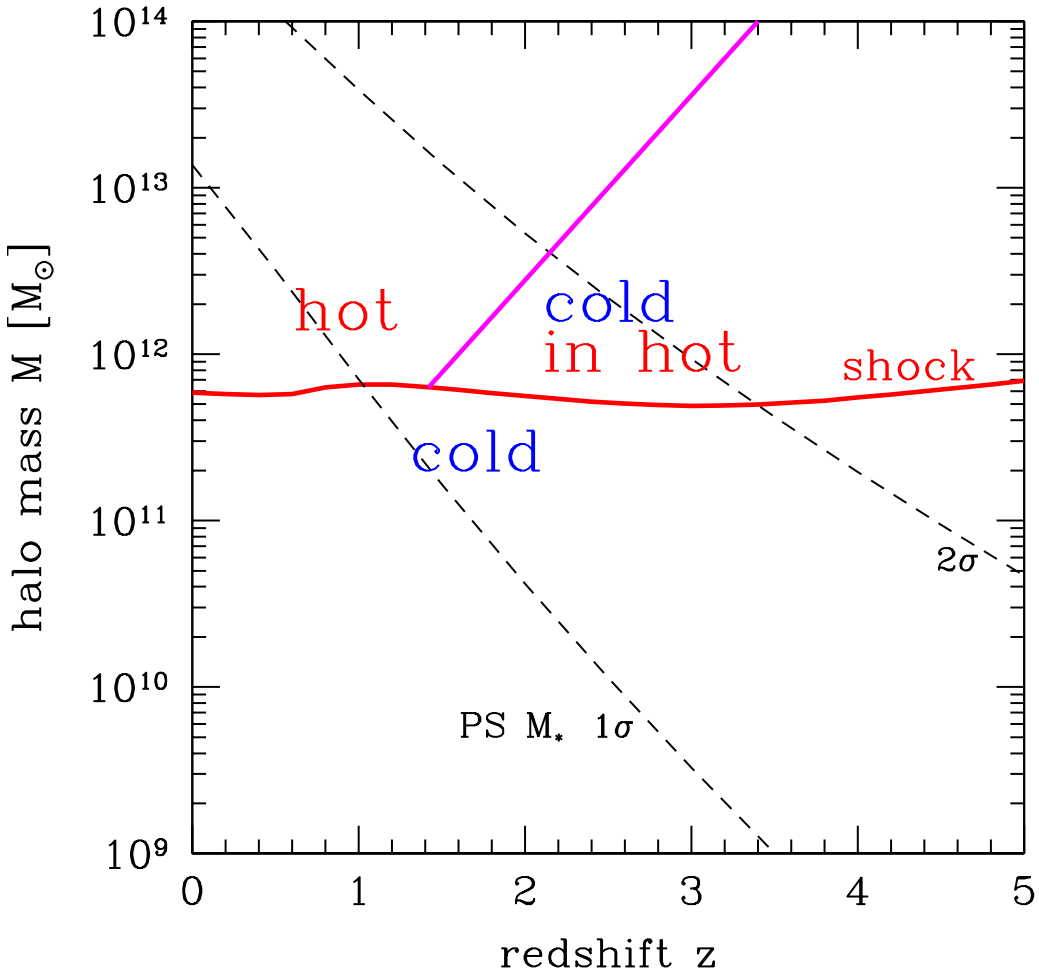

Figure 1.4: Determination of the accretion mode and its evolution across cosmic time. The dashed lines show the evolution of typical halos according to the Press-Schechter (Press and Schechter, 1974) formalism. The horizontal red line shows that halos with masses below $10^{11}\mathrm{M}_{\odot}$ can accrete via the cold mode. The pink line divides halos that can only accrete via the hot mode from those whose filaments can survive even in a hot halo. Reproduced from Dekel and Birnboim (2006).

radiation from the streams which would be observable. The KHI was also found to be responsible for 10-50% of the dissipation of energy gained from accretion by the DM halo, which could be partly responsible for the lack of acceleration in gas accreted by filaments (Dekel et al., 2009; Goerdt and Ceverino, 2015). While these studies tend to look at whether the filaments can remain stable, if this is not the case, then their subsequent breakup could go on to form cold clouds dispersed across the hot halo, which would still carry angular momentum (Kereš and Hernquist, 2009; Wetzel and Nagai, 2015; Oppenheimer, 2018; Melso et al., 2019). This could be partially responsible for the creation of the High Velocity Clouds around the Milky Way (Oort, 1970; Fraternali et al., 2015)

In all these cases the filament is highly idealised, and as more complex physics is included, the more difficult and time consuming the parameter space becomes to explore. It quickly becomes necessary to study filaments using full cosmological simulations to capture their environment and formation processes, external DM potential as well as cooling. A pioneer study looking at the accretion history of the gas was Kereš et al. (2005). They found that approximately half of the gas for a Milky Way-like galaxy accretes via the cold mode, preferentially arriving via filaments. In addition they also found that galaxies in halos with masses less than $10^{11.4}\mathrm{M}_{\odot}$ have their accretion histories dominated by the cold mode, in agreement with Dekel and Birnboim (2006). Note that in spite of questions of stability, cold mode accretion flows are ubiquitous in cosmological simulations (e.g. Ocvirk et al., 2008b; Ceverino et al., 2010; Faucher-Giguère and Kereš, 2011; van de Voort et al., 2011; Harford and Hamilton, 2011; Tillson et al., 2015; Katz et al., 2019), no matter the technique employed to model the hydrodynamics, even though meshless codes such as AREPO (Vogelsberger et al., 2012) suggest that the streams break up before reaching $0.5R_{\mathrm{vir}}$ (Nelson et al., 2013).

As a result of being thermalised in the hot halo of a galaxy, the angular momentum accreted by the galaxy is relatively small. Thus, in order to build a large gas disk it is necessary to accrete gas via the cold mode. Pichon et al. (2011) propose that filaments join smoothly onto the gas disk, building the disk from the inside out as more angular momentum rich gas is accreted, and converts its orbital velocity into rotation (Kereš et al., 2005; Keres, 2009; Tillson et al., 2015; Stewart et al., 2017; El-Badry et al., 2018; Ho and Martin, 2019). Tillson et al. (2015) find that 90% of gas mass and angular momentum is accreted via the cold mode for a Milky Way-like galaxy at high redshift. In addition Klessen and Hennebelle (2010) suggests that cold mode accretion could be a driver of the highly turbulent star forming disks seen around $z = 2$.

1.5 Observational Evidence for Filaments

At present, direct evidence for filamentary gas accretion remains weak. In this section I will first focus on the direct observations of the cosmic web and cold streams before moving onto less direct methods that imply the presence of filamentary accretion.

1.5.1 Direct Detection of the Cosmic Web

The cosmic web is made up of two visible components, the galaxies of the Universe, and the gas which also exists within the filamentary network. While the galaxies are easily observable, and is itself used to probe the cosmic web, (e.g. Erdoğdu et al., 2004), the gas filling these filaments, the Warm Hot Intergalactic Medium (WHIM), is not. The WHIM is predicted by simulations to contain approximately 30-40% of the baryonic matter in the Universe. The "missing baryon problem" represented an issue for cosmology as the observed baryonic matter making up galaxies only accounts for $\sim$ 50% of all baryonic matter. However, X-ray emitting bridges of hot gas have been detected (Werner et al., 2008), and inverse scattering off of CMB photons (Planck Collaboration et al., 2013) has been able to show that vast quantities of gas are present in the filaments between clusters. This constitutes the large scale cosmic web, within which the cold mode accretion flows must reside.

While the WHIM contains hot gas observable in X-rays, the cold mode, smaller scale accretion filaments do not. The gas within these filaments is accreting onto galaxies for the first time, and as a result is nearly pristine with primordial metal abundances. As a result, the only significant cooling that can occur is collisional excitation followed by decay to the ground state of hydrogen. This process becomes extremely inefficient at temperatures below 10^4 K. Indeed, direct observations in emission of the distant cosmic web are extremely challenging (Giavalisco et al., 2011; Ribaudo et al., 2011; Kacprzak et al., 2012; Martin et al., 2016; Gallego et al., 2017) as they are also hampered by the the unfavourable scaling of surface brightness with redshift.

Novel techniques have been required for the detection of cold mode accretion filaments as a result of this. Gallego et al. (2017) stacked images of galaxies, rotating them such that nearest neighbours were aligned (see Fig. 1.5). This resulted in a 3σ detection of the filaments, comparing the profile of emitted radiation from the region in the direction of the nearest neighbour to the perpendicular direction. Essentially comparing the profile from the centre of the image to the purple arrow and any other direction yields an enhancement above the noise, seen as the small grey enhancement in this direction in the image. The structure does not extend far from the galaxy's influence. Part of the problem with this technique lies

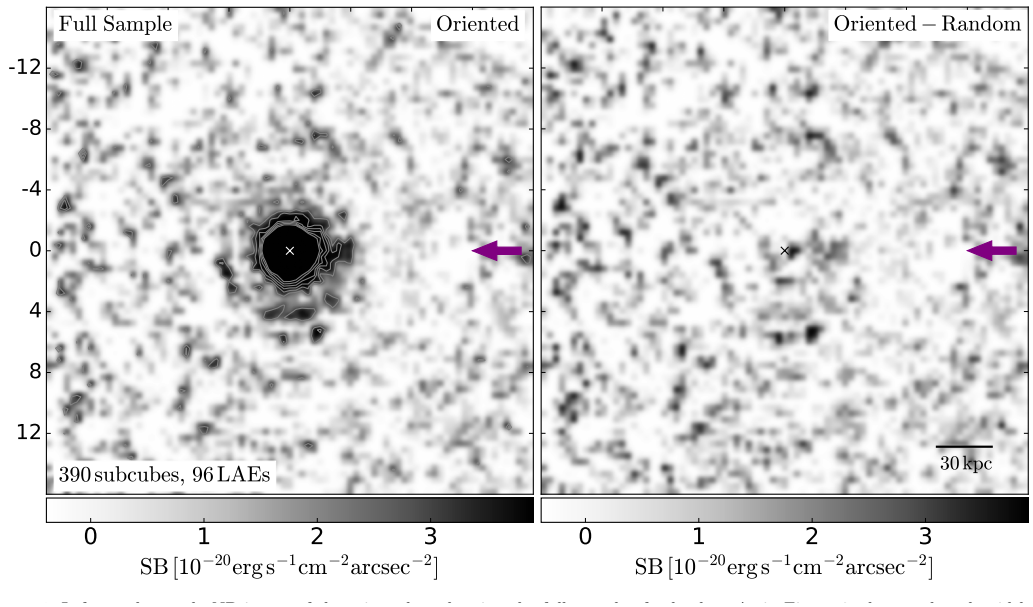

Figure 1.5: Detection of an asymmetry in the Lyman-α emission around galaxies. The *left* panel represents a stack of 390 reoriented subcubes, with nearest neighbours oriented towards the *purple* arrow. On the *right* randomly oriented subcubes are subtracted from the previous stack, removing most of the rotationally symmetric noise, but crucially leaving the slight asymmetry in the image. The effect of the stacking is not obvious, however, taking transects from the centre of the image to the edge yields a 3 σ signal towards nearest neighbours compared to background noise in other directions. The signal also does not extend far from the galaxy stack centre. Reproduced from Gallego et al. (2017)

in the lack of knowledge of the cosmic web. It is not a priori possible to determine whether or not two galaxies are connected by a filament and thus an enhancement of the signal is not always guaranteed.

An alternative relying on the passive emission of hydrogen is to probe environments that have an additional energy source. Cantalupo et al. (2014) used the Lyman-α fluorescence of the cosmic web in order to detect the cold gas component, stimulated by the close proximity of a bright quasar, distinguished by using a narrow band filter to detect only Lyman-α emitted directly by the filament gas. Umehata et al. (2019); Kikuta et al. (2019) find evidence of filaments extending out to Mpc scales, with particular enhancements in Lyman-α blobs (LABs) and Lyman-α emitters (LAEs) tracing the cosmic web. This is shown in Fig. 1.6.

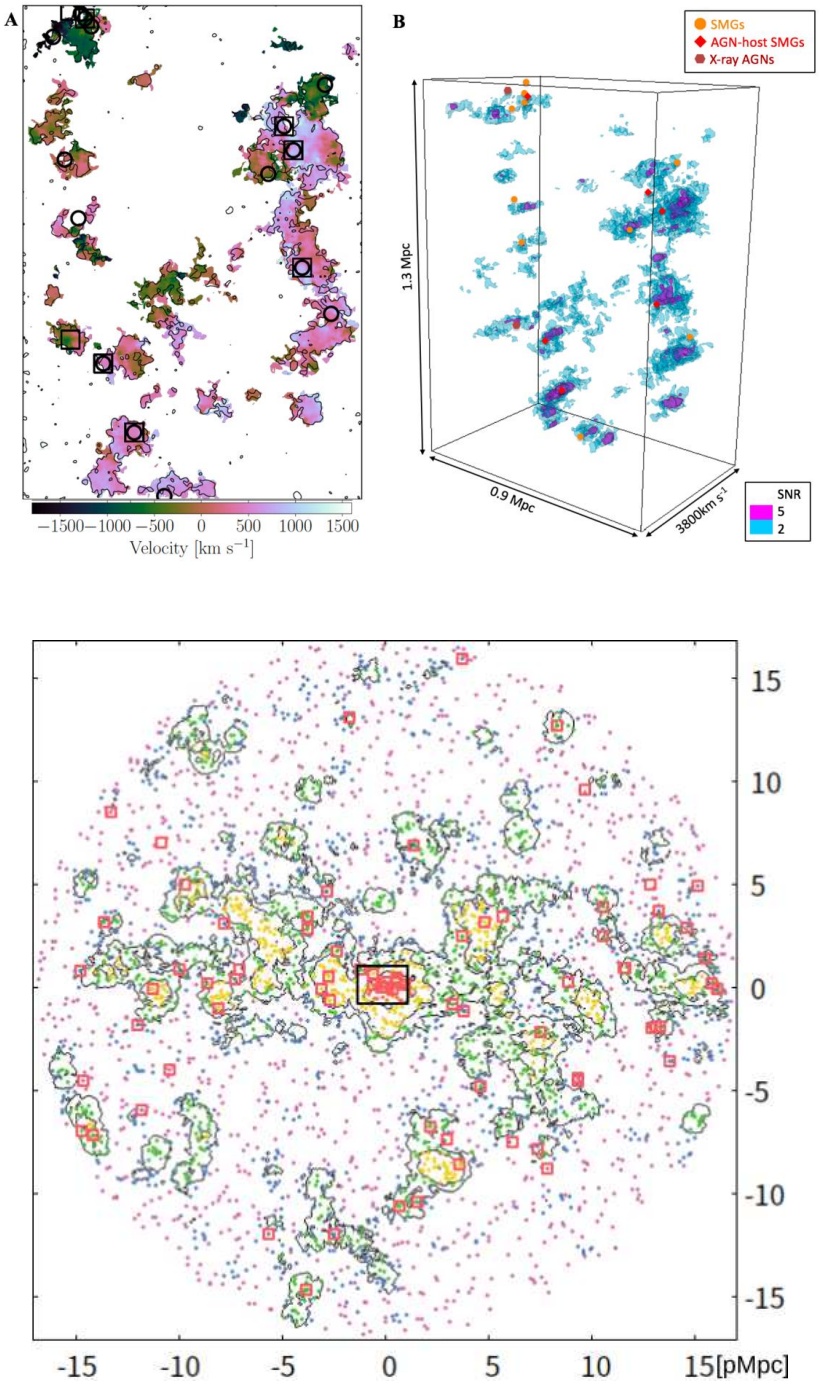

Figure 1.6: *Top left* panel shows velocity map of the Ly-α emission, showing coherent velocities along the filaments. In the *top right* panel colour represents the signal to noise ratio of the Ly-α detection, with galaxies marked by symbols. Reproduced from Umehata et al. (2019). *Bottom* shows distribution of LAEs as points, with LABs indicated by the red squares around a central quasar located within the black rectangle. Reproduced from Kikuta et al. (2019). In all panels the filaments are traced by the Ly-α blobs and emitters.

1.5.2 Indirect Detections of the Cosmic Web

1.5.2.1 Extended Disks

Some indirect observations take advantage of grazing incidence of quasar sightlines around galaxies in order to detect corotating extended disks, Stewart et al. (2011, 2013); Ho and Martin (2019) suggest that these disks could extend out to 100kpc, see Fig. 1.7. The presence of coherent rotating flows driven by accretion provides a much greater volume for interception of quasar sightlines than the filament alone. The filaments themselves are typically confined to a plane surrounding the galaxy (Danovich et al., 2012), and have a very small covering fraction.

While extended disks are not a direct detection of the filament itself, they are strong evidence of recent filamentary accretion, as they form from angular momentum rich filamentary gas, before later draining onto the galactic disk. Extended disks have been observed in the distribution of Mg II velocities (e.g. Charlton and Churchill, 1998; Steidel et al., 2002; Kacprzak et al., 2010; Bouché et al., 2013; Prochaska et al., 2014; Bouché et al., 2016; Ho et al., 2017; Ho and Martin, 2019; Zabl et al., 2019) in absorption and as well as in emission (e.g. Steidel et al., 2000; Matsuda et al., 2006, 2011; Cantalupo et al., 2014; Martin et al., 2014a,b; Borisova et al., 2016; Fumagalli et al., 2017; Leclercq et al., 2017; Arrigoni Battaia et al., 2018; Martin et al., 2019). This is also consistent with corotation detected in other bands, e.g. Ly-α (French and Wakker, 2020) and reveals large quantities of cold gas in spatial coherence with the galaxy itself. Such extended disks are predicted in simulations (e.g. Fumagalli et al., 2011; Goerdt et al., 2012; van de Voort et al., 2012).

As well as detections of extended disks, filamentary accretion of gas onto the disk can create a warp (e.g. Rahmani et al., 2018). This has been observed in Bournaud et al. (2005) in isolated galaxies, which suggested that the warp signature could not be entirely explained by interactions with neighbours.

1.5.2.2 Observations in Lyman-α

The Lyman-α forest is a spectral feature caused by the absorption of radiation by intervening gas atoms along the line of sight from a bright background source. As the radiation travels it gets redshifted by the expansion of the Universe and radiation is resonantly scattered out of the line of sight by intervening hydrogen at the Lyman-α wavelength local to that hydrogen cloud, or 'Lyman-α blob'. A 'forest' structure emerges as the process occurs many times, leaving a series of spikes as described in Bahcall and Salpeter (1965). Various authors (Cen et al., 1994; Petitjean et al., 1995; Hernquist et al., 1996; Bi and Davidsen,

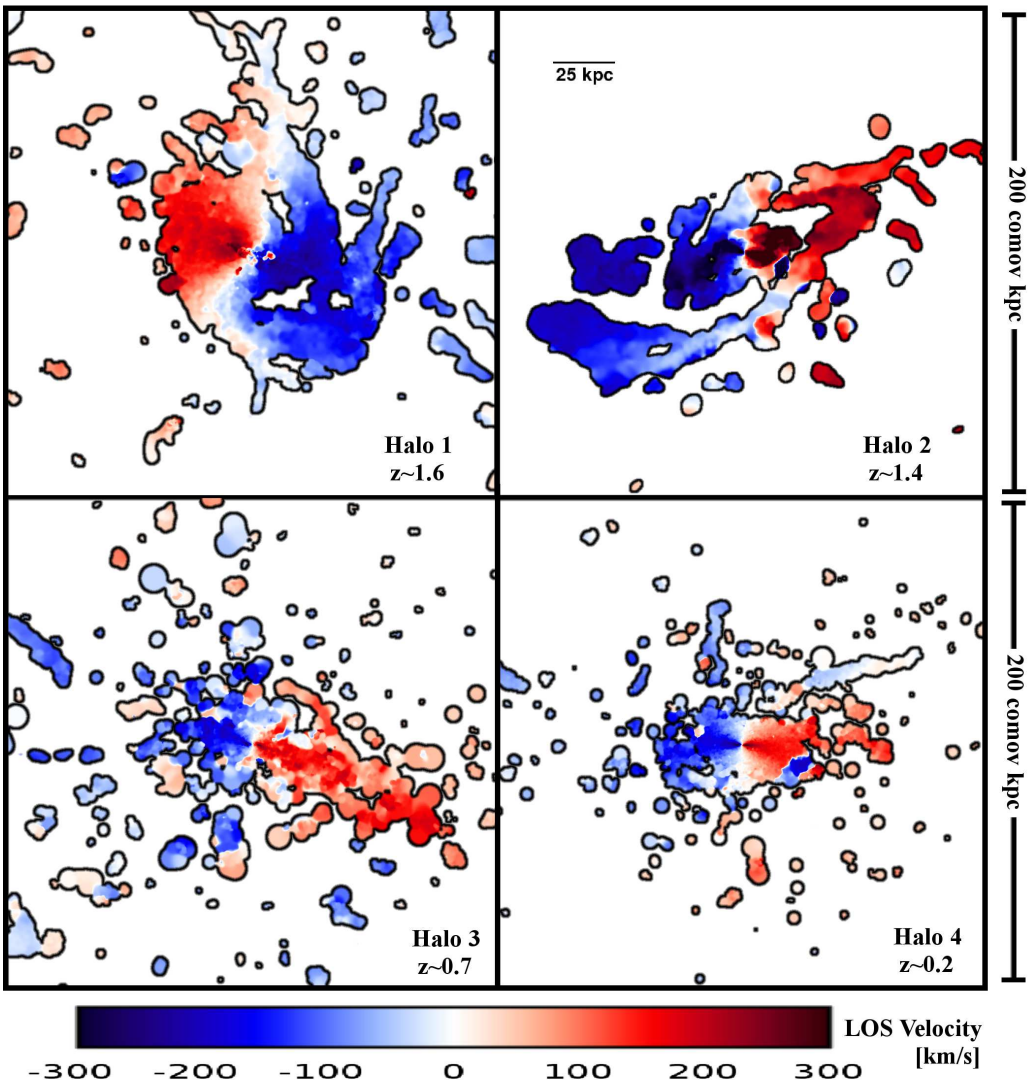

Figure 1.7: The line of sight velocities for 4 simulated halos. Each exhibit an extended disk, far beyond the confines of the central galaxy, each fed by cold mode accretion streams, accounting for 70% of the angular momentum accreted by these galaxies. Note that the streams themselves are lower density than the threshold used to create the image so are not visible themselves. The disk here is viewed nearly edge on, with $i > 65°$. Reproduced from Stewart et al. (2013).

1997) showed that the Lyman α forest seen in observations could be reproduced if primordial gas within filaments were the absorbing medium, with successive models able to place constraints on cosmology. These structures appear to be coherent over 2Mpc, while only being 30kpc across. Since scattering is $\propto \rho^2$, the expected overdensity of these structures is 10, and are as such only weakly non linear. Lyman-α surveys have been conducted (Press et al., 1993; Press and Rybicki, 1993; Lee et al., 2013) to extract the statistical properties of these structures.

Related to the Lyman-α forest are the Damped Lyman Alpha systems (DLAs). These have higher column densities of $N_{\rm HI} > 10^{20}{\rm cm}^{-2}$ and are more closely associated galaxies. The observations only give access to line of sight variation and not angular variation. Bright sources that can be used for Lyman-α forest detection are rare on the sky, so are difficult to use for constraining the angular extent of these objects. However, Dijkstra and Loeb (2009) was able to show that Lyman-α blobs could be powered by undergoing cold mode accretion. This could, in the future provide constraints on these elusive structures.

1.5.2.3 High Redshift Kinematics

At $z = 2$ galaxies are observed to be highly turbulent and star forming (Genzel et al., 2006). Since turbulence tends to decay on a sound crossing timescale (Mac Low and Klessen, 2004) this requires a constant driving force, ruling out catastrophic mergers. The disky nature of the galaxies places additional constraints on the driving force, requiring it to coherently add angular momentum, thus limiting the role played by supernova feedback. This strongly suggests that these galaxies are stream fed (Klessen and Hennebelle, 2010).

It has also been shown that $z = 2$ is the epoch of disk settling (Kassin et al., 2012; Simons et al., 2017), with galaxies of higher masses tending to settle earlier, both observationally and in simulations (Pillepich et al., 2019; Park et al., 2019). This epoch coincides with the dwindling of filamentary accretion in cosmological simulations (e.g. Kereš et al., 2005, shows that cold mode accretion is at half the peak accretion rate around $z = 2$, and continues to decline exponentially), suggesting that they are indeed responsible for the elevated level of turbulence present in high redshift disks. Simons et al. (2017) show that turbulence is decaying towards the $z = 0$ value at this time.

1.5.2.4 Miscellaneous Evidence

In this category I include observations of the Milky Way and other nearby galaxies that suggest that gas accretion has occurred over a period of time, even at the modest $1\ {\rm M}_\odot{\rm yr}^{-1}$ necessary to fuel the star formation rate of the Milky Way (Larson, 1972). More distant galaxies with redshifts $1 < z < 4$ have extremely high star formation rates of $100\ {\rm M}_\odot{\rm yr}^{-1}$

and depletion times on the order of 100 Myr (Genzel et al., 2006; Förster Schreiber et al., 2006; Elmegreen et al., 2007; Genzel et al., 2008; Stark et al., 2008). It is necessary for fresh gas to be accreted rapidly in order to prevent quenching.

In addition to the limited supply of gas available for star formation, successive generations of stars enrich the interstellar medium and are reborn from their ashes with enhanced metallicity. The stars in our local neighbourhood have too low a metallicity to have evolved in a 'closed box' system. Assuming the gas starts from zero metallicity and is enriched purely by the successive generations of stars (Schmidt, 1963) it produces stars with higher metallicities than observed, requiring an influx of pristine gas. This was referred to as the G Dwarf Problem (van den Bergh, 1962; Schmidt, 1963), though similar issues arise in other classes of stars such as K (Casuso and Beckman, 2004) and M (Woolf and West, 2012) dwarfs. Taken together with the rest of the observational evidence and theoretical underpinnings, and ubiquity in cosmological simulations, it is highly probable that filamentary structures do indeed exist.

Chapter 2

Numerical Methods

2.1 Cosmological Simulations

While the initial conditions of the Universe are well understood through (Planck Collaboration et al., 2018), we cannot follow the evolution of dark matter from these initial conditions far into the non-linear regime characteristic of the present state of the Universe where stars are bound to the centres of massive halos. These galaxies also exert an influence on the larger scales which makes the problem of modelling them analytically completely intractable. To get around this issue we turn to computer models, allowing the brute force solution of the equations that govern the evolution of matter from the initial conditions to the present day of the distribution of stars and galaxies in our night sky.

A number of different techniques have been developed to solve these equations. Smooth Particle Hydrodynamics (SPH) codes such as GASOLINE (Wadsley et al., 2004) and GADGET (Springel, 2005) sample the density field with individual particles. As a result the simulations are Lagrangian as the fluid elements follow the fluid flow. There also exist grid based codes such as ART (Kravtsov et al., 1997), FLASH (Fryxell et al., 2000), RAMSES (Teyssier, 2002), ATHENA++ (Stone et al., 2008) and ENZO (Bryan et al., 2014). These exploit Adaptive Mesh Refinement (AMR) in order to focus resolution in higher density regions. A hybrid option exists in codes like AREPO (Springel, 2010) which have particle like fluid elements like SPH, but with transfer of mass, momentum and energy between neighbouring elements as in a grid code.

Each implementation has its advantages and disadvantages, see Agertz et al. (2007) for a comparative study. Observing the same phenomena numerically with completely independent implementations helps us to be confident that the phenomenon is likely real, such as in Stewart et al. (2017). In this thesis I will only consider the AMR code RAMSES however, which I will present in the following Section 2.2. Next I will explain how the

large scale structure of the simulation is extracted, specifically the filaments of the cosmic web in Section 2.4. Finally I discuss the implementation of the halo finder in Section 2.5

2.2 RAMSES

The details of the three simulations I use for the work presented in this thesis, namely the NUT , NEW HORIZON and SPHINX simulations will be discussed in their respective chapters. In this section I will only summarise the basics of the code used to run them: RAMSES.

2.2.1 Initial Conditions

Initial conditions are generated by programs such as MPGRAFIC (Prunet et al., 2008) and MUSIC (Hahn and Abel, 2013), which take a power spectrum (such as those obtained from Dunkley et al. (2009); Planck Collaboration et al. (2018)) to derive a random realisation compatible with the amplitude of each mode.

A limitation of this approach is that modes that are larger than the simulation volume are not accounted for, such as the over or under density of the region, or large scale tidal forces. Zoom simulations get around this to a certain extent by having the region of interest simulated at high resolution surrounded by a less well resolved region, where AMR and subgrid models are disabled. This is significantly cheaper in terms of computational resources to run than simulating the entire volume at the full resolution. When generating the initial conditions for a zoom simulation care must be taken to ensure that the zoom region is not polluted with low resolution DM particles from the low resolution zone, as these can cause unphysical scattering of the particles contained within these halos. This will be important for the NEW HORIZON simulation discussed later, where I use a 10 % contamination tolerance threshold.

2.3 Adaptive Mesh Refinement

While it is desirable to solve the fluid equations on a regular grid, it is computationally infeasible to evaluate the entirety of a simulation at parsec resolution if the simulator wants to study any sizeable volume of the universe. Driven primarily by the collapse of matter into smaller structures, we may ignore, or at least expend less computational power on the lower density regions of the universe while focusing on the higher density and highly dynamic regions. In RAMSES , such a patchwork of resolutions is maintained by using an AMR scheme, the fundamental unit of which is an oct, shown in Fig. 2.1 (for a 2D

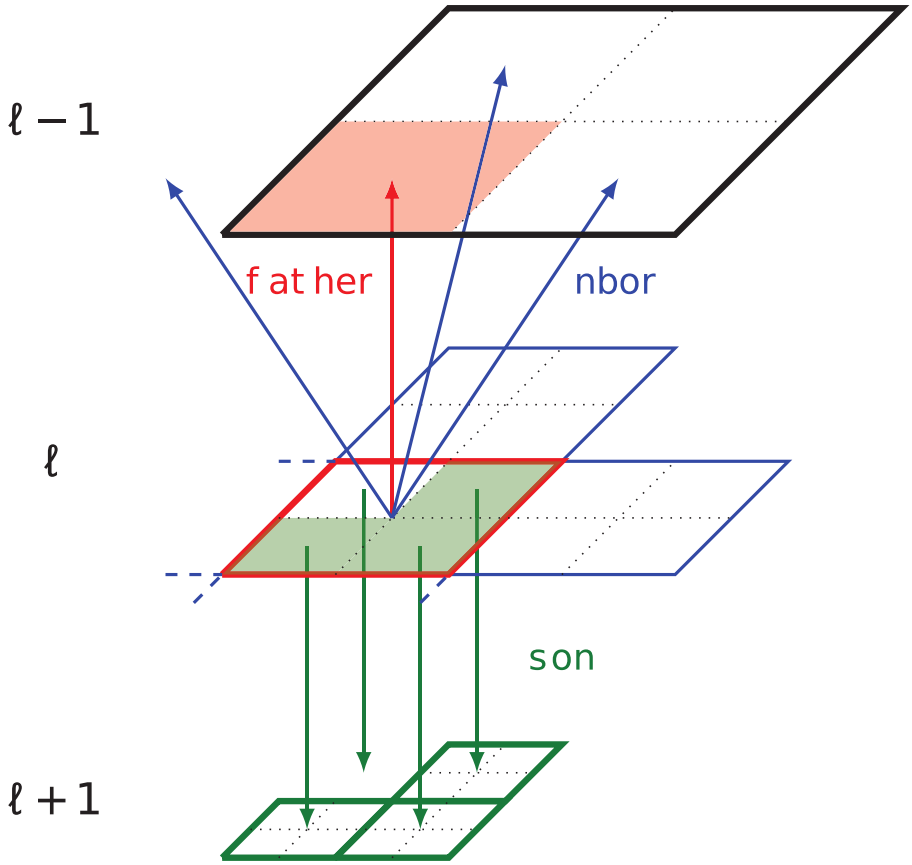

Figure 2.1: The refinement of the AMR grid showing the octree structure of RAMSES in 2 dimensions. Reproduced from Maxime Trebitsch's PhD thesis.

case). Each oct consists of 8 cells, storing the density, velocity, energy, metallicity and additional variables such as magnetic field strength in MHD simulations. Each oct points to its father cell and its father cell's neighbours on the level above, and each son cell points to its oct. At level 1 the whole simulation is contained within a single cell, but this is progressively refined by splitting the cell side in half to form $2^{n_{\mathrm{dim}}}$ cells from each cell as the level is increased until the maximum level is reached. Further refinement occurs if the cell is flagged for refinement up to a maximum level of refinement, but the reverse may also occur if the cell no longer qualifies for refinement: the cell is "derefined" in that case. An additional constraint is that neighbouring cells may only differ in level by a maximum of one. As well as increasing the spatial resolution, refinement also results in a halving of the timestep. Level $l + 1$ executes two timesteps for every timestep taken by l.

In RAMSES a quasi-Lagrangian approach is used in order to follow matter as it collapses under gravity. Cells are refined if the total mass in a cell, including both DM and

baryonic matter, increases by a factor of 8 above a threshold value, thus maintaining a roughly constant mass in each cell. It is also possible to use different criteria for refinement, for example refining on the vorticity of a cell as in Rosdahl and Blaizot (2012) or making sure the Jeans length is resolved by a given number of cells in star forming regions as in e.g. Renaud et al. (2013).

2.3.1 Evolution of Dark Matter

DM in RAMSES (and indeed most simulations) is treated as a collisionless fluid, modelled with a particle distribution function $f(\mathbf{r}, \mathbf{v}, t)$, which evolves according to the Vlasov-Poisson equation:

$$\frac{\partial f}{\partial t} + \mathbf{v} \cdot \nabla f - \nabla \phi \cdot \frac{\partial f}{\partial \mathbf{v}} = 0\,, \tag{2.1}$$

where the potential, ϕ, is found by solving the Poisson equation:

$$\nabla^2 \phi = 4\pi G \left[\int m f d\mathbf{v} + \rho_b \right] . \tag{2.2}$$

The integral over velocity space converts the particle distribution function into a density, and ρ_b is the baryonic matter density, representing both gas and stars. Gravity is the only interaction between dark matter and baryonic matter in the simulation. The dark matter phase space is sampled using individual particles, with masses typically $10^4 - 10^7 \mathrm{M}_\odot$ depending on the resolution. In zoom simulations higher mass particles (corresponding to coarser sampling) are employed outside the zoom region.

Ignoring the baryonic component of the simulation for the moment, computing the trajectories of the dark matter particles is essentially a sum over the gravitational forces of all the particles in the simulation, hence, a scaling of N^2, where N is the number of particles. This quickly becomes infeasible, especially as current state of the art simulations have billions of particles. In RAMSES this problem is overcome using a particle-mesh method (Teyssier, 2002) by assigning the particles to the AMR grid to produce a dark matter density field using Cloud In Cell interpolation. The mass is apportioned to the cells surrounding the particle proportional to the volume of a 'cloud' with the size of the host cell, centred on the particle present in each of the cells. This prevents discontinuities in the density field arising from particles crossing cell boundaries. The potential is then calculated from the total density (including the stellar particles computed in the same way, as well as the gas) using a *relaxation method*, which takes an initial guess and iteratively solves the Poisson Equation. From the resultant potential, the forces on each particle are calculated. As a result of this method, the algorithm scales only as $N\log(N)$, making it considerably more scalable than direct computation of the forces, and is comparable to tree codes such as

Barnes and Hut (1986) and FFT methods (e.g. Kravtsov et al., 1997). In practice, however, the hydrodynamic step tends to dominate the computation time.

Particle positions and velocities are then updated using a leapfrog integrator, a second order accurate technique. Velocities are updated for half a timestep, which is referred to as a 'kick', and the positions are updated with this new velocity for the full timestep (the 'drift'). A second kick is applied for another half timestep. Note that the force applied to the particle uses the new particle positions.

2.3.2 Evolution of Baryonic Matter

While the stellar component of the Universe behaves as a collisionless fluid, much like the DM and can be treated as such, the gaseous component is described using the conservation of mass, momentum and energy, encapsulated within the Euler Equations:

$$\frac{d\rho}{dt} + \nabla \cdot (\rho \mathbf{u}) = 0\,; \tag{2.3}$$

$$\rho \frac{d(\rho \mathbf{u})}{dt} + \nabla P = -\rho \nabla \phi\,; \tag{2.4}$$

$$\rho \frac{d(\rho E)}{dt} + \nabla \cdot \left[\rho \mathbf{u}(P + E)\right] = -\rho \mathbf{u} \cdot \nabla \phi\,, \tag{2.5}$$

where ρ, $\mathbf{u}$, P and E are the gas density, velocity, thermal pressure and total energy respectively. Additional sources and sinks to these equations will be discussed in the section on subgrid models. In order to close these equations the equation of state of an ideal monatomic gas for the pressure is used. The adiabatic index, γ, is set to $5/3$.

The variables are discretised on the AMR grid, and are evolved by solving the Riemann problem at the cell interfaces. This is an initial value problem with a single discontinuity within the domain (Toro et al., 1994).

In order to maintain numerical stability of the code, the time step is halved in every successive level, with each level performing two time steps for the level below. This ensures that the CFL (Courant–Friedrichs–Lewy) condition (Courant et al., 1928) is not violated by the increased spatial resolution. The timestep must be sufficiently small that material cannot cross more than a single cell travelling at the bulk flow velocity or sound wave within that timestep.

2.3.3 Subgrid Models

As computer systems are finite in both computational power and memory we can not resolve simulations down to arbitrary small scales. However, the physics of small scales,

from atomic and molecular physics to stars and supermassive black holes have major effects on the evolution of galaxies and as such need to be taken into account. I summarise some commonly used subgrid models used in RAMSES and other cosmological simulations in this section.

2.3.3.1 Heating and Cooling

An important distinction between dark matter and gas is the latter's ability to radiate away internal energy. Indeed, this is one of the most important processes in astrophysics, allowing gas to be accreted into halos and converted to stars.

Depending on the temperature, there are multiple regimes where different processes become important. At temperatures $\log_{10}(T) > 7$ Bremstrahlung radiation is the dominant cooling mechanism, occurring as electrons experience rapid acceleration upon interaction with a nucleus. As the temperature falls, atomic processes come to dominate from collisional excitation of atoms and subsequent decay to a ground state. For a primordial gas these processes are important down to $\log_{10}(T) = 4$. If the gas is chemically enriched then this process remains important to lower temperatures, but is less effective. At lower temperatures still, the formation of molecules allow a plethora of new transitions and enable efficient cooling down to a few tens of Kelvin, though this is only possible in dense environments.

Depending on the temperature, density and local radiation field the gas may also be heated by external photons. Important processes here are photoionisation and Compton scattering, where high energy photons scatter off charged particles. In RAMSES these processes are modelled as source/sink terms in the energy equation. The gas cooling rates are calculated by Sutherland and Dopita (1993) for a hydrogen helium and metal mixture of gas, valid down to 10^4 K. For lower temperatures Rosen and Bregman (1995) covers molecular cooling channels. Most simulations also have a UV background prescribed by Haardt and Madau (1996) turned on at $z \sim 10$ to simulate the reionisation of the Universe as a heating term.

2.3.3.2 Star Formation

Star formation is often implemented as a density threshold, beyond which the gas in a cell is transformed into a collisionless stellar particle. The rate of transformation is inspired by the Kennicutt-Schmidt relation (Schmidt, 1959; Kennicutt, 1998) where star formation is proportional to the gas surface density:

$$\Sigma_{\rm SFR} = A\Sigma_g^n \,. \tag{2.6}$$

The index n is measured to be 1.4 ± 0.5. This behaviour can be approximately reproduced with the toy model:

$$\mathrm{SFR} = \epsilon_{\mathrm{ff}} \frac{\rho_g}{t_{\mathrm{ff}}} \propto \rho_g^{3/2} \,, \tag{2.7}$$

which has approximately the correct scaling, with t_{ff} being the free fall time

$$t_{\mathrm{ff}} = \sqrt{\frac{3\pi}{32 G \rho_{\mathrm{g}}}} \,, \tag{2.8}$$

and ϵ_{ff} being the formation efficiency, controlling how much of the cell's mass can be converted into star particles per free fall time. This parameter is typically set at the observed value, 0.01 (Krumholz and Tan, 2007). The efficiency depends both on the scale and the effects of feedback. With sufficient resolution it should be possible to use an efficiency factor of 100% and compute proto-stellar feedback self consistently. In order to use more physically motivated star formation recipes the efficiency is thus often modified by local conditions, such as the local molecular hydrogen fraction, the virial parameter (how bound the gas is) or the turbulent motion.

One of the recipes used in this thesis is a thermo-turbulent star formation model developed by Devriendt et al. (in prep.), based on the theoretical work of Federrath and Klessen (2012). The turbulent nature of the ISM ensures that the gas density field may be described by the log-normal distribution:

$$p_s = \frac{1}{\sqrt{2\pi\sigma_s}} \exp\left(-\frac{(s-s_0)^2}{2\sigma_s}\right) \,, \tag{2.9}$$

where $s \equiv \log(\rho/\rho_0)$ is the normalised density and ρ_0 is the mean density. σ_s is the dispersion of the distribution which is driven by turbulence.

To find the fraction of the cell that will collapse to form a star the distribution is integrated from a lower limit s_{crit} (see e.g. Padoan and Nordlund, 2011). One can then show that the star formation efficiency can be given by:

$$\epsilon_{\mathrm{ff}} = \frac{\epsilon_{\mathrm{acc}}}{2\phi_t} \exp\left(\frac{3\sigma_s^2}{8}\right) \left(1 + \mathrm{erf}\left(\frac{\sigma_s^2 - s_{\mathrm{crit}}^2}{\sqrt{2\sigma_s^2}}\right)\right) \,, \tag{2.10}$$

where ϵ_{acc} is the fraction of the collapsing star that is accreted onto the protostar,the rest being returned to the ISM as a hot wind. ϕ_t is a factor introduced by Krumholz and McKee (2005), accounting for uncertainties in free fall time. Simulations of GMCs by Federrath and Klessen (2012) find a value of 0.57 for this parameter. By this definition it is possible for a cell to have a star formation efficiency greater than 100%. This just means that the collapse is accelerated by turbulence to the point where it becomes faster than the free fall time .

In Hopkins et al. (2013) the authors test a wide range of star formation models and find that while the *total* stellar mass formed is generally similar between prescriptions, the resultant distributions of stars are very different. This can have implications for the observable quantities of the galaxies as well as the effectiveness of various forms of feedback.

In RAMSES the number of stars produced when a a cell is flagged for star formation follows a Poisson distribution:

$$P(N) = \frac{\lambda^N \exp(-\lambda)}{N!}\,, \tag{2.11}$$

where N is the number of stars to form, and

$$\lambda = \frac{m_g}{m_*}\frac{\epsilon_{\rm ff}\Delta t}{t_{\rm ff}}\,, \tag{2.12}$$

is the expected number of particles to form, based on the mass of gas in the cell and the relative length of the time step to the free fall time.

2.3.3.3 Stellar Feedback

In order to produce galaxies with realistic stellar masses, sizes and star formation rate it is necessary to inject extra energy and momentum into the gas. An important channel, particularly for low mass galaxies is stellar feedback. This includes all feedback generated by stars, from stellar winds, type II and Ia supernova. Due to the limited resolution of cosmological simulations, star particles typically represent a population of stars, the evolution of which determines the type of feedback is relevant at which time. In RAMSES, the user chosen initial mass function for each population is evolved according to the stellar evolution code STARBURST99 (Leitherer et al., 1999). In all cases, stellar feedback is implemented as a deposit of energy, momentum, mass and metals in the cells around the stellar particle, however particular care must be taken with the high energies of supernovae. A naïve thermal energy dump results in the energy supplied rapidly (and unphysically) radiated away. This is known as the overcooling problem (Katz, 1992; Ceverino and Klypin, 2009). Various methods have been proposed for overcoming this problem, from artificially increasing the supernova yield (e.g. Kay et al., 2003), propagating non-interacting particles for a short time (≈ 50 Myr) to disperse the energy (Hummels and Bryan, 2012), or passive scalars that locally disable cooling (Teyssier et al., 2013). These all create their own unique problems, though they do tend to produce more realistic galaxies. These are 'thermal' feedback prescriptions. The alternative is to implement kinetic feedback where the energy is supplied in kinetic form rather than internal (e.g. Navarro and White, 1993; Dubois and Teyssier, 2008).

In the simulations I will present in later chapters, a more physically motivated prescription developed by Kimm and Cen (2014) is used. In this implementation, the method of injection depends on the resolvable phase of the SN explosion, giving a physical motivation behind the form of feedback chosen. There are two important phases during the course of the expansion of the supernova remnant. The first is an energy conserving phase, where the ejecta sweeps up material. At this point cooling of the material is not important, resulting in the momentum building up as the square root of the total shell mass, The shell of material evolves self similary during this phase. The second important stage is the snowplough phase, where cooling of the gas leads to momentum being conserved. In cosmological simulations resolution is typically too low to resolve the first stage, with cells being much larger than the final radius of the SN remnant at the end of this phase. Insufficient resolution both spatially and temporally prevent the gas from expanding adiabatically and accruing the correct amount of momentum, resulting in the overcooling phenomenon. To overcome this issue Kimm and Cen (2014) use the function:

$$\Delta p = \frac{\Delta\Omega}{4\pi} \begin{cases} \sqrt{2\chi(\Omega) M_{\rm ej} f_e E_{\rm SN}}\,, & \chi(\Omega) \leq \chi_{\rm tr}(\Omega) \\ p_{\rm SN}(E_{\rm SN}, n_H, Z)\,, & \chi(\Omega) > \chi_{\rm tr}(\Omega) \end{cases}, \tag{2.13}$$

where $M_{\rm ej}$ and $E_{\rm SN}$ is the mass and energy ejected by the supernova, and f_e is a parameter which smoothly interpolates between the energy conserving and momentum conserving regimes. The parameter $p_{\rm SN}$ is the final momentum injected by a supernova, as calculated by Chevalier (1974); Cioffi et al. (1988); Blondin et al. (1998)

$$p_{\rm SN}(E, n_H, Z) \approx 3 \times 10^5 {\rm kms}^{-1} {\rm M}_\odot E_{51}^{16/17} n_H^{-2/17} f(Z)\,, \tag{2.14}$$

where E_{51} is the energy of the supernova in units of 10^{51} ergs. The function $f(Z)$ introduces the effect of metals as $f(Z) = \max(Z/Z_\odot, 0.01)^{-0.14}$ (Thornton et al., 1998). This functional form is used as atomic cooling processes come to dominate at metallicities below $0.01 Z_\odot$, and the metallicity below this point has negligible impact on momentum transfer.

Equation 2.13 determines the momentum deposited in each cell depending on the solid angle subtended by the cell from the exploding stellar particle Ω. The regime chosen for each cell depends on the parameter:

$$\chi = \Delta M_{\rm shell}(\Omega) / \Delta M_{\rm ej}(\Omega)\,, \tag{2.15}$$

the ratio of matter swept up (including the initial ejected material) to mass ejected into each cell. The transition value between the two regimes, $\chi_{\rm tr}$, is found by equating Equation: 2.14 with $\sqrt{2\chi_{\rm tr} M_{\rm ej} N_{\rm SN} E_{\rm SN,tr}}$. This is the number of expected SN explosions, $N_{\rm SN}$, with

the kinetic energy expected at transition. With the momentum to add to each of the cells neighbouring the explosion determined, the excess energy not taken up by kinetic energy is finally added. Kimm and Cen (2014) find that thermal feedback schemes require at least parsec resolution for overcooling to be insignificant in high density regions, while their results are insensitive to resolution between 0.1 pc and 100 pc.

2.3.3.4 AGN Feedback

In addition to stellar feedback, most large scale simulations also need to take into account the effect of supermassive BHs on the largest of galaxies.

In simulations, BHs are seeded in a similar way to star formation. Cells which have a sufficient density spawn a black hole conditional on the distance to previously formed black holes (Dubois et al., 2014b). This prevents the spawning of multiple black holes from the same cell in the same timestep. Accretion rates onto BHs are derived assuming point masses in infinite uniform media both moving (Hoyle and Lyttleton, 1939) and at rest (Bondi and Hoyle, 1944). Due to the similarity between the two solutions the equations are combined to give:

$$\dot{M}_{\rm BH} = \frac{4\pi G^2 M_{\rm BH}^2 \rho_\infty}{(c_{\rm s,\infty}^2 + v_\infty^2)^{3/2}}\,, \tag{2.16}$$

where densities, velocities and sound speeds are measured far from the BH. In practice, the subgrid model uses values which are those of the cell the sink particle resides in. In a cosmological simulation the resolution achieved is not sufficient to resolve accretion flows on the scales of astronomical units around the BH, so the cell is a decent description of the far away environment of the BH.

In the NEW HORIZON simulation the magnitude of AGN feedback is determined by the accretion onto the sink particle (Dubois et al., 2014b), according to:

$$\dot{E}_{\rm AGN} = \epsilon_r \epsilon_f \dot{M}_{\rm BH} c^2\,, \tag{2.17}$$

where ϵ_r is a radiative efficiency which is dependent on the spin of the BH, $\dot{M}_{\rm BH}$ is the accretion rate and ϵ_f is dependent on the ratio of the accretion rate to the Eddington rate, defined as:

$$\dot{M}_{\rm edd} = \frac{4\pi G M_{\rm BH} m_p}{\epsilon_r \sigma_T c}\,, \tag{2.18}$$

where m_p is the mass of a proton, σ_T is the Thompson scattering cross section. In the case of low rates of accretion, less than 1% of the Eddington accretion rate, the BH operates in radio or jet mode, driving a bipolar outflow by injecting a momentum into a cylinder of radius Δx and height $2\Delta x$ and ϵ_f is set to 100%. For higher accretion rates the feedback

switches to the quasar mode, where thermal energy is deposited isotropically in a sphere around the sink particle with radius Δx, and $\epsilon_f = 0.15$. The efficiencies are chosen to reproduce the black hole scaling relations with bulge mass (Magorrian et al., 1998) and dispersion (Ferrarese and Merritt, 2000). The action of the feedback allows the black hole to regulate its own accretion rate as well as lowering the star formation rate of the host galaxy. This helps to bring the upper end of the mass function of simulated galaxies in line with those observed (Kaviraj et al., 2017).

In RAMSES, as in all cosmological simulations, the subgrid models chosen have various free parameters controlling the rates of star formation, cooling, feedback efficiency, etc. Ideally these parameters should be possible to derive from first principle. An example of this is using the knowledge of the spectral lines and chemical makeup of gas to calculate the cooling and heating rates as in Sutherland and Dopita (1993). Alternatively, high resolution simulations of a physical process can also be used to measure the subgrid model parameters directly. An example of this is in NEW HORIZON (Dubois et al., 2020) where the subgrid model for the forces on an accreting black hole is based on high resolution accretion simulations of Beckmann et al. (2018). In a third case the parameter is fitted to reproduce some well measured astrophysical relation, such as the present day galaxy mass function, such as in EAGLE (Schaye et al., 2015). The subgrid model is then validated by comparing the resultant simulation with another relation which it was not tuned to reproduce. Crucially, these subgrid models are not true representations of reality, and are typically only valid within a narrow range of resolutions. Cosmological simulations are always a compromise between achieving the highest degree of realism in the simulation and minimising the simulation run time, memory required to run the simulation and eventual storage requirements. For example, all simulations could use full radiative transfer to model reionisation as in Chapter 5, or model reionisation as a UV background as in Chapter 3. The effect of reionisation is to heat the IGM, which is captured by both models, however the exact details are less relevant at lower redshifts for sufficiently massive galaxies. The key point here is that subgrid models should only be used if they are relevant to the process under study, and should be no more complex than necessary to capture the essence of the process it is supposed to represent.

2.3.4 RAMSES-RT

In order to study the impact of reionisation it is necessary to extend RAMSES to model the transport of radiation and its interaction with matter, which is enabled by RAMSES-RT (Rosdahl et al., 2013). In contrast to various forms of ray tracing and Monte-Carlo methods, RAMSES-RT treats the radiation as a fluid by taking moments of the radiative transfer

equation, which can be discretised on the AMR grid. While other methods tend to scale poorly with the number of rays cast or sources, fluid approaches are largely independent of this. However the disadvantage of this approach is that the light tends to diffuse rather unphysically in low optical depth environments as well as being subject to collisions with fluid elements propagating in different directions.

The basic equation of radiative transfer describes the intensity as a function of frequency, I_ν as it propagates and is dependant on the local absorption, κ_ν and emission η_ν (Mihalas and Mihalas, 1984):

$$\frac{1}{c}\frac{\partial I_\nu}{\partial t} + \mathbf{n}\cdot\nabla I_\nu = -\kappa_\nu I_\nu + \eta_\nu \,, \tag{2.19}$$

where c is the speed of light and $\mathbf{n}$ is a normalised direction vector. Moments of this equation are taken, analogous to how the Euler Equations are generated from the Maxwell-Boltzmann equations, to produce the moment-based RT equations (Aubert and Teyssier, 2008):

$$\frac{\partial N_\nu}{\partial t} + \nabla\cdot \mathrm{F}_\nu = -\kappa_\nu N_\nu + S_\nu \,; \tag{2.20}$$

$$\frac{\partial \mathrm{F}}{\partial t} + c^2\nabla\cdot\mathbb{P}_\nu = -\kappa_\nu c\mathrm{F}_\nu \,, \tag{2.21}$$

where N_ν is the number density of photons with frequency ν and F_ν is the flux of photons of frequency ν. Hidden in the variable κ_ν are the frequency and density dependencies on all the chemical species making up the gas, obtained by summing over all the cross sections of all the present chemical species. S_ν contains all the information on emission, whether from recombination or from stellar particles within the simulation. Finally we have the radiation pressure tensor, $\mathbb{P}_\nu$ which requires a relation in order to close the set of equations. The M1 closure (Levermore, 1984) was first implemented on a uniform grid by González et al. (2007). This is defined as:

$$\mathbb{P}_\nu = \mathbb{D}_\nu N_\nu \,, \tag{2.22}$$

where the Eddington Tensor, $\mathbb{D}_\nu$ is modelled as:

$$\mathbb{D}_\nu = \frac{1-\chi_\nu}{2}\mathbb{I}_\nu + \frac{\chi_\nu - 1}{2}\mathrm{n}_\nu \otimes \mathrm{n}_\nu \,, \tag{2.23}$$

with

$$\mathrm{n}_\nu = \frac{\mathrm{F}_\nu}{|\mathrm{F}_\nu|} \,, \quad \chi_\nu = \frac{3+4f_\nu^2}{5+2\sqrt{4-3f_\nu^2}} \,, \quad f_\nu = \frac{|\mathrm{F}_\nu|}{cN_\nu} \,, \tag{2.24}$$

where n_ν is the unit vector in the direction of radiation flux, and f_ν is the reduced flux. Essentially the Eddington tensor is an interpolation between the regimes of radiation in an

optically thick regime $f_\nu = 0$, where the photons are diffused through the medium, and the optically thin $f_\nu = 1$, where the photons are free to travel in straight lines. RAMSES-RT (Rosdahl et al., 2013) implemented this radiative transfer scheme on the AMR grid.

2.4 DISPERSE

Filaments are identified using the structure finding algorithm DISPERSE (Sousbie, 2011). Other filament extraction algorithms are available, e.g. SKELETON (Novikov et al., 2006; Sousbie et al., 2008), MMF-2 (Aragón-Calvo et al., 2007a; Aragon-Calvo and Yang, 2014), T-WEB (Forero-Romero et al., 2009), SPINEWEB (Aragon-Calvo et al., 2010), FINE (González and Padilla, 2010), V-WEB (Hoffman et al., 2012), ORIGAMI (Falck et al., 2012; Falck and Neyrinck, 2015), CLASSIC (Kitaura and Angulo, 2012), NEXUS+ (Cautun et al., 2013), Adapted Minimal Spanning Tree (Alpaslan et al., 2014), Bisous (Tempel et al., 2014; Tempel et al., 2016), MSWA (Ramachandra and Shandarin, 2017). For a study on how resulting filaments depend on the exact method used (see Leclercq et al., 2016; Libeskind et al., 2018). I use DISPERSE as the filaments obtained are mathematically motivated by Morse theory and robust against the numerical noise inherent to the simulation. I detail the approach below.

2.4.1 Delaunay Tessellation

DISPERSE runs on the Delaunay tessellation of a particle density field. In 2D, this is a triangular tessellation such that each point is circumscribed (lie on the circumference of a circle) with its neighbours while not enclosing any points within that circle, as in Fig. 2.2. The particles of the tessellation are joined if they share the same circle. This is closely related to the Voronoi tessellation, which divides neighbouring points at the half way point. The Voronoi cells thus enclose the area which is closest to each of the defining points. The corners of these cells correspond to the centres of the circles in the Delaunay tessellation. To extend the Delaunay tessellation to three dimensions replace the circles with spheres and triangles with tetrahedra. The density at every point in space is thereby defined as being inversely proportional to the area (volume) of the triangles (tetrahedra) in 2D (3D).

2.4.2 Morse Theory

The DISPERSE algorithm is based on Morse Theory. The Morse Small Complex defines a set of integral lines that uniquely join together different critical points (points of zero gradient) of the density field. These lines are tangent to the gradient field at every point and

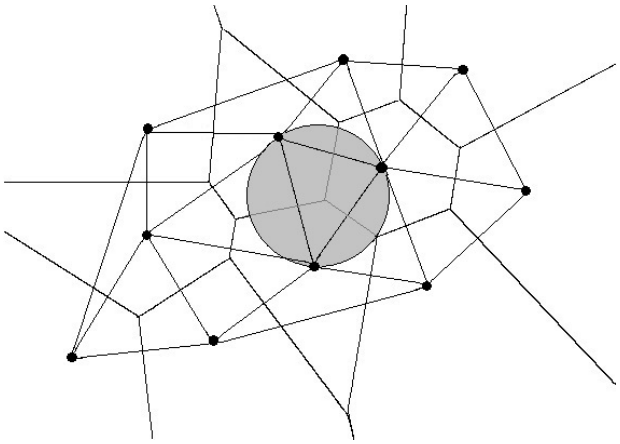

Figure 2.2: Delaunay tessellation of a set of particles in 2D, as lines joining neighbouring particles. The Voronoi tessellation is also shown as the lines half way between neighbouring particles. The circle shows the definition of the Delaunay tessellation, with each of the neighbours on the circumference of a circle which encloses no other points. Reproduced from Sharma et al. (2015)

partition space into volumes that belong to a critical point, which are termed manifolds. In two dimensions there are 3 types of critical points, minima, maxima and saddle points. In three dimensions there are two types of saddle points, giving four types of critical point.

2.4.3 Persistence

In order to ensure the structures are robust vis-à-vis noise, the concept of persistence is introduced. Persistence is best thought of as the difference in the density at the point of creation and destruction of topological features. This can be visualised as an underwater mountain. For example, as the water drains and a new island appears, this is the creation of a new topological feature. As the water level continues to fall the new island eventually joins the mainland, at which point the topological feature has been destroyed. The main island plus smaller island is a very different situation to having a slightly larger island. Furthermore, if we have to change the water level a lot to create and destroy islands then these are robust (or persistent) islands. Small boulders lying on the slopes of the mountain will create mini-islands as well, but these will have low persistence as it takes a very small change in water level to drown them or to rejoin them to the mainland. Such points are cancelled in the field as they are unimportant to the overall topology. DISPERSE offers a robust way to identify topological features in this way, using a single parameter, namely the persistence. From the topology of the persistent field DISPERSE uses the ascending 1-manifolds in order to define the filament.

The end result of the process is shown in Fig. 2.3, showing the effect of changing the persistence threshold on the filaments obtained. While the low persistence filaments probe into the voids, the highest persistence structures are seen to occupy the densest regions. The filaments marked in yellow have noticeably more halos associated with them than the green or turquoise structures.

2.5 Halo Finder

Amongst the first stages of analysing a simulation is to generate halo and galaxy catalogues by grouping together clusters of stellar and dark matter particles. I use the catalogues computed with the HOP (Eisenstein and Hut, 1998) catalogue for the galaxies, and ADAPTAHOP (Aubert et al., 2004) for the DM halos. The difference between the two different algorithms is that ADAPTAHOP is used to identify substructures. However due to the high resolution employed by NEW HORIZON massive globular clusters within galaxies are identified as separate structures, and since I am only interested in global galaxy properties in this thesis, I ignore their internal structure.

The HOP algorithm (Eisenstein and Hut, 1998) essentially links together particles in chains with each particle pointing towards its densest neighbour until a particle is found which points at itself. All particles belonging to this group are considered part of this structure, subject to being sufficiently dense. This prevents every particle in the simulation from being associated with a structure. Additional parameters merge together multiple maxima in different substructures into single structures if the saddle point between a pair of maxima is high enough density, or the maximum of a substructure is not above a given threshold density. The classification of the subsucture by ADAPTAHOP is shown schematically in Fig. 2.4. The algorithm is found to be robust to variation in all parameters except the density threshold which defines the edge of the galaxy. A value of 178 times the mean density of the Universe is chosen by analogy with the analytic top hat collapse model which describes the formation of virialised objects.

ADAPTAHOP extends the algorithm to identify substructures hierarchically, recursively identifying subhalos within halos. This is ideal as satellite galaxies will reside within these DM substructures.

Both algorithms are based only on the position of the particles, rather than the six dimensional phase space they actually occupy, which are exploited by halo finders such as ROCKSTAR (Behroozi et al., 2013). Using phase space clustering allows the tracking of subhalos more reliably even while structures are merging. Knebe et al. (2011) compares various clustering algorithms and finds that provided the number of particles sampling the

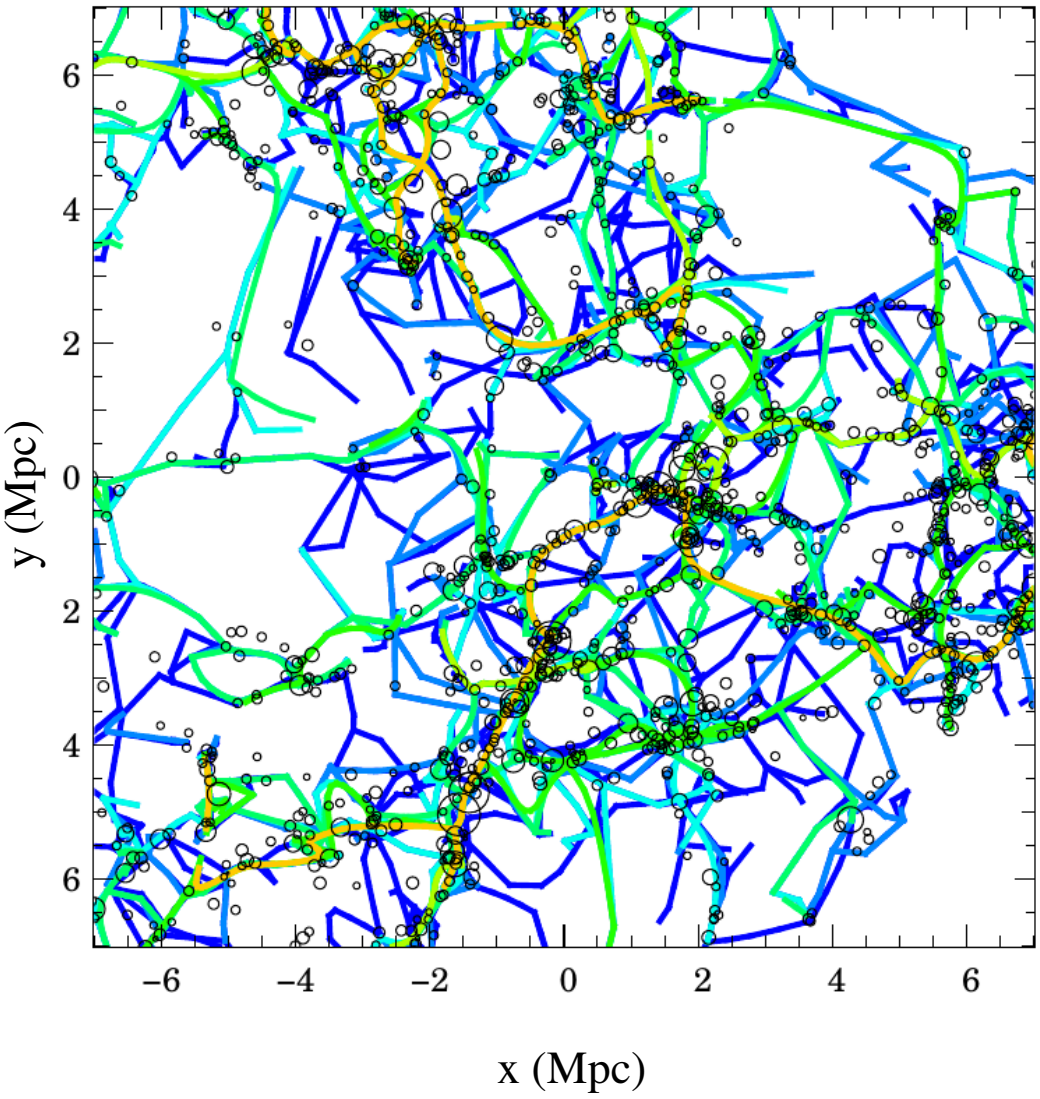

Figure 2.3: The filaments of NEW HORIZON as identified by DISPERSE at $z = 4$. The persistence is 1 σ for the deepest blue lines, incrementing by 1 σ, up to 7 in yellow. Each circle is a DM halo, scaled to represent 10 virial radii. Note that the highest persistence skeleton is also traced by the greatest number of halos, and also by the most massive ones.

halo is sufficiently high, differences between 6D and 3D halo finders are minimal. In this thesis, all halos used in the analysis have over 1000 particles, so should be independently identified regardless of halo finder choice. The galaxy and halo catalogue are identified independently of each other.

From the halo or galaxy catalogue a merger tree is built using the method outlined in Tweed et al. (2009). Halos merge and smaller halos may be tidally stripped of material as they enter a larger object. The same halo across two snapshots is identified by tracking its individual particles, and enforcing that the halo only has one descendent in the later snapshot: that with the largest fraction of the original halo's material. In this way subhalos may also be tracked after infall into a larger halo. Mergers occur when two or more progenitors are mapped to the same object. An example is shown in the lower panel of Fig. 2.4 This technique is also applied to the galaxy catalogue which will be used throughout this thesis. At low redshift there exists very little difference between the galaxy and halo merger trees. However as the first galaxies form halos large enough to cross the atomic cooling limit and become capable of accreting significant amounts of gas, the difference between merger trees of halos and galaxies will be more pronounced at high redshift.

2.6 Summary

In this chapter I summarised the basic numerical tools that were used to generate and analyse the simulations.

- RAMSES allows the self consistent evolution of both the DM and baryonic component of the Universe from high redshift down to the present day.
- DISPERSE allows the numerically robust and mathematically rigorous extraction of filament structures from a density field.
- Halo and galaxy catalogues were extracted using ADAPTAHOP, and the galaxy catalogues are used to construct merger trees.

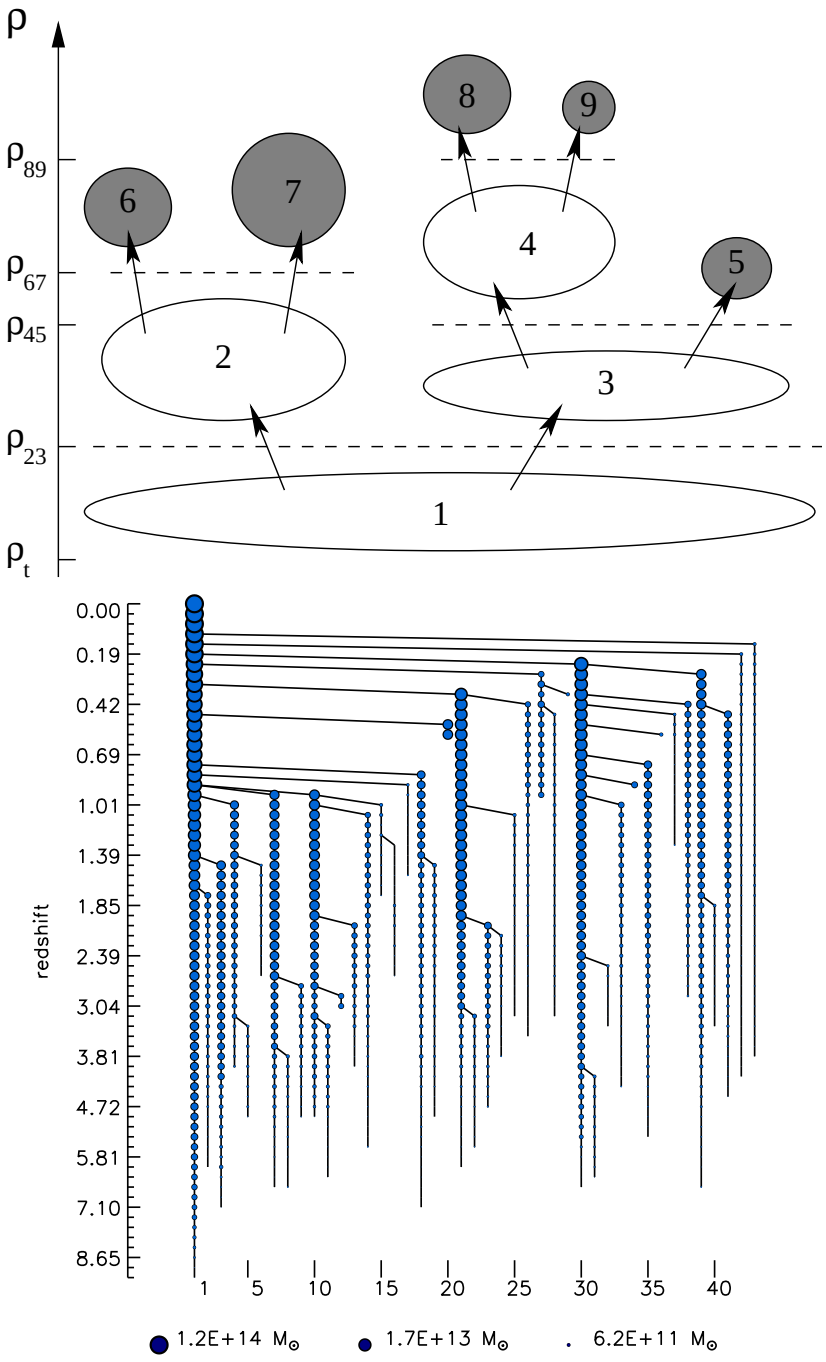

Figure 2.4: A typical subhalo structure produced by ADAPTAHOP (*Top*). The size of the ellipse represents the mass of the halo component, with 'leaves' of the halo tree represented by grey circles. Saddle points between two subcomponents are separated by a dashed line. HOP terminates after finding the halo. In the LOWER plot an example halo tree is shown. Vertical lines connect the same structure between simulation snapshots, while horizontal lines show mergers between halos. The use of merger trees allows us to easily follow objects from their birth in the simulation and quantify the contributions of mergers on the history of the halos. Figures reproduced from Tweed et al. (2009)

Chapter 3

Pilot Study of a Typical Filament

In this chapter I develop the techniques for studying the filaments of a single Milky Way-like galaxy. This will lay the foundation for a pair of statistical studies of a larger sample of galaxies in Chapters 4 and 5.

The structure of this chapter is as follows: in section 3.1 I motivate the chapter, while in section 3.2 I outline the simulation set up. In section 3.3 I describe how we identify the filaments and perform the analysis. Section 3.4 presents the results of our work, compares filament properties to an analytic model and discusses the robustness of the measurements vis-à-vis resolution. I summarise the results in section 3.5.

3.1 Introduction

Galactic surveys have revealed the presence of anisotropic structure on scales of Mpc, made up of nodes, voids, sheets and filaments (e.g. Davis et al., 1982; de Lapparent et al., 1986; Geller and Huchra, 1989). Cosmological simulations are able to reproduce this network, the so-called cosmic web (Bond et al., 1996; Pogosyan et al., 1998), and unveil its existence not just for the distribution of galaxies but also for the underlying gas and DM density, as a consequence of the hierarchical growth of structures in ΛCDM. Gravity amplifies small anisotropies, resulting in a near homogenous background collapsing to form sheets which can collapse again along another axis to form filaments. Halos form at filament intersections where, according to cosmological hydrodynamics simulations, galaxies at high redshift grow in mass and angular momentum primarily by material transported along these filaments (Birnboim and Dekel, 2003; Kereš et al., 2005; Ocvirk et al., 2008b; Pichon et al., 2011; Danovich et al., 2012; Stewart et al., 2013).

While at large scale gas filaments closely follow the structure of their DM counterparts in the cosmic web, at the scale of halos they can penetrate deep into the virial radius and even connect to galactic disks triggering star formation episodes (e.g. Katz et al., 2003;

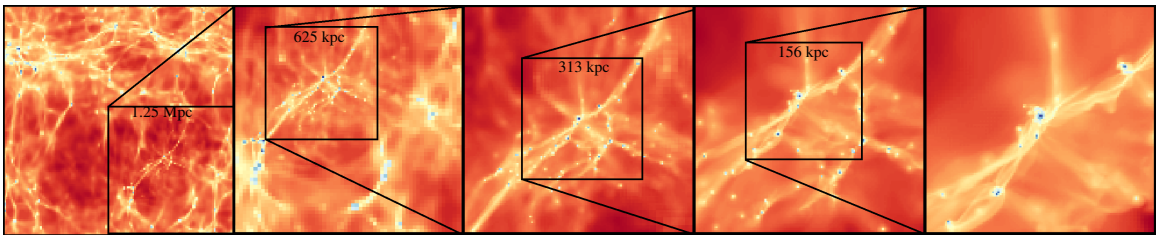

Figure 3.1: Zooming in on the NUT galaxy gas density field at $z = 4$. The leftmost panel shows a gas density projection of the entire simulation volume (12.5 comoving Mpc), with the high resolution zoom region enclosed in the square located in the bottom right corner of the first panel. Each subsequent panel, going from left to right, displays a projection of $1/8^{\text{th}}$ of the volume of the previous panel. The size of each volume in physical units is indicated. The *middle* panel shows the region within which the analysis in this chapter is performed, chosen so as to maximize the length of the studied filament.

Kereš et al., 2005; Woods et al., 2014; Stewart et al., 2017). The erosion of these small-scale gas filaments at lower redshifts is argued to be at least partly responsible for the bimodal distribution in colour, star formation rates and morphology of galaxies (Dekel and Birnboim, 2006), though quenching of the largest galaxies is dependent on AGN feedback (see e.g. Croton et al., 2006). Other implicit evidence for the presence of inflows is the presence of low metallicity G-dwarfs in the solar neighbourhood, as established in the seminal work of van den Bergh (1962). As gas depletion timescales are estimated to be on the order of a few Gyrs for local disk galaxies (e.g. Bigiel et al., 2011; Rahman et al., 2012; Leroy et al., 2013), replenishment by inflow of pristine gas is required to match the observations. This finding is also supported by observations of extended gas disks around galaxies (co-rotating with the stellar disk), either directly in emission (e.g. from Lyman-α Prescott et al., 2015)) or indirectly in absorption (e.g. from galaxy-quasar pairs, as studied in Zabl et al., 2019; Ho and Martin, 2019), all suggesting filamentary accretion from the cosmic web.

Rather than directly pursuing the filament properties themselves, it is possible to infer them through indirect methods. On large-scales, many authors have measured halo or galaxy spin alignment with cosmic filaments both in simulations (see e.g. Aragón-Calvo et al., 2007a; Codis et al., 2012; Dubois et al., 2014a; Laigle et al., 2015; Ganeshaiah Veena et al., 2018; Kraljic et al., 2019) and low-z spectroscopic observations (see e.g. Tempel and Libeskind, 2013; Chen et al., 2019; Krolewski et al., 2019, among others). These results highlight a redshift and mass dependence of the alignment signal, with halos with masses above $M_{\rm h} > 10^{12}\mathrm{M}_{\odot}$ displaying spins perpendicularly oriented with respect to the nearest filament, whereas spins of halos with masses below $M_{\rm h} < 10^{12}\mathrm{M}_{\odot}$ align with the nearest filament. At low masses this is thought to be due to accretion of vorticity rich gas that drive

spins to align with the filament. At high masses this behaviour is overcome by mergers, or as Laigle et al. (2015) argues, the accretion of material from multiple vorticity domains. This dichotomy in galaxy spins shows the profound impact of cosmic filaments on the galaxies embedded within them.

On smaller scales, the misalignment of gas and DM angular momenta in simulations has been attributed to different redistribution processes during halo virialisation (e.g. Kimm et al., 2011a; Stewart et al., 2013). However, it has also been argued that instabilities within the filaments could develop, leading to their fragmentation and breakup, thereby preventing cold gas from being smoothly accreted by the host galaxy. In such a scenario, the angular momentum segregation between DM and gas could be construed as an artefact of poor numerical resolution in filaments. Several authors (Freundlich et al., 2014; Mandelker et al., 2016; Padnos et al., 2018; Mandelker et al., 2019; Berlok and Pfrommer, 2019b) carried out idealised simulations of filaments entering a halo, and concluded that they should be stable, given their width and velocity. Cornuault et al. (2018) used a phenomenological model of a gas stream to explore the possibility of a turbulent, multi-phase filament. The accretion efficiency of such a filament would be reduced, but it remains unclear as to whether such a multi-phase model constitutes an acceptable description of cosmological filaments. Using a cosmological zoom simulation tailored to achieve maximum resolution in the filaments, Rosdahl and Blaizot (2012) find that they remain stable within halos with masses of up to a few $10^{11}\mathrm{M}_{\odot}$ at least as to low as $z = 3$, whilst they show more disruption within halos of larger masses in line with arguments made in Birnboim and Dekel (2003).

Ultimately, to distinguish between these scenarios and better assess the role played by filaments on galaxy evolution, quantitative direct measurements of their properties need to be made. However, these have proven notoriously elusive so far (see e.g. Kimm et al., 2011a) for a more detailed discussion. Indeed, direct observations of the distant cosmic web suffer from the steep scaling of surface brightness with redshift, which makes the cold filaments extremely hard to detect in emission (though not impossible, see e.g. Giavalisco et al., 2011; Ribaudo et al., 2011; Kacprzak et al., 2012; Martin et al., 2016; Gallego et al., 2017; Elias et al., 2020), and thus rely on stacking, or back-lighting by a bright source. Efforts to understand observed filament properties are correspondingly mirrored by simulations (e.g. Gheller et al., 2015, 2016). On large scales, filaments of the cosmic web are reported to have a radial power law profile in density with a power law index comprised between -1 and -2 (see e.g. Colberg et al., 2005; Dolag et al., 2006; Aragon-Calvo et al., 2010). Smaller scale studies have been performed by e.g. Ocvirk et al. (2016a), who determined the outer radii of filaments in their simulation to be about $50h^{-1}$kpc at $z = 4.3$

by looking at the separation between temperature peaks caused by the accretion shock, although these authors acknowledge that they did not separate edge-on sheets from filaments in their sample. Using cosmological simulations, Dekel et al. (2009) found that DM filament radii are comparable to the virial radius of the halos they connect, and that the cold gas streams residing within the halos are considerably narrower, typically a few percent of the virial radius.

To date, the rich complexity of the filamentary network connecting halos of various masses and its evolution with redshift has yet to be investigated systematically. In this chapter we argue that to do so, it is pivotal to work on a cosmological sample of *well-resolved* filaments and take a step in this direction by measuring filament profiles from the density, vorticity, and temperature field information available in a zoom-in cosmological simulation. Our focus is on intermediate-scale filaments, that is, those connecting to a $M_\star$ galaxy, at moderate to high redshift ($z \geq 3$). We also investigate how stellar feedback can perturb these filaments. Given the limited sample considered in this work, it should be considered a pilot study. In the next chapter, the methods developed here will be applied to NEW HORIZON (Dubois et al., 2020), a cosmological zoom of the HORIZON-AGN (Dubois et al., 2014b) simulation, covering a sphere 20 Mpc in diameter with similar resolution to the NUT simulation, where a statistical sample of filaments can be obtained, connecting a more diverse ensemble of galaxies.

3.2 The NUT simulation suite

The analysis is performed on two simulations of the NUT suite (Powell et al., 2011), a series of cosmological zoom-in simulations of a Milky Way like galaxy designed to study the effects of resolution and various physical processes on its formation and evolution using the Adaptive Mesh Refinement (AMR) code RAMSES (Teyssier, 2002). Initial conditions are generated at redshift $z = 499$ using the MPGrafic code (Prunet et al., 2008) with cosmological parameters set in accordance with the WMAP5 results (Dunkley et al., 2009). The simulation volume is a cubic box $9h^{-1}$Mpc on a side and a coarse root grid of 128^3 cells. A series of three nested grids are then centred on a sphere with radius $2.7h^{-1}$Mpc which encompasses the Lagrangian volume occupied by the galaxy (host dark matter halo mass of $M_{\rm vir} = 5 \times 10^{11} {\rm M}_\odot$ by $z = 0$). AMR refinement is then enabled within that sphere using a quasi-Lagrangian refinement criterion to achieve a maximal spatial resolution of 10pc at all times whilst forcing the mass of each individual cell to remain roughly constant. The collisionless fluid in this high resolution region consists of dark matter (DM) particles each with mass $5.6 \times 10^4 M_\odot$, whereas the gas evolution equations are solved on the AMR

grid by means of a Godunov method (HLLC Riemann solver) with a MinMod limiter to reconstruct variables at cell interfaces. The gas density field in the simulation is shown in Fig. 3.1 at $z = 4$, gradually zooming in from the full box onto the central galaxy itself.

In this chapter, we use a NUT simulation with no feedback, and one with mechanical supernova feedback as defined in Kimm et al. (2015). In the following, we refer to these two simulations as the "no-feedback" and "feedback" runs respectively. The feedback recipe of Kimm et al. (2015) ensures that the appropriate energy or momentum is deposited into the cells around the supernova, depending on whether the Sedov-Taylor phase of the blast wave is resolved or not. This prevents the supernova energy from being artificially radiated away, as would happen if solely thermal energy was injected (the so called over-cooling problem described in Katz, 1992). Both runs under study use cooling tables calculated by Sutherland and Dopita (1993), down to 10^4 K, and the Rosen and Bregman (1995) approximation for temperatures below this threshold. A UV background is instantaneously turned on at $z = 8.5$ to account for the re-ionisation of the Universe, while star formation is allowed to proceed when gas densities become greater than $4 \times 10^2 \mathrm{H.cm}^{-3}$ with an efficiency of 1% per free-fall time, calibrated on observations by Kennicutt (1998). A detailed description of the implementation of star formation used in this version of RAMSES may be found in Rasera and Teyssier (2006) and Dubois and Teyssier (2008). For the feedback run, a Chabrier initial mass function (Chabrier, 2003) is adopted, with 31.7% of the mass fraction of each star particle ending up as a single type II supernovae and releasing $10^{50}\,\mathrm{erg\,M}_\odot^{-1}$ of energy after a 10 Myr time delay and expelling heavy elements with a 5% yield.

3.3 Filament Identification

As we aim to measure the properties of the cosmic web filaments, both in the DM and gas density fields, we now describe how we identify these structures in the simulations.

3.3.0.1 Method

The DM particle distribution is tessellated using the Delaunay Tessellation Field Estimator tool (Schaap, 2007) and fed to the code DISPERSE (Sousbie, 2011). DISPERSE computes stationary points (maxima, minima and saddle points) of the density field using the Hessian matrix and assigns to each pair of critical points (e.g. maxima-saddle) a persistence, namely a measure of how significant it is with respect to a Poisson distribution. The persistence threshold is the single parameter that determines which features are considered as noise and which robustly pertain to the topology of the underlying density field. From this set of stationary points that characterize the topology of the field, DISPERSE connects saddles

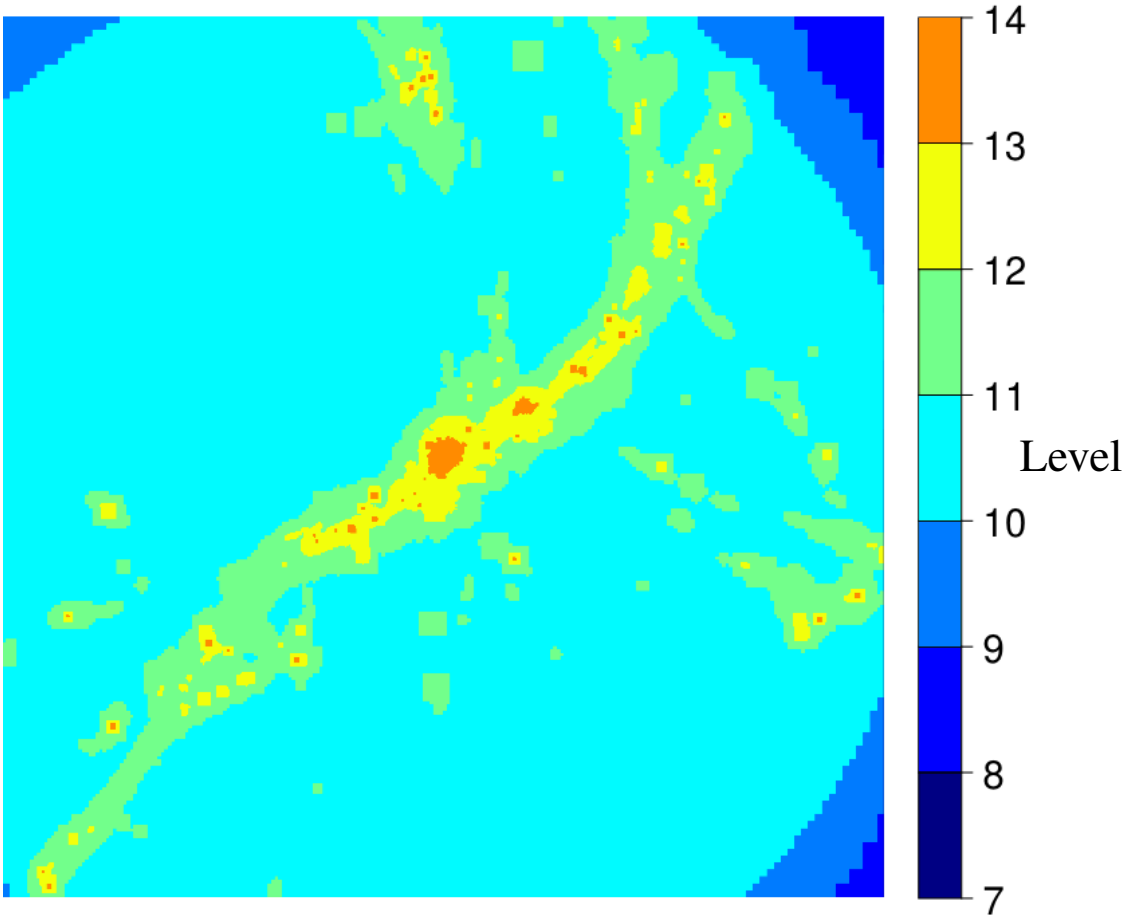

Figure 3.2: Resolution map for a slice of thickness 300pc, across a $(625\text{kpc})^2$ region of the computational domain at $z = 4$, with each colour representing a different resolution level as indicated on the figure. At this redshift, the filament is uniformely sampled at 1.2 kpc resolution (AMR level 11: green) and partly at 0.61 kpc (AMR level 12: yellow) around the most massive halos embedded in it. Even though the highest spatial resolution reached in the simulation is 10 pc, which corresponds to AMR level 20, levels above 13 are not shown as they are confined to the galaxies themselves and their immediate vicinity.

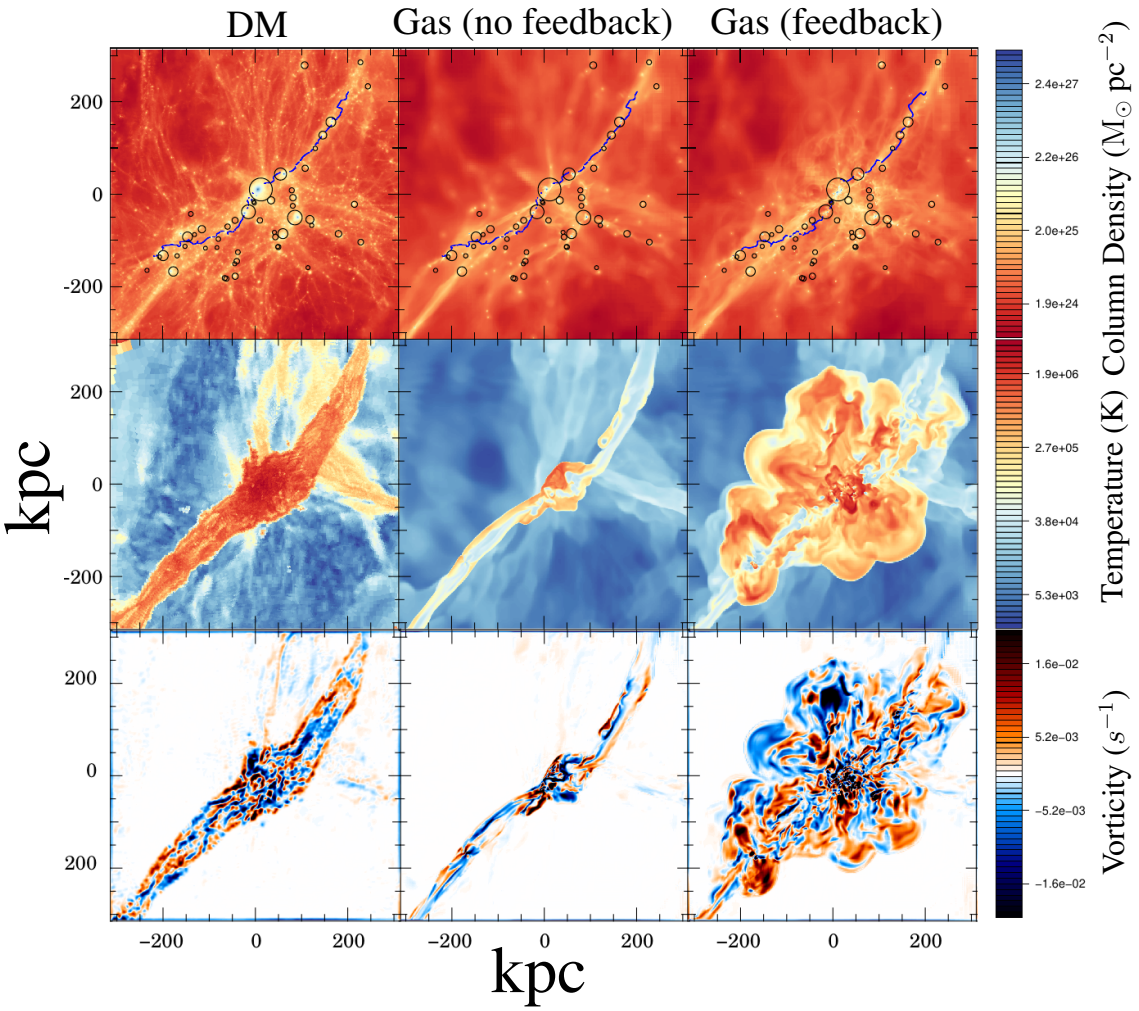

Figure 3.3: DM (left column) and gas (no-feedback run, middle column; feedback run, right column), with each row showing column density (*top*), temperature (*middle*) and vorticity (*bottom*) in a slice 625 kpc across and 1 kpc thick at $z = 4$. The main filament, as extracted from the DM density field, is overplotted (*b*lue solid line) on the column density maps. The virial radii of the 50 largest halos are marked as circles. The differences between the feedback and no-feedback skeletons are caused by small differences in the noise level associated with DM particles: they yield slightly different paths which have a very similar length, so that either path can be chosen by the algorithm described in the text. The colour bar for the density represents the gas. To estimate it for the DM, one simply needs to divide the numbers shown by the universal baryon fraction. For the DM temperature, velocity dispersion is used as a proxy, with dark blue corresponding to regions of ~ 0.02 km s^{-1} and deep red with ~ 100 km s^{-1}. In the vorticity panels, red represents matter swirling counter clockwise around the filament, and blue is for matter rotating in the opposite direction. The vorticity and enhanced temperature (or DM dispersion) neatly coincide with each other giving an excellent proxy for the width of the filament. For the feedback run however, energy and vorticity is injected onto large scales, making this proxy useless in the gas. In spite of this however, the cold core of the filament does survive the energy injection.

to maxima following the direction of least gradient to create a network of filaments which will be referred to in this chapter as the "skeleton", and we will call "nodes" the maxima of the density field.

3.3.0.2 Extraction of the skeleton from the simulations

For each simulation, filaments are extracted from the Delaunay tessellation reconstruction of the DM density field, setting a persistence threshold of 10σ. This persistence threshold is chosen such that the observed skeleton is in good visual agreement with the DM density field. Our results are in fact insensitive to the exact value chosen for this threshold, as we are only studying the main filaments feeding the galaxy (see Section 3.3.1). The skeleton is additionally processed with SKELCONV (see DISPERSE manual[1]) using the BREAKDOWN and SMOOTH functions. BREAKDOWN removes duplicate segments entering a node from two different starting points. These segments can be so close as to be indistinguishable from one another and as such are removed to prevent their over-representation in the final skeleton. The skeleton is then smoothed by averaging over the positions of the 30 nearest neighbours of each segment. This mitigates the effects of Poisson noise on the skeleton, ensuring that individual segments locally follow the global direction of the filament they belong to.

In both the feedback and no-feedback runs, 1.22 physical kpc is the maximum spatial resolution reached in filaments, defined as the size of an individual cell on the highest AMR grid level that entirely maps the filament (see Fig. 3.2). As is clear from Figure 3.2, higher refinement levels are triggered within filaments but their coverage is patchy, and mostly concentrated around halos/galaxies embedded within these elongated structures. As we argue in our convergence analysis (Section 3.4), we believe 1.22 kpc is enough to resolve the radial structure of filaments, at least those that connect to halos/galaxies with masses similar (or larger) to the one we study in this chapter (roughly $M_\star$). We emphasize that this is a much higher resolution than that currently reached in large-scale cosmological hydrodynamic simulations, where $\simeq$ 1 kpc resolution is only attained within galaxies (e.g. Dubois et al., 2014a; Vogelsberger et al., 2014; Schaye et al., 2015; Nelson et al., 2018; Davé et al., 2019; Nelson et al., 2019). The main drawback of our study is that such resolution is obtained at the cost of simulating a much smaller volume, and thus focuses on a single object. Filament extraction is performed at the maximum level of resolution thus defined. However, as highlighted by Rosdahl and Blaizot (2012) and in our convergence study (Section 3.4), increasing the resolution does not seem to affect the filament properties much, and we thus expect that our results only weakly depend on resolution.

[1] http://www2.iap.fr/users/sousbie/web/html/index4f3e.html?category/Manual

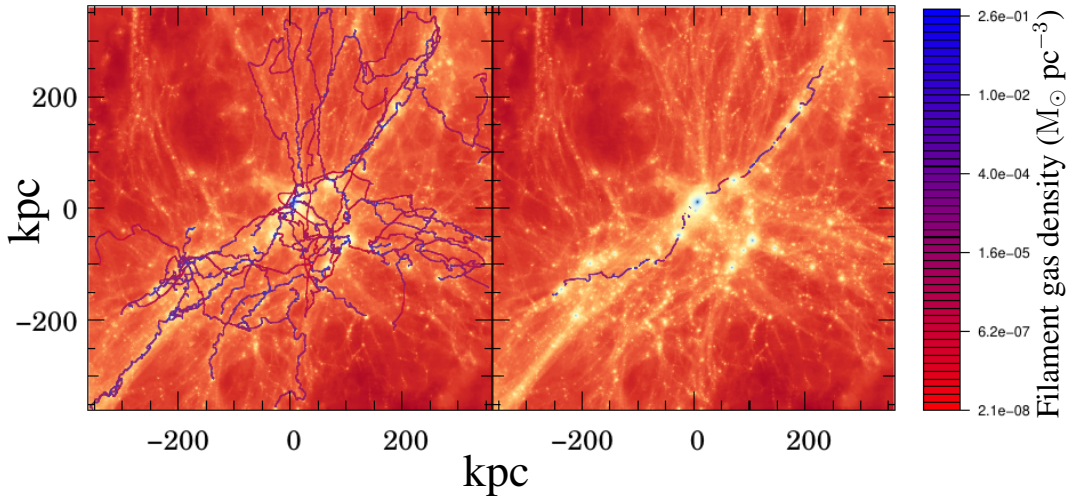

Figure 3.4: The *left* plot shows the raw skeleton extracted by DISPERSE, which traces all the filaments of the DM density field, coloured according to the relative density (with low density in red and higher density in blue) . Using Dijkstra's algorithm we then obtain the skeleton on the right, where we have removed filament segments from regions with densities greater than 130 times the mean density, resulting in gaps around virialized halos and sub-halos (indicated by circles enclosing their virial radii on Fig. 3.3). In both panels, the skeleton is overplotted on a $z = 4$ projection of the DM density field. This cleaned version of the output of DISPERSE is what we use for our analysis in this Chapter 3 and Chapter 4.

Finally, we note that DISPERSE applied to the DM particle distribution, as is done in this chapter, only allows the extraction of the filaments down to a scale comparable with the virial radius of DM halos. Below this scale, DM filaments (at least in standard 3D space) are washed out by the virialisation process at the origin of halo formation and evolution. Therefore, we restrict our measurements of filament properties to filament segments located outside of the virial radii of embedded DM halos.

3.3.1 Identifying the main filament

The gas and DM distributions differ significantly even for the no-feedback run (compare *left* and *middle* panels of Fig. 3.3), with the gas density field presenting much fewer filamentary structures than the DM[2] In addition, even though dwarf galaxies residing within filaments are affected by feedback, the impact of this feedback on the growth of the central galaxy is minimal (it does not lead to the disruption of the main filament) as the majority of the gas feeding it at high redshift is accreted via filaments, and not from mergers (Danovich

[2]This is a consequence of re-ionisation reheating the gas of the IGM and preventing accretion into the shallow potentials of DM filaments (Katz et al., 2019).

et al., 2012; Tillson et al., 2015). However, the gas density field in the run with feedback will be more perturbed due to interactions with galaxy winds and shocks (see *middle* and *right* panels of Fig. 3.3), making the comparison between feedback and no-feedback runs difficult. Furthermore, DISPERSE is designed to work with particle data, as it allows in this case a meaningful definition of persistence (the very concept of which relies on quantifying the significance of a feature with respect to Poisson noise). For these reasons, and given that we are not interested in probing the existence of filaments within the virial radius of DM halos in this work, the DM density field seems more appropriate to carry out filament extraction.

We therefore elect to extract the skeleton from the DM density field, but trim it in order to keep only the main filament, along which most material flows onto the galaxy. For an $M_\star$ central galaxy, the main filament traced in the gas clearly coincides with its DM counterpart (see *top* panels of Fig. 3.3). As we are analysing a filament connecting to a single object, we identify the approximate region where it begins and ends by eye, and select the highest density point in this region as its starting/end point[3]. We then use Dijkstra's algorithm (Dijkstra, 1959) to compute the shortest path (following the skeleton) between the start and end points. This works by assigning to each segment a distance from the start point, travelling along all the various possible paths of the skeleton. Whenever a shorter path to a given segment, s, is found, then the selected path is updated up to s, and the distances to all segments connected to s along this path which have a longer path length, are updated. This process is iterated until the network is traversed, yielding the shortest path between the given start and end point. The method is valid provided the main filament flows mostly straight onto the galaxy, which, in turn, holds until the filament gets close to the galaxy disk (Powell et al., 2011).

In order to avoid the filament passing through halos, filament segments located in regions with densities higher than 130 times the mean density of the Universe were excluded[4]. This density threshold is chosen empirically, but the resulting skeleton does not depend very sensitively on the chosen value provided this latter is on the order of 100 times the mean density of the Universe. The entire initial filamentary network and the resulting main filament extracted after post-processing are shown in Fig. 3.4. Fig. 3.3 highlights that the skeletons extracted from the DM density fields of the feedback and no-feedback runs are

[3]For larger volume cosmological simulations where an ensemble of filaments is available one can forgo the inspection by eye and simply use the closest pair of galaxies with similar masses which are linked by the skeleton as the starting and end points of a filament.

[4]This value is lower than 200 times the critical density of the Universe which is commonly used in the literature to define virialised structures. This reflects the fact that the density of halos at the virial radius is lower than their average density by about a factor 3.

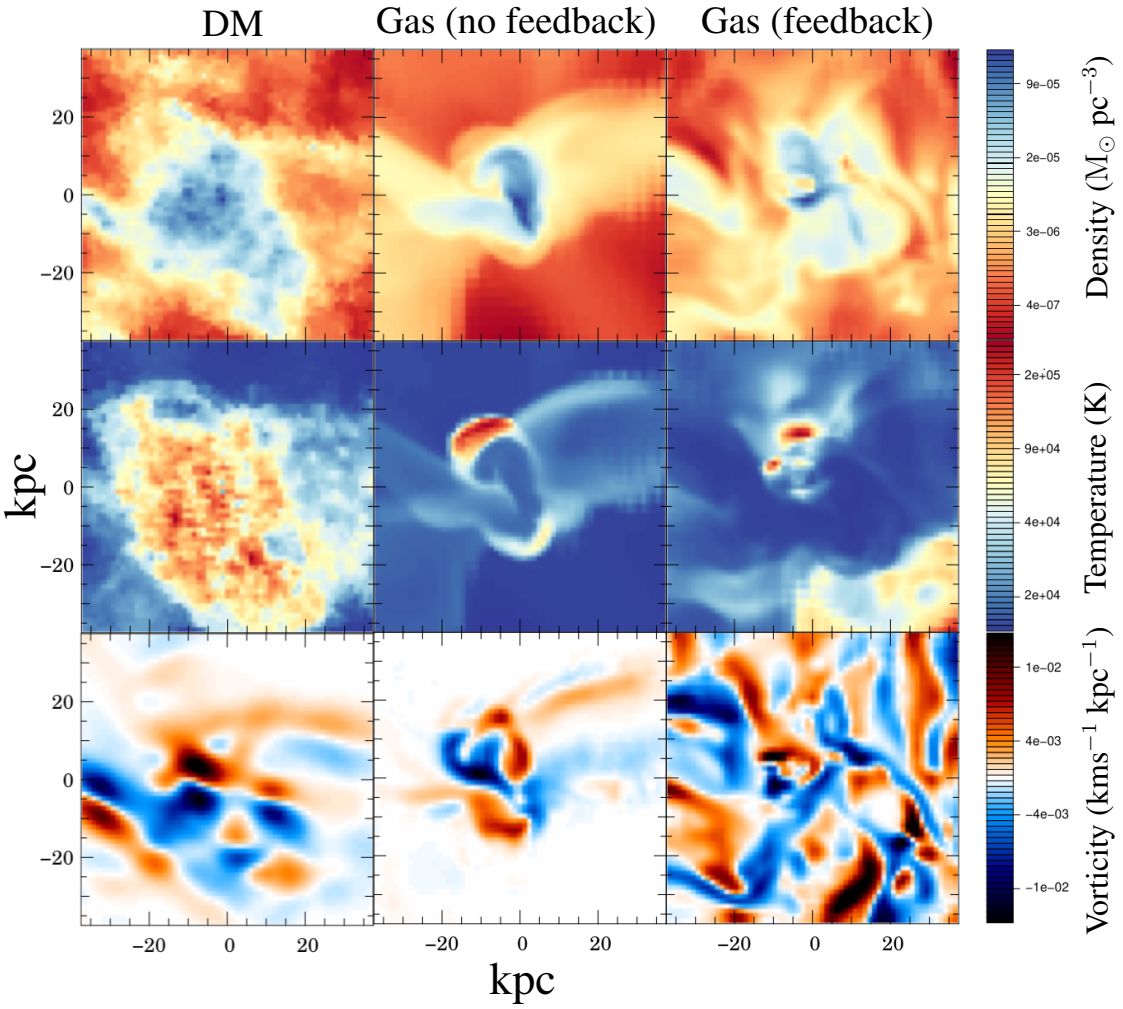

Figure 3.5: A typical filament cross-section, extracted 200 kpc away from the central galaxy in DM (left column) and gas (no-feedback run, middle column; feedback run, right column) at $z = 4$. The thickness of the slice is of order 1 kpc. Note how the central filament (density peak in the 2D slice) is embedded in a weaker wall structure (which appears as a thick elongated tube encompassing the peak). From *top* to *bottom* row: density, temperature (or velocity dispersion for DM, running from 0 to 25 kms^{-1}, dark blue to red) and vorticity along the filament, with red representing matter rotating counter-clockwise and blue in the opposite direction. As in Fig. 3.3 the correlation between the vorticity and temperature field should be noted. The vorticity is low outside the point where the shell crossing and shocking occurs, again suggesting that this is an excellent proxy for the size of the filament. The truncation radius is not available for the gas when feedback is important.

slightly different. In this Figure, one can clearly see a pair of filaments on the left side of the central galaxy, which are in the final stages of merging. As a result, our algorithm identifies two possible paths along which the main filament would have essentially the same length. Small changes in the noise level associated with the DM particles in the two different runs change the exact way that segments connect, resulting in the algorithm picking one of these paths in one run and the other path in the other run. Our results are, by and large, independent of such small randomly induced differences.

3.3.2 Cross-section measurements

3.3.2.1 Calculating DM temperature and vorticity fields

Due to the discrete Lagrangian nature of the numerical technique used to evolve the DM density field, a simple cloud-in-cell interpolation onto a reasonably sized regular grid generates a non-smooth density field in poorly sampled, low density regions. To get around this difficulty, a Delaunay tessellation (Schaap and van de Weygaert, 2000) is computed from the DM density and velocity fields (see e.g. Schaap, 2007), which ensures their spatial continuity. The Delaunay grid is then projected onto a regular uniform grid, coinciding with AMR grid level 11, which corresponds to the maximum resolution mapping of the entire filament (cubic cells 1.22 kpc on a side, see Fig. 3.2). This uniform grid is used for measurement of all quantities in this chapter unless otherwise stated. The DM velocity dispersion field – used as a proxy for temperature – is then obtained by computing the square of the difference between each particle velocity and the value of its nearest neighbour grid cell and re-applying the Delaunay tessellation with this dispersion as the weight. Every time the Delaunay tessellation is projected onto the grid, we average all the tetrahedra (or volume fractions of) that co-exist in each grid cell. The vorticity, on the other hand, is simply calculated by taking the curl of the velocity field on the uniform grid. As this latter is extremely noisy, a Gaussian smoothing is applied prior to computing vorticity, with a width of 2 cells.

3.3.2.2 Cross-section extraction and radial profiles

For each segment of the skeleton, a field (density, temperature or vorticity) is linearly interpolated in a plane, the thickness of which is equal to the skeleton segment length (typically 0.3 kpc, though this depends on the local density). This plane is perpendicular to the segment and centred on it. An example of individual cross-sections in the density, temperature and vorticity fields is displayed in Fig. 3.5. Note that the position of the DM or gas density peak does not necessarily lie exactly at the centre of the plane due to the smoothing of the

skeleton. Smoothing is required to ensure that individual segments point along the filament direction, and thus that the extracted planes are truly perpendicular to the filament. The gas density maximum is not tied to the DM density maximum and thus is also unlikely to be at the centre of the plane. In order to correct for such small offsets which nevertheless do affect profile measurements, each plane is to better align the plane with the filament centre. Competing methods are shown in Fig. 3.6, for high and low redshift, and for gas and DM profiles.

The first and most obvious approach is to define the centre as the maximum density density point subject to constraints on how far from the skeleton the centre can be moved. However, this results in the profile artificially jumping to halos within or near the filament, resulting in profiles with steep slopes and small core sizes, opening to the NFW profile of the halo polluting the filament profile. The centre of mass is also shown, however this occasionally places the filament centre between high density peaks, resulting in a profile that rises before falling. The chosen solution was to use the shrinking sphere (Power et al., 2003) method, consisting of iteratively calculating the centre of mass within a shrinking radius, centred on the previous guess. This ensures that the final position is a local maximum, while respecting the larger scale filament. This can be particularly problematic in DM filaments as the structure is significantly clumpier than the gas filaments. To further reduce the impact of filamentary halos, the density field was truncated at $40\langle\rho\rangle$, which is a typical density at the virial radius of a halo. This tends to remove objects marked by the red cross in the figure. The centre of mass of a circle centred (with a radius greater than the truncation radius) on the initial guess from DisPerSE is calculated. The circle is moved to the centre of mass before the procedure is repeated with a smaller circle. This method is more robust to the presence of additional substructure within the filament, particularly as cells with $\rho > 40\langle\rho\rangle$ have had their density reduced to $40\langle\rho\rangle$ for the calculation of the centre of mass. This prevents halos existing within or near the filament from being chosen as the filament centre and distorting the filament profile. DM and gas planes are therefore translated independently. This procedure allows us to align all segments when stacking cross-sections.

Vorticity and temperature fields interpolated onto the plane perpendicular to the segments are then translated with the same shift as the density field. When looking in the plane perpendicular to them, filaments appear as strong peaks in the projected density field (see top row of Fig. 3.5). Alongside this, the major walls associated with these filaments is often visible extending out from the peaks, forming thick elongated structures which are not necessarily straight. In the temperature field (middle row and middle column of Fig. 3.5), strong radial shocks are observed around the filaments themselves, with weaker

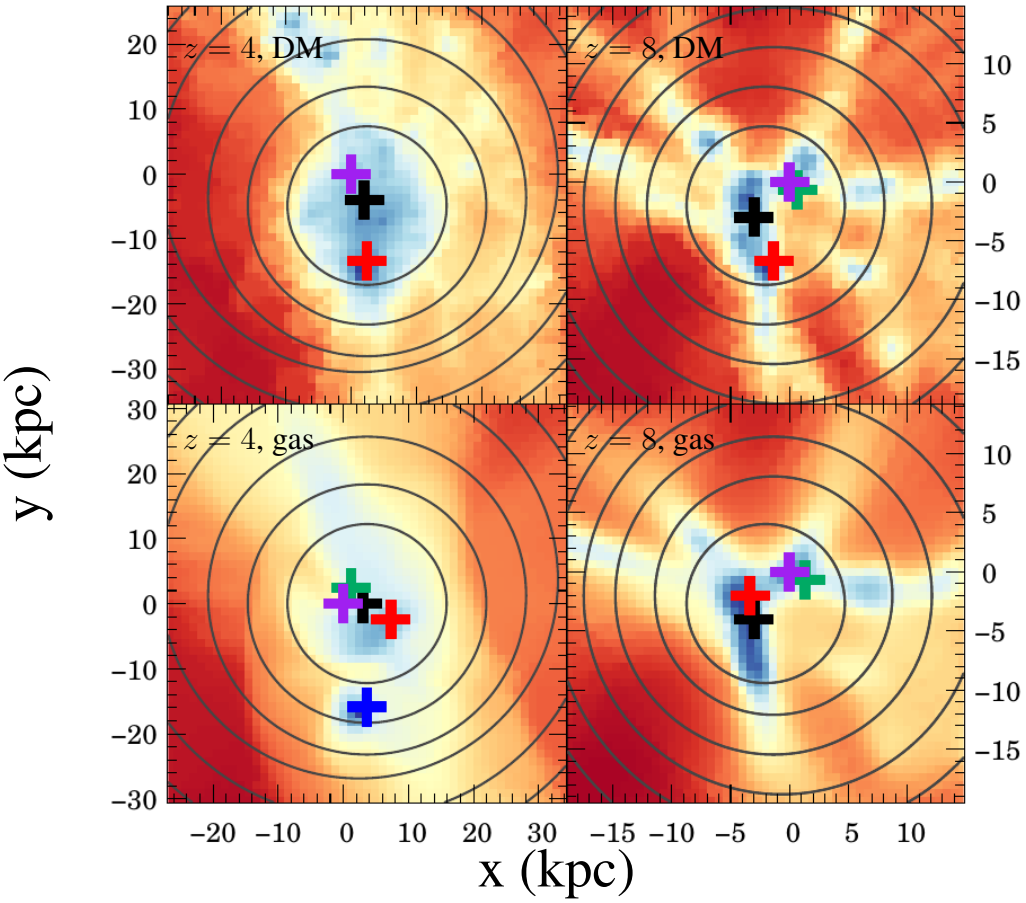

Figure 3.6: Different implementations for finding the filament centre. The *black* cross represents the centre as found by the shrinking circle method. The centre of mass enclosed by each of the *grey* circles is used as the centre for the next iteration. The *green* cross is the centre of mass of the plane, *red* is the local maximum within 10 cells of the centre defined by DISPERSE (*purple*). The global maximum across the entire plane is shown in *blue*. This is coincident with the local maximum in the $z = 8$ snapshot. These slices were randomly chosen for the two redshifts as two extremes of the types of filaments encountered by the algorithm to ensure that a sensible result would be obtained in such cases.

shocks also present at the wall boundaries and where the walls intersect to form the filaments. In the vorticity field (bottom row, middle column of Fig. 3.5) both filaments and walls are identified with the regions of highest vorticity amplitude. The DM filaments (left column of Figs. 3.3 and 3.5) appear wider than their gaseous counterparts. Supernovae feedback (right column of Figs. 3.3 and 3.5) renders filaments and walls imperceptible in the gas vorticity field (bottom right panels) although radial shocks are still present at the filament edges (middle right panel) and the gas density peak remains clearly visible (top right panel).

Radial profiles are measured from the 2D cross-sections by computing the azimuthal average in concentric shells centred on the highest density point. When discussing the effects of resolution on the filament profile, we take the median value for the distribution of all filament segments at a given resolution and for each radius, as a single profile is required. However, for the rest of the measurements in this chapter, we consider individual profiles fitted to each cross-section over the entire radius range. In Fig. 3.7 the median profile obtained in that way (filled red disk symbols joined by the red solid line) can clearly be seen to follow the shape of the other 10 randomly chosen profiles (thin black dashed lines). The advantage of this second method (fitting the whole profile) is that we can easily bin results according to other filament properties, such as distance to the central galaxy. This should more accurately reflect the underlying filament property distribution.

3.3.2.3 The special case of vorticity cross-sections

Vorticity being a vector, the structure of the vorticity field is far more complex than density or temperature (as illustrated by the bottom panels of Figs. 3.3 and 3.5) and, as a result, it not easy to stack individual vorticity profiles obtained for each skeleton segment. When stacking is required, we therefore use the modulus of the vorticity parallel to the direction of the filament and ignore azimuthal variations in vorticity. The vorticity field in the direction of the filament is extracted in the same way as described in the previous section for the density and temperature. As shown in the *bottom* panels of Fig. 3.5, the vorticity has a multipolar structure, with several rotating and counter-rotating vortices surrounding the filament. Outside the filament the amplitude of vorticity rapidly declines. Within filaments, the geometry of the vorticity field is mainly quadrupolar (see Laigle et al., 2015), though we found that dipoles and higher order structures are not uncommon reflecting that the flow have shell-crossed several times). This larger diversity in the structure of the vorticity field probably reflects the fact that the analysis in this chapter looks at smaller scale vorticity than Laigle et al. (2015), and extends the measurement to gas. We recall that primordial vorticity is destroyed in an expanding Universe, and therefore voids are extremely vorticity

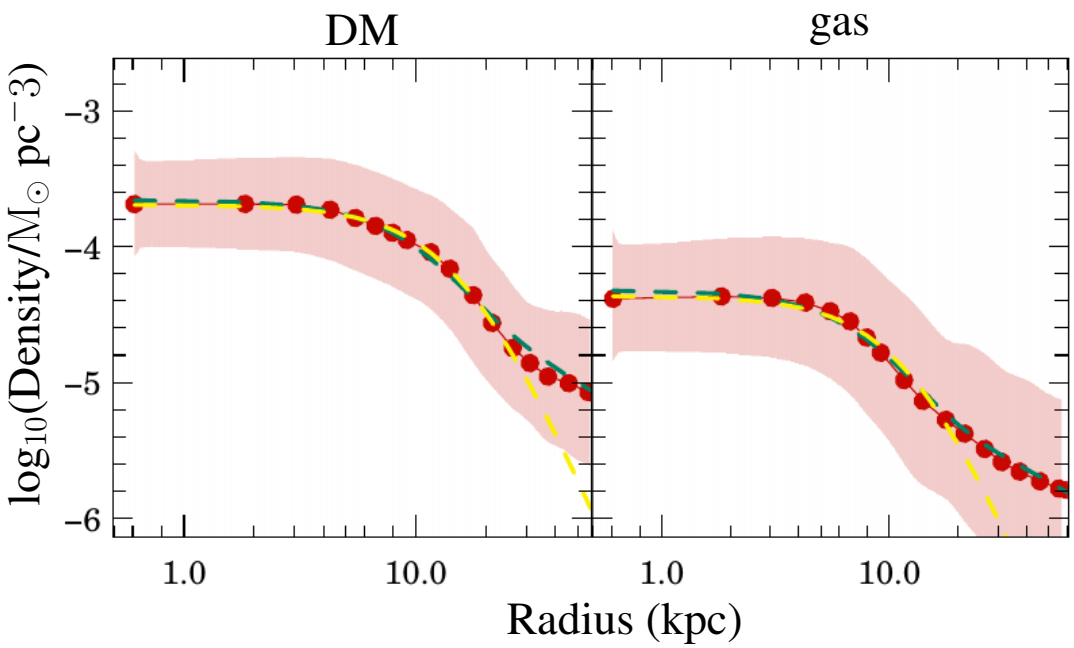

Figure 3.7: Fits of the median DM (left panel) and gas (right panel) density profiles (red solid line and red disk symbols) at $z = 4$, using a filament plus wall $\mathcal{M}_{\rm fil+wall}$ (green dashed line)or a filament only $\mathcal{M}_{\rm fil}$ (yellow dashed line) model. The shaded area represents a 1 sigma deviation estimated by bootstrap re-sampling the values at each radial distance. Though the inner profile appears to be well fitted by both models, the core radius returned by $\mathcal{M}_{\rm fil}$ is twice that of $\mathcal{M}_{\rm fil+wall}$. At larger scales the pure filament model also underpredicts the density.

poor. Vorticity can later be produced by shocks or shell-crossing (respectively for gas and DM), and as result is chiefly confined to walls, filaments and nodes (see e.g. Pichon and Bernardeau, 1999).

3.4 Results: measuring the filament profiles

In the following, we first derive analytically the radial profiles of filaments under the assumption that they are in hydrostatic equilibrium, and then compare them to the profiles directly measured in the simulation.

3.4.1 An analytic description of DM and gas filament profiles

To obtain our analytic solution, we make the simple assumption that filaments may be modelled as infinite self-gravitating isothermal cylinders. Fig. 3.9 presents the sound speed and velocity dispersion profiles in filaments. We have been careful to subtract the bulk velocity of the material when extracting this data. Within the filament, the sound speed

and velocity dispersion are flat and dominate over the accretion velocity onto the filament, which suggests – for the centre of the filament at least – that the filament may indeed be treated as an isothermal cylinder in hydrostatic equilibrium[5] , i.e.

$$\nabla\phi = -\frac{\nabla P}{\rho}\,, \tag{3.1}$$

where $P = \mathcal{K}\rho$, and $\mathcal{K} = \mathrm{k_B}T/(\mu\,\mathrm{m_p})$, with ρ the density, T the temperature, $\mathrm{k_B}$ the Boltzmann constant, $\mathrm{m_p}$ the proton mass and μ the mean molecular weight of the gas. Stodólkiewicz (1963) solved this equation in the case of cylindrical symmetry (see also Ostriker, 1964), and we will discuss the solution shortly. However, before we do, we briefly outline why it also applies to the collisionless DM fluid. Let us consider the time independent Jeans equations (Jeans, 1915) for such a collisionless system:

$$\frac{\partial}{\partial x_i}(n v_i) = 0 \quad ; \quad n v_i \frac{\partial v_j}{\partial x_i} = -n\frac{\partial \phi}{\partial x_j} - \frac{\partial (n\sigma_{ij}^2)}{\partial x_i}\,. \tag{3.2}$$

where v_i are the velocities, σ_{ij} are velocity dispersions and n is the DM number density. Under cylindrical symmetry, we may neglect all but the radial component of these equations. Further assuming steady state (i.e. that $v_r = 0$, such that accretion onto the filament is negligible compared to internal pressure support) and that velocity dispersion is isotropic, the equations simplify to:

$$\frac{d}{dr}(n v_r) = 0 \quad ; \quad \frac{d\phi}{dr} = -\frac{1}{n}\frac{d(n\sigma^2)}{dr}\,. \tag{3.3}$$

The second equation in (3.3) is entirely analogous to equation (3.1), with $\mathcal{K} = \sigma^2$, though it is clear that accretion flow onto the filament cannot be ignored at large radii (see Fig. 3.9). The solution to both equations are therefore identical. The differential equation may be solved analytically as in Stodólkiewicz (1963):

$$\rho(r) = \frac{\rho_0}{(1 + (r/r_0)^2)^2} \quad \text{with} \quad r_0 = \sqrt{\frac{2\mathcal{K}}{\pi G \rho_0}}\,. \tag{3.4}$$

where G is Newton's gravitational constant, ρ_0 is the central density and r_0 the core radius of the filament. Note however that it is the gravitational potential common to both components which should appear on the left hand side in both the second equation in (3.3) and in eq. (3.1), so that technically speaking only the DM is truly close to a self-gravitating isothermal cylinder, the gas being in hydrostatic equilibrium in the potential well of the DM filament.

[5] At least in the plane perpendicular to the filament, as we know that eventually, DM and gas flow along the filament into dark matter halos. In the steady state regime however, such a flow should not perturb the equilibrium.

As a preliminary test of the model, we can use a typical DM filament central density of $\rho_0 \sim 1.7 \times 10^{-26} \mathrm{g\,cm^{-3}}$, i.e. $\sim$100 times the mean density of the Universe (the central filament density is subject to significant variations but this is typical of the median DM density, see left panel of Fig. 3.7, also Ocvirk et al., 2008a; Mandelker et al., 2016, for upper bound on filament overdensity)) at $z = 4$ for our choice of cosmological parameters, and a velocity dispersion $\sigma \sim 10\,\mathrm{km/s}$ (typical of the median DM velocity dispersion we measure, see Fig. 3.9). Plugging these values in the second equation (3.4), we find a scale radius $r_0 \sim 8\mathrm{kpc}$, which is broadly in agreement with the typical radius of the inner profile measured in the simulation, as shown in Fig. 3.7 (left panel) and in table 2. As the width of the gas filament is set by the depth of the DM potential and the gas temperature, one needs to artificially use the DM central density for ρ_0 in equation (3.4) rather than that of the gas to obtain an estimate of r_0 for this latter (as shown on Fig 3.7 the gas density is about a factor 5 lower than that of the DM throughout the filament, in agreement with the universal value $\Omega_{\mathrm{DM}}/\Omega_B$). As the DM velocity dispersion for the particular filament we study is comparable to the gas sound speed (i.e. $\sim 10\,\mathrm{km/s}$ or 10^4K which corresponds the bottom temperature of the cooling curve for atomic hydrogen, see Fig. 3.9) we expect a core radius for the gas similar to that of the DM, i.e. $r_0 \sim 8\mathrm{kpc}$, and this indeed seems to be within a factor of 2 of the measured value (see right panel of Fig. 3.7 and table 2).

However, the isolated, infinite isothermal cylinder appears too highly idealised a model in at least one aspect, as can be seen by the failure of the yellow dashed curves (best fit obtained using the first equation (3.4)) to match the measured median profiles (solid red lines and red disk symbols) in Fig. 3.7. In reality filaments are born from the intersection of walls (see Fig. 3.5 middle column panels), the presence of which will modify the filament profile, especially in the outer regions. The filament can be represented in cartoon form in Fig. 3.8. Here the central filament (the black cylinder) is embedded in a wall like structure. Further out, the red cylinder represents the point at which fresh matter is accreted onto the filament, where the filament profile is expected to break down. The left hand side gives a comparison of the planes to this highly idealised representation of the filament.

Assuming that the walls may also be treated as hydrostatic atmospheres, but this time confined to a plane containing the filament, the equations governing their profiles are identical to eqs. (3.1) and (3.3). These latter simply need to be solved in 1D instead of 2D, yielding in the direction y perpendicular to the plane (Spitzer, 1978):

$$\rho(y) = \rho_{\mathrm{y_0}}\,\mathrm{sech}^2(y/h)\,, \tag{3.5}$$

with the scale height $h = \sqrt{\mathcal{K}/(2\pi G\rho_{\mathrm{y_0}})}$ taking a very similar functional form as r_0 in eq. (3.4), and $\rho_{\mathrm{y_0}}$ standing for the density in the mid-plane ($y = 0$) of the wall. However,

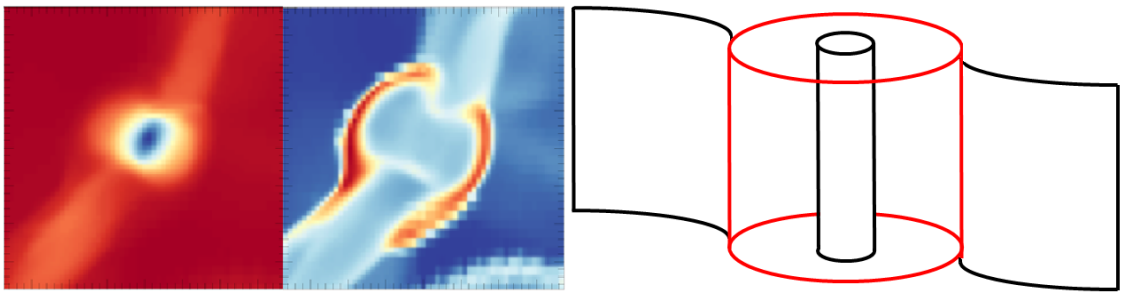

Figure 3.8: A cartoon representation of the filament (*right*), alongside a couple of slices across the filament density (*left*) and temperature (*middle*). The key filament features are the core radius delineated by the central black cylinder in the cartoon, the truncation radius in red at the position of the accretion shock, all embedded in the black wall structure. Note that the cartoon version is viewed near perpendicular to its length rather than face on as in the slices.

we need to integrate this wall profile over concentric cylindrical shells to evaluate how it modifies the filament profile. Unfortunately, this integral does not possess a simple analytic closed form, so we approximate the azimuthally averaged density of the wall by:

$$\rho(r) = \frac{\rho_{\mathrm{y0}}}{\alpha} \frac{\tanh(\alpha r/h)}{r/h} \,, \tag{3.6}$$

with $\alpha = \pi/2$. Such an approximation captures the asymptotic behaviour of the correct solution for $r \gg h$, and is accurate to better than 14% for all values of r. As can be seen in Fig. 3.7, the inclusion of a wall modifies the shape of the outer filament. This might (at least partially) explain the discrepancy between filament density profiles previously reported in the literature, with power-law slopes ranging between -1 and -2 (see e.g. Colberg et al., 2005; Dolag et al., 2006; Aragon-Calvo et al., 2010). However we caution that these studies were performed on much larger scales and so may not be directly comparable to our work as they might potentially be affected by different biases.

One can easily show that in the case where the gas isothermal sound speed $c_s = \sqrt{\mathrm{k_B} T/(\mu\, \mathrm{m_p})}$ equals the DM dispersion velocity σ, the density profiles of the gas and DM have the same exact shape, differing only by their normalisation, i.e. the value of the central density. In the more general case where these two velocities differ, one can solve Eq. (3.1), assuming that the DM dominates the potential (LHS) and is resisted by the gas pressure on the RHS. This once again gives an analytic solution:

$$\rho_g(r) = \rho_{\mathrm{g0}} \left(1 + (r/r_0)^2\right)^{-2\sigma^2/c_s^2} \,, \tag{3.7}$$

so that if $c_s > \sigma$, it is shallower than that of the DM, and vice-versa. Katz et al. (2019) measured this effect by comparing two versions of the same cosmological simulation with

and without reionisation. They find that narrow streams are widened by the photo-heating of the gas, and that the gas counterparts of the lightest DM filaments can even be entirely erased.

Note that this reasoning also applies to the isothermal gas density profile of a DM dominated isolated wall: when c_s and σ differ, it becomes

$$\rho_g(y) = \rho_{\mathrm{gy_0}} \,\mathrm{sech}^{2\sigma^2/c_s^2}(y/h)\,, \tag{3.8}$$

3.4.2 Testing the simple model

The first assumption we have made concerns the isothermality of the filament-wall system and that accretion onto the filament provides it with negligible support. In Fig. 3.9 we can see that for the no feedback run both the gas sound speed (black solid line and solid disk symbols) and the DM velocity dispersion (red solid line and solid disk symbols) stay constant over most of the width of the filament, indicating that the isothermal approximation does indeed hold rather well. In addition, the gas and DM accretion velocities are considerably lower than the sound speed and velocity dispersion respectively, and as such the dynamics of the system should be mainly driven by the pressure support. Moreover, the accretion shock itself is also non-adiabatic. Indeed, the upstream mach number (beyond 20 kpc) is $\mathcal{M}_u \approx 50/10 = 5$ (from Fig. 3.9, comparing the outer gas accretion velocity with the sound speed), thus the Rankine-Hugoniot jump conditions lead to a downstream Mach number $\mathcal{M}_d = 0.47$, and it thus follows that the downstream sound speed (within 10 kpc of filament centre) should be $40\,\mathrm{km\,s^{-1}}$, i.e. twice the value of that measured. This indicates that the filament accretion shock is radiative rather than adiabatic. Finally, we also plot on Fig. 3.9, the circular velocity $V_c \equiv (GM/r)^{1/2}$ (blue solid line with solid disk symbols) measured for the filament, where M is the mass enclosed by a cylindrical shell of radius r. We find that it is comparable to or lower than the sound speed/velocity dispersion, which further indicates that the filament is chiefly supported by pressure rather than by rotation, contrarily to what is argued in Mandelker et al. (2018a).

In Fig. 3.7 we present 2 models, pure filament ($\mathcal{M}_{\mathrm{fil}}$), filament with wall ($\mathcal{M}_{\mathrm{fil+wall}}$). In practice, this means that along each individual skeleton segment, we fit the radial density using the formula:

$$\rho(r) = \frac{\rho_0}{(1+(r/r_0)^2)^2} + \rho_1 \tanh(\alpha r/r_1)\frac{r_1}{r}\,, \tag{3.9}$$

where $r_1 = h$, and $\rho_1 = \rho_{\mathrm{y_0}}\alpha^{-1}$. In principle, the values for σ and c_s could be different for the wall and embedded filament. However, for sake of simplicity and since we expect these two quantities to roughly behave in a similar manner, at least in the vicinity of the

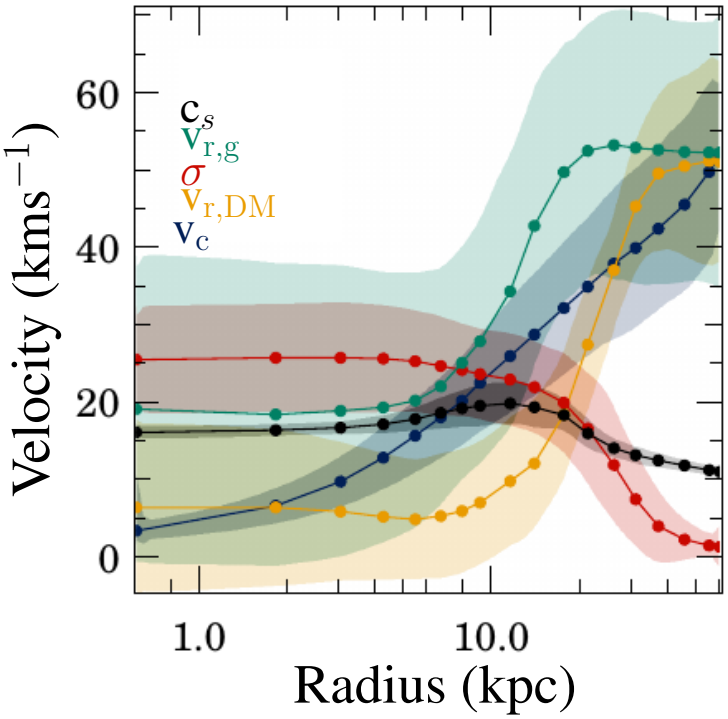

Figure 3.9: Median values for gas sound speed (black) from the no feedback run, DM velocity dispersion (red), gas (green) and DM (yellow) accretion velocity and circular velocity (blue) profiles at $z = 4$, with shaded regions representing the 1 sigma scatter about the mode for each data point. Note that in the inner filament region, one measures a near constant sound speed and velocity dispersion, which indicates the filament is, to a large extent, isothermal. This breaks down at larger radii, due to both higher rates of radial inflow and falling sound speed and velocity dispersion. The velocity dispersion and sound speed are significantly higher over the inner filament than the circular velocity, indicating that the structures do not require rotational support.

filament, we ignore the possible change in the ratio of σ^2/c_s^2 in our $\mathcal{M}_{\rm fil+wall}$ model (see Fig 3.9 for the validity of this assumption). The fit is performed using the Levenberg-Marquardt algorithm where the wall is first fit to the outer half of the profile with the filament contribution set to zero. The wall parameters are then frozen in place while fitting the filament parameters. In the case of a pure filament model (i.e. $\mathcal{M}_{\rm fil}$), the filament is fit to the entire profile, setting $\rho_1 = 0$. The procedure was tested by applying it to a sample of artificial profiles, which typically returned radii within 1 cell of the input radius, but does break down when the filament is too wide (i.e. extends into the region where the wall is fitted). While this is a suitable range for the purposes of this chapter, filaments continue to grow as time progresses, and this method may become unsuitable at later times. In Fig. 3.7, we show how each of the two models fares against the measured median density profile of the DM (left panel) or gas (right panel) at $z = 4$. Errors on the radius are estimated by considering the full distribution of density profiles measured from individual skeleton segments, and fitting this distribution with the best matched normal distribution to evaluate the value of the standard deviation. For errors on the density, we use the best matched log-normal distribution instead, which is better suited to density distributions in filaments(see e.g. Cautun et al., 2014).

Looking at Fig 3.7, it is not possible to distinguish the two models, $\mathcal{M}_{\rm fil+wall}$ (green curve) and $\mathcal{M}_{\rm fil}$ (yellow curve), in the inner region ($r \leq$20 kpc). When the profiles are stacked as in this figure the fits work equally well with or without the wall. However the size of the core radius that these models return are very different when considering individual profiles: $r_0 = 19.34 \pm 7.15$ kpc for $\mathcal{M}_{\rm fil}$ compared to $r_0 = 8.39 \pm 3.82$ kpc for $\mathcal{M}_{\rm fil+wall}$ for the DM filament. This factor of 2 discrepancy is also present for the gas filament: $r_0 = 8.99 \pm 1.86$ kpc for $\mathcal{M}_{\rm fil}$ compared to $r_0 = 5.04 \pm 1.96$ kpc for $\mathcal{M}_{\rm fil+wall}$. The core radii given by the $\mathcal{M}_{\rm fil}$ model can be rejected by simple visual inspection of Fig. 3.3: they are comparable to the outer edge radius of the filaments.

Although we only show the $z = 4$ median profiles, this behaviour of the two models holds for all redshift outputs examined in this work (see table 2 for a list).

We now discuss how each model fits individual cross-section density profiles (examples of these are shown as thin dashed curves on Fig. 3.7) rather than the median. In this case, errors on the density are estimated by calculating the gradient of the density profile and multiplying it by the spatial resolution (size of cell). For the DM density, a Poisson noise contribution is also added in quadrature to the error estimate. We plot in Fig 3.10 the corresponding distributions of reduced χ^2_ν which peaks at 3 for the DM density profile and 0.5 for the gas in the preferred model $\mathcal{M}_{\rm fil+wall}$ (dashed and solid green lines in Fig 3.10 respectively). For the $\mathcal{M}_{\rm fil}$ model these same distributions are much less strongly peaked

around $\chi^2_\nu = 6$ and $\chi^2_\nu = 4$ for the DM and gas density profiles respectively (dashed and solid yellow curves). Note that the measurement errors are relatively large, especially at the centre of the filament for the gas, and overall for the DM because of a significant Poisson noise contribution. Though these values of χ^2 suggest a fit to the simulation data which lies somewhat on the poor side, it is unclear that the validity of the model should be measured by χ^2 statistics in the first place. Indeed individual profiles deviations from the model are very likely correlated with one another when substructures residing within the filament perturb its density field.

For sake of completeness, let us mention that at $z = 4$, the fits of the full set of skeleton segments using the $\mathcal{M}_{\rm fil+wall}$ model to the DM component for the no feedback run returns $r_0 = 8.39 \pm 3.82$ kpc as the mode and width of the fitted gaussian for the core radius of the filament (as previously mentioned), and $r_1 = 6.79 \pm 2.80$ kpc for the scale height of the wall. Similarly we fit a log normal distribution to the DM central densities to obtain $\log_{10}(\rho_0/\mathrm{M}_\odot \mathrm{pc}^{-3}) = -3.67 \pm 0.49$ for the filament and $\log_{10}(\rho_1/\mathrm{M}_\odot \mathrm{pc}^{-3}) = -4.29 \pm 0.45$ for the wall. As for the gas, we obtain $r_0 = 5.04 \pm 1.96$ kpc and $r_1 = 7.70 \pm 3.00$ kpc, with densities of $\log_{10}(\rho_0/\mathrm{M}_\odot \mathrm{pc}^{-3}) = -4.37 \pm 0.45$ and $\log_{10}(\rho_1/\mathrm{M}_\odot \mathrm{pc}^{-3}) = -4.96 \pm 0.37$. A list of values for the filament radii and densities at other redshifts is provided in tables 2 and 4.

As gas filament temperature remains around 10^4 K at all times after re-ionization, their density profile flattens rapidly as the mass of their DM counterpart decreases and the sound speed approaches the critical value of $c_s = \sqrt{2}\sigma$. This means that low mass filaments will only exist in the DM component (compare the top left and middle panels in Fig 3.3), as a 10^4 K gas has too much pressure to be trapped in the DM potential well in that case, and thus, talking about a gas r_0 becomes quite meaningless. On the other side of the mass range, we expect more massive filaments, where DM has a larger velocity dispersion, to have better defined cores in the gas than DM, as this former should still radiatively cool down to $\sim 10^4$ K and thus have a much steeper density profile than its DM counterpart. As a result of this cooling, it is possible that the central gas density of massive filaments will become comparable to that of the DM, in which case our assumption that the DM sets the gravitational potential would cease to be valid and the core radii of the two components might then differ substantially. However, for the filament system considered in this chapter, the approximation of similar DM and gas density profiles seems to hold quite well (see Fig 3.7).

In light of the previous discussion, we interpret the difference between the measured and predicted median values of r_0 as a departure from the isothermal/hydrostatic approximations for the filament (see Fig. 3.11, middle panels), rather than to asymmetry or a

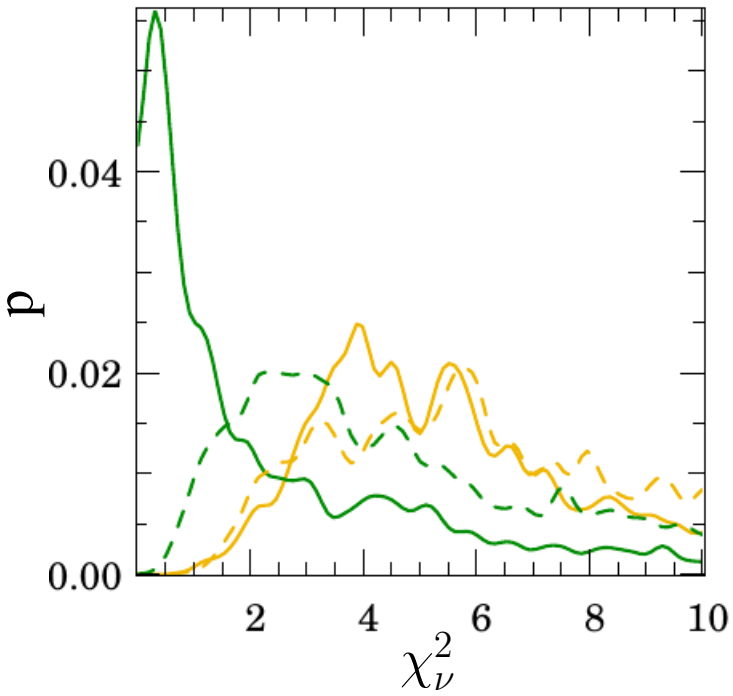

Figure 3.10: Normalised distributions of reduced χ^2_ν obtained when fitting the filament only (yellow), or filament plus wall (green) models to filament density projections in individual slices perpendicular to each skeleton segment at $z = 4$ (see text for detail). The gas filament is represented by the solid curves, whilst the DM counterpart is shown as dashed lines. Though the fits for the $\mathcal{M}_{\rm fil+wall}$ model are better than $\mathcal{M}_{\rm fil}$, it is hard to see this in the χ^2_ν. The filament fit works by optimising the wall, followed by the filament, which does not guarantee that the full fit itself will have a reasonable χ^2_ν.

systematic variation of core size as a function of distance to the galaxy (see section 3.13 for more detail concerning this latter variation). For the DM, the filament median velocity dispersion varies by 10% within $\sim 2-3$ core radii. For the gas, where a shock is clearly visible around 15 kpc away from the centre of the filament (middle right panel of Fig. 3.11), the temperature varies by less than 60% between the centre of the filament and the maximum of the shock.

These discrepancies notwithstanding, it is striking how filaments in our cosmological simulations resemble those obtained in a much more idealised set-up with similar resolution presented in Klar and Mücket (2012). More specifically, even though these authors ignore the DM component as well as the fragmentation and mergers of filaments, they find that their gaseous linear structures are in radial hydrostatic equilibrium and exhibit an isothermal core several kpc wide with central densities and temperatures remarkably similar to those we measure in a more realistic context. They also identify an outer shocked region with similar properties as ours, but with a gravitational focusing which reduces r_0 and increases ρ_0 as the filament approaches the DM halo to which it is connected. As previously mentioned, we will come back to this latter point in section 3.4.4 of our results devoted to the temporal and spatial evolution of filament properties, but already note that such a focusing effect is not as pronounced in our simulations.

3.4.3 Vorticity, temperature and the radial extent of filaments

Having extracted the main filament from the simulation and measured the characteristic radius of its core through the use of a simplified model of hydrostatic equilibrium for its density profile, we now turn to the question of determining its outer size, or *truncation* radius, as the analytic profile cannot extend to infinity in the radial direction.

Beyond a certain radius it is no longer true that sound and dispersion velocities dominate over the accretion velocity, as can be seen in Fig. 3.9. A failure of the hydrostatic model will thus occur, leading to a potential definition of the truncation radius, which also coincides with the position of the accretion shock onto the filament for the gas. We have opted not to use the peak temperature position as a definition of the truncation radius, as individual skeleton segment profiles, both in temperature and vorticity are often asymmetric and/or distorted by their environment, and may contain multiple peaks when averaged over concentric radial shells as a result (see Fig 3.5 for an example). Moreover, such a definition would not apply to DM velocity dispersion profiles. We have therefore chosen to use a universal method for all physical quantities and types of filament (gas or DM), which also has the benefit of providing internal consistency between measurements. We

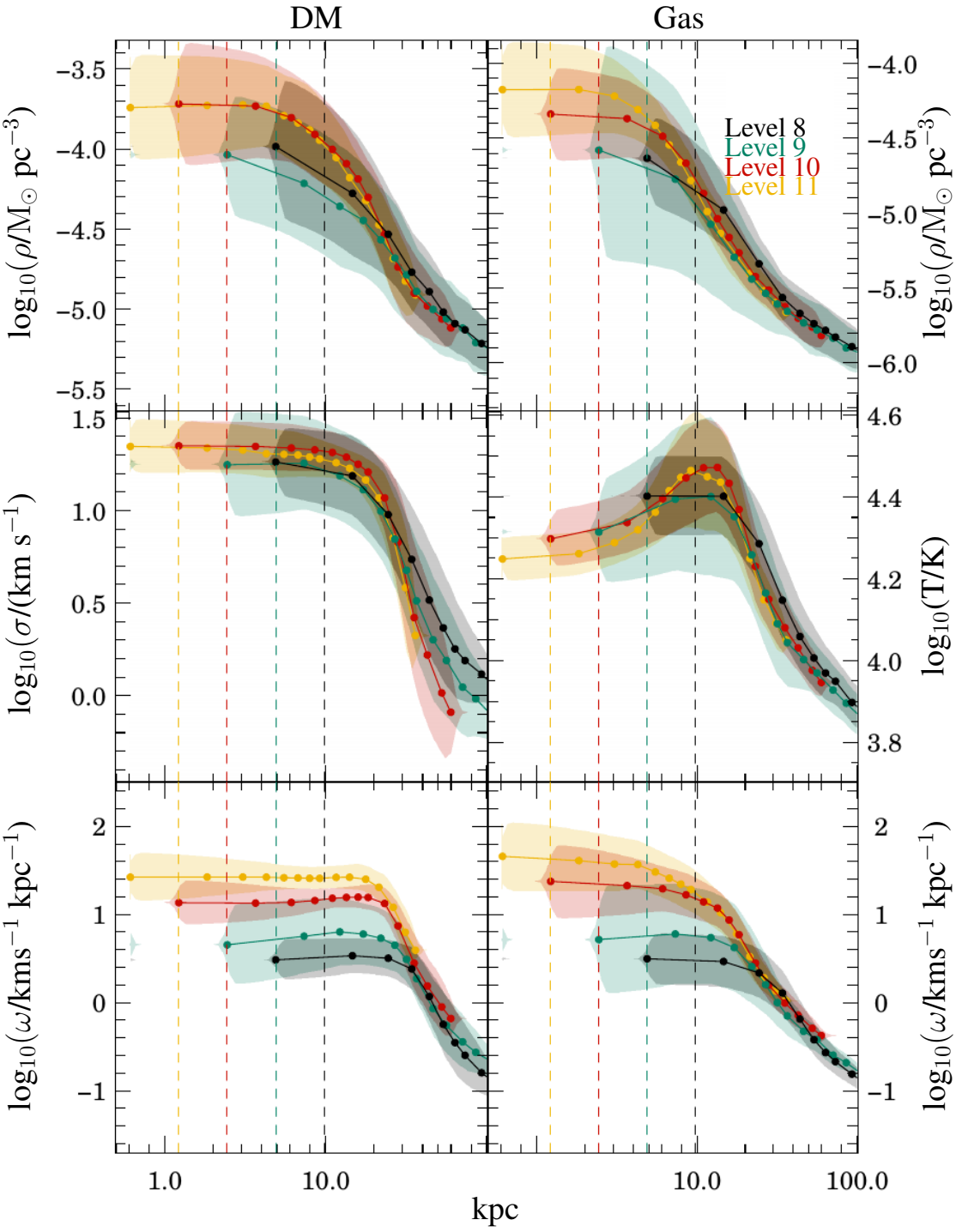

Figure 3.11: The median radial profiles of the filaments in DM (left column) and gas in the no-feedback run (right column), for density (top row), temperature (middle row) and vorticity (bottom row) at $z = 4$. Displayed profiles (from black to yellow) represent data extracted at different spatial resolutions of the AMR simulation grid (vertical dashed lines or levels 8 to 11 respectively, see text for detail). Error bars are generated by bootstrapping the distribution of individual filaments profiles, and taking the root mean square at each radius. The profiles converge to the same value as the resolution is increased.

thus define the truncation radius as the point where the steepest descent in the temperature/vorticity/velocity dispersion profile is attained. At $z = 4$ this yields a truncation radius of 18.6 ± 4.0 kpc for the gas temperature profile, while the gas vorticity profile gives 21.7 ± 6.6 kpc. The DM filament at the same redshift has a measured truncation radius of 28.6 ± 6.5 kpc when using the velocity dispersion profile, and 25.9 ± 4.5 kpc if we consider its vorticity profile (see Table 2). It is interesting to note that the accretion shock of the gas filament seems positioned well within the DM filament (roughly at half the DM truncation radius). In order to check the robustness of these measurements vis-à-vis resolution the data was extracted at four different spatial resolutions. Note that this is *not* a study where we change the resolution and re-run the simulation, but simply a post-processing of the *same* simulation at different resolutions, so we expect to achieve better agreement than if we had done a proper resolution study. As resolution increases progressively from 10 kpc to 1.22 kpc (level 8 to 11), the profiles are seen to converge across every panel of Fig 3.11. Note that for comparison, our *lowest* level of resolution, i.e. 10 kpc roughly corresponds to the *highest* level of resolution available to capture filaments in current cosmological simulations with volumes on the order of 100 Mpc on the side, like MARE NOSTRUM (Ocvirk et al., 2008b), HORIZON-AGN (Dubois et al., 2014a), MassiveBlackII (Khandai et al., 2015), EAGLE (Schaye et al., 2015), ILLUSTRISTNG (Nelson et al., 2018) or SIMBA (Davé et al., 2019).

Looking first at the density profiles both of the DM and gas filaments (top panels of Fig. 3.11), one can see that in going from the highest resolution level to the lowest one, the central density (inside the core) is underestimated by about an order of magnitude, and one becomes unable to measure the core radius of the profile with a reasonable accuracy. On the other hand, the DM velocity dispersion profiles (middle left panel of Fig 3.11) seem to converge faster than the density ones, with the lower resolution estimates compatible with the higher resolution ones at all radii. This seemingly rapid convergence is induced by the shape of the isothermal profiles which are, by definition, flat, especially in the case of the DM. For the gas (middle right panel of Fig 3.11), the temperature does not show as marked a convergence as the DM velocity dispersion because of the presence of the accretion shock: the low resolution data (black curve), which barely resolves the truncation radius of the filament underestimates the shock temperature and overestimates the core temperature by a similar amount. Having said that, the shock position is fairly robust to resolution changes despite being radially asymmetric, which leads to its 'smearing'. A minimum resolution of 2.4 kpc is required to correctly capture both the temperature of the accretion shock and that of the gas filament core.

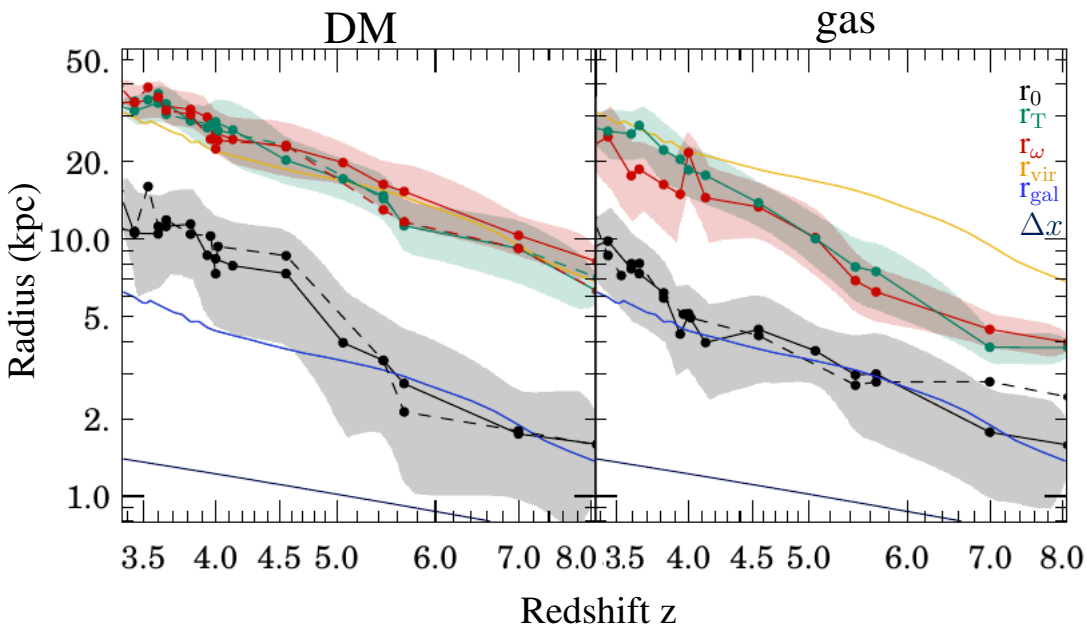

Figure 3.12: Evolution of the core (black curves) and truncation radii (red and green curves for estimates based on the vorticity and temperature respectively) of the filaments with redshift. The left panel represents the DM filament, and its gas counterpart is on the right. Dashed lines represent the feedback run. The virial radius is shown in orange and the approximate extent of the central galaxy (20% of virial radius) in yellow. Finally, the spatial resolution of the simulation in the filament is indicated by the solid blue line at the bottom of each panel. The core radii scale roughly as the galactic radius, particularly the gas, while the DM truncation radius scales as the virial radius. The gas truncation radius catches up to the DM by approximately $z = 3.5$.

3.4.4 Evolution of filament profiles over cosmic time and distance from central halo

Having focused, so far, the discussion of the filament profile at $z = 4$, we now address the issue of its temporal evolution. Since $r_0 = \sqrt{2\mathcal{K}/\pi G\rho_0}$, we naively expect that $r_0 \propto (1+z)^{-3/2}$, provided the filament central density scales with that of the background Universe — which we measure to be the case (see Table 4) — and its central temperature/velocity dispersion remains roughly constant with redshift. Conversely, we can deduce the scaling of filament temperature/velocity dispersion with redshift by measuring the departure of r_0 from this specific power law scaling. In our simulation, we find that for the gaseous filament, the central radius grows as $r_0 \propto (1+z)^{-2.72\pm0.26}$, which means that the sound speed should scale like $c_s \propto (1+z)^{-1.22\pm0.12}$ whereas we measure $c_s \propto (1+z)^{-1.41\pm0.28}$, i.e. an evolution quite consistent with the naive expectation.

For the DM filament counterpart, the growth of r_0 is faster, with a measurement of $r_0 \propto$

$(1+z)^{-3.18\pm0.28}$ (see Fig 3.12), a faster rate than the approximate size of the central galaxy ($r_{\rm gal} = 0.2r_{\rm vir}$, blue solid line on the Figure). This implies that $\sigma \propto (1+z)^{-1.68\pm0.15}$ as redshift decreases, whereas we measure in the simulation that σ scales as $(1+z)^{-1.46\pm0.39}$. The evolution of both gas and DM filament core radii are therefore consistent with the naive expectation at a $\sim 1\ \sigma$ confidence level. The explanation for the somewhat faster growth of the core radius of the filaments than the radius of the central halo to which it is connected is that the 'old' core material is preferentially drained by halos residing within the filament, while a 'new' core forms out of more freshly accreted matter onto the filament (see e.g. Pichon et al., 2011). As a result, the filament core radius is more sensitive to the recent accretion history onto the filament than the halo. Such a behaviour is reminiscent, at least qualitatively, to that of the Navarro–Frenk–White density profile scale radius, r_s, found by e.g. Muñoz-Cuartas et al. (2011) whose time evolution also differs significantly from that of the virial radius of the DM halo (except in that case it is the opposite: r_s, which is less sensitive to the halo recent accretion history, starts decreasing with redshift earlier than $r_{\rm vir}$, see their Figure 5). As the gas can be considered, to first order, in hydrostatic equilibrium in the DM filament potential well, we expect the evolution of its core radius to be somewhat influenced by that of the DM, i.e. that its growth also be sped up. We intend to explore this effect in more detail and with a larger sample of filaments to better assess the universality of this behaviour in the next chapter. It should be noted that the scaling is a consistency check rather than a prediction. The predicted filament index from Eqn. 3.7, $n = (\sigma/c_s)^2 \propto (1+z)^{-0.1\pm0.03}$. This is a rather slow evolution, which is close to constant. It does have the wrong sign compared to what we will discover later in Chapter 4. It is also in conflict with the gradual disintegration of filaments as the Universe expands and hints that the underlying assumption that the filaments themselves are not truly in isothermal equilibrium. Under this assumption neither the temperature nor the velocity dispersion can evolve. Rapid changes in the gravitational potential is what allows the DM particles to exchange energy during shell crossing. This moves the DM closer to equilibrium and reduces the temporal variation in the potential. This slows the process which moves the DM towards equilibrium, and ensures that equilibrium can never truly be reached. This is particularly true on the outer edges of the filament.

As for the truncation radius for the gas/DM filaments, determined from either the vorticity or the temperature/velocity dispersion, it represents the locus where fresh material is accreting, and as such is the rough equivalent of the halo virial radius. Fig. 3.12 shows the evolution of this radius as a function of redshift, along with the size of the main halo embedded in the filament ($r_{\rm vir}$, orange solid line). For the DM filament, the truncation radius evolves as $r_\omega \propto (1+z)^{-1.99\pm0.09}$ or $r_T \propto (1+z)^{-2.16\pm0.12}$, depending on whether ones

uses vorticity or velocity dispersion to define it. This is a growth rate very similar to that of the halo size $r_{\rm vir} \propto (1+z)^{-2.11\pm0.02}$ in this range of redshifts. However, the gas truncation radius, either derived from the vorticity or temperature of the gas filament which scale as $r_\omega \propto (1+z)^{-2.85\pm0.17}$ and $r_T \propto (1+z)^{-3.36\pm0.12}$ respectively, grows significantly faster than its DM counterpart. This is reminiscent of the stability driven argument for the propagation of a radiative shock within DM halos advanced by Birnboim and Dekel (2003), but this time applied to the filament: as time progresses and density drops the shock is able to propagate outwards and ends up filling the entire DM filament volume. Practically, this means that even though the gas filament starts off being smaller than the central halo embedded within it (see Fig. 3.12) at high redshift, the truncation radius rapidly catches up with the virial radius. In our specific case, they are essentially the same size by $z = 3.5$.
The exact extent of the truncation radius for the gas is highly sensitive the nature of the shock and the nature of the feedback. Indeed, in the feedback run no such equilibrium is established, with the filament existing inside a supernova superbubble. The accretion shock is completely overpowered by the influx of energy from stellar feedback. This sensitivity could potentially be probe of the nature of galactic feedback.
The truncation radius is entirely analogous to the splash radius defined by Diemer and Kravtsov (2014). This is the radius to which DM is capable of returning to once accreted by a halo, defining a caustic. The splash radius is the point at which the rate of decrease with radius of the density is at its minimum. Adhikari et al. (2014) present a simple model which predicts the size of this splash radius from the rate of accretion alone. Mass dependence is suppressed if the splash radius is expressed in terms of the virial radius. The relation between splash radius and accretion rate is given by:

$$R_{\rm splash} \propto (1+z)^{-1-\Gamma/D} \,\text{with}\, \Gamma = \frac{d\log(M_{\rm vir})}{d\log(a)}\,, \tag{3.10}$$

where a is the scale factor. D is the number of dimensions that the object has collapsed over, in this case 3. Note that strictly speaking the mass within the splash radius should be used, however, the difference in accretion rate is typically within 0.1 dex between the two mass definitions provided $\Gamma > 0.5$. In our case, since we have the splash radius equivalent, we can use the mass enclosed within the truncation radius. Measuring the accretion rate onto the filament in the NUT simulation yields $\Gamma = 2.9 \pm 0.1$, and setting $D = 2$ for filamentary collapse suggests that $r_{\rm tr} \propto (1+z)^{-2.45\pm0.05}$, which disagrees with the scaling of the truncation radius obtained. It is possible that lower densities in filaments compared to halos results in slower relaxation towards equilibrium, giving a slower growth rate in truncation radius. It is also possible that drainage of matter from within the filaments onto substructure within them removes dispersion support. In any case, further work is required

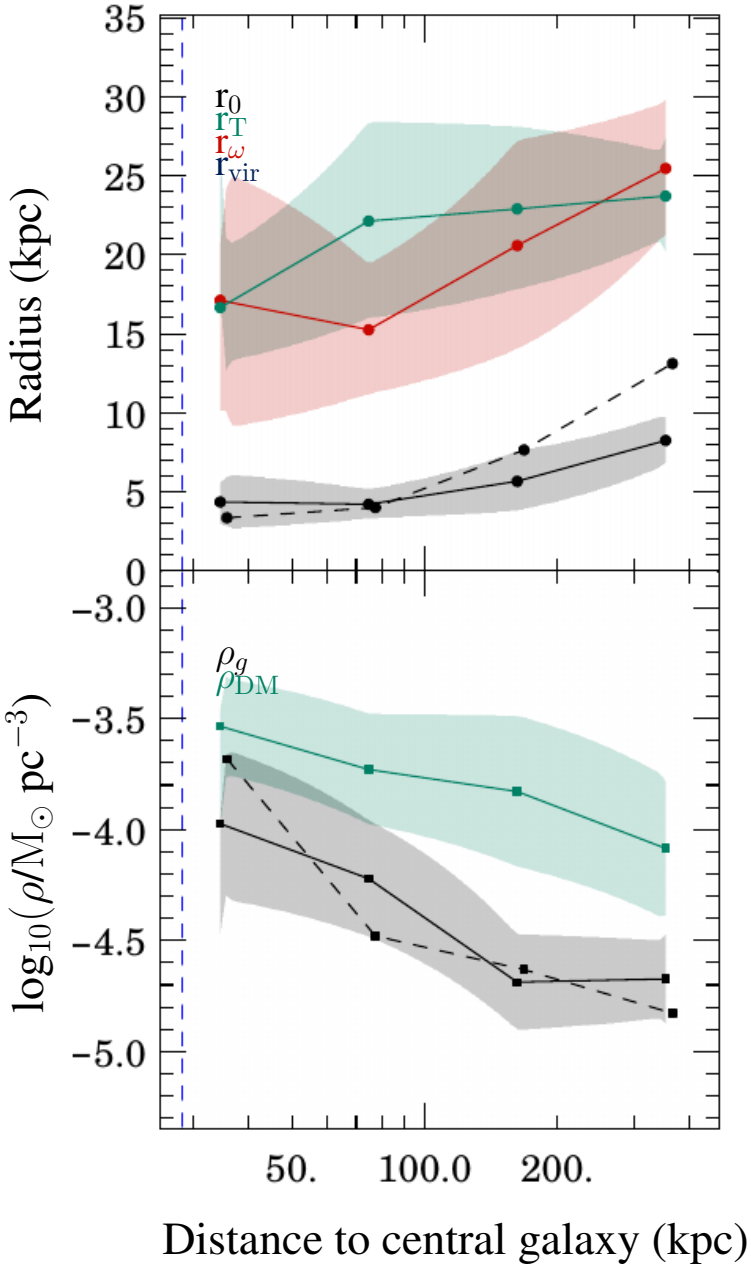

Figure 3.13: *Top:* Gas filament radii as a function of distance to the galaxy, in the no-feedback (*solid* line) and feedback runs (*dashed* line) at $z = 4$. The core radius is in black, whereas the truncation radius estimated from the temperature and the vorticity profiles are in green and red respectively. Note that the truncation radius cannot be determined from either the vorticity or temperature when feedback is included. *Bottom:* Central density of the filament as a function of distance to the galaxy. Gas is black, DM is green, with solid and dashed lines representing no feedback and feedback runs respectively. The vertical blue dashed line indicates the virial radius of the halo. The filaments narrow slightly as they approach the NUT galaxy, while their central density rises.

to establish the impact of filaments of a variety of masses and accretion rates on their truncation radii.

We now go back to $z = 4$ to explore the effect of distance to the galaxy on the width of the filament. As can be seen in Fig. 3.13 (top panel), both the core and truncation radii of the gas filament decrease by less than a factor 2 as a function of the distance to the main galaxy embedded within it. This decrease is progressive, from a maximum radius at 300 kpc away, which corresponds to the distance of either ends of the filament (see Fig. 3.1), to the virial radius of the central galaxy. We caution the reader that this is somewhat different to the reported behaviour of the filament once it enters the virial radius of the embedded DM halo (e.g. Danovich et al., 2012). Indeed, within the virial radius, one expects the gas filament to undergo more important gravitational focusing (Klar and Mücket, 2012). The reason why this does not happen as strongly in our case very likely has to do with the fact that, as previously mentioned, we chose to excise embedded DM halos to focus our analysis on filament properties. However, while the filament radii do not decrease much as the gas approaches the halo, it is still enough to increase the central density, rising by a factor of ~ 5 (dark solid line and symbols in the bottom panel of Fig. 3.13). Note that such a behaviour is not specific to the gas as the DM central density (green solid line in the bottom panel of Fig. 3.13) undergoes a similar change with distance to the galaxy, which is consistent with an interpretation in terms of mild gravitational focusing but also of the progressive draining of the filament core draining by the halo, as previously mentioned. Finally we want to emphasize that the NUT galaxy, essentially connected to one (two if counting each direction as an individual object) filament(s) could be somewhat of a peculiar case. Once again, further high resolution work on a much larger sample of filament/galaxies is required to properly investigate the influence of connectivity and/or halo mass on the results.

3.4.5 The impact of stellar feedback on filaments

Stellar feedback has a profound impact on the region surrounding the galaxy and filament. Given enough time, the superbubbles it generates extend most of the way up the filament, as can be seen in the central and bottom right panels of Fig. 3.3. These galactic winds inject vorticity on large scales, and as such, this physical quantity is no longer confined to the filamentary gas. Note that, in spite of this, larger scale cosmic web filaments (i.e. larger than the superbubble) could still have well defined vorticity quadrants. More importantly, vorticity in the dark matter filament counterpart (bottom left panel of Fig. 3.3) remains by-and-large unaffected, to the point that we do not deem it necessary to plot it on Fig. 3.13 for the run with feedback.

The CGM/IGM gas is also strongly heated by this stellar feedback, and so the temperature signature of the accretion shock onto the filament is lost as well, as the middle right panel of Fig 3.3 demonstrates. Once again, this signature survives in the velocity dispersion of the DM component (middle left panel of Fig 3.3). Despite such significant perturbations, the presence of a DM filament potential well coupled to the relatively high density of the gas ensures that the cooling time within the filament remains short. As a result, the filament is still visible as a cold stream cutting through the hot superbubble in the middle right panel of Fig. 3.3.

Due to these consequent perturbations induced by the stellar feedback, we cannot use either the temperature or vorticity to define the gas filament truncation radii in the feedback run. It should also be noted that our assumption of isothermality of the filaments becomes less valid than in the no stellar feedback case as stronger temperature gradients develop between core and outer envelope. To be more specific, in the no feedback case, the temperature varies between core and truncation radius by about a factor of two, but in the feedback case in can reach an order of magnitude. However, most of this gradient is localised in the outer parts of the filament, so that the central region retains a significantly large isothermal core. This can be understood by performing the following simple calculation. Neglecting the presence of the wall, we may integrate both the gas and DM density profiles (from Eq. 3.4) to obtain the filament mass per unit length, μ, and its half-mass radius:

$$\mu(r) = \int_0^r \frac{2\pi r' \rho_0}{(1+(r'/r_0)^2)^2} dr' = \frac{\rho_0\, \pi r^2}{1+(r/r_0)^2} \quad \text{and} \quad r_{1/2} = r_0\,. \tag{3.11}$$

The fact that the (small) core radius contains half of the mass makes the filamentary material relatively impervious to the stellar feedback/filament interaction: provided the core is shielded from it, there can only be a minor change in the amount of gas mass the filament carries. It has been suggested in the literature that Kelvin-Helmholtz instabilities could be triggered at the interface between cold filament gas and the feedback powered, hot, galactic wind (e.g. Mandelker et al., 2016, and subsequent work). These will depend non trivially on redshift and the distance of a filament segment to the central galaxy, so it is quite difficult to define a unique characteristic timescale, $t_{\rm KH}$. Nevertheless, writing $t_{\rm KH}(r) = (r/v_w)\sqrt{\rho(r)/\rho_w}$ where v_w is the relative velocity between the wind and the gas filament and ρ_w the density of the wind, we can see that given the steepness of the filament density profile we measure, $t_{\rm KH}$ becomes larger as the perturbation progresses deeper in the filament. This means that the timescale is ultimately set by $t_{\rm KH}(r_0)$. Plugging in typical numbers for our feedback run at $z = 4$, i.e. $r_0 \sim 5$ kpc, $\rho(r_0) \sim 4 \times 10^{-5} {\rm M}_\odot$ pc^{-3}, $v_w \sim 100$ km/s, and $\rho_w \sim 4 \times 10^{-6} {\rm M}_\odot$ pc^{-3}, we thus get $t_{\rm KH} \sim 20$ Myr which is about an

order of magnitude shorter than the infall time from the virial radius of the embedded halo. The conclusion is thus that our gas filaments should not survive the interaction.

Notwithstanding that this does not happen in our simulations, which might admittedly be of too low a resolution to capture the instability properly, the calculation ignores both the importance of radiative cooling within the filament which might confine the perturbations at the surface (Vietri et al., 1997), and the important fact that, as we have previously discussed, gas filaments are *not* self-gravitating but are located within a dominant DM filament potential well. Because of this, it is unclear as to whether Kelvin-Helmholtz instabilities can impart to the gas a radial velocity (as in perpendicular to the filament axis) larger than the escape velocity necessary to climb out of this potential well. Should they not, they would simply render the gas flow within the filament turbulent without affecting the filamentary nature of gas accretion onto halos.

In the feedback case, we measure that the core radius of the gas filament evolves with redshift as $r_0 \propto (1+z)^{-2.24\pm0.34}$, i.e. with a scaling very similar to the no feedback run (see Fig 3.12). Nevertheless, given the importance of the stellar feedback perturbations, one expects gas accretion onto the filament to be reduced in their presence. To quantify this effect, we plot the ratio of median feedback to no feedback gas density profiles along the filament as a function of redshift in Fig. 3.14. From the figure, one can see that while the size of core radius is not significantly affected by feedback, the central density is, to a larger extent. At $z = 7$ a 40% reduction is measured, though this falls to 20% at $z = 3.6$, at which point the feedback ceases to have an effect on the filament core. We emphasize that contrary to the growth of the core/truncation radii, the impact of feedback does not scale monotonically with redshift, as it depends both on the global properties of the IGM/filament *and* the star formation history of the galaxy which drives the feedback. Indeed, as shown on Fig. 3.14, at early times ($z \sim 8$) the filament core density is even *enhanced* by the action of feedback. It is possible that some of this extra gas will be entrained in the filament, but another possibility is that it will act as a shield from fresh feedback at later times. In future work, we plan to use tracer particles developed in Cadiou et al. (2019) to distinguish between these two situations. Outside the filament, the density is seen to be enhanced in the simulation with feedback, which is somehow expected from mass conservation of the filamentary gas and the presence of the extra material brought by the galactic winds.

It should be noted that the stellar feedback implemented in our simulation is the supernova prescription of Kimm et al. (2015), which ensures that the correct energy/momentum is given to the gas irrespective of whether the Taylor-Sedov phase of the supernova is spatially resolved. As such if the filaments are not destroyed by this supernova feedback then they are unlikely to be destroyed by any 'realistic' supernova feedback. Yet, other types

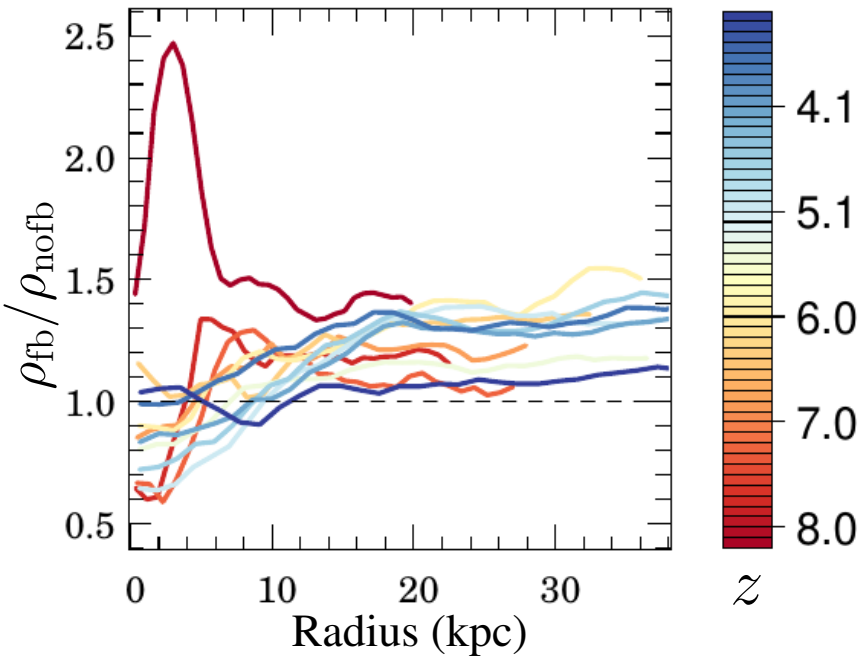

Figure 3.14: Ratio of the median gas density profiles in the feedback and no feedback runs, $\rho_{\rm fb}/\rho_{\rm nofb}$, as a function of distance to the filament center. Curves of different colours represent different redshifts, as indicated on the figure. Very early in the simulation ($z = 8$) feedback enhances the density of gas in the filament. However, at almost all other redshifts, the reverse happens: the filament is depleted of gas in the feedback run as compared to the no-feedback run. The amplitude of the effect is *not* monotonic with redshift.

of stellar feedback are also present which could alter filament properties, whether by direct action of the feedback on the filaments or through suppression of star formation and thereby the supernova feedback (e.g. resonant scattering of Lyman alpha photons in high redshift dwarf galaxies (Kimm et al., 2018)). There is, of course, photo-heating due to ionising radiation which can induce an important gas density depletion especially in filaments connecting low mass halos (e.g. Katz et al., 2019) for detail). We believe that this effect is, by-and-large, captured by the UV background model implementation present in both the stellar feedback and no-feedback runs. However, another mode of stellar feedback which we do not account for, might be more effective at filament disruption as it is less confined to the galaxy: cosmic rays (see e.g. Pfrommer et al., 2017). Finally, for filaments connecting halos of higher mass, Dubois et al. (2013) showed that AGN are also very effective at disrupting filaments, and can even destroy their cores.

3.5 Conclusion and Discussion

Theory suggests (e.g. Kereš et al., 2005; Dekel and Birnboim, 2006; Pichon et al., 2011) that filaments play an extremely important role in the evolution of galaxies at high redshift. However, their basic characteristics are, as yet, not completely understood, and they are extremely hard to detect observationally. We used a suite of high resolution cosmological zoom-in simulations, progressively including more of the relevant physics, to place constraints on the physical properties of such a filament, from large (Mpc) scales to the point where it connects to the virial sphere of the central galaxy. Our main findings are as follows:

- The filament in both DM and gas simulations can be described fairly accurately by a density profile $\rho = \frac{\rho_o}{(1+(r/r_0)^2)^2}$ corresponding to a cylinder in isothermal equilibrium .

- The filament core radius, r_0 for the gas grows as $r_0 \propto (1+z)^{-2.72\pm0.26}$, with the DM filament core radius evolving as $r_0 \propto (1+z)^{-3.18\pm0.28}$. The evolution of r_0 for the gas closely tracks that of the size of the galaxy ($0.2r_{\rm vir}$).

- The filament has a second characteristic radius, the truncation radius, which is detectable (at least in simulations) in the temperature/velocity dispersion or vorticity fields. This radius scales as $r_{\rm tr} \propto (1+z)^{-2.07\pm0.07}$ for DM and $r_{\rm tr} \propto (1+z)^{-3.10\pm0.10}$ for the gas in simulations without feedback. The DM truncation radius is comparable in size to the DM halo virial radius. The gas truncation radius is smaller at early times but catches up to the dark matter by $z = 3$.

- The filament properties are mildly affected by stellar feedback from the central galaxy. The core radius of the gas filament hardly changes, with its central density generally reduced by $\sim$20-30 %, but this does not happen monotonically with redshift. The DM filament properties hardly undergo any change.

Our simulations also establish that filaments need to be resolved with a minimum of ~ 2 kpc for a Milky Way sized halo in order to capture the filament properties. This might have important consequences for the angular momentum content of the gas transported to the galaxy. Still higher resolution will be required to capture the filaments around dwarf galaxies, though these are far more vulnerable to photoionisation and so probably do not need be resolved in detail beyond $z = 6$. While the mass brought by the inflowing filament gas is affected to a level of $\sim$20-30 percent as a result of stellar feedback from the central galaxy, a further reduction is likely to occur as the filament enters the virial radius. We plan to tackle this issue using tracer particles in the near future. The interaction of the filament with galactic winds and the virialised halo hot atmosphere will also be a function of the halo mass, and therefore our results need to be extended to a larger sample.

Indeed, our analysis was performed on the filament feeding one galaxy at high resolution. The next chapter will apply the techniques developed in this chapter to the NEW HORIZON (Dubois et al., 2020), a cosmological zoom of the Horizon-AGN (Dubois et al., 2014a) which will have tens of galaxies of a similar stellar mass to the one we studied in this chapter, along with several more massive objects. NEW HORIZON also features AGN feedback and has reached $z = 0.25$, (though it was only at $z = 0.7$ when this research was being done) which also allows to comprehensively extend the redshift range of the analysis. Such a simulation will thus permit the extraction of a large sample of filaments from which to derive statistically meaningful quantities.

Chapter 4

A Statistical Study of the Filamentary Network of NEW HORIZON

This chapter extends the analysis of Chapter 3 to the NEW HORIZON simulation, thereby allowing a statistical analysis of a population of filaments connecting galaxies of a variety of morphological types and masses. In Section 4.1 I explain the detailed set up of the NEW HORIZON simulation. In Section 4.1.2 I explain how the filaments extracted by DISPERSE are processed in order to only use the main filaments that connect halos together. Section 4.2 summarises the properties of the halos connected to the filament network, and compares them to those that are not connected. I then look at the filament profiles in Section 4.3 and the evolution of the filament index in Section 4.4. Finally I compare the properties of the NEW HORIZON filaments with those of the NUT in Section 4.5

4.1 Methodology

4.1.1 The NEW HORIZON Simulation

NEW HORIZON (Dubois et al., 2020) is a cosmological zoom of a region extracted from the HORIZON-AGN (Dubois et al., 2014a) cosmological simulation of a periodic volume 100 cMpc/h on a side. The zoom region is a sphere of diameter 20 cMpc centred on a region of average density. By $z = 0.7$ NEW HORIZON has several hundred galaxies with stellar masses above $10^9 \mathrm{M}_\odot$, resolved to a maximum physical spatial resolution of 40pc with a DM mass resolution of $10^6 \mathrm{M}_\odot$ and stars resolved with a minimum mass of $10^4 \mathrm{M}_\odot$. NEW HORIZON's cosmological parameters are drawn from WMAP-7 (Komatsu et al., 2011) with values of $H_0 = 70.4 \mathrm{kms}^{-1}\mathrm{Mpc}^{-1}$ for the Hubble constant, $\Omega_m = 0.272$ for the mass density, $\Omega_b = 0.0455$ for the baryon fraction and $\Omega_\Lambda = 0.728$ for the dark energy density. The power spectrum amplitude is $\sigma_8 = 0.809$ and spectral index is $n_s =$

0.967. Radiative cooling is handled with Sutherland and Dopita (1993) and Rosen and Bregman (1995), allowing temperatures to reach 1K through metal line cooling. A uniform UV background is turned on at $z = 10$ to model reionisation (Haardt and Madau, 1996). Star formation is allowed in cells with a temperature below 2×10^4 K and a gas density greater than $0.24 \mathrm{M}_\odot \mathrm{pc}^{-3}$, following the Kennicut-Schmidt law (Schmidt, 1959; Kennicutt, 1998). The star formation efficiency parameter is, however, allowed to vary according to the thermo-turbulent condition (Kimm et al., 2011b), Devriendt et al. *in prep.*. Supernovae return 31% of the mass of a stellar particle to its surroundings once a star particle reaches 5 Myr, using the SN feedback scheme of (Kimm et al., 2015). A Chabrier initial mass function with a lower and upper mass cutoff of $0.1 \mathrm{M}_\odot$ and $150 \mathrm{M}_\odot$ is adopted. Black holes are modelled as sink particles accreting according to Bondi-Hoyle-Lyttleton with seed mass of $10^4 \mathrm{M}_\odot$. Maximum accretion rates are limited by the Eddington limit. See Chapter 2 for more details on the cooling, star formation, supernovae and AGN feedback implementation. By 2019, the simulation reached $z = 0.7$, and this is thus the lowest redshift considered in this thesis. Since the cold mode accretion filaments disappear below $z = 1$ one of my main objectives here is to quantify the long term effects that cold mode accretion has on the resulting galaxy long after the accretion has stopped.

4.1.2 Defining the Cosmic Web

Figs. 4.1 and 4.2 show the environment surrounding the 20 most massive galaxies identified to be part of the cosmic web at two different redshifts. In the $z = 6$ (Fig. 4.1) case filaments are seen to be ubiquitous, with each galaxy being fed by multiple streams. The number of streams shown is likely an underestimate in most cases as each plot is only a thin 12.5 ckpc slice through the volume. Also surrounding the galaxies are superbubbles from the combined supernova feedback of the stars that have already exploded in these galaxies, and/or AGN as clearly seen in the temperature maps.

By $z = 0.7$ (Fig. 4.2) the state of the IGM has changed. While it was previously composed of cold gas ($\approx 10^4$ K), the superbubbles have expanded to fill most of the frame. The filaments feeding these galaxies have for the most part been puffed up well beyond the size of the galaxy and cold mode accretion has ceased. The second column of rows 3 and 4 show the gas density and temperature of a galaxy which has managed to keep hold of its filaments, but the vast majority have not.

Filament extraction in NEW HORIZON differs from the pilot study of Chapter 3 in that the filament ends in NEW HORIZON are defined by the positions of halos, which could not be done for the NUT simulations due to the lack of halos with masses comparable to the central object. A new issue arises: the physical extent of the filaments. Naïvely, all galaxies

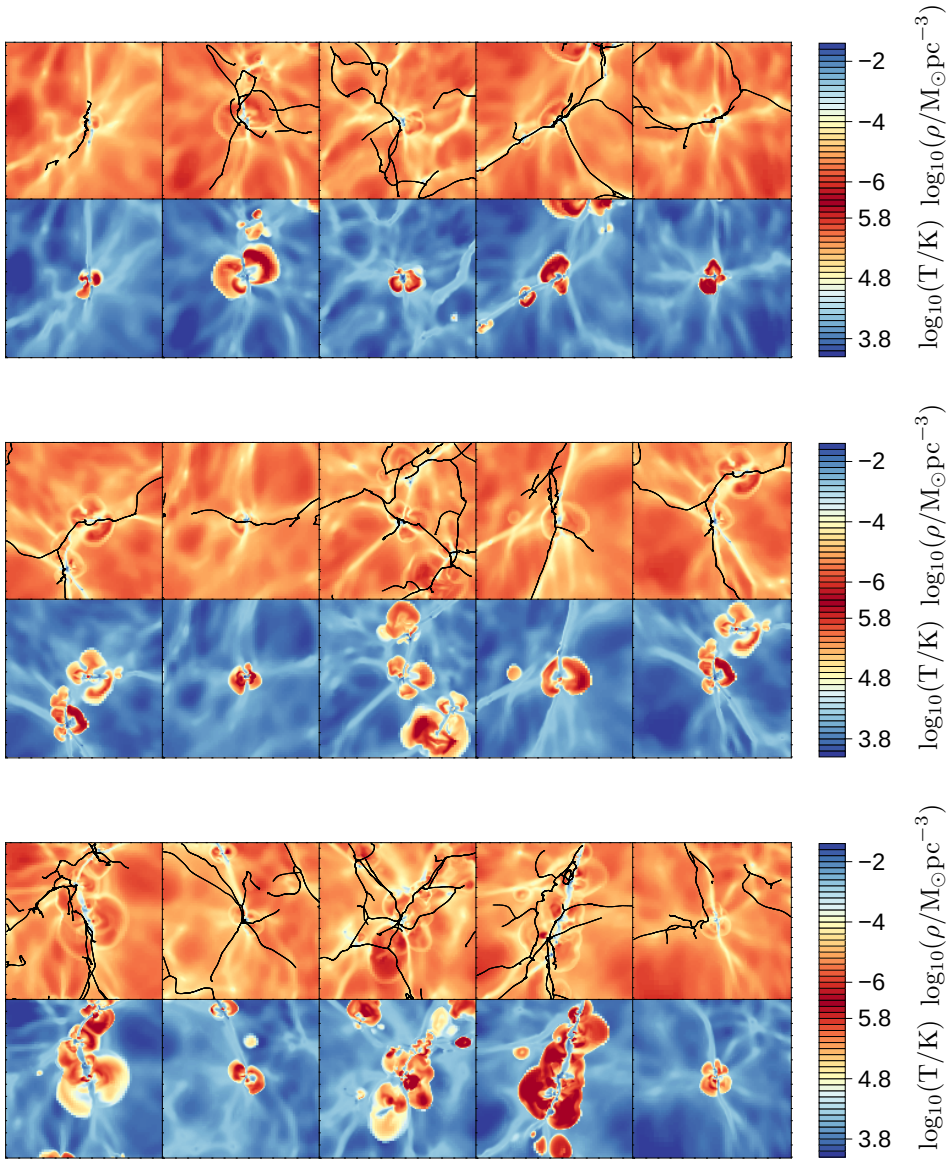

Figure 4.1: 15 most massive galaxies within the cosmic web and their environments at $z = 6$, showing the cold mode of accretion. Each panel shows a thin slice through the density field (*top* rows) and temperature (*bottom* rows), 12.5 ckpc thick, with each panel having a side length of 30 cMpc, centred on 20 different galaxies. Overplotted in *black* on the density field is the skeleton, as defined by DISPERSE . In each panel the galaxies can be seen to be fed by multiple streams, and surrounded by a small bubble of hot gas, generated by supernovae.

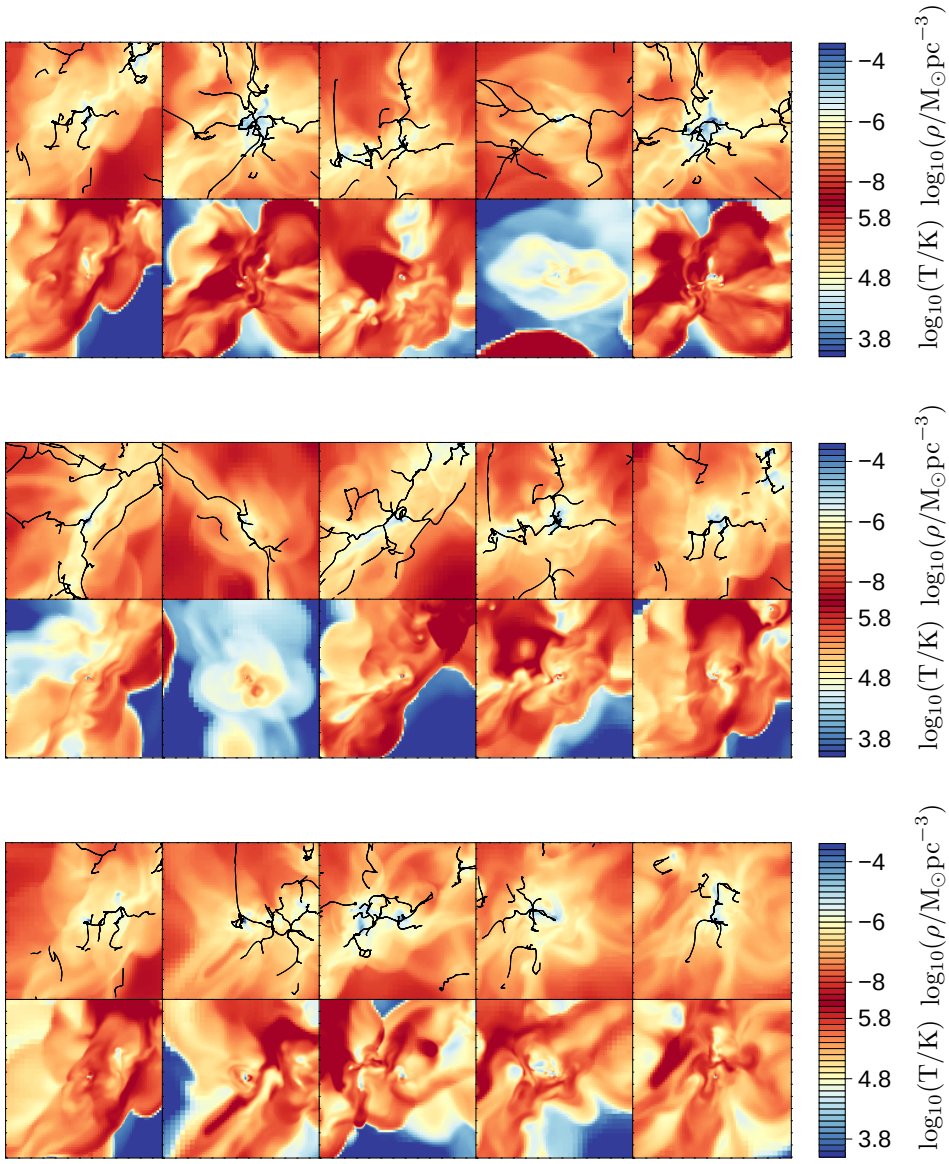

Figure 4.2: 15 most massive galaxies within the cosmic web and their environments at $z = 0.7$. Each panel shows a thin slice through the density field (*top* rows) and temperature (*bottom* rows), 12.5 ckpc thick, with each panel having a side length of 30 cMpc, centred on the galaxies. Overplotted in *black* on the density field is the skeleton, as defined by DISPERSE . By this point in the simulation the supernova bubbles have grown to encompass most of the local environment. The nature of the filaments has also changed, becoming considerably wider, and rarely feeding the galaxies as narrow, coherent streams of gas.

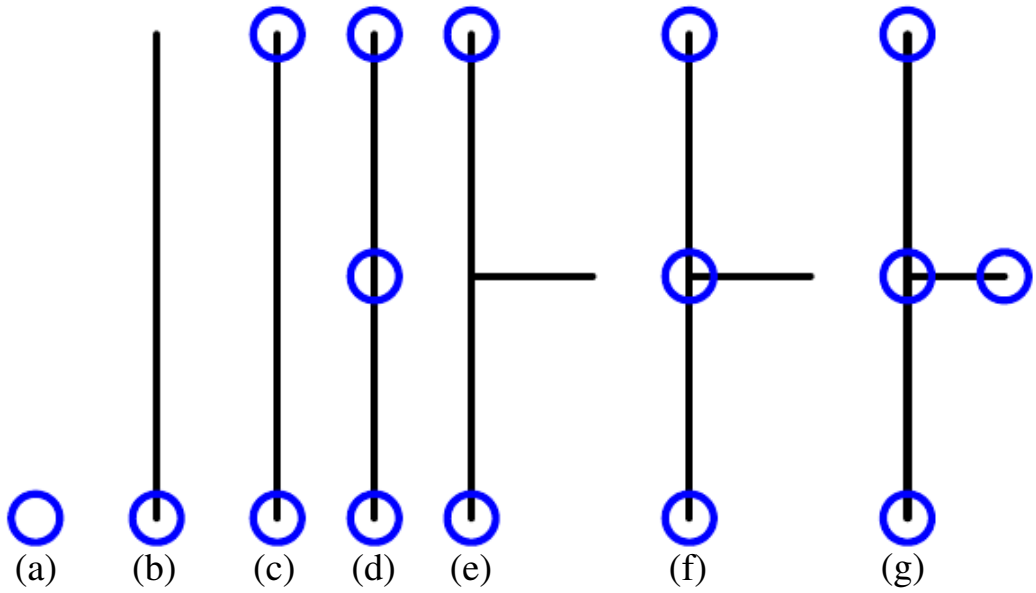

Figure 4.3: A cartoon representation of various configurations of halos (blue circles) and filaments (black lines).

in the cosmic web are connected to each other but it is quite arbitrary to decide where one filament should end and the next should begin.

Therefore for the purposes of this thesis, filaments are identified in a two step process: first connected pairs of halos are identified using a coarse skeleton. This is generated using DISPERSE on the DM halo distribution. Various configurations of filament and halos are shown in Fig. 4.3.

- (a) Isolated halo, zero connection to either filaments or halos.
- (b) Halo connected to isolated filament, zero connection to other halos.
- (c) Pair of halos connected by single filament. Each halo has a connectivity of 1.
- (d) A halo splits the filament in two. End halos have a connectivity of 1, but middle halo has a connectivity of 2
- (e) Connecting filament has a branch, invalidating the connection between the halos. Each gets a connectivity of zero.
- (f) Adding another halo on the branch point of (e) makes the filaments significant again. End halos get a connectivity of 1 and the central halo's connectivity is still 2 since the branch does not connect an additional halo pair.

- (g) Central halo has a connectivity of 3 now that all filaments end in a halo. The rest of the halos get a connectivity of 1.

Note that in case (e) there likely is a halo at the node (a node being a point where 3 or more filaments join). However, due to the shape of the halo mass function, the simulation is dominated by low mass objects, and since the number of potential filaments scales as N^2 a minimum halo mass is used in defining these filaments as the numbers quickly become unmanageable. The mass threshold below which halos are not considered is defined as:

$$M_{\rm thresh} = \begin{cases} 10^{10}{\rm M}_\odot\,, & z \geq 4 \\ \frac{5}{1+z}10^{10}{\rm M}_\odot\,, & z < 4 \end{cases}. \tag{4.1}$$

The choice of threshold keeps the number of halos above the threshold roughly constant below $z = 4$, see the black dashed line in Fig. 4.11, top left panel.

In order to limit the effect of spurious long range connections between halos the condition that no nodes can be present between a pair of connected halos is included. A limitation of this method is that filaments that do not connect two halos are not included, which can occasionally be seen in the original filament sample, for example at (0,-5) in the top left panel of Fig. 4.4, encircled in green. The halo within this circle has two filaments, but only one of these is terminated by a sufficiently massive halo,and as a result the longer of the filaments is discarded.

As shown in Fig. 4.5 at high redshift the virial radius of halos is too small and the halo skeleton too coarse for many connections to be made. Indeed, unlike in the DM particle skeleton case, DisPerSE draws filaments between peaks in the halo density field rather than the underlying DM density field, resulting in the skeleton often not passing through the halos. In order to correct for this the volume that the halo must reside in to be considered as belonging to a filament is a cylinder of length $l + \max(nr_{\rm vir}, l/2)$, with radius $\max(nr_{\rm vir}, l/2)$ where l is the length of the segment under consideration, and n is the distance of the halo from the filament in units of the virial radius. This is illustrated in 2D by the cartoon in Fig. 4.5. In this case for a halo to be identified as belonging to the segment marked by the filled circles the halo centre must be enclosed within its corresponding rectangle. The red halo uses the red rectangle without any modification, however the blue halo is smaller than the resolution of the segments, and as such uses the black rectangle instead of the blue rectangle. Halos are defined to be connected to the skeleton if they are within 2 $r_{\rm vir}$ of the filament. The effect of varying this distance is shown in Fig. 4.5.

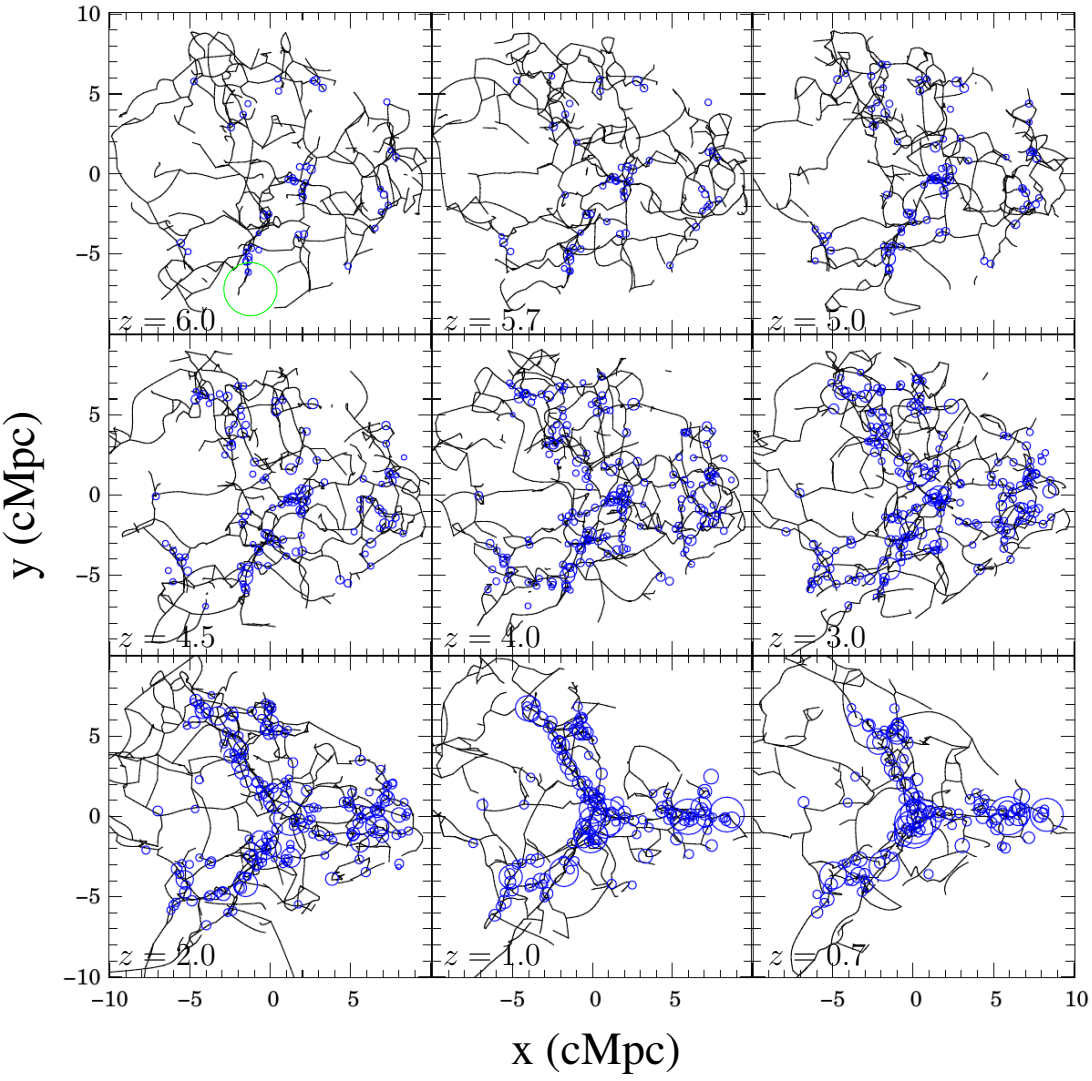

Figure 4.4: A 3 cMpc thick slice through the halo skeleton. The size of each circle is proportional to the proper virial radius. From $z = 6$ to $z = 0.7$ three major cosmic web filaments are assembled through the mergers of smaller scale filaments. The green circle in the $z = 6$ panel indicates a filament which does not terminate with a mass greater than the threshold mass, which are not considered in this chapter, as in case (b) in Fig 4.3. The filaments shown in this figure only determine whether or not a pair of neighbouring and sufficiently massive (above $M_{\rm thresh}$) halos should be connected. The actual path taken is determined using the DM particle skeleton.

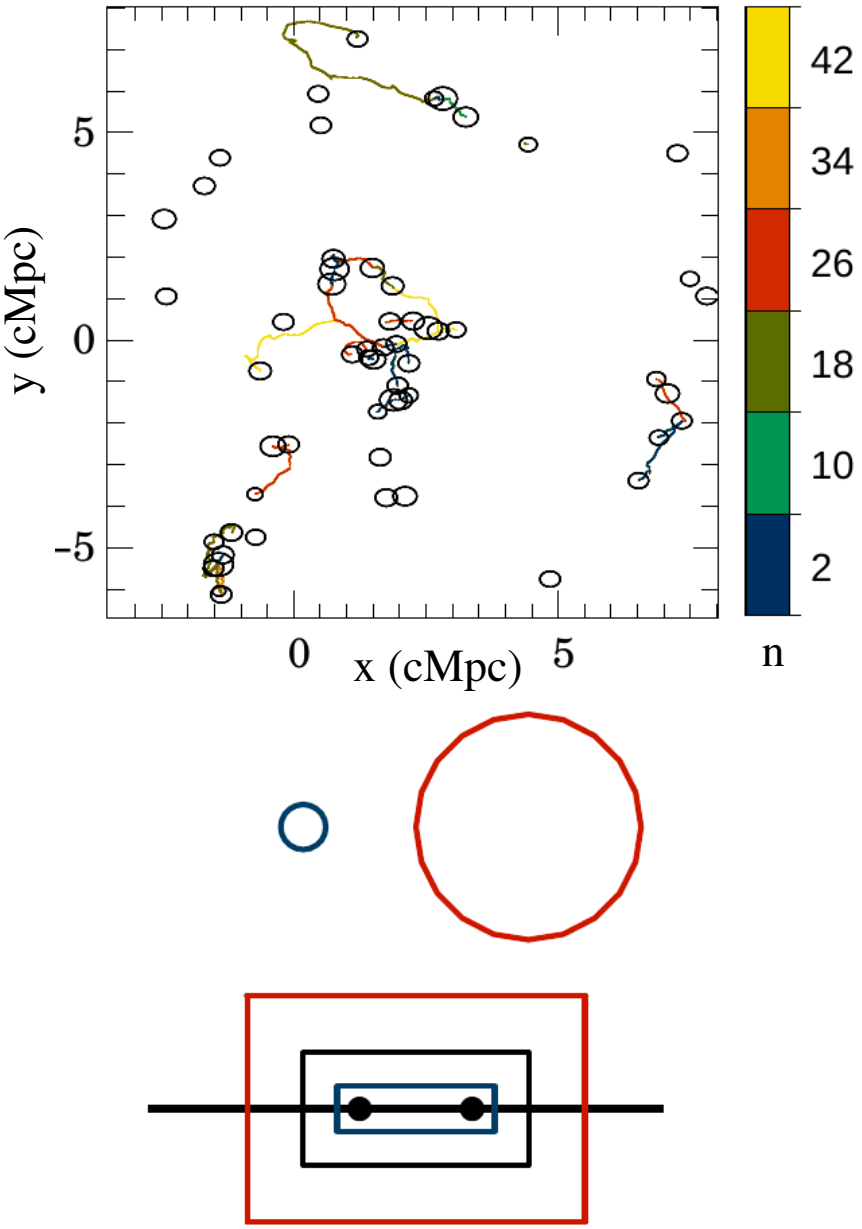

Figure 4.5: *Top* panel the connectivity of the $z = 6$ halos as a function of n is shown, where n is the distance to the skeleton in terms of virial radii. For values higher than 10 spurious connections can be seen, for example the rather indirect route at (1,6.5) to (2.5,6). The actual skeleton used in the analysis is marked in *dark blue*, as two groups of galaxies at (7,-3) and (1.5,-1). *Bottom* shows a 2D cartoon representation of how I determine whether or not a halo belongs to an individual segment (black horizontal line with segment endpoints delineated by black filled circles). This depends on the distance of a halo in units of its virial radius from the filament segment. See text in Section 4.1.2 for a detailed discussion of this.

As the number of virial radii allowed for connection is increased, non-local connections become allowed. I find that provided this parameter is less than $10r_{\rm vir}$ these spurious connections are prevented.

The second part of identification of the filament network uses the method of Chapter 3. This time around the skeleton is generated by running DISPERSE directly on the DM particles rather than on the DM halos. The end points of each filament are the positions of the confirmed halo pairs as indicated in the previous paragraph, and the chosen segments lie on the shortest path between connected halo pairs. A thin slice through the full DM skeleton is shown in Fig. 4.7 and processing of the DM skeleton as just described is illustrated in Fig. 4.8. Here the cyan skeleton represents the filaments between all pairs of halos with mass greater than $10^{10}{\rm M}_{\odot}$, rather than the full skeleton. As one can see, applying the methodology set out above to remove the long range connections, yields the blue DM skeleton, that connects halos which are within two virial radii of the halo skeleton. Note that the circles in the figure are 30 virial radii (and some circles are comparable to the line thickness) and as such it does look as though more filaments should be connected. These halos may be further from the skeleton than they appear or are missing a halo partner to connect to.

Finally, note that the filaments identified by DISPERSE are closely associated with regions of higher density, as shown by the fact that the filament regions are more highly refined than the rest of the volume (see Fig. 4.6).

The evolution of the filament network is shown in Fig. 4.9, from the 12 pairs of connected halos between the 19 halos found at $z = 6$, to over a hundred pairs by $z = 0.7$. The network evolves from small isolated groups to long continuous chains of pairs that define the large scale cosmic web.

Attempting to use the halo skeleton to define endpoints for the skeleton network with the same mass threshold as this chapter on the NUT suite presented in Chapter 3 only preserves the lower filament on Fig. 3.3. This is due to selection effects. Powell et al. (2011) chose the initial conditions for a MW-like galaxy to exist in relatively isolated conditions. As such there is one halo above the threshold mass at the end of the lower filament, but no comparable halo connected to the upper filament. Ideally a lower halo mass threshold should be used but this is constrained by the resolution of the simulation, with the NUT suite having better DM mass resolution than NEW HORIZON by a factor of 10.

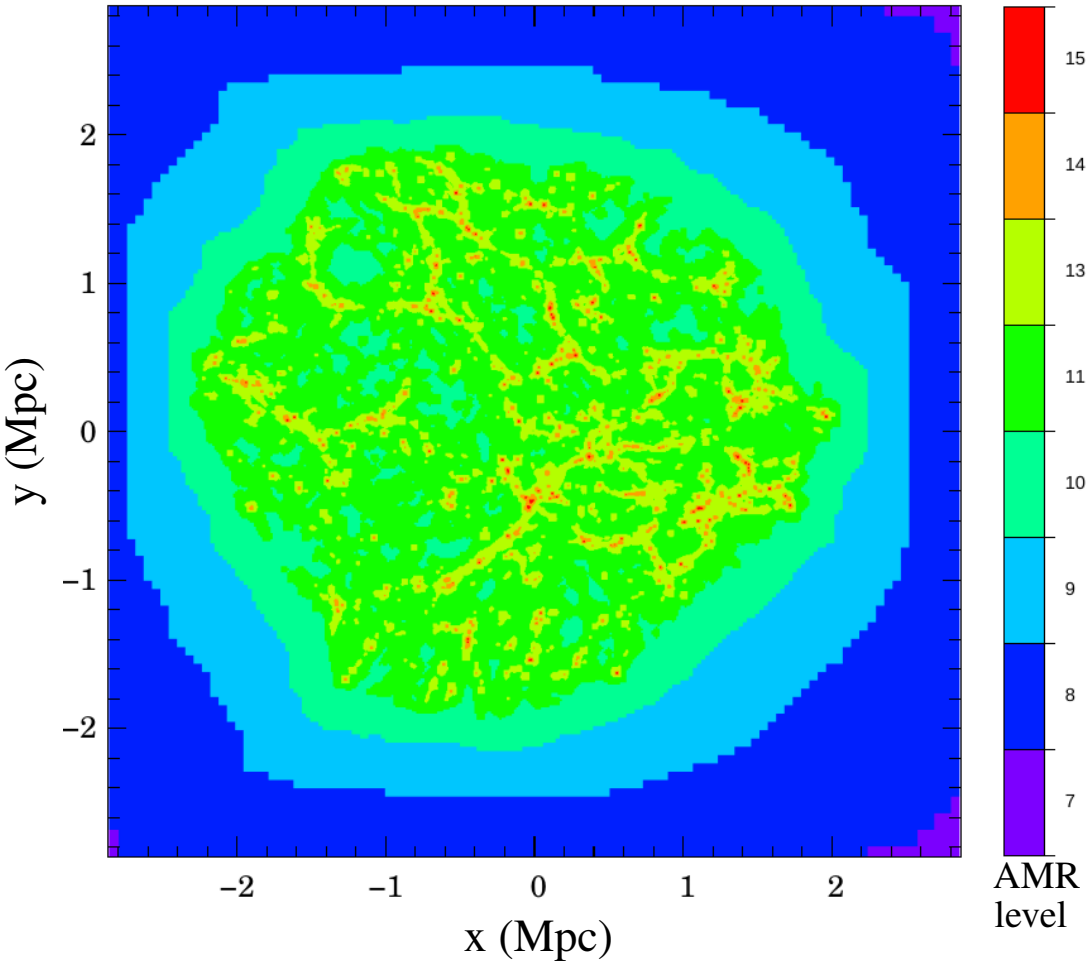

Figure 4.6: AMR levels of the NEW HORIZON simulation for a 3 kpc slice at $z = 4$ showing only the NEW HORIZON zoom region. The edge of the zoom region can be seen in *blue* and *purple* as well as the embedding of the halos in *red* within the *yellow* of the cosmic web filaments and walls. Filaments are mostly resolved with 13 levels of refinement, corresponding to a resolution of 12.5 ckpc.

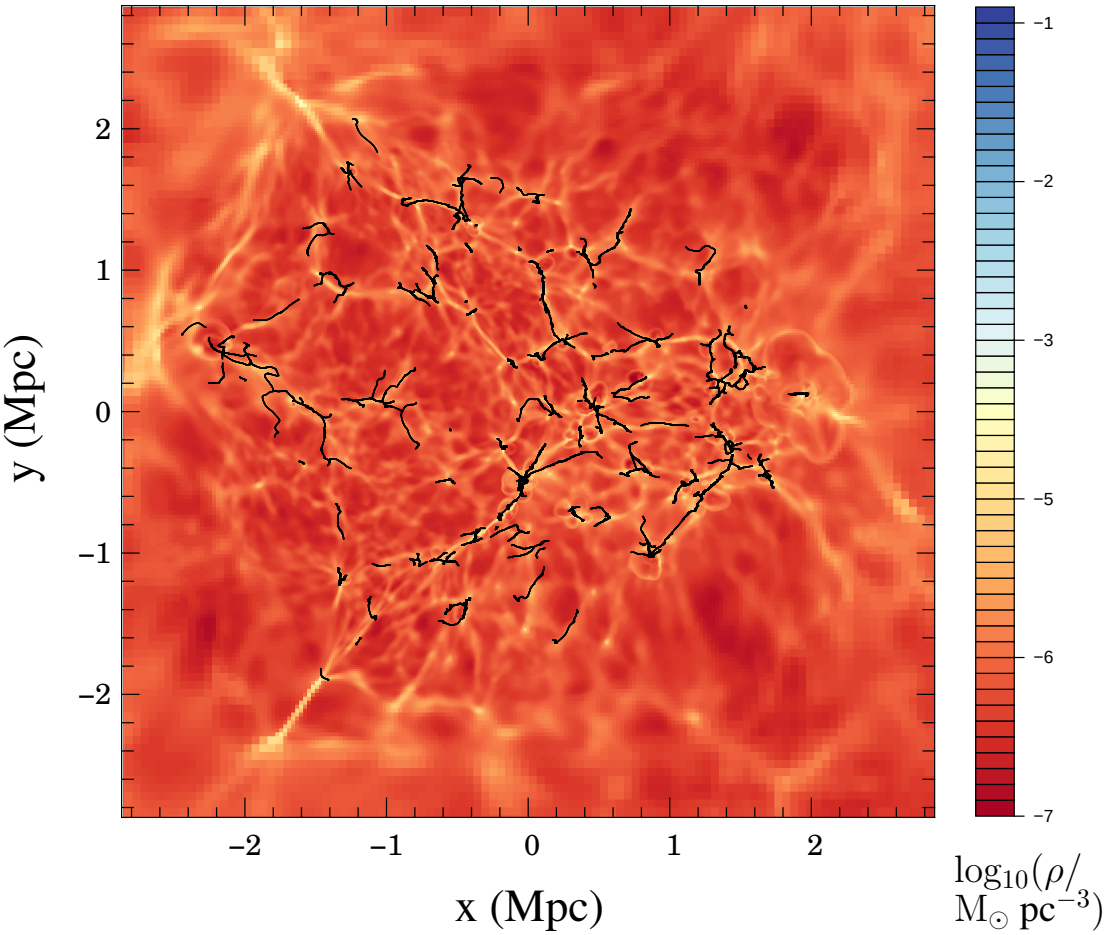

Figure 4.7: The gas density field for a 3 kpc slice at $z = 4$ showing only the NEW HORIZON zoom region. The edge of the zoom region can be seen as the blurring of the image towards the edges. Overplotted is the skeleton in *black*. Note that not all the filament-like structures are indeed filaments, but instead edges of walls.

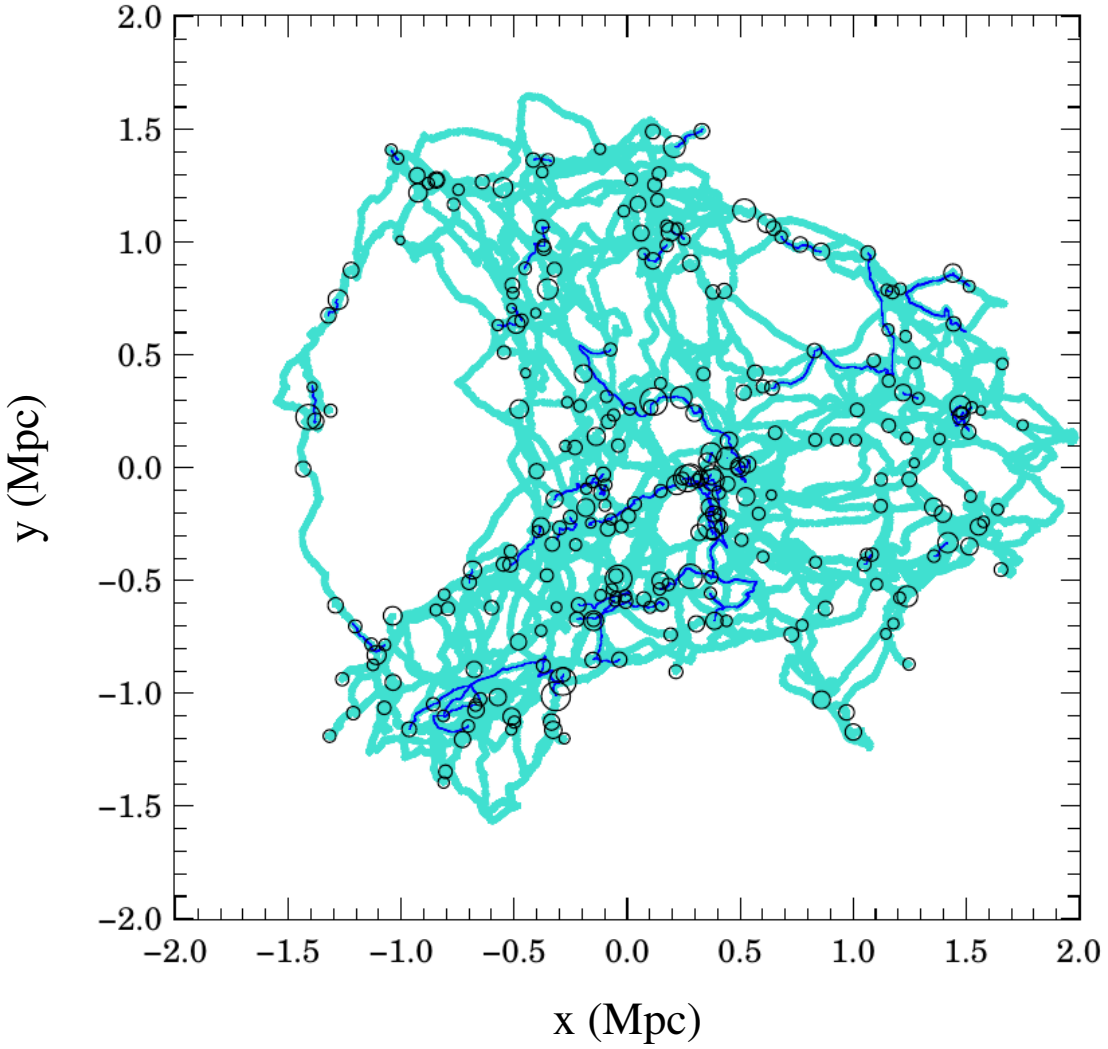

Figure 4.8: The main filaments throughout the zoom region identified as the shortest path between halos with masses exceeding $10^{10}\mathrm{M}_{\odot}$ represented as circles along the cosmic web (*cyan*) at $z = 4$. Filaments which directly connect halos are marked in *blue*. These are the filaments studied in this chapter.

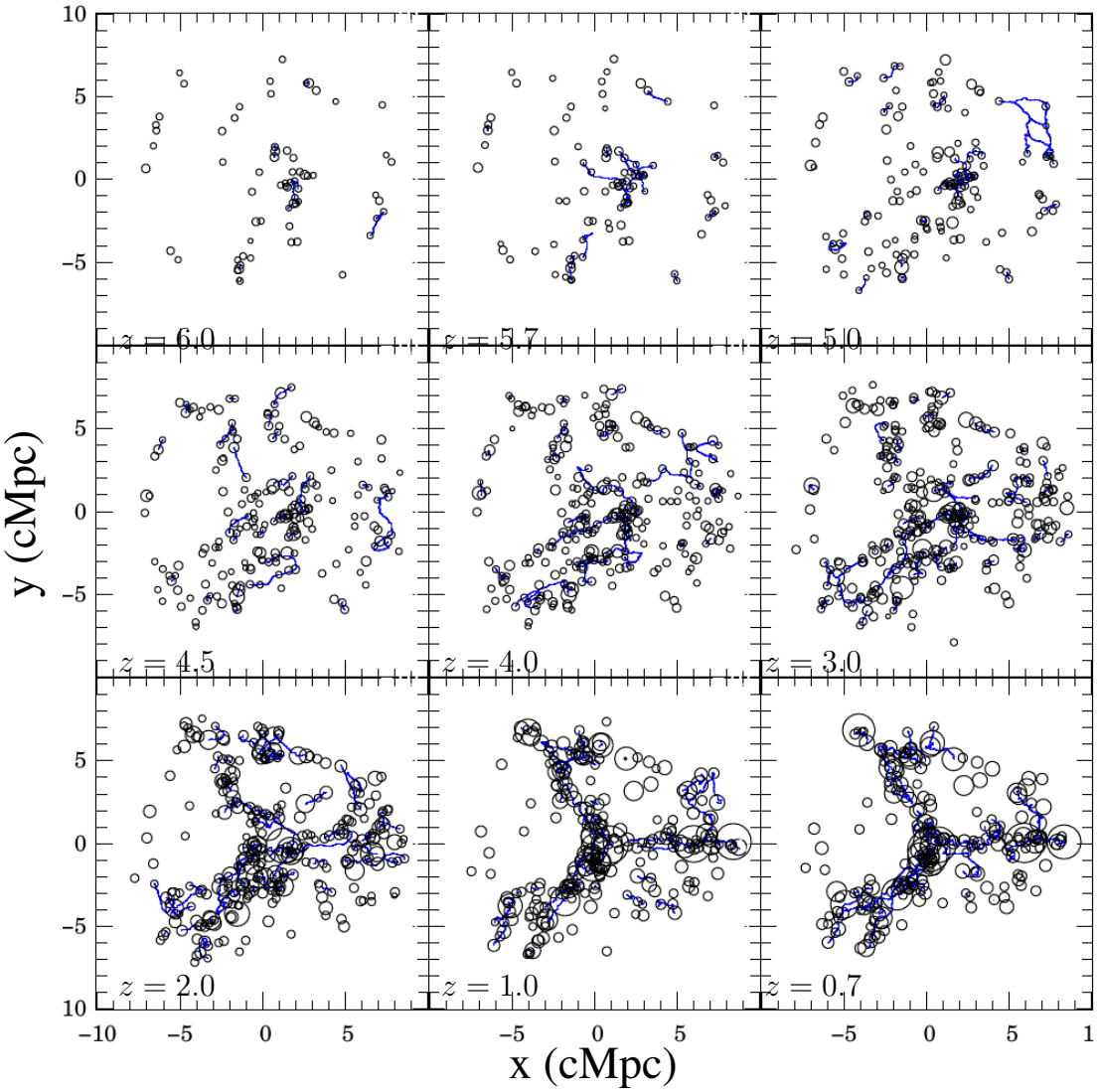

Figure 4.9: The evolution of the cosmic web for the full volume of the zoom region. The cosmic web evolves from an extremely sparse network at high redshift to one which is multiply connected. Redshift is indicated in the lower left corner of each panel. The halos are represented with circles of radius 30 $r_{\rm vir}$. The blue line here is the fully processed skeleton.

4.2 Impact of Filaments on Galaxy Properties

In order to explore the impact of filaments on galaxies I bin these according to their properties (e.g. halo mass, stellar mass) and look at the filaments connecting them. Due to the relatively small sample of galaxies (on the order of 1300 by $z = 0.7$) and the fact that not all galaxies are found to be part of the halo network, only 2 or 3 bins in any of the properties were used to avoid small number statistics. Note that galaxies were binned in two ways. In the first case I consider each redshift independently to the others and separate galaxies at each redshift as follows:

- DM Halo Mass: $M_{\rm thresh} < M_{\rm DM} < 10^{10.6}{\rm M}_\odot$, $10^{10.6}{\rm M}_\odot < M_{\rm DM} < 10^{11.4}{\rm M}_\odot$, $M_{\rm DM} > 10^{11.4}{\rm M}_\odot$
- Stellar Mass: $M_* < 10^8{\rm M}_\odot$, $10^8{\rm M}_\odot < M_* < 10^9{\rm M}_\odot$, $M_* > 10^9{\rm M}_\odot$
- Galaxy formation Efficiency: $e_* < 10^{-3}$, $10^{-3} < e_* < 10^{-2}$, $e_* > 10^{-2}$
- Specific star formation rate: ${\rm sSFR} < 10^{-12}{\rm yr}^{-1}$, $10^{-12}{\rm yr}^{-1} < {\rm sSFR} < 10^{-9}{\rm yr}^{-1}$, ${\rm sSFR} > 10^{-9}{\rm yr}^{-1}$

where galaxy formation efficiency is defined as $M_*/M_{\rm DM}$ and specific star formation rate is defined as ${\rm SFR}/M_{\rm DM}$, the ratio of the star formation rate to the DM halo mass, averaged over the last 100 Myr. The number of galaxies falling into the three bins for each property is detailed in Tables 4.1 and 4.2, while for the other galaxy properties the highest and lowest value bins are open ended, limited by the maximum and minimum values found in the simulation. For all galaxies the DM halo mass must be above the threshold mass, $M_{\rm thresh}$, given by eq. 4.1.

In the second case I bin the galaxies according to their final properties, here defined as their properties at $z = 0.7$, and track their progenitors to a higher redshift, in a similar way to what was done in the pilot study presented in Chapter 3. For each galaxy I then simply define a high and low value bin, separated by $10^{11}{\rm M}_\odot$, $10^{8.5}{\rm M}_\odot$, $10^{-2.5}$ and $10^{-11.5}{\rm yr}^{-1}$ for DM halo mass, stellar mass, galaxy formation efficiency and specific star formation rate respectively. These boundaries are meant to populate the upper and lower bins with a reasonable number of objects. Exact numbers are given in Table 4.3.

	$M_{DM}(M_\odot)$			$M_*(M_\odot)$		
z	$< 10^{10.6}$	$10^{10.6} - 10^{11.4}$	$> 10^{11.4}$	$< 10^8$	$10^8 - 10^9$	$> 10^9$
0.70	25	58	22	28	36	39
0.79	27	74	21	31	36	54
0.89	28	70	22	24	42	53
1.00	29	77	20	31	36	54
1.25	30	60	25	29	41	43
1.61	55	63	16	39	59	36
2.00	71	66	13	45	70	34
2.13	79	62	10	51	71	28
2.29	90	72	6	55	80	30
2.49	93	56	5	58	73	21
2.65	102	61	2	57	91	15
2.81	88	45	4	50	73	14
3.01	102	46	1	62	73	13
3.18	110	38	3	62	83	5
3.33	104	37	1	62	70	9
3.50	112	33	1	65	74	6
3.65	155	37	1	95	93	4
3.79	107	32	0	66	64	7
3.97	84	18	0	49	47	3
4.13	93	16	0	62	44	2
4.34	65	8	0	43	26	3
4.50	59	11	0	35	33	2
4.66	42	7	0	20	27	2
4.85	50	10	0	31	27	0
4.99	54	4	0	40	18	0
5.31	44	4	0	30	16	0
5.67	35	2	0	28	7	0
6.02	17	2	0	12	7	0

Table 4.1: Numbers of galaxies in each of the bins at each redshift, according to the DM halo or stellar mass of the galaxy at that specific redshift. The bin boundaries are indicated in the column headings. Note that there is an additional constraint on the halo mass given by $M_{\rm thresh}(z)$, as defined in the text.

	e_*			$\mathrm{sSFR}_{100}(\mathrm{yr}^{-1})$		
z	$< 10^{-3}$	$10^{-3} - 10^{-2}$	$> 10^{-2}$	$< 10^{-12}$	$10^{-12} - 10^{-9}$	$> 10^{-9}$
0.70	28	19	58	22	72	11
0.79	30	19	73	29	86	7
0.89	21	26	73	20	93	7
1.00	33	20	73	30	90	6
1.25	28	25	62	29	82	4
1.61	33	38	63	23	68	43
2.00	32	47	71	24	65	61
2.13	32	65	54	24	70	57
2.29	34	69	65	29	66	73
2.49	35	75	44	23	54	77
2.65	34	86	45	24	56	85
2.81	28	71	38	19	40	78
3.01	28	83	38	15	41	93
3.18	25	97	29	17	34	100
3.33	21	87	34	12	30	100
3.50	19	91	36	9	33	104
3.65	23	130	40	6	38	149
3.79	13	87	39	7	10	122
3.97	13	67	22	4	3	95
4.13	16	76	17	8	7	94
4.34	9	53	11	4	3	66
4.50	5	57	8	0	5	65
4.66	3	38	8	0	2	47
4.85	5	51	4	4	1	55
4.99	9	46	3	0	1	57
5.31	7	37	4	2	1	45
5.67	5	31	1	2	1	34
6.02	2	17	0	0	0	19

Table 4.2: Numbers of galaxies in each of the bins at each redshift, according to the galaxy formation efficiency or specific star formation rate of the galaxy at that specific redshift. The bin boundaries are indicated in the column headings. Note that there is an implicit additional constraint on the halo mass since I only consider galaxies located in halos with masses above $M_{\mathrm{thresh}}(z)$, as defined in the text.

	$M_{DM}(M_\odot)$		$M_*(M_\odot)$		e_*		$sSFR_{100}(yr^{-1})$	
z	$10^{11} <$	$> 10^{11}$	$10^{8.5} <$	$> 10^{8.5}$	$10^{-2.5} <$	$> 10^{-2.5}$	$10^{-11.5} <$	$> 10^{-11.5}$
0.70	55	20	47	28	28	47	36	39
0.79	63	22	55	30	34	51	45	40
0.89	60	22	54	28	34	48	43	39
1.00	56	21	49	28	30	47	38	39
1.25	52	19	43	28	26	45	33	38
1.61	52	19	43	28	26	45	33	38
2.00	48	18	39	27	23	43	30	36
2.13	41	17	33	25	20	38	26	32
2.29	52	19	43	28	26	45	33	38
2.49	44	17	36	25	22	39	28	33
2.65	39	15	32	22	19	35	25	29
2.81	36	14	30	20	17	33	22	28
3.01	34	14	29	19	17	31	21	27
3.18	37	14	31	20	18	33	23	28
3.33	32	12	27	17	15	29	19	25
3.50	33	12	28	17	16	29	20	25
3.65	40	15	32	23	19	36	25	30
3.79	28	11	25	14	14	25	18	21
3.97	15	9	14	10	9	15	10	14
4.13	17	10	15	12	9	18	11	16
4.34	14	7	13	8	8	13	9	12
4.50	12	6	10	8	6	12	7	11
4.66	6	5	5	6	4	7	3	8
4.85	10	6	8	8	5	11	5	11
4.99	10	6	8	8	5	11	5	11
5.31	4	5	4	5	4	5	2	7
5.67	3	2	2	3	2	3	1	4
6.02	3	2	2	3	2	3	1	4

Table 4.3: Numbers of galaxies at each redshift, which are progenitors of the galaxies at the final redshift considered, $z = 0.7$. The bin boundaries are indicated in the column headings. As for the previous tables, there is an implicit constraint on the halo mass since only galaxies located in halos with masses above $M_{\rm thresh}(z)$ are included in the analysis.

4.2.1 Global Properties of the Main Filaments Connecting Halos

In Fig. 4.11 I show the effect of DM halo mass on the filament characteristics as a function of redshift. This applies only to the halos which pertain to the filamentary network. The upper left panel of Fig. 4.11 shows that below $z = 4$ the number of low mass galaxies plateau before declining. This is artificial and is the result of the moving mass threshold applied after this redshift (see eq. 4.1). In the *top right* panel the connectivity of the halos is shown. This is the mean number of filaments that a given halo is connected to (see Fig. 4.3 and accompanying text). The connectivity is fairly independent of redshift but more massive halos tend to have higher connectivity than their lower mass counterparts. Codis et al. (2018a) studied the connectivity of significantly larger halos ($M_{\rm DM} > 10^{12}{\rm M}_{\odot}$), finding a relation $\kappa(M) \approx 10/3 \log_{10}(M/10^{11} M_{\odot})$, where κ is the connectivity, which is valid over two decades of halo mass, however, this relation breaks down for masses below $10^{12.5}{\rm M}_{\odot}$, with halos showing greater connectivity than expected by the relation. The filaments in Codis et al. (2018b) are found to have connectivities of 4 for halos of mass $10^{12} M_{\odot}$, compatible with the dispersion in connectivity of large halo masses in NEW HORIZON , in spite of the different methods used to select filaments, with Codis et al. (2018b) using the number of saddle points surrounding a peak in the density field to compute connectivity.

Similar to the connectivity, the mean length of a filament (bottom left panel of Fig. 4.11), here defined as the (comoving) distance between the connected halo pairs does not appear to show any significant trend with redshift, and furthermore, unlike connectivity, the mean comoving length of a filament also seems to be independent of mass. Note that there exists a large scatter in possible filament lengths. In Cautun et al. (2014) the distribution of filament lengths are found to scale differently with redshift, growing slower than the expansion of the Universe. However, this is likely down to the definition of filaments used.

Besides halo number, the other case where there is a visible evolution with redshift is the DM halo mass ratio (bottom right in 4.11). This is defined as the ratio between the mass of the larger to the smaller member of connected halo pairs. Interestingly, the highest mass bin shows a rise in value with decreasing redshift, while the lowest shows a decline, and the intermediate bin is unchanging. Whilst it is possible that this evolution is partly driven by the removal of low mass halos at $z < 4$ as the mass threshold grows, the decline in the DM halo mass ratio for the full sample already occurs at higher redshift. Since low mass galaxies dominate the galaxy population, it is naturally expected they also dominate the population of connected galaxies (black dashed line).

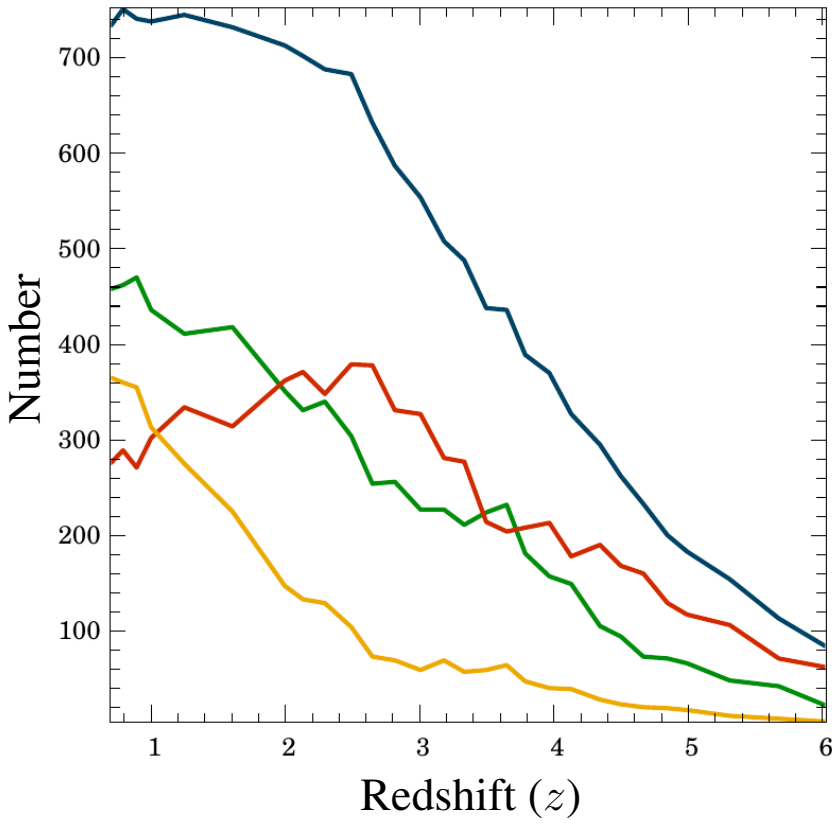

Figure 4.10: The redshift evolution of the number of galaxies in four groups: all (*blue*), connected (*green*), not connected to a filament(*red*) and connected to a filament but with the additional constraint that the highest mass progenitor can be tracked from $z = 0.7$ to high redshift (*yellow*). As the number of galaxies continues to increase, the ratio of those within the filament network to those outside grows, finally staying greater than 1 after $z = 2$.

4.2.2 Comparing Galaxies in Filaments to Those Outside Filaments

In order to investigate the effect of the presence of filaments on the galaxy population I split galaxies into groups using the cases set out in Fig 4.3: all; connected to a filament, as in cases (c)-(g); not connected, as in cases (a) and (b); and connected to at least one filament but with the additional requirement that the highest mass progenitor can be tracked from $z = 0.7$ to high redshift, also satisfying any of the conditions (c)-(g). Note that halos categorised as (b) have no valid partner, but would, by visual inspection, be classed as being part of the network. In Fig. 4.10 I find that from high to low redshift the majority of galaxies go from residing outside the filamentary network (red line) to within (green line), crossing over at $z = 2$. Comparing Fig. 4.10 with Fig. 4.17 reveals the same trend in spite of a distance based criterion to determine a halo's inclusion to a filament. As a result it is expected that the number of halos characterised by case (b) is small.

In order to suppress the effect of the changing number of galaxies in the different groups I normalise the distributions. Fig. 4.12 shows that at low redshift ($z \sim 0.7$) redshift there is an overabundance of low mass halos within the filaments, resulting in a steeper mass function as compared to the mass function of the non-filamentary and full sample of galaxies. Regardless of the group, all mass functions show an apparent flattening, towards higher masses for decreasing redshifts. At high redshift the halos within filaments for which I track the largest progenitor show a mass skewed towards higher masses compared to the full set of halos. Indeed, the lines from $z = 6$ to $z = 2$ in the bottom right panel, are shallower than their counterparts in the upper right panel up until this redshift. This is expected since the largest galaxies are most likely to be the largest progenitors in every merger they go on to complete.

The stellar mass functions, shown in Fig. 4.13 are significantly different. At high redshift regardless of whether the halos are connected to filaments or not, the stellar mass functions are very similar in terms of width and the position of the peak. With decreasing redshift, filament based galaxies tend to have enhanced stellar masses when compared to their non-connected counterparts. By $z = 0.7$ the peaks of the stellar mass function for the "filament" and "non-filamentary" case are separated by about an order of magnitude with the stellar mass function for the non-filamentary case peaking at $m_* \sim 10^7 \mathrm{M}_\odot$ and the stellar mass function for the filamentary case peaking at $m_* \sim 10^{8.5} \mathrm{M}_\odot$. The "non-filamentary" case therefore has an enhanced number of smaller galaxies as compared to the filamentary case. This suggests that galaxy formation efficiency is higher within the filament environment.

To explore this further, I look at the galaxy formation efficiency M_*/M_{DM} in Fig. 4.14. At high redshift there is very little difference between those galaxies connected to filaments and those not connected, but filament galaxies do grow more efficiently at lower redshifts. Main progenitor galaxies have a higher peak efficiency than the full sample of filament galaxies, but a narrower spread in values suggesting that the filament environment is more conducive to forming more efficient galaxies. Such an effect should be visible in the specific star formation rate, which I explore next.

Comparing the specific star formation rate at different redshifts averaged over the last 100 Myr in Fig. 4.15 shows the gradual slow down of star formation with redshift, but sheds no light on why the galaxy formation efficiency is higher in galaxies connected to the filaments, with very little discernible difference in the specific star formation rate evolution between the filamentary and non-filamentary case. The peaks of the distribution are slightly lower for the non-filamentary case, suggesting a greater spread in values. The filamentary case also has a slightly steeper decline in number of highly star forming galaxies

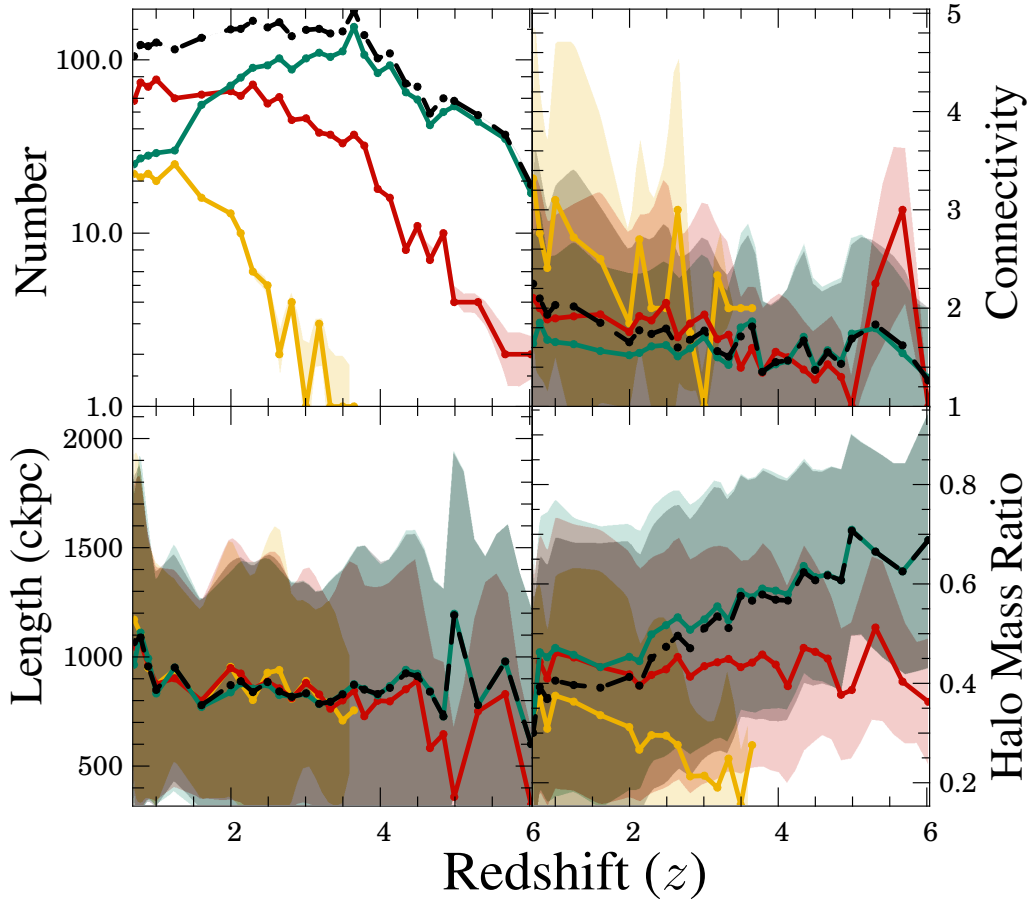

Figure 4.11: Evolution of halo number, connectivity, filament length and mass ratio of connected halo pairs over cosmic time. The *dashed* line is the full sample, *green, red* and *yellow* are the bins from Table 4.1 from least to most massive DM halos. The shaded areas are 1 standard deviation from the mean value. In the top left these errors are Poisson errors. The function $M_{\rm thresh}(z)$ was chosen to keep the total number of galaxies after $z = 4$ roughly constant. As it continues to rise, the lowest mass galaxies become less abundant in the sample. Only the highest mass galaxies show any significant difference in the number of neighbours they connect to. The length of these filaments do not depend on the nature of the connected galaxy. While low mass galaxies tend to form filaments with objects of similar mass at early times, they typically connect to objects larger than themselves at later times. Typically high mass halos connect to much lower mass halos at early times, evolving to a very similar mass ratio to the low mass galaxies.

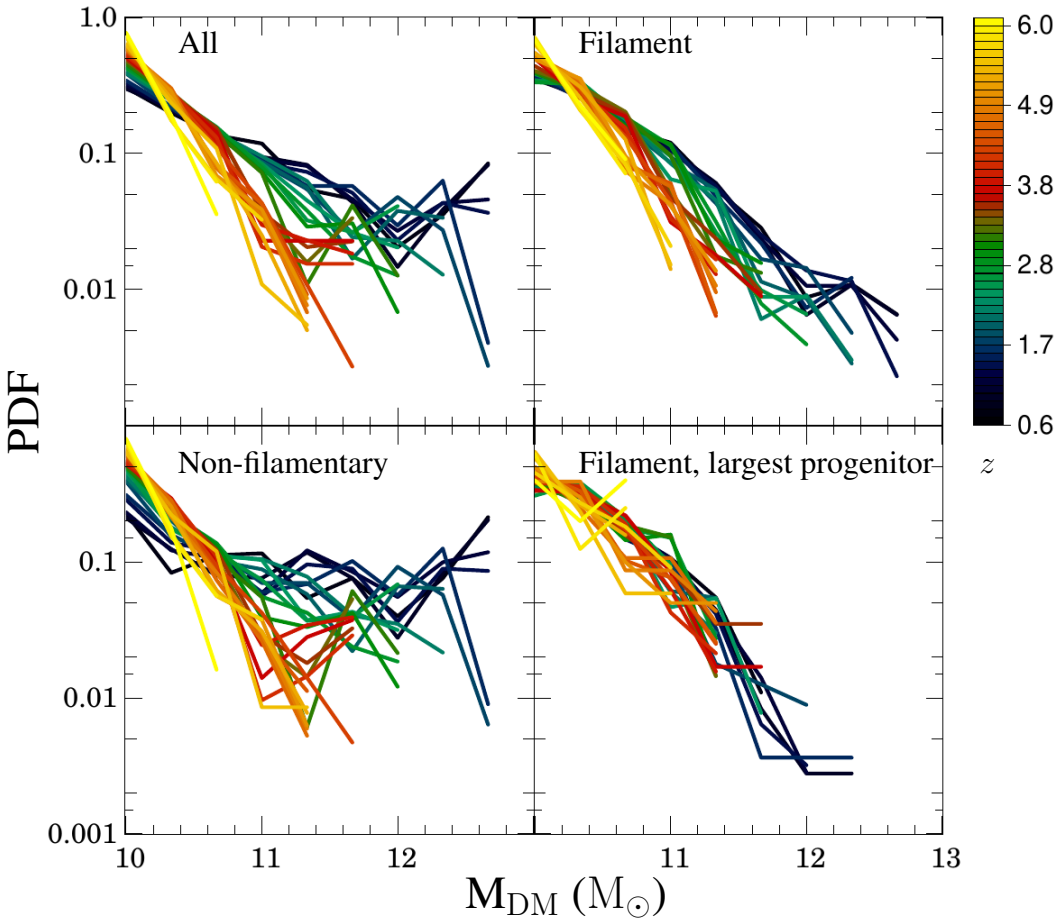

Figure 4.12: The effect of environment on the halo mass function across cosmic time. Line colours represent redshift as indicated by the colour bar. At high redshifts, the filaments tend to to be skewed towards higher mass objects, as indicated by the shallower slope of the distribution, and is even more exaggerated when considering only the largest progenitors.

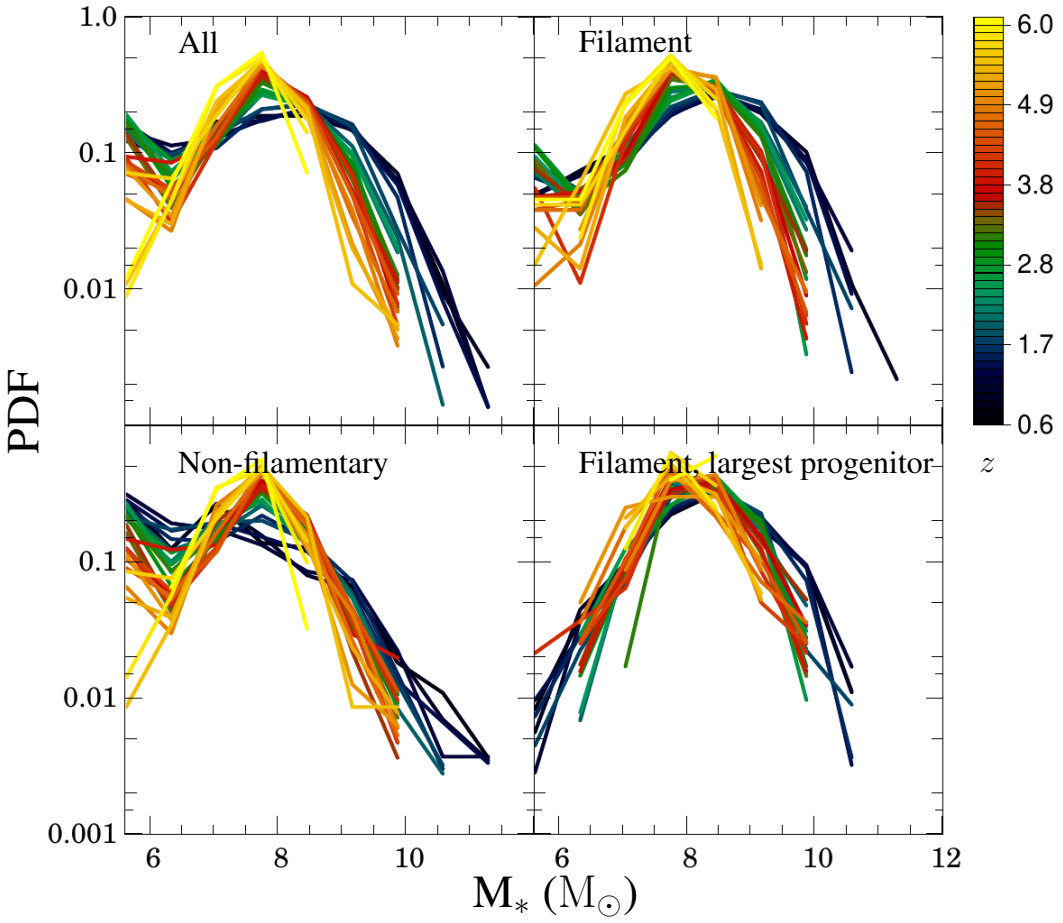

Figure 4.13: The effect of environment on the galaxy mass function across cosmic time. Here the peak position and width is impacted by the environment, with a wider range of masses (and therefore efficiencies, since the halo mass is not so greatly impacted in Fig. 4.12). Galaxies frequently have an extremely low mass in this environment compared to the filamentary environment. The peak mass of filamentary galaxies lies at approximately $10^8 M_\odot$.

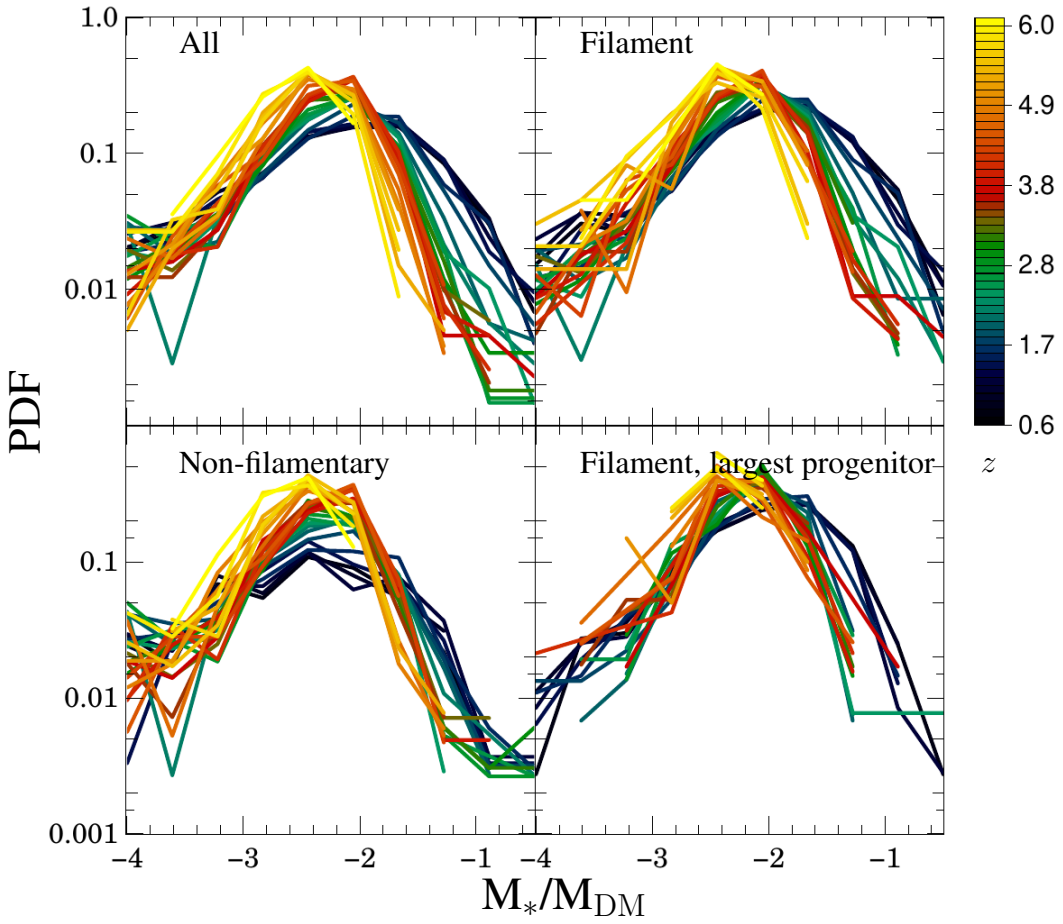

Figure 4.14: The effect of environment on the galaxy formation efficiency. Here we explicitly see that the efficiency is more variable for non-filamentary galaxy. The modal efficiency is reduced compared to galaxies which reside in filaments.

after the peak at low redshift, which is suggestive of suppression in star formation rate. At high redshift, the largest progenitor group shows slightly larger star formation rates than the connected galaxies up to $z = 2.8$, however this was not reflected in the galaxy formation efficiency (Fig. 4.14). These trends however are quite weak, due to the 100 Myr being too short a timescale to average over, with star formation rates being much greater or lower than average covering any underlying effects of the filamentary environment on galaxies. I have therefore averaged over 1 Gyr in Fig. 4.16. This does penalise the specific star formation rate for the earliest redshifts considered since the Universe is only 1 Gyr old at $z = 6$, and star formation begins at the start of the simulation. Regardless, the specific star formation rate is $10^{-8.5}$ yr^{-1} until $z = 4$ for nearly every galaxy when averaged over a billion year timescale. With decreasing redshift the specific star formation rates fall first in the non-filamentary galaxies, followed by the filament galaxies. Below $z = 2$ the number of galaxies with specific star formation rates greater than 10^{-10} yr^{-1}, begins to fall, with an even greater decline observed in the filamentary progenitor galaxies. The suppression however is not significant with respect to non-filamentary galaxies in this case. Poudel et al. (2017), using the SDSS catalogue found that galaxies in filaments were typically redder than those in the field, however, this was due to filaments typically containing more elliptical galaxies. A similar explanation is likely to hold for the filament progenitor group, with these galaxies more likely to experience merging events and morphological transformation into ellipticals (Martin et al., 2018). In spite of this decline in high star formation rates after $z = 2$, the cosmic peak of star formation, 25% of the stellar mass of the universe at $z = 0$ (Madau and Dickinson, 2014) is already in place and as such the galaxy formation efficiency for filament galaxies remains higher than for field galaxies up to $z = 0.7$, suggesting that galaxies can build a significant fraction of their stellar mass at to maintain their high level of formation efficiency.

4.2.3 Impact of Distance to and Density of Filaments on Galaxy Properties

In order to further understand how filaments affect the properties of the galaxies embedded within them, in Figs. 4.17 and 4.18 I plot galaxy properties in a two dimensional plane of local filament gas density versus distance to the nearest filament. Fig. 4.17 contain the high and intermediate DM halo mass bins as detailed in Table 4.1 while Fig. 4.18 contains only galaxies from the lowest halo mass bin. Distances have been rescaled in terms of the DM truncation radius,as defined by vorticity, r_ω, using the median of the 5 nearest segments to each galaxy. The median gas density of these segments is used as a proxy for the local gas density. In the first column of Figs. 4.17 and 4.18, a bimodal

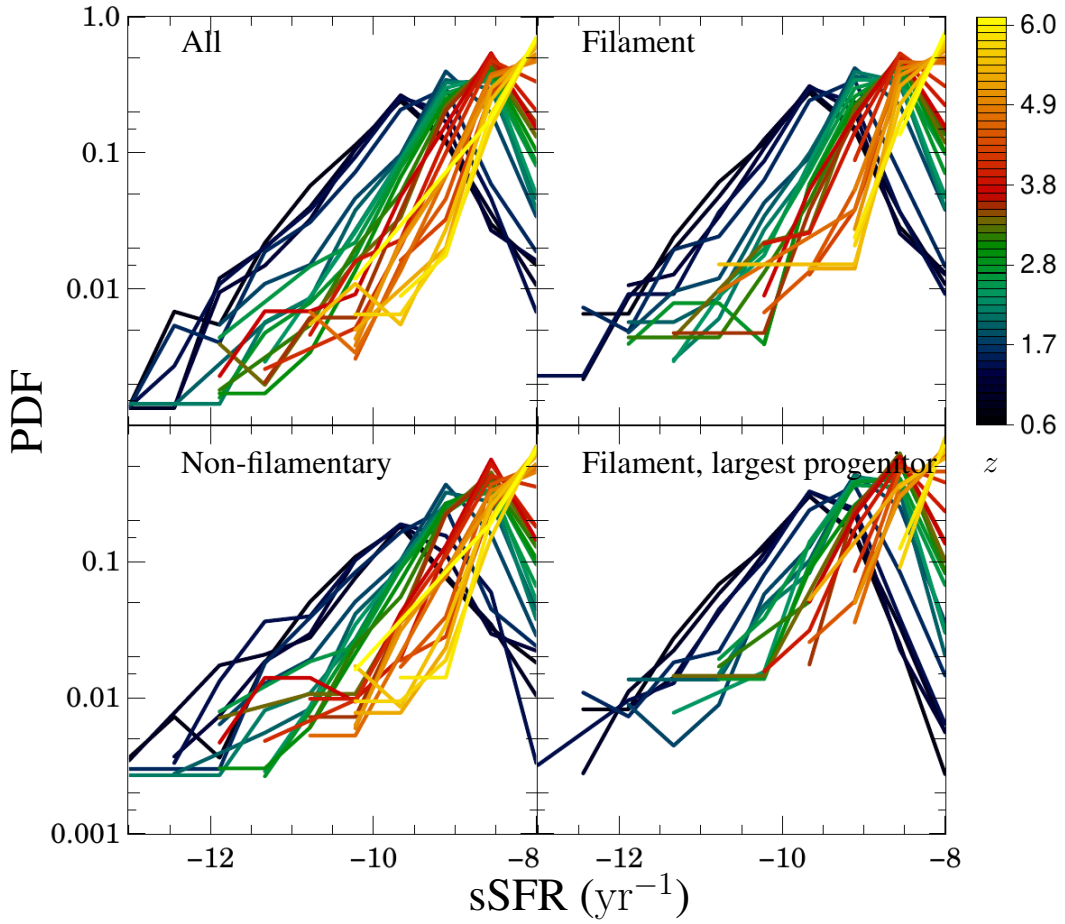

Figure 4.15: The effects of environment on the specific star formation rate averaged over 100 Myr. The difference here is quite subtle due to the variability of the star formation across a 100 Myr timescale. The final distribution looks very similar between the filamentary and non-filamentary groups, however, the non-filamentary distributions are slightly skewed towards lower specific star formation rates.

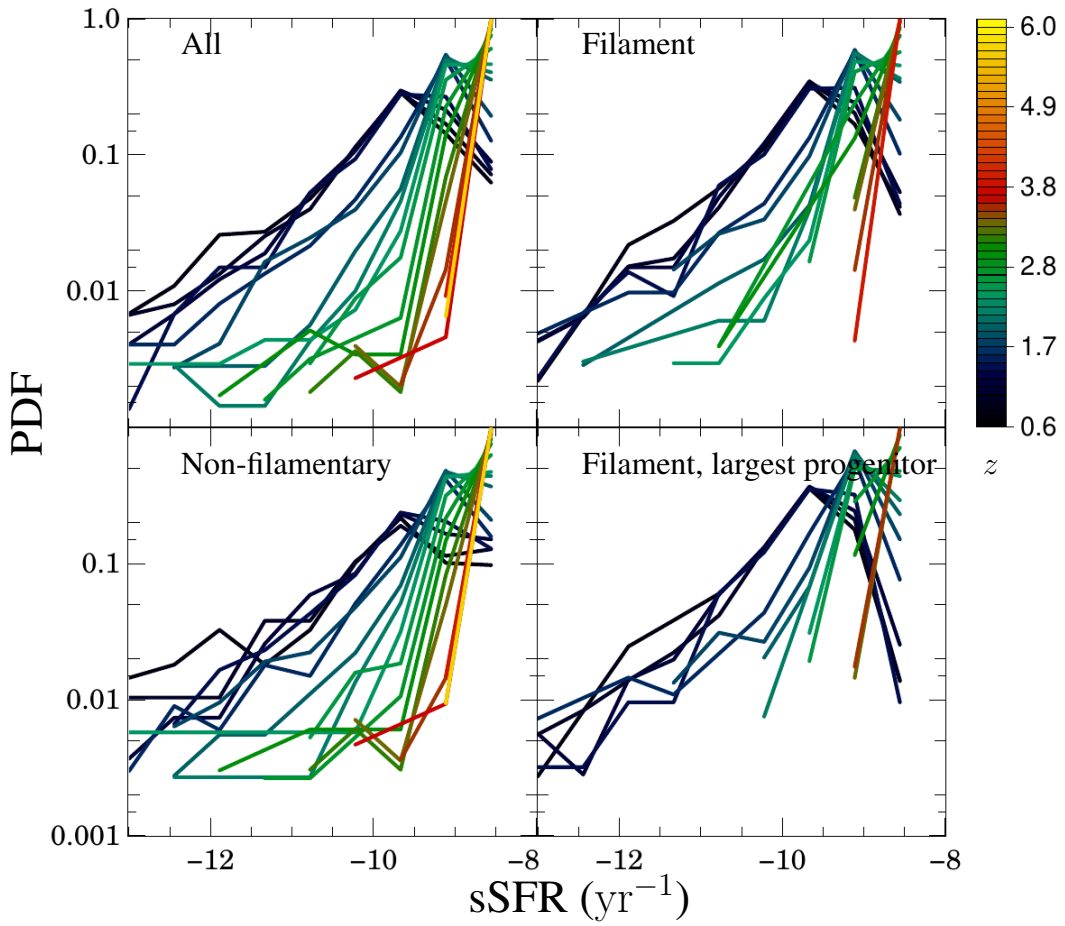

Figure 4.16: The effects of environment on the specific star formation rate averaged over 1 Gyr. The effect in Fig. 4.15 is amplified here. The distribution in sSFR evolves very little up until after $z = 4$ for the filamentary galaxies. A slow evolution towards lower sSFR is shown in the non-filamentary group. This group is also able to maintain more highly star forming galaxies at low redshift, which is particularly exaggerated when comparing with the largest progenitor group.

distribution in distance is clearly visible, with very few galaxies residing between the two regimes. This indicates that galaxies get trapped as they approach a filament. Galaxies inside a filament are concentrated to within a distance of approximately $0.1\ r_\omega$ comparable to the core size of the filament. The sinking of the galaxies towards the filament centre is due to dynamical friction. The galaxies that reside outside the filament are more broadly spread out in distance extending out to about $10\ r_\omega$. As time progresses more objects enter the filaments, though the trend reverses at $z = 4$ for the low mass bin. This is, however, accentuated by the varying mass floor, $m_{\rm thresh}$, which increases rises after $z = 4$. It is interesting to note that the galaxies in the filaments are the ones most impacted by this however, indicating that there are disproportionately more low mass halos within than outside the filaments. Considering the dependence on local gas density instead, Figs. 4.17 and 4.18 show the obvious trend that filament galaxies sit in slightly higher density regions.

The other columns of Figs. 4.17 and 4.18 are 2D histograms weighted by galaxy properties. More specifically, the second column is weighted by stellar mass, the third by specific star formation rate (averaged over the last 100 Myr) and the fourth by the galaxy formation efficiency. Any systematic effect of the local density or distance to the filament spine should be visible as a colour gradient. There does not appear to be any dependence of the stellar mass of the galaxies on local density or distance to the filament, with galaxies of similar stellar mass existing regardless of the local filament density or whether inside or outside the filament. For the high mass galaxies however, there appears to be a very slight enhancement at the truncation radius, which suggests that higher mass galaxies accrete onto the filament more slowly. There also appears to be an enhancement in specific star formation rate for the galaxies within filaments, indicated by the darker shading. After $z = 4$ the specific star formation rate falls for both populations, but additional suppression within the filament is not seen, in agreement with Figs. 4.15 and 4.16. These trends in the specific star formation rate is reflected in the the galaxy formation efficiency, which appears very slightly boosted by being inside the filament, particularly for low mass halos. These plots cover only the mean galaxy properties, which according to Figs. 4.12-4.16, are not strongly affected by membership or otherwise of the filamentary network, rather than the shape of the distribution of galactic properties. It is perhaps not so surprising that little variation in the mean galactic properties is seen with density or distance to the nearest filament.

4.3 Filament Profiles

Filaments are the means by which the large scale environment is able to forge a direct connection with the galaxies they connect to. In this section I will explore this connection

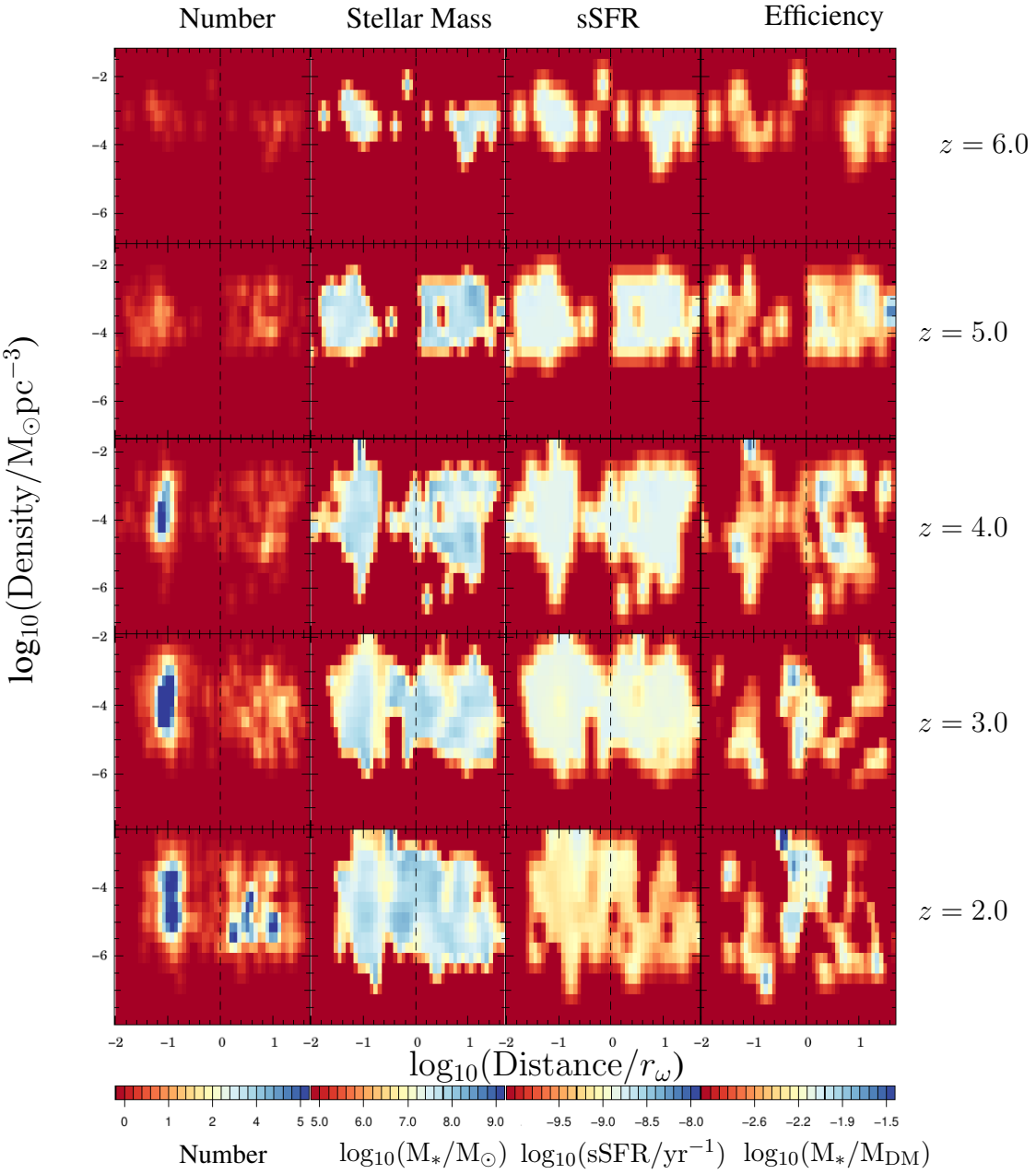

Figure 4.17: Weighted histograms of galactic properties as a function of distance from filament (in units of its truncation radius, r_ω) and local gas density for galaxies hosted by halos with DM masses greater than $10^{10.6}\mathrm{M}_\odot$. The columns show the total number, the stellar mass, specific star formation rate and the galactic formation efficiency between $z = 6$ and $z = 2$. The dashed black line indicates the truncation radius of the DM filament, dividing the non-filament from filamentary galaxies clearly into two distinct groups, as show by the first column. The lack of clear colour gradients suggest that distance and density of the local filament do not strongly impact *average* stellar mass, specific star formation and efficiency. It does not exclude the variation in the distribution as suggested in Figs. 4.12-4.16.

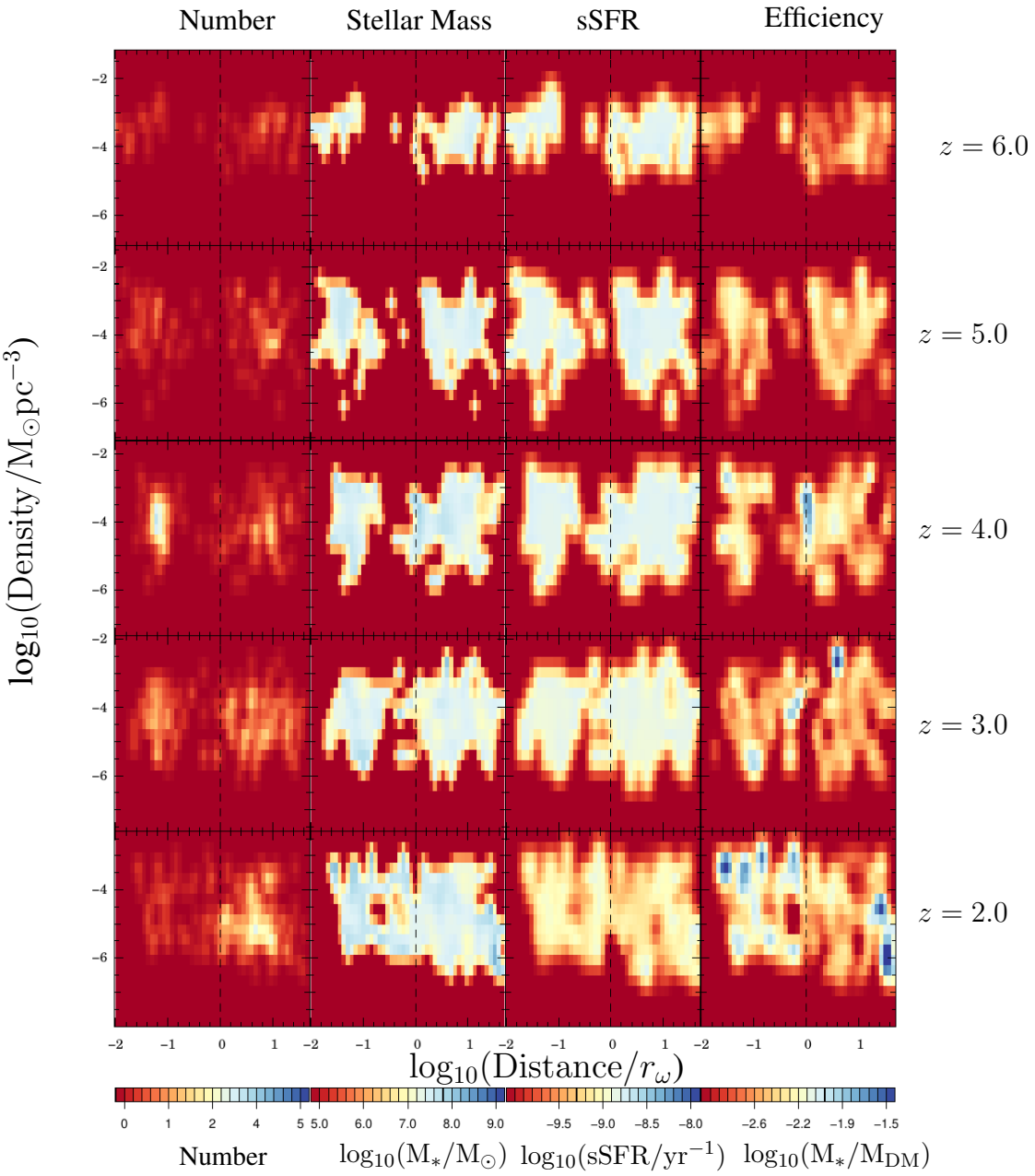

Figure 4.18: Weighted histograms of galactic properties as a function of distance from filament (in units of its truncation radius, r_ω) and local gas density for galaxies hosted by halos with DM masses less than $10^{10.6}\mathrm{M}_\odot$, but above the mass floor, M_{thresh}. The columns show the total number, the stellar mass, specific star formation rate and the galactic formation efficiency between $z = 6$ and $z = 2$. The dashed black line indicates the truncation radius of the DM filament. As in Fig. 4.17 it is unclear that distance to the filament or local filament density have a significant impact on the average stellar mass, specific star formation rate and efficiency.

using stacked filaments profiles connected to similar galaxies to enhance the signal.

4.3.1 Constructing Median Filament Profiles According to Instantaneous Galaxy Properties

The most obvious way of stacking is to use the raw halo catalogue and to bin by some desired property, for example DM mass of the host halo, at a given redshift. This does however, obscure the fact that the galaxies themselves are evolving. A typical galaxy of a given mass at one redshift would be considered an extreme object if it was found at much higher redshift. The trends across redshift seen in the filament profiles stacked in this way do not reflect the evolution of the filaments profiles, but rather in the distribution of filament profiles. Note that in all cases considered throughout this chapter filaments are binned exclusively on the properties of the largest in the pair of galaxies they connect, in order to prevent double counting.

Fig. 4.19 reveals the entirely intuitive result that the densest gas (dashed line) and DM (solid) filaments tend to connect galaxies hosted in the highest DM mass bin. In nearly all of the panels the median densities appear ordered, with filaments connecting galaxies in the highest mass bin possessing the largest density, filaments connecting galaxies in the lowest mass bin having the lowest density, and filaments connecting intermediate mass galaxies sitting in between. In both figures the intrinsic scatter within one bin is significantly greater than the separation of the median density profiles. The one exception to this is in the $z = 5.3$ panel for the DM, though this is likely a resolution issue combined with the rarity of objects (only 4) in the intermediate DM halo mass bin. As can be seen from the figure, at this redshift the green and blue profiles intersect around 15 ckpc resulting from the reduced slope of the green curve, which is completely different from the behaviour one expects and measures at all other redshifts. The median gas and DM densities vary by at most 0.2 dex for all mass bins at all redshifts. It is likely that pursuing filaments connecting ever smaller halos will result in probing smaller filaments with even lower densities. Finally each of the gas and DM median density profiles show the characteristic shape of the filament and wall revealed in the NUT pilot study (Chapter 3). A broken powerlaw transitioning to a shallower wall slope at larger radii. This is highly suggestive of this form of the profile being universal to filaments, and is discussed further in Section 4.5.

The median gas temperature profiles (Fig. 4.20, solid lines) show a greater diversity with varying halo mass than the median gas density profiles. Despite this we still see the features that were presented when we evaluated the NUT temperature profiles (Fig. 3.11), namely a flattening of the profile in the central region followed by a rise to a peak temperature due to an accretion shock, followed by a gradual decline at still larger radii. Higher

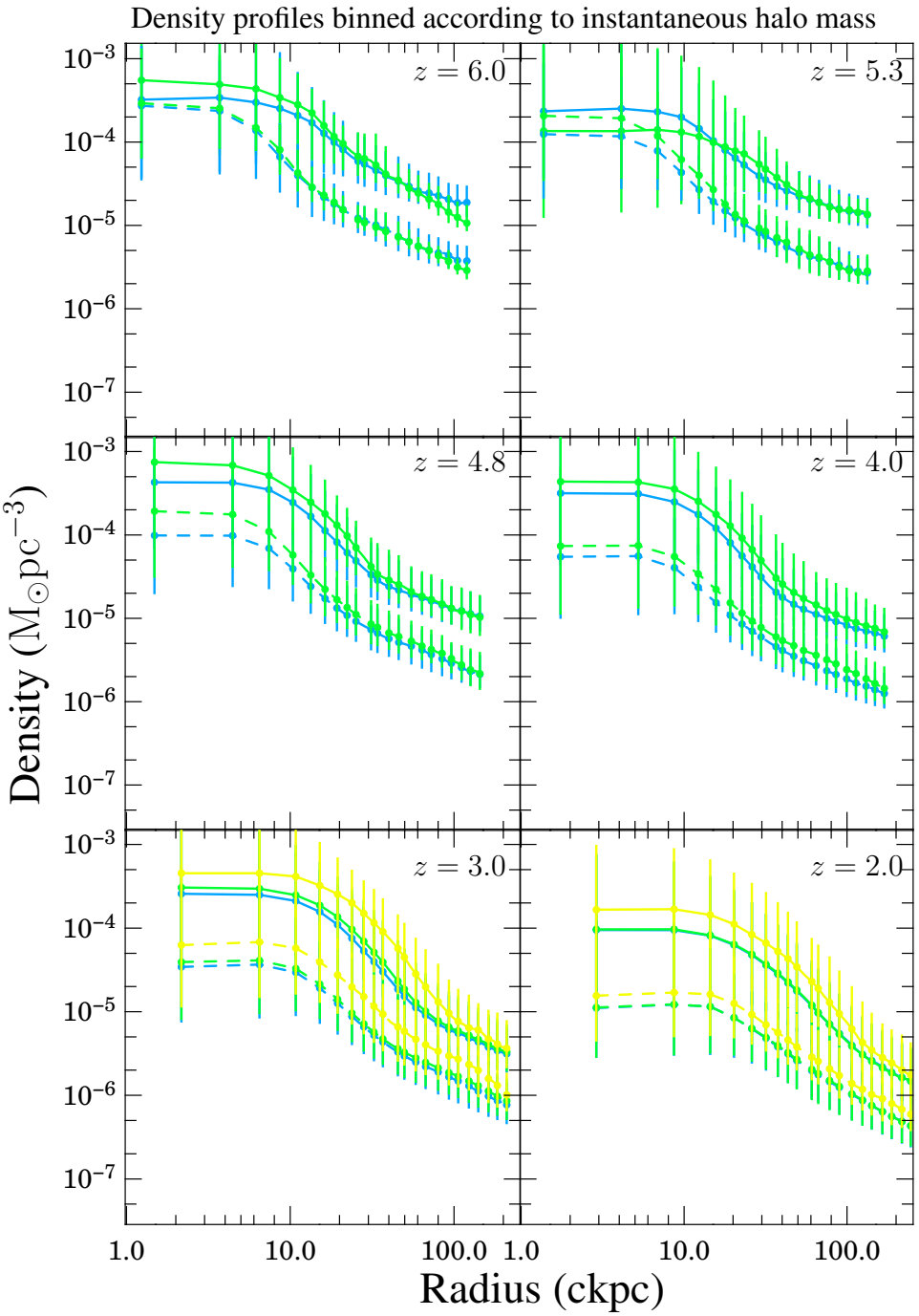

Figure 4.19: Evolution of the filament median density profiles from $z = 6$ down to $z = 2$, with gas in *dashed* lines. The filaments are here binned by halo mass, with lowest in blue, through green and yellow, according to Table 4.1. The error bars show a 1 σ error. The curves are well-behaved in that the lowest mass galaxies have a tendency of connecting to lower density filaments. However, there is significant variation in this as indicated by the overlapping error bars.

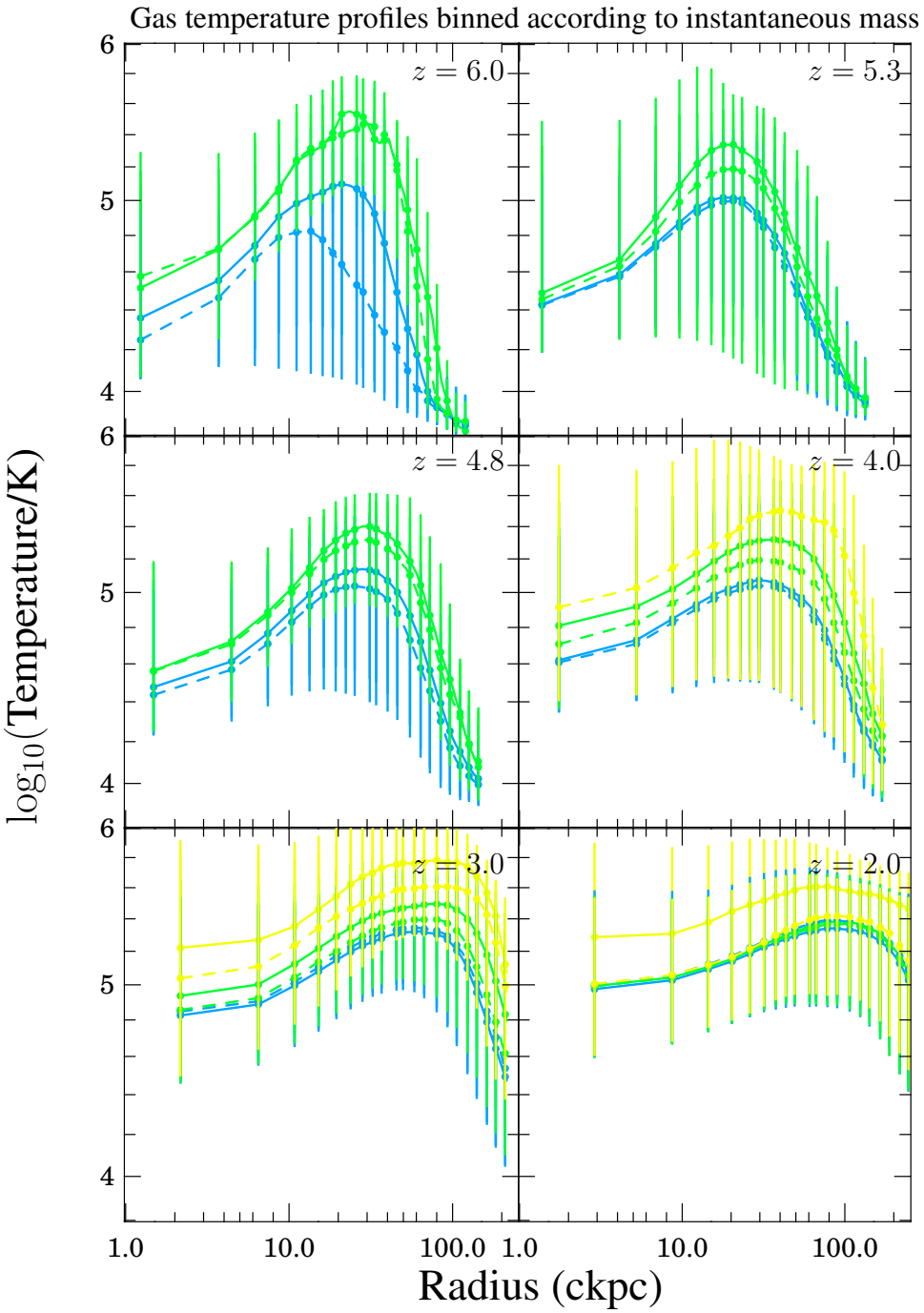

Figure 4.20: Evolution of the median filament temperature profiles from $z = 6$ down to $z = 2$. The filaments are here binned by halo mass (*solid*) and stellar mass (*dashed*), with lowest in blue, through green and yellow, according to Table 4.1. The error bars show a 1 σ error. Binning in this way shows similar behaviour as in Fig. 4.19, in that the profiles are ordered, and higher mass objects tend to connect to hotter filaments. However, at lower redshift, the separation declines and vanishes by $z = 2$ for nearly every bin.

mass halos in general reside in filaments with both higher core temperatures and higher peak temperatures. The peak temperature also tends to occur at slightly larger radii, though for $z = 2$ the peaks are extremely broad and hence the exact position of the peak is not well defined. The fall in the temperature outside the accretion shock is less steep than at higher redshifts. The accretion shock appears to be unimportant in slowing accretion onto the filament as the DM and gas density profiles for different halo mass bins are separated by similar amounts. The effect is even more pronounced in Fig. 4.20 when the temperature profiles are binned according to stellar mass, with an initially much larger separation between stellar mass bins dwindling until there is no discernible difference between the different profiles at $z = 2$. As the filaments evolve to lower redshifts, the core of the filament is heated, but the peak temperature stays nearly constant regardless of the galaxy property binned over. An estimate of the relevant timescales is useful to determine that this effect arises from filament cooling becoming inefficient.

The relevant timescales are the free-fall time

$$t_{\rm ff} = \sqrt{\frac{1}{4G\rho_0}}\,, \tag{4.2}$$

for a cylindrical collapse, evaluated for a test particle at r_0, which encloses half the filament mass. The exact geometry used determines the prefactor, not the scaling of the relation however. The density used, ρ_0 should be that of the DM, as this is the mass component which dominates the gravitational influence of the system. The cooling timescale is defined as the ratio of the thermal energy of the gas to the cooling rate, given by:

$$t_{cool} = \frac{3nk_BT}{2n_H^2\Lambda(T)}\,, \tag{4.3}$$

where n is the total number density, n_H is the hydrogen number density, and Λ is the cooling function. Even without substituting numbers into these equations it is apparent that the cooling time grows faster than either the sound crossing time or the free fall time. Computing these timescales according to the densities and temperatures for the low halo mass bin and using the cooling function from Sutherland and Dopita (1993) yields $t_{\rm ff} = 620$ Myr and $t_{\rm cool} = 3.2$ Myr for $z = 6$. By $z = 2$, $t_{\rm ff}$ has roughly doubled, reaching 1.1 Gyr whereas $t_{\rm cool} = 170$ Myr, a factor of nearly 50 times as long as before. While these values have not yet crossed over there are three caveats to bear in mind with this estimation. The first is that the cooling time was evaluated at the filament centre and it is highly sensitive to the density which drops precipitously outside of the filament core. The second point is about the cooling function itself. As the temperature rises above 10^5 K cooling becomes less efficient as the gas becomes ionised and Bremsstrahlung does not

become an important cooling mode until $T > 10^6$ K. Both of these effects reduce the efficiency of cooling in the filament, resulting in a widening density profile which in turn decreases the cooling efficiency. The third and most important caveat however, is that these are the median timescales. The 1 σ dispersion of the distribution includes densities that are nearly an order of magnitude below the median, which could give rise to filaments that already have cooling timescales longer than their free fall timescales, resulting in hotter and wider filaments. The rest of the population will not be far behind in this fate. This can be seen around the galaxies in Fig. 4.2 as the absence of narrow, collimated cold flows onto the galaxies.

Finally, I have included the DM velocity dispersion for completeness in Fig. 4.21. Note that the profiles are much flatter than than those measured in Chapter 3, particularly at lower redshifts. This is discussed further in Section 4.5. In spite of this difference, a similar trend as in the previous gas temperature profile plots is seen, with higher mass halos being connected to filaments with higher velocity dispersions.

4.3.2 The Effect of Filaments on the Final Galactic Properties

In order to make direct comparisons with Chapter 3 it is necessary to use the merger tree to ensure the same galaxies are being followed through the simulation, such that the same objects are binned together across cosmic time and the intrinsic evolution of the object does not cause it to switch bin. This has the caveat that while objects may end up with similar properties at the end of the simulation it is possible that they have wildly different accretion histories, e.g. Jian et al. (2012) finds a strong dependence on merger rate on the local overdensity. In an extreme example, these can be two halos which end up with the same halo mass, but one becomes incorporated into a cosmic web filament at high redshift, while the other is only accreted at late times. The higher density environment of the cosmic web means that the first halo is more likely to experience a greater number of mergers, growing primarily by this mechanism rather than by direct accretion of matter, as for the second halo. Ideally, a larger simulation would allow more cuts on the sample of galaxies to avoid such a situation, while still avoiding small number statistics.

The merger tree is constructed from the galaxy catalogue. For each snapshot the progenitors of each object is found. If there are more than one progenitor then the most massive one is identified as the main progenitor. While I could also compute the merger history of the smaller progenitors I only track the main progenitors back to formation in this thesis. As a result only galaxies that were the most massive at every merger event are represented in the merger tree, all other galaxies are branches along this tree trunk and are therefore discarded.

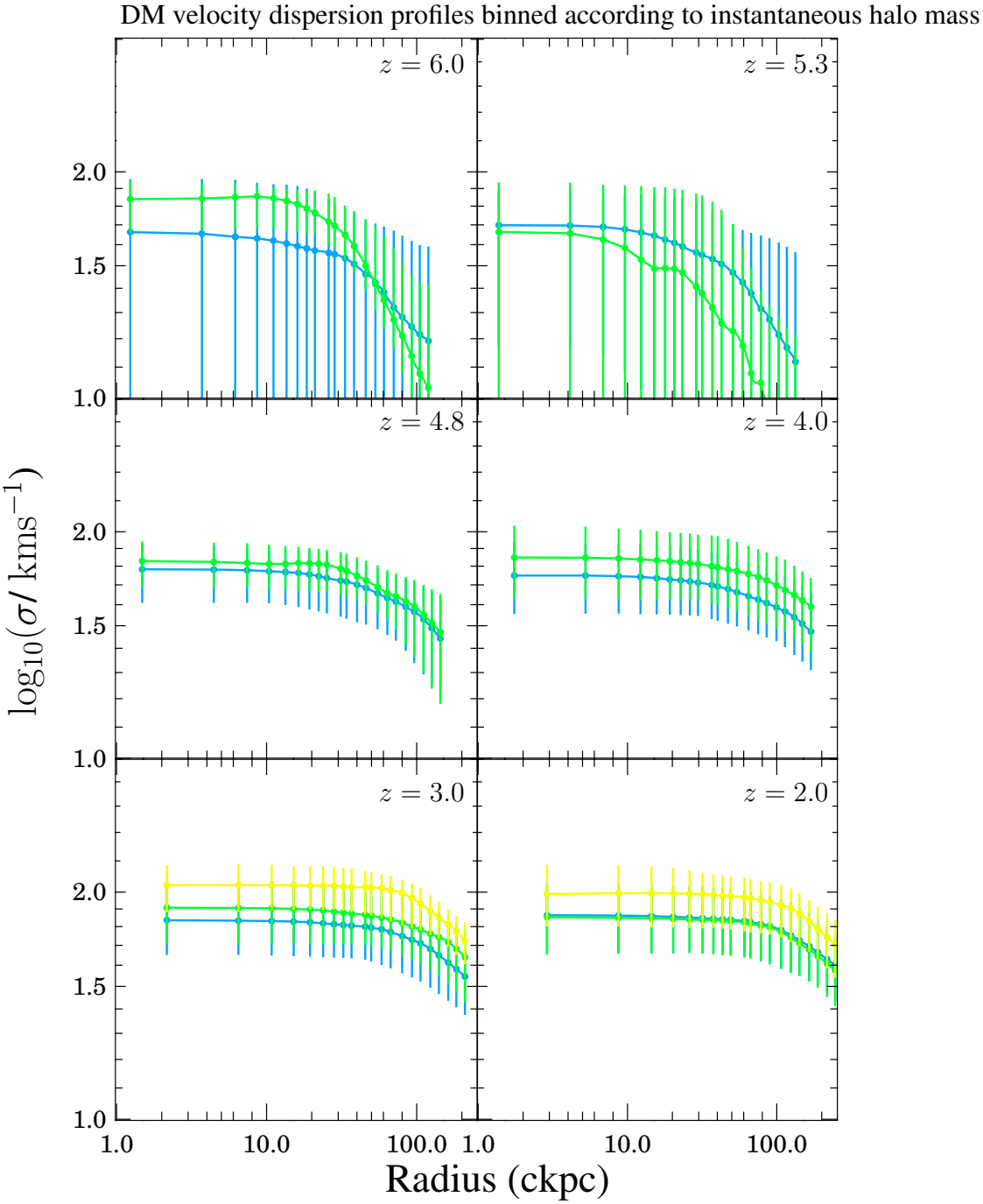

Figure 4.21: Evolution of the filament median DM velocity dispersion profiles from $z = 6$ down to $z = 2$. The filaments are here binned by halo mass, with lowest in blue, through green and yellow, according to Table 4.1. The error bars show a 1 σ error. While the central velocity dispersion has a sensible value, the shape of these profiles are not at all like Fig. 3.11, except at high redshift. The likely reason for this departure is explained in the text.

Due to the filaments being in overdense regions the galaxies here have higher merger rates than field galaxies. Very few main progenitors are therefore part of the filamentary network at all times. At $z = 6$ for example, there are only 5 galaxies left that will go on to merge with objects smaller than themselves down to $z = 0.7$, whereas there are 19 galaxies in the network which are above the mass threshold at this redshift.

It becomes immediately clear that the monotonic evolution of filament profiles as a function of galaxy property (Figs. 4.19, 4.20 and 4.21) is lost. Despite only having two bins, the higher mass objects do not always correspond to the densest filament profiles (see Fig. 4.22). In fact, when binning according to the halo mass at $z = 0.7$ as in Fig. 4.22 the separation initially seen between the two lines at $z > 4$ shrinks until the mass bins have essentially the same median profiles at lower redshift. In addition, the order (colour) of the lines is reversed multiple times. There is no obvious pattern in the ordering of the profiles, suggesting that the nature of the filament has little impact on the final properties of the galaxy. Binning at an earlier time, $z = 3$, as shown in Fig. 4.24 reveals the same pattern, with no major difference between the profiles binned at the two different times.. It seems that other processes, rather than the density or size of the local filaments is more important in determining the fate of the galaxies within the filaments. This agrees with Figs. 4.17 and 4.18 which show that the local filament density has no significant impact on the galaxy properties I considered in this thesis.

However, as these filament density profiles appear very similar to one another, it may be more informative to look at the gas temperature profiles instead. From Fig. 4.25 it is apparent that the halo mass also has little bearing on the temperature profiles of filaments at earlier epochs. For instance, the difference between the two mass bins are negligible for the last two redshifts as they were for the density profiles The median temperature profiles are otherwise not correlated with halo mass. However, at the final redshift displayed, $z = 2$, the gap in the temperature profiles reopens when binning by stellar mass. Here the low stellar mass bin in cyan has a higher temperature than the green high stellar mass bin. This is suggestive of lower mass galaxies being less able to accrete gas from the filament, thereby suppressing their growth.

This agrees with the perspective given by Fig. 4.26. Here at $z = 2$ the less efficiently formed galaxies are connected to filaments with greater temperatures, as shown by the cyan line being above the green. This regime extends up to $z = 4.8$, indicating that more efficient galaxy formation occurs in cooler filaments. Since stellar mass is at zeroth order dictated by halo mass, galaxy formation efficiency is a much more sensitive probe of suppression and enhancement by filamentary accretion.

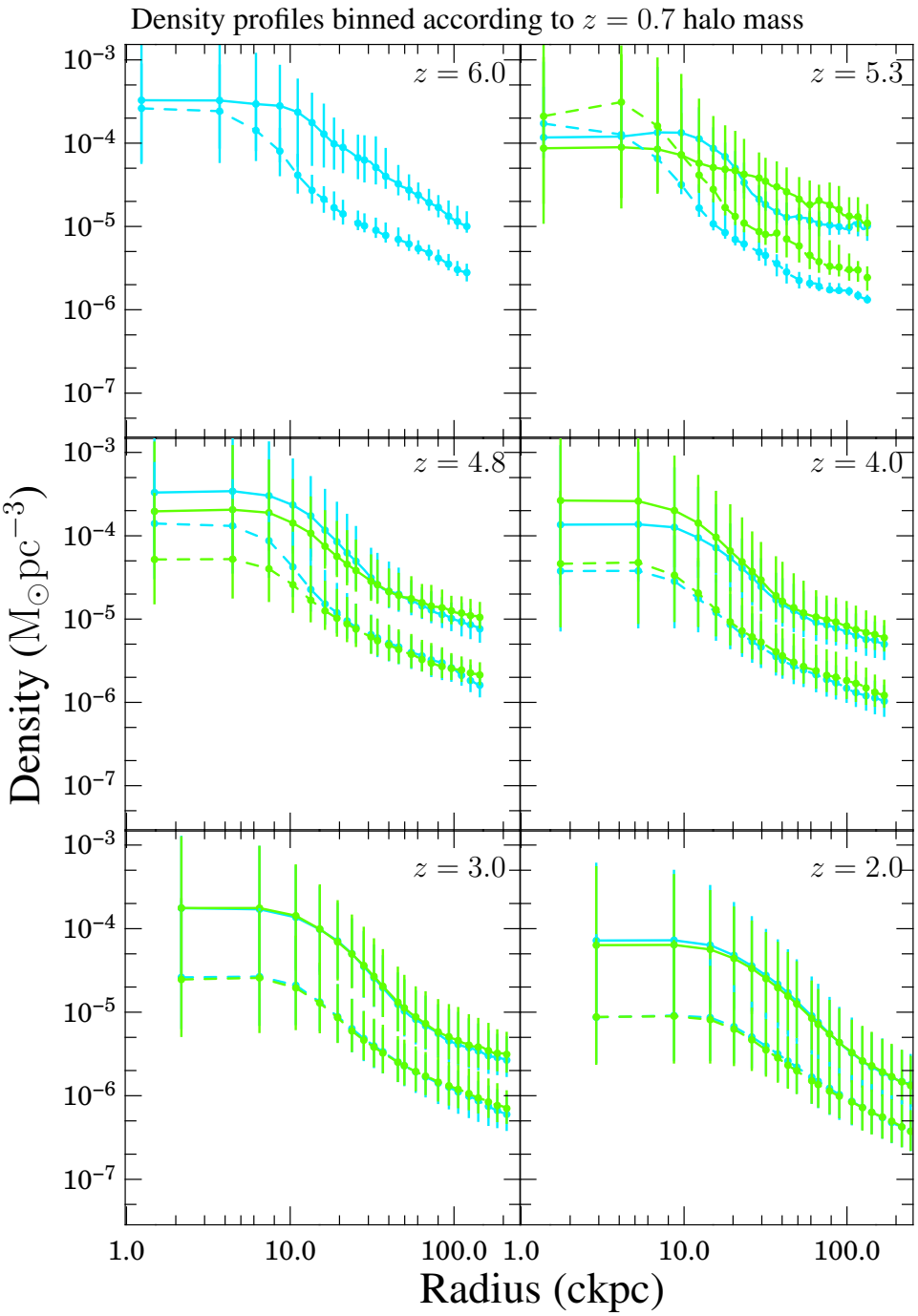

Figure 4.22: Evolution of the filament median density profiles from $z = 6$ down to $z = 2$. Gas is indicated with a *dashed* line. The filaments are here binned by the $z = 0.7$ mass, with lower bin in cyan, and the higher bin in green, according to Table 4.3. The error bars show a 1 σ error. The $z = 0.7$ halo mass does not generate a consistent separation in the density of the filaments, particularly at lower redshift.

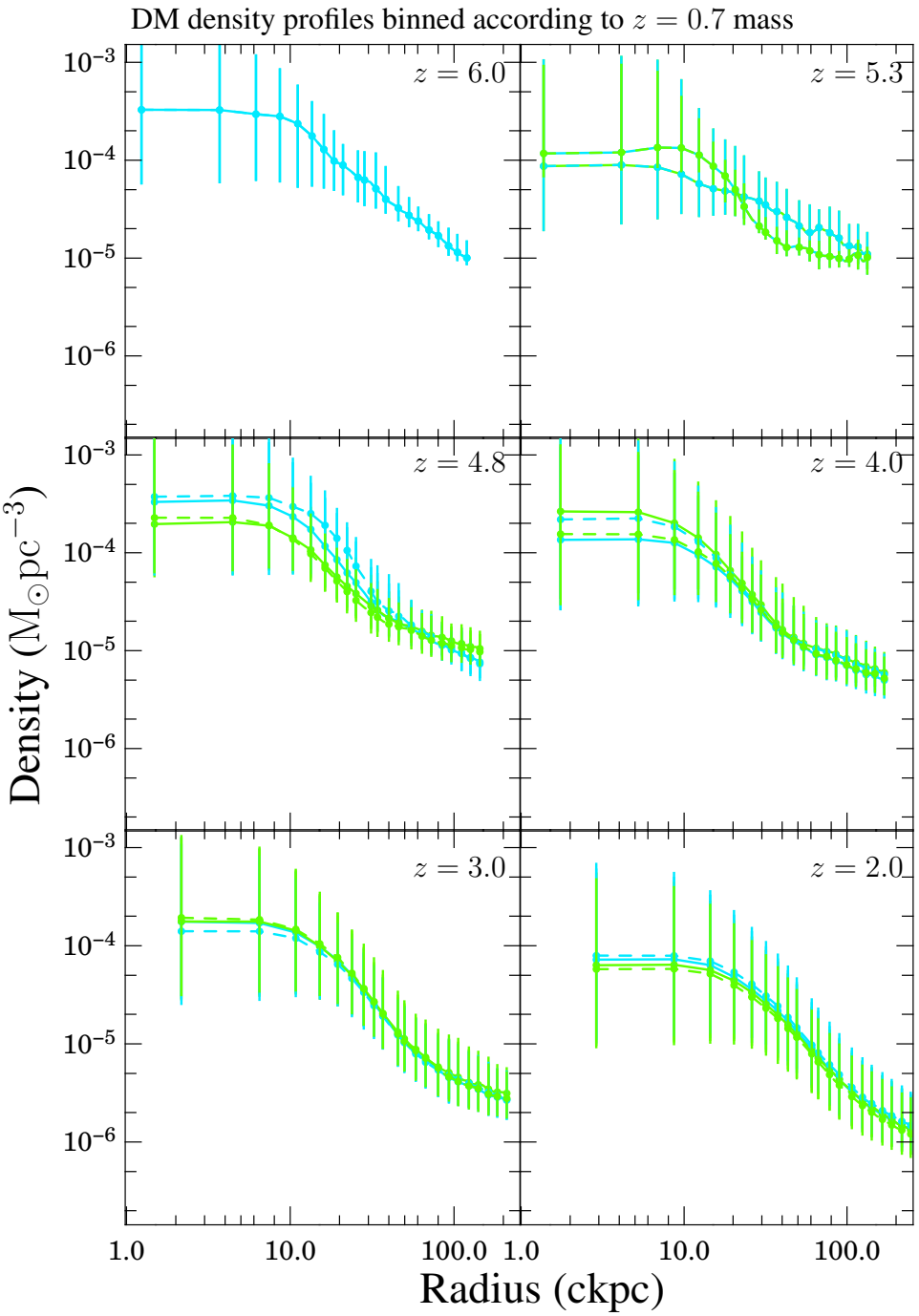

Figure 4.23: Evolution of the filament median DM density profiles from $z = 6$ down to $z = 2$. The filaments are here binned by the $z = 0.7$ stellar mass (*solid*) and halo mass (*dashed*), with lower bin in cyan, and the higher bin in green, according to Table 4.3. The error bars show a 1 σ error. The filament DM profiles appear to have very little bearing on the final $z = 0.7$ mass of the galaxy or halo.

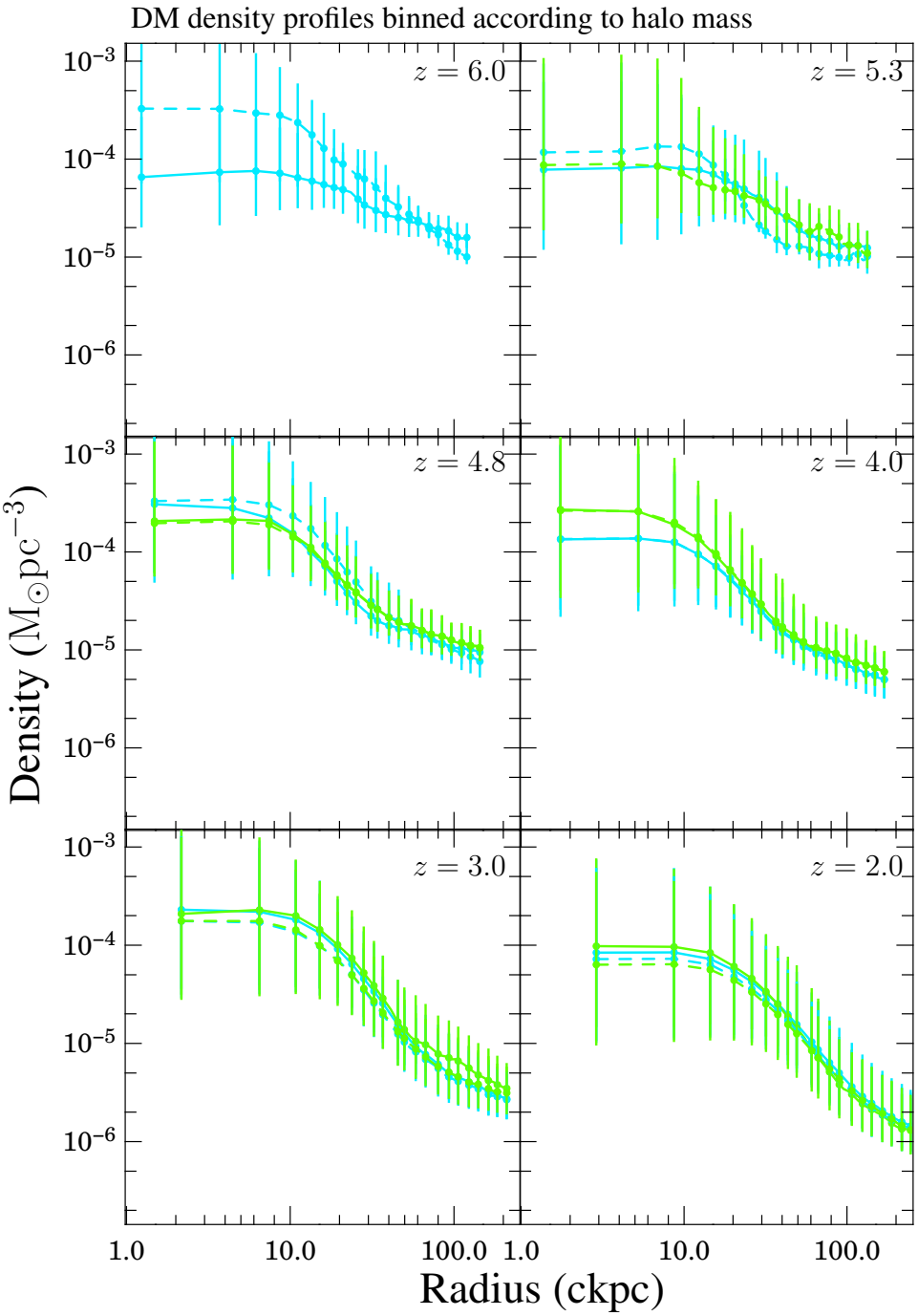

Figure 4.24: Evolution of the filament median DM density profiles from $z = 6$ down to $z = 2$. The filaments are here binned by the $z = 3$ mass (*solid* line), and $z = 0.7$ indicated with a *dashed* line, with lower bin in cyan, and the higher bin in green, according to Table 4.3. The error bars show a 1 σ error. The density ordering seen in Figs. 4.19-4.21 is not maintained when binning by the mass at a specific redshift, and the difference between the two bins declines towards lower redshift.

Binning by specific star formation rate, I find that the filaments feeding objects with higher specific star formation rate tend to have higher shock temperatures at high redshifts, as compared to galaxies with lower specific star formation rates. This difference declines below $z = 4$ and seems to reverse by $z = 2$. This can also be seen in Fig. 4.29 (bottom right panel). It appears as though the gas accretion onto these filaments is suppressed by excessive heating early on, and becomes available for star formation at later times.

Despite filaments connected to galaxies with high specific star formation rates (Fig. 4.27) and those connected to galaxies with high galaxy formation efficiency (Fig. 4.26) having different temperatures at high redshift, it appears that they become very similar at late times. This appears to be due to the heating of the filaments that supply the gas. Indeed, Fig. 4.29 shows that as the redshift decreases to $z = 2$ the peak temperature and central temperature in Fig. 4.29 approach each other.

4.3.3 Summarising Information from Filament Profiles

Rather than assessing the effect of various binning methods by viewing the profiles, it is more convenient to view a summary of these in the form of Figs. 4.28 and 4.29. In Fig. 4.28 each panel shows the central densities for the gas in solid and DM in dashed lines. The mean density of the universe multiplied by a factor of 100 is also shown as a dashed black line. Regardless of binning strategy, the gas always follows the same scaling in evolution as the mean density of the Universe. The DM however, begins to deviate from this scaling by $z = 4$. This is likely due to resolution effects. The evolution of the gas central density for the NUT filaments are also plotted. It is interesting to note that only when binning by final property do the densities for the NUT and NEW HORIZON line up. This is due to the method only considering the largest progenitor after each merger being equivalent to tracking the same filament back in time as done in the NUT analysis in Chapter 3. Regardless of this, it appears that the filament considered in the NUT simulation has a density in the low tail of the NEW HORIZON distribution.

In the left column of Fig. 4.28 the central densities monotonically increase when moving from the lowest to the highest halo and stellar mass bins. The galaxy formation efficiency and specific star formation rate show no such ordering, as it is not the density which determines whether or not the gas can be accreted and fuel star formation, but more likely the temperature. In the right hand column, where the density is binned by the $z = 0.7$ properties, no obvious trend in central density is seen.

In Fig. 4.29 the evolution of the filament temperature is summarised. In this case only the central (solid line) and peak temperature (dashed line) are plotted. Regardless of binning scheme, two things are immediately apparent. The first is that the core temperature is

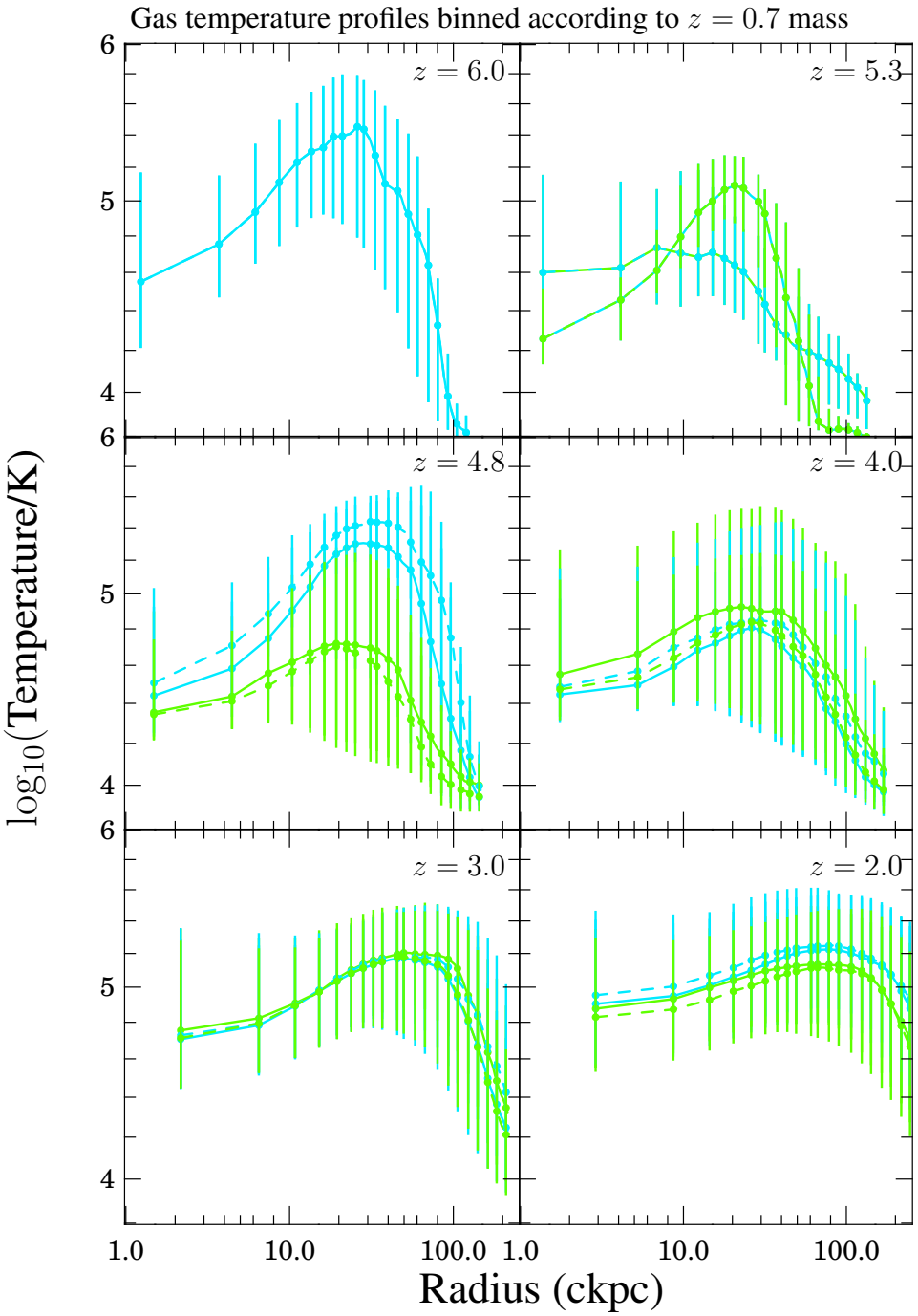

Figure 4.25: Evolution of the filament median temperature profiles from $z = 6$ down to $z = 2$. The filaments are here binned by the $z = 0.7$ halo mass (*solid*) and stellar mass (*dashed*), with lower bin in cyan, and the higher bin in green, according to Table 4.3. The error bars show a 1 σ error. The final stellar mass is enhanced if the galaxy resides in a low temperature filament, which is more conducive to accretion onto the galaxy, as shown by the divergence in the temperature profiles at this redshift for the dashed lines only.

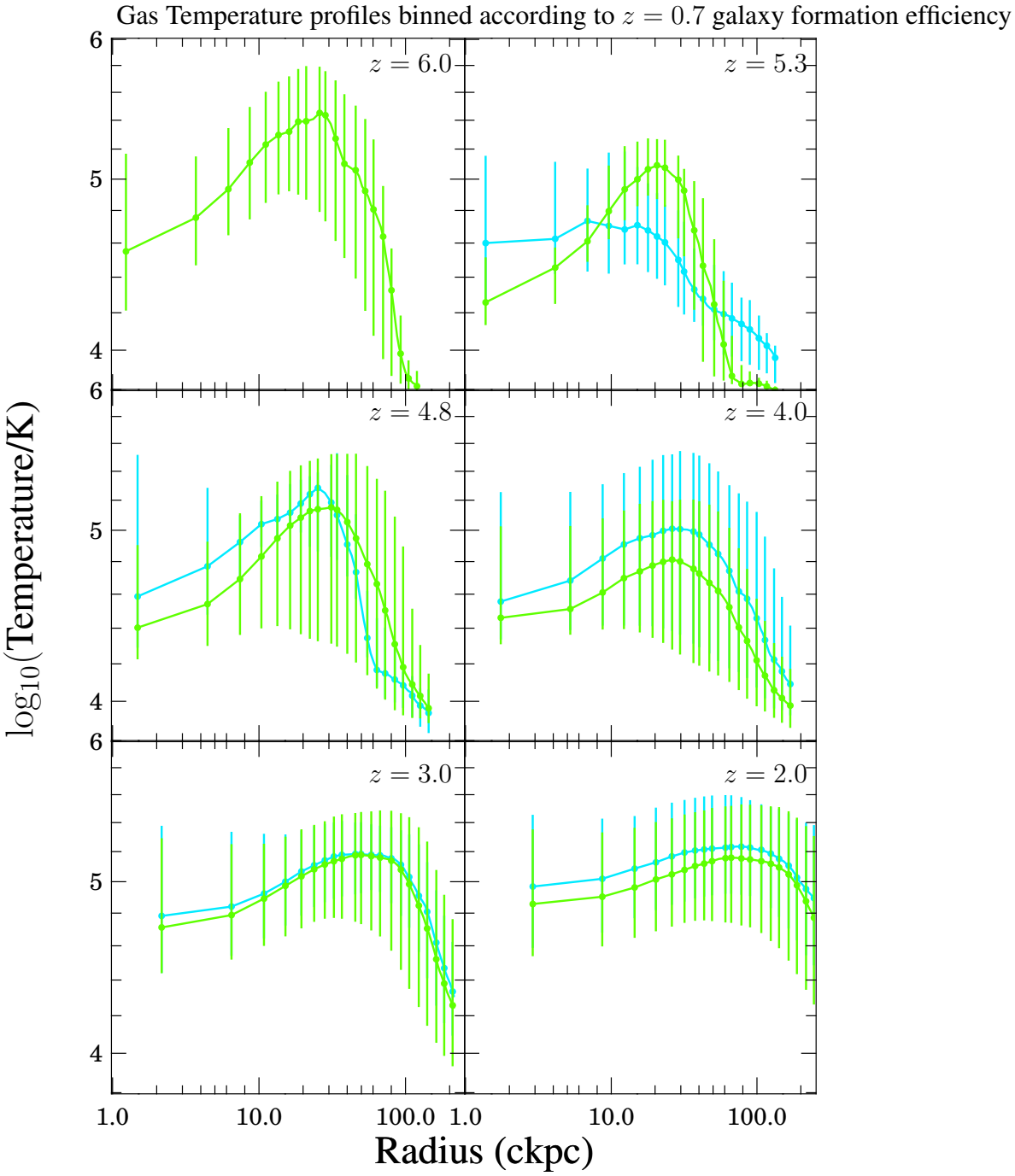

Figure 4.26: Evolution of the filament median temperature profiles from $z = 6$ down to $z = 2$. The filaments are here binned by the $z = 0.7$ galaxy formation efficiency, with lower bin in cyan, and the higher bin in green, according to Table 4.3. The error bars show a 1 σ error. More efficient galaxy formation occurs in the low temperature filaments.

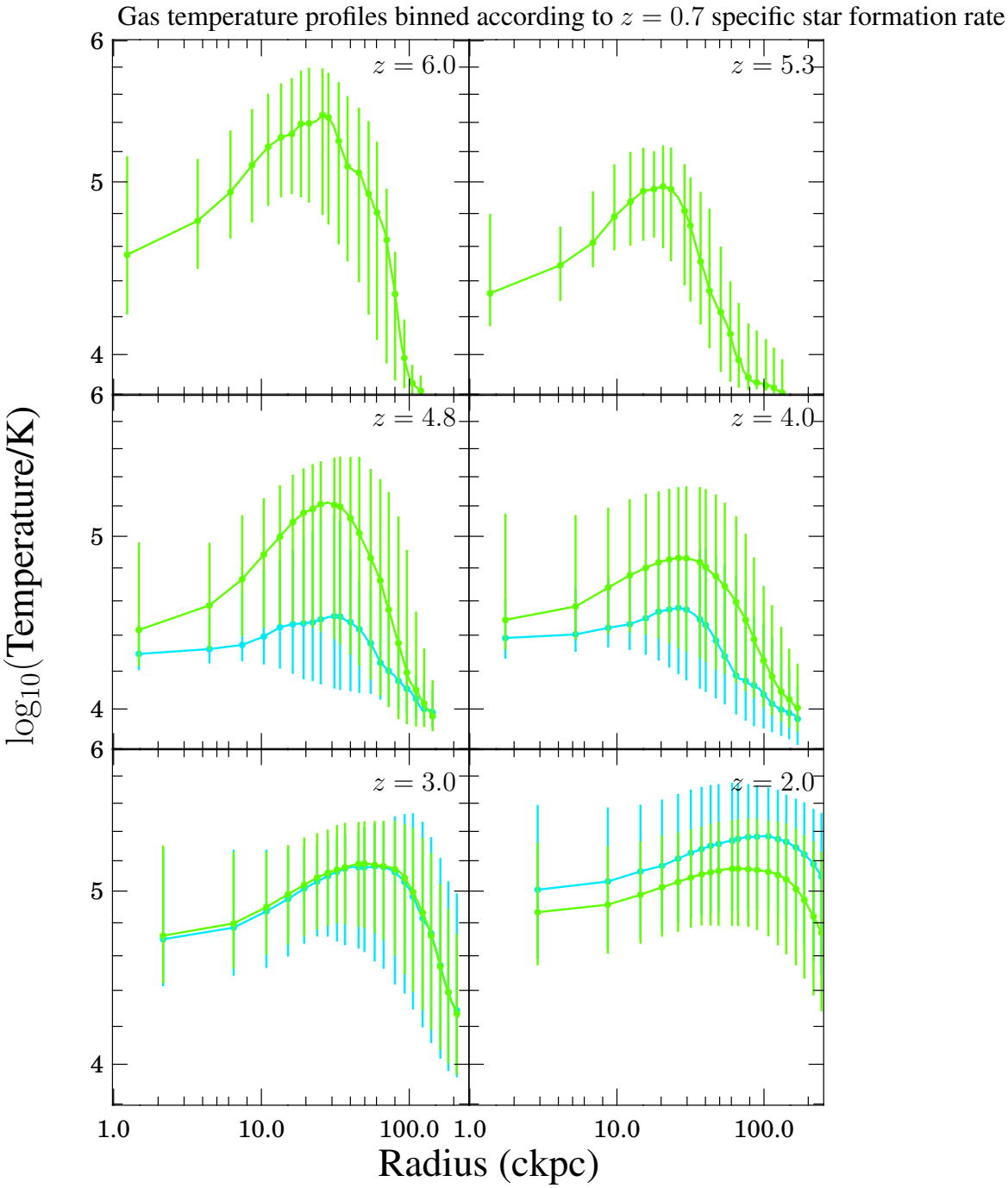

Figure 4.27: Evolution of the filament temperature profiles from $z = 6$ down to $z = 2$. The filaments are here binned by the $z = 0.7$ specific star formation rate, with lower bin in cyan, and the higher bin in green, according to Table 4.3. The error bars show a 1 σ error. Galaxies which are highly star forming at low redshift tend to reside in colder filaments at low redshift ($z = 2$). However, these galaxies resided in filaments which were hotter earlier, suggesting that accretion at earlier times was suppressed, resulting in the high specific star formation rates seen later (at $z = 0.7$).

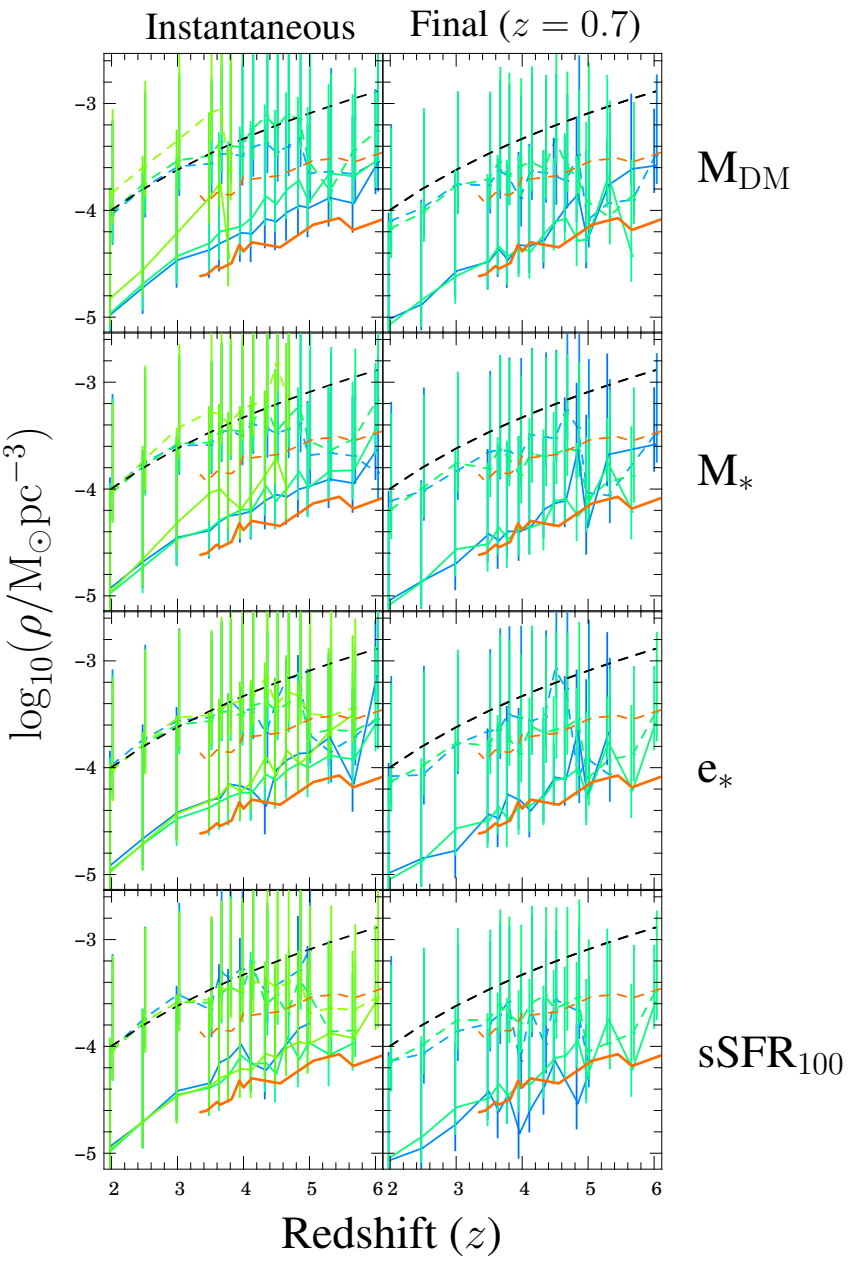

Figure 4.28: Evolution of the filament median central density with redshift, binned according to halo mass *top*, stellar mass *second from top*, galaxy formation efficiency in the *third row* and specific star formation rate at the *bottom* The *dashed* coloured lines represent DM and *solid* lines are gas. The NUT simulation is shown in *orange*. Lowest value properties are represented by the *blue* lines. The *left* column bins by the current instantaneous quantities and the *right* by final ($z = 0.7$) properties. One hundred times the mean density of the Universe is shown as the *dashed black* line. The gas density scales exactly as the expansion of the universe predicts. The DM departs from this scaling at high redshift due to resolution effects. The NUT filaments is seen to follow the same scaling. The central density is ordered from lowest to highest instantaneous galaxy and halo mass, but not for the other two properties. The ordering of the central densities is not seen when binned according to final properties.

rising with decreasing redshift, and the second is that the peak temperature stays roughly constant for $z < 5$. This suggests that at some point around $z = 2$ the filaments will cease to have cold cores and cold mode accretion from these filaments will end. The difference between the NUT (in orange) and NEW HORIZON (the other profiles) here is that the NUT starts off with no gap between the peak and filament central temperatures. Before this point the filament is unable to maintain a stable accretion shock, similar to the case that Birnboim and Dekel (2003) studied for a spherically symmetric distribution. The NEW HORIZON accretion shock is partially maintained by the addition of hot gas from SN feedback. It is unclear whether or not the gap between the peak and central temperatures will decline for the NUT from the plots, however, analytic considerations for the cooling and free fall timescales suggest that cooling will become less effective with time so this gap must eventually close.

In the left column of Fig. 4.29 the temperature profiles are binned according to the instantaneous galaxy properties. Like the densities before them (Fig. 4.28), mass binning, whether by DM or stellar mass, results in the same ordered temperature profiles, with hotter filaments typically connected to more massive halos and galaxies. The ordering breaks down for the galaxy formation efficiency with no clear trend visible, and no real separation between the median profiles. This is likely due to that fact that when binning by galaxy formation efficiency groups together objects of different masses. In Fig. 4.29 the low specific star formation rate median central temperature (blue) is systematically above the other bins, sometimes rising much further above. The reduction in specific star formation rate appears to be linked to the heating of the filament. The similarity between the other bins in this panel could in part be due to the bursty nature of the star formation rate. The galaxies can rapidly switch between bins if they undergo a starburst event when the properties are measured, while changes in the filament temperature occur on much slower time scales. It is important to note that the sSFR is averaged over the previous 100 Myr, but the star formation here could be using gas accreted much earlier.

Binning by the final halo mass (right column, Fig. 4.29) there is no difference between the two bins, as indicated by the two lines being extremely similar. If binning by the stellar mass instead, a small gap opens up below $z = 4$ for the peak filament temperature. The blue line here represents the low mass bin, suggesting that the final galaxy mass is suppressed by being grown in a hotter filament. A different subset of the galaxy population from those with high stellar masses are those with high formation efficiency. These galaxies typically have filaments which are colder at high redshift, as shown in the 3rd row, right column. Binning by specific star formation rate instead shows the reverse trend with high specific star formation rate galaxies typically having had hotter filaments at high redshift. The gap

between the two bins disappears around $z = 3.8$. By comparing the 3rd and 4th panel of the right hand side, it is apparent that these are two distinct populations, given that the thermal histories are the reverse of one another.
In both Figs. 4.28 and 4.29, in spite of the diversity in gas and DM densities and temperatures, the underlying scalings appear to be very similar for the two simulations, the NUT suite and NEW HORIZON simulation, irrespective of the way that the data is binned. This is of course ignoring the scaling of the peak temperature of the NUT simulation at early times. It would be interesting to investigate if this curve would rejoin the core temperature and whether the timing of this event is significantly different to that of the NEW HORIZON simulation. The scalings of these density and temperature parameters are highly suggestive of an underlying universality to the scaling of the filament profiles. This is also likely far more robust (up to the resolution effects seen at early times in these two figures) than the exact shape of the filament profiles. Whether the baryons continue to obey the same density scaling after $z = 2$ remains to be seen.

4.4 Confinement of Gas Filaments

In this section I briefly retest a theoretical underpinning of the filament profile suggested in Chapter 3, Eq. 3.7 allows the index of the gas filament to be modified. The analytic profile (Eq. 3.7) is obtained by assuming that the ratio of the velocity dispersion to sound speed is fixed, but not necessarily unity, with the filament index $n = (\sigma/c_s)^2$. While the velocity dispersion stays nearly constant (Fig. 4.21), the gas temperature (Fig. 4.25) increases, and thereby the sound speed. The evolution in n causes the slope of the profile to become shallower. Physically, this is the result of the gas, initially trapped in the DM potential well of the filament, becoming less trapped as it heated. While the DM velocity dispersion cannot be reliably estimated for NEW HORIZON , it is still possible to fit the resultant profiles. The gas filament index is separated into two important regimes by a critical index, $n_{\rm crit}$. If the gas filament density profile is integrated to give the total mass of the filament, then for the supercritical regime $n > 0.5$, as the radius approaches infinity the filament has a finite mass. At or below this index, in the subcritical regime, the mass increases without bound as radius increases. These two regimes correspond to a confined gas filament, and one which is not trapped by the gravitational potential of its DM counterpart and clearly more susceptible to feedback, photoevaporation and disruption. Fig. 4.30 shows the distribution of the index over all filaments from $z = 6$ to $z = 2$, regardless of the properties of the galaxies they connect.

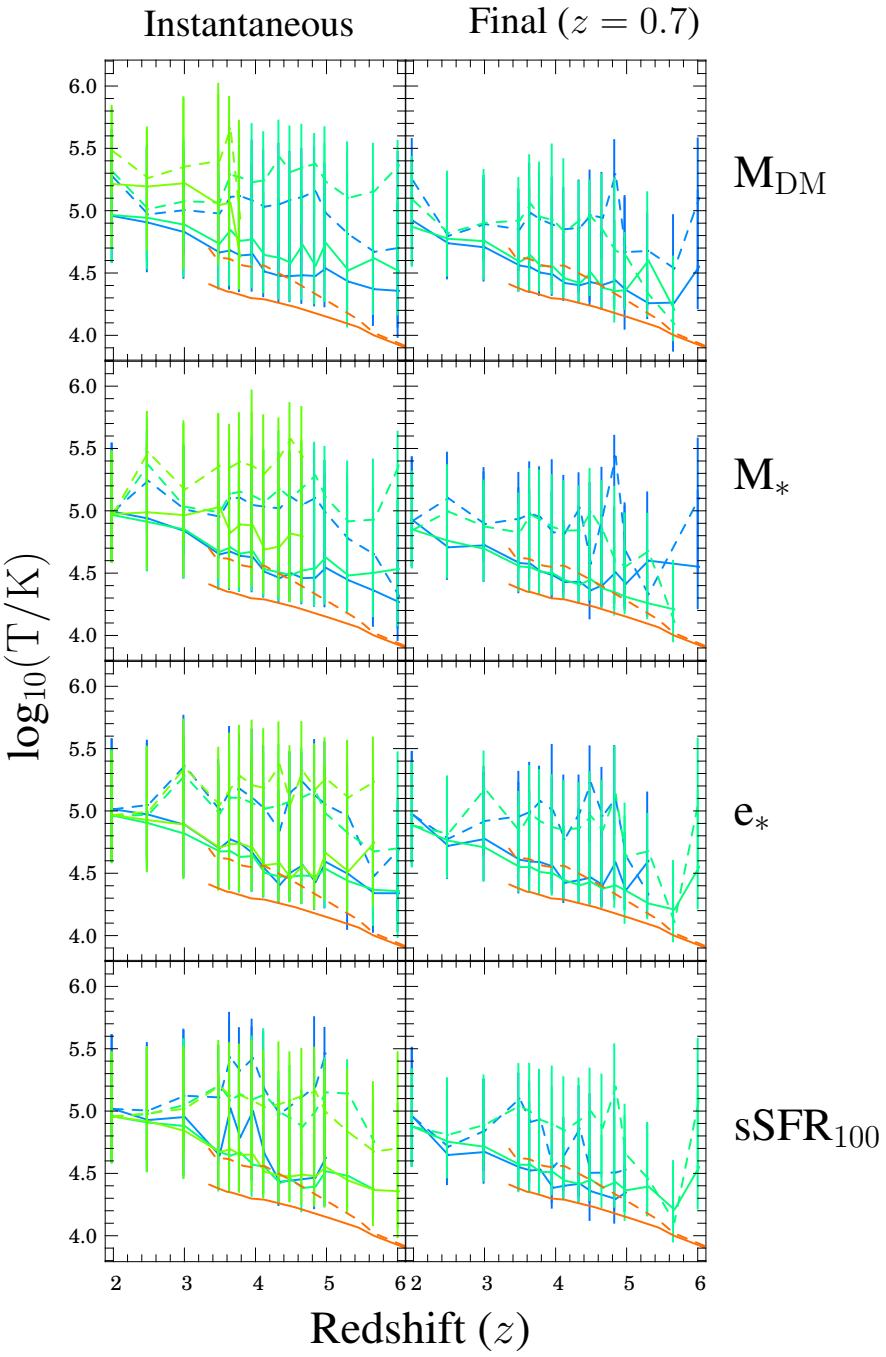

Figure 4.29: Evolution of the filament median temperature with redshift, binned according to halo mass *top*, stellar mass *second from top*, galaxy formation efficiency in the *third row* and specific star formation rate at the *bottom* The *dashed* coloured lines represent the peak temperature and *solid* lines are central gas temperatures. The NUT simulation is shown in *orange*. Lowest value properties are represented by the *blue* lines. The *left* column bins by the current instantaneous quantities and the *right* by final ($z = 0.7$) properties. The core temperature rises faster than the peak temperature, appearing to cross around $z = 2$. This is the point at which the filaments start to evaporate. Filaments remain well-behaved as in Fig. 4.28, though additionally this persists even when binning according to the final ($z = 0.7$) efficiency and sSFR.

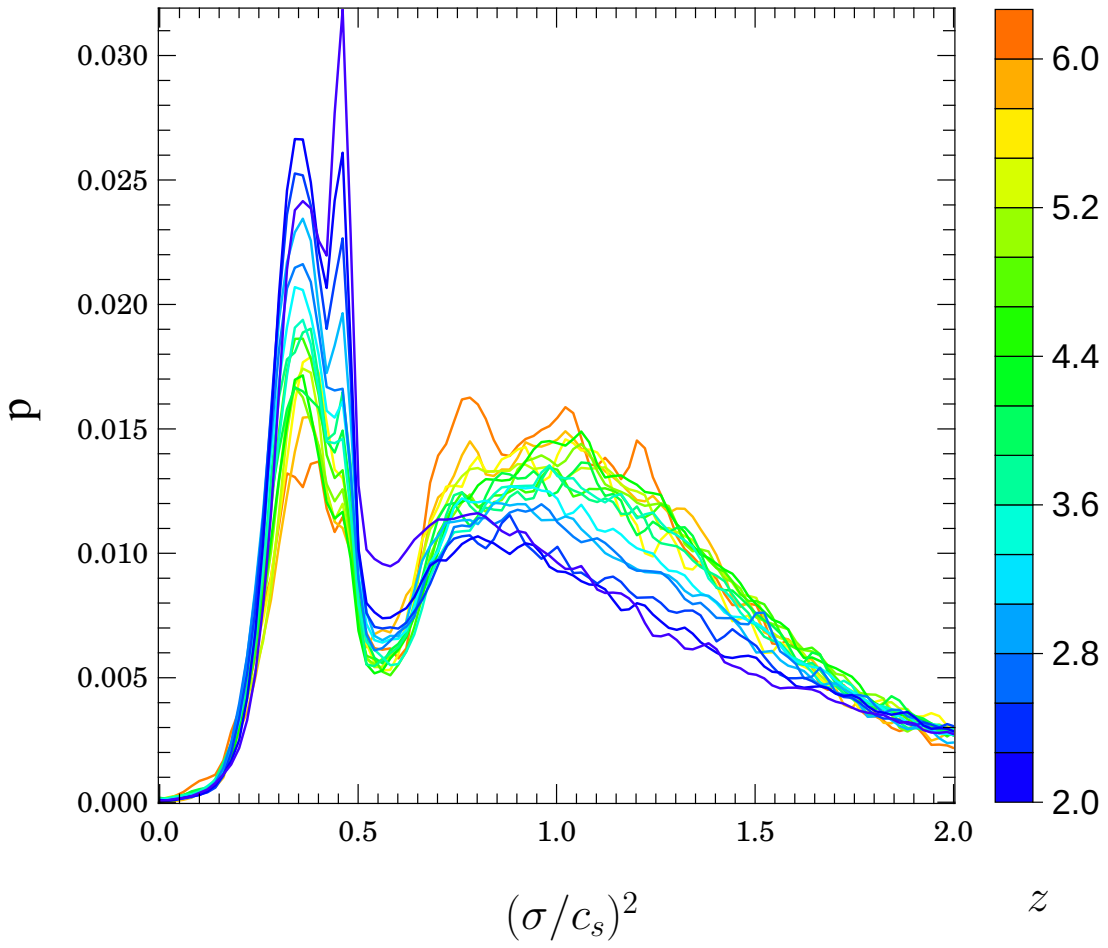

Figure 4.30: Histogram of the index returned by using the modified profile of Eq. 3.7. The distribution is clearly bimodal, initially starting with profiles which are 'normal', or indices close to 1, and evolving towards the critical index of 0.5.

Immediately it is apparent that the population is bimodal, with a population peaking around 1, for confined filaments which justifies my use of the profile with $n = 1$ over the course of the thesis, and a second population with a gas filament index around $n = 0.5$. As the simulation progresses there is an evolution from a mostly supercritical filament population to a mostly critical one. The distribution is sharply peaked at $n = 0.5$, with numbers rapidly dropping for even slightly lower or higher values. Most of the gas filaments have the bare maximal internal energy required to be confined, and thus cannot develop lower indices than this. Also within the supercritical regime there is a trend towards the gas filaments lowering their index, which is also suggestive of them being heated faster than the DM potential well which confines their growth. Of the two competing effects here, the growth of DM filaments on the one hand and increased heating of the gas filaments on the other, the latter wins.

4.5 Comparing with the NUT suite

I now evaluate whether the filaments studied in the NEW HORIZON simulation are comparable to those of the NUT . The counterpart of Fig 3.12 for the NUT is Fig. 4.31, showing the evolution of both the truncation radius for the DM and core radii for the gas and DM. There are some obvious differences between the NUT and NEW HORIZON . First of all, for $4 < z < 6$ the NUT DM filaments appear to have smaller core and truncation radii. Secondly, in NEW HORIZON the core radius for the gas is not only considerably larger than that of the NUT , but also appears to scale differently below $z = 4$. Note that the core radius was found with the fully general filament profile of Eq. 3.7 in addition to the wall profile. Below $z = 4$ the filaments are switching to a shallower profile, as indicated by Fig. 4.30. It is possible that the difference in scaling in both cases are due to resolution effects, but in different ways, with DM particularly affected by mass resolution, and the gas affected by spatial resolution. The NUT has 64 times better DM mass resolution and twice the spatial resolution within filaments (comparing Figs. 3.2 and 4.6), resulting in a factor 8 times fewer particles per cell in NEW HORIZON , making the Poisson noise nearly 3 times as significant. In Chapter 3 I concluded that a resolution of 2 kpc at $z = 4$ was sufficient to resolve the filaments, however, this was based on extracting the same simulation at different resolutions, rather than rerunning the simulation at different resolutions. The NEW HORIZON filaments were simulated with a lower spatial resolution, (~ 2.5 kpc for NEW HORIZON and ~ 1.2 kpc for the NUT), and as a result have a greater softening length in the local gravitational potential. This could be responsible for the larger DM filaments in NEW HORIZON . The gravitational potential of these filaments are therefore

also less able to hold on to gas, making the gas filaments considerably larger. Chabanier et al. (2020) reran the HORIZON-AGN simulation with kpc resolution in the filaments and find significantly more compact galaxies than in HORIZON-AGN which has a less aggressive refinement criterion. In spite of the resolution affecting filament core radii, the NEW HORIZON DM truncation radius appear larger but only slightly (within the errors of most redshifts of the NUT simulation), and they scale exactly like the NUT DM truncation radii. This is tentative evidence for a universal scaling for the truncation radii of filaments. Due to the limitation of the NEW HORIZON filament network, we can only conclude this for objects with $10^{10} < \mathrm{M_{DM}}/\mathrm{M_{\odot}} < 10^{12.6}$. This represents less than an order of magnitude in virial radius, so it is difficult to draw definitive conclusions about how the filament size evolves in comparison to the size of the halos and galaxies embedded within them.

The NUT feedback run produces gas filaments which do not have a turn over at large radii for all redshifts in either their temperature or vorticity, making it difficult to define a truncation radius. A direct comparison of filament profiles for the no feedback NUT and NEW HORIZON is shown in Fig. 4.32. Interestingly, despite having identical star formation recipes and feedback prescriptions as the NUT feedback run, the NEW HORIZON temperature profiles still have a definite peak despite the feedback. This is likely a resolution issue again. The NUT is capable of producing more stars (of lower mass), which are able to continuously inject energy into the IGM around them. Crucially this happens all along the filament as lower mass objects are able to make a contribution, rather than just around large objects, compare Fig. 3.3 ($z = 4$), right column with Fig.4.1 ($z = 6$). This does break down at later times however, see Fig. 4.2 ($z = 0.7$), where the feedback is able to extend much further into the environment around the galaxy. The NEW HORIZON filaments are seen to be expanded compared to the NUT , with the higher mass halos hosted by fractionally larger filaments driven by the feedback in the embedded galaxies.

Turning to the DM velocity dispersion in Fig. 4.32 it quickly becomes apparent that there are significant differences between the NUT and NEW HORIZON filaments. While the central dispersions are very similar, the profiles for NEW HORIZON do not decay as steeply. This is most likely due to the 2$^{\mathrm{nd}}$ order nature of the velocity dispersion being more sensitive to the poorer mass resolution. The median number of DM particles per cell in NEW HORIZON is around 20 in the filament centre, giving rise to a 20% Poisson error. As the density drops over an order of magnitude there are areas that have over 100% Poisson errors. For the other profiles this can be made more reliable by using annular averaging to compute the profiles in combination with the DTFE (Delaunay Tessellation Field Estimator) to smoothly estimate the field value from sparse data, but the velocity dispersion is constructed from the velocity field by subtracting the local velocity from each

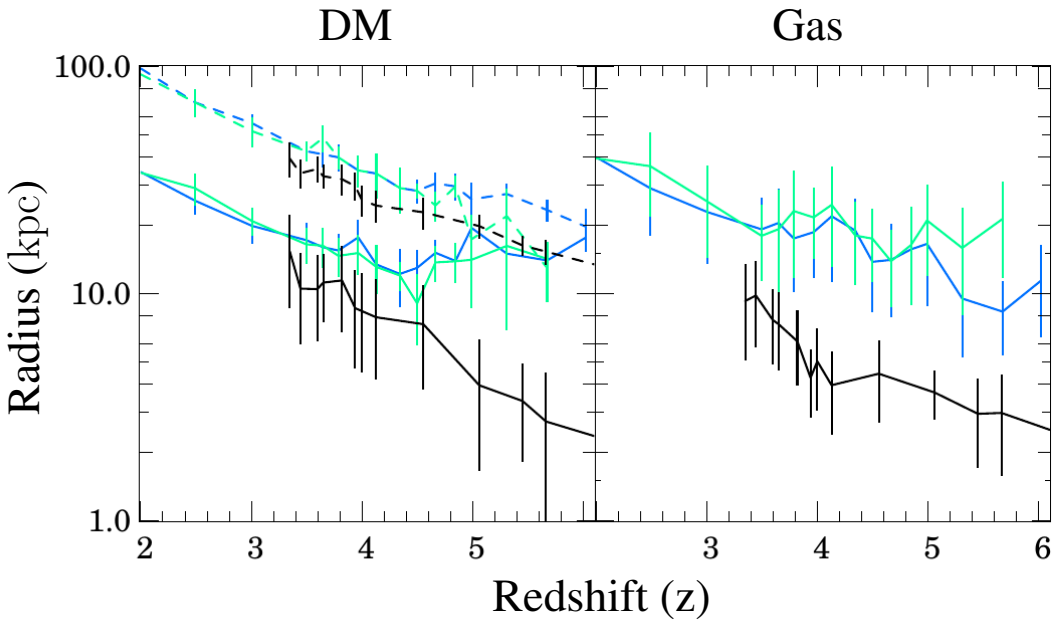

Figure 4.31: Evolution of the filament median DM (*left*) and gas (*right*) core (*solid*) radius (using the fully generalised filament profile of Eq. 3.7) and vorticity derived truncation radius for the DM (*dashed*) across cosmic time. The (*coloured*) lines are NEW HORIZON binned according to the final ($z = 0.7$) halo mass according to Table 4.3, with the low mass bin in *blue* and higher mass bin *cyan*. The NUT no-feedback run, whose halo mass sits between the two bins, is overplotted in *black*. The feedback run is not shown as there is little difference in the core and truncation radii derived from the two simulations. Error bars show 1 σ deviations from the median. The truncation radii for the DM scale identically to those of the NUT suite, while the core radius appears to scale very similarly after $z = 4.5$, before which resolution effects cause the profile fitting to overestimate the filament size. The core radius of the gas appears to scale slower with redshift than the NUT suite, and is also significantly larger.

of the particles, so does not get the benefit of the annular averaging, and has fewer than one particle per cell. In the ΛCDM regime DM particles initially start with extremely small thermal velocities. As a result neighbouring particles experience similar potentials. Only when structures collapse, such as the formation of a wall, filament, or virialisation in a halo do particles undergo shell-crossing. This is how dispersion is generated in DM. In Fig. 4.21 the $z = 6$ when the filament potentials are relatively small, the velocity dispersion profiles show similar exponential decline with radius as the NUT DM velocity dispersion profiles. As redshift decreases however the dispersion declines much less rapidly with radius. In order to prevent resolution effects from dominating, the DM particle mass would need to be 30 times lower to ensure there is always more than one particle per cell at the same spatial resolution. I am as a result of this unable to use the velocity dispersion to reliably estimate the truncation radius in NEW HORIZON , however, the vorticity is less affected.

In the top row of Fig. 4.32 I compare the NUT density filament profiles with those of NEW HORIZON at $z = 4$. The density profiles are almost identical, with the exception that halos with higher masses in NEW HORIZON have higher density DM filaments. The NEW HORIZON gas filaments are slightly higher in density than those in the NUT , though they are within the errors of the NUT simulation. There is no significant difference in density between the two mass bins. This is also observed in Fig. 4.19. Despite differences in the DM potential and gas temperatures, the gas density profiles appear to conspire to form the same profile. The profiles are fitted using Eq. 3.9. Taken together with the other density profile plots, filaments connecting halos in the mass range $10^{10} < \mathrm{M/M_{\odot}} < 10^{12.6}$ show a universal profile, of the form of Eq. 3.9. This rather narrow range of values are constrained at both ends. For the moment, the filamentary network itself is defined using the mass threshold, M_{thresh}, though in future the analysis could be extended to lower mass galaxies without changing the filaments. Secondly, at the high mass end the simulation is constrained by the non-linear mass scale. At later times in the simulation than those considered in the simulation (i.e. after $z = 2$) ever larger structures have time to form. This will be considered in future.

4.6 Conclusions

The analysis performed in Chapter 3 focused on a filament feeding one galaxy at high resolution. I applied the techniques developed in Chapter 3 to the NEW HORIZON simulation (Dubois et al., 2020), a cosmological zoom of a region extracted from HORIZON-AGN (Dubois et al., 2014a) which has have tens of galaxies of a similar stellar mass to the one we studied in Chapter 3, along with several more massive objects. NEW HORIZON also

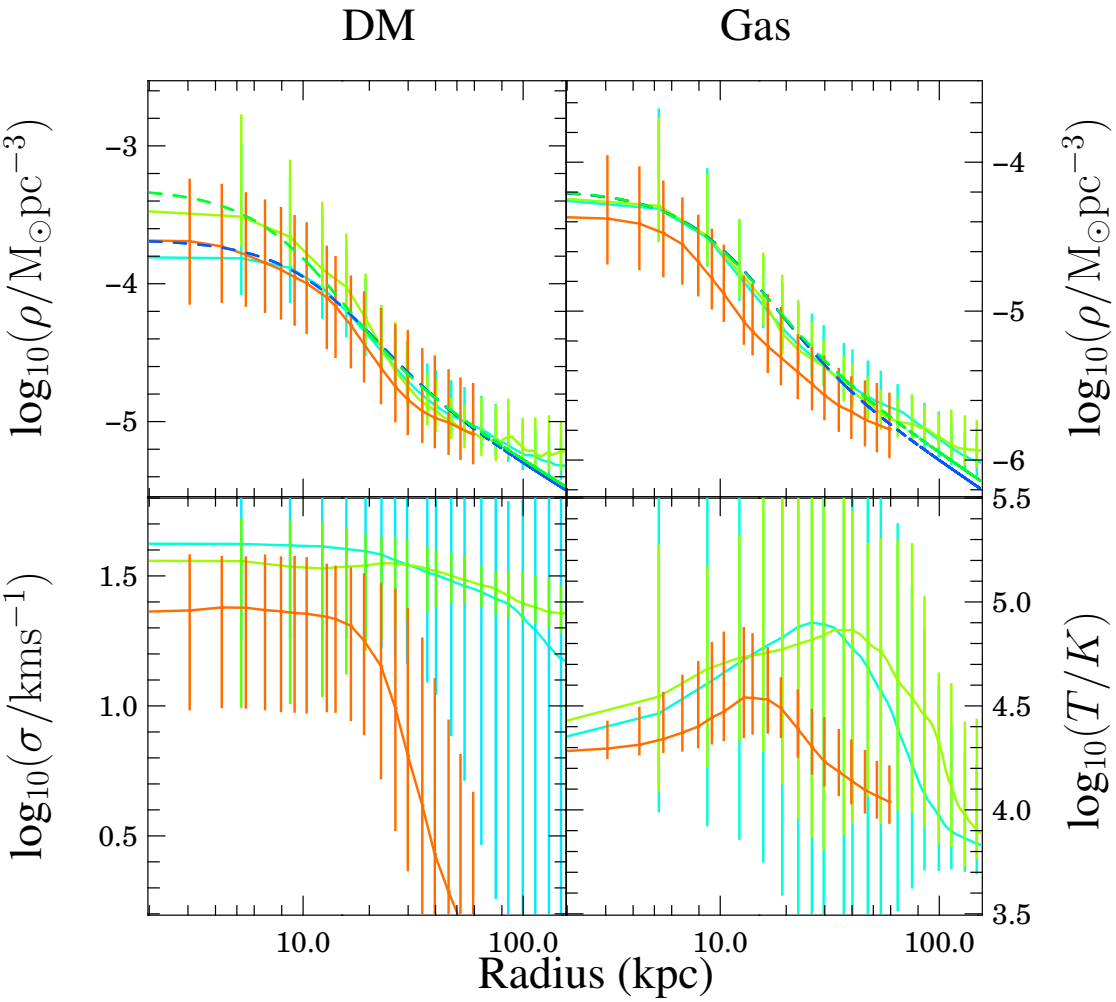

Figure 4.32: Comparison of the NUT no-feedback profiles with NEW HORIZON profiles at $z = 4$ for low mass halos (*blue*) and high mass halos (*green*) as defined in Table 4.1. The *left* column is for dark matter, while the *right* is gas. The rows show density and temperature and velocity dispersion for gas and DM respectively. Overplotted on the NEW HORIZON density profiles are the analytic fits of Eq. 3.7 found in Chapter 3 in addition to the wall profile. These are in a shade darker than the fit they correspond to. In order to make a fair comparison to the NUT, the NEW HORIZON halos are binned according to their mass at $z = 0.7$. The error bars are 1 σ deviations from the median. Note how similar the profile shapes are for the median gas and DM density profiles are. The truncation radii of the NEW HORIZON are enhanced in the gas temperature profile, though this is to be expected since there is feedback in the simulation. In spite of this, the core filament temperature remains very similar. The dispersion profiles for NEW HORIZON are affected by relatively poor resolution (see text), resulting in the overestimate in the value at all radii.

features AGN feedback and has reached $z = 0.25$, which also allows to comprehensively extend the redshift range of the analysis, although in this thesis I only analyse filaments down to $z = 0.7$. Such a simulation will thus permit the extraction of a large sample of filaments from which to derive statistically meaningful quantities. Building on the work of Chapter 3 a sample of filaments were constructed connecting halos of masses greater than $M_{\rm thresh}$. The main results were:

- Mean filament connectivity is approximately 1.5 for low mass halos, rising to 3 for halos with masses greater than $10^{11.4}\mathrm{M}_{\odot}$.
- Halos which reside within the filament network typically have a higher galaxy formation efficiency.
- Once a halo is accreted by a filament it is a rapidly trapped, making it easy to distinguish between two distinct populations: inside and outside the filament truncation radius.
- Exact distance to a filament and local filament density have little effect on instantaneous dark matter halo mass, stellar mass, and specific star formation rate. Galaxy formation efficiency shows a slight enhancement when the galaxy is inside the filament.
- Filaments connected to higher mass galaxies and halos are typically fed by denser and hotter gas and DM filaments.
- The median density profiles of filaments in NEW HORIZON are compatible with the analytic profile fit to the filaments in the NUT simulation, regardless of redshift, or the properties of the galaxies the filaments connect to, suggesting a universal profile.
- The filament truncation radius for the dark matter scales like the NUT filaments as a function of redshift.
- Filament densities do not correlate well with the final ($z = 0.7$) galactic properties, suggesting that other processes are at least as important in shaping the low redshift properties of galaxies. This result holds independently of the chosen final redshift value.
- The central gas filament temperature rises faster than the peak filament temperature, which suggests that cold accretion from the filament steeply declines below $z = 2$.

- In order to study the DM filament velocity dispersion it is necessary to use a higher mass resolution. More specifically extracting the filaments at a spatial resolution of 8 ckpc. The mass resolution must be at least $4 \times 10^4 \mathrm{M}_\odot$ to ensure that there is at least one particle per cell in the outer filament.

- The filaments exhibit a bimodal distribution for the index $n = (\sigma/c_s)^2$ appearing in the more general analytic profile for the filament (Eq. 3.7), corresponding to gas being confined or not by the filament. The filament in general evolves away from the confined state.

Chapter 5

The Impact of Reionisation on Filamentary Accretion

5.1 Introduction

In this chapter the effect of reionisation on filaments and their associated galaxies will be explored. Reionisation is the last phase transition experienced by the Universe as a whole. At reionisation the gas in the Universe transitions from being composed mostly of atomic hydrogen, which is opaque to photons above 13.6eV, to ionised hydrogen, which is transparent to these photons. Due to the hierarchical nature of ΛCDM, larger halos are built up from the mergers of smaller halos. However galaxies residing within the lowest mass halos are unlikely to be the products of mergers even though they often exhibit older and metal-poor populations of stars. For halos with virial temperatures below the atomic cooling limit the presence of pristine stars are expected as these halos are incapable of accreting gas from the IGM once it has been heated by reionisation to 20-30 kK (Miralda-Escudé and Rees, 1994; McQuinn, 2012), a higher temperature than their virial temperature, thereby suppressing star formation (Efstathiou, 1992; Gnedin, 2000; Hoeft et al., 2006; Okamoto et al., 2008; Noh and McQuinn, 2014). This state of affairs continues well into the dwarf regime, with virial masses $10^8 M_\odot$.

As it stands, ΛCDM has a number of problems:

- The core-cusp problem (Moore, 1994; Oh et al., 2015), is a tension between pure DM simulations and galaxy rotation curve observations. Observations suggest inner rotation curve profiles have a 'core', with densities approaching a finite value, while simulations predict it should be a cusp.

- The missing dwarf problem (Mateo, 1998; Moore et al., 1999; Klypin et al., 1999) is a tension between the number of observed and predicted dwarf galaxies. The tension

arises from two effects: the ΛCDM mass function is very steep at lower masses, and dwarf galaxies are extremely faint and difficult to detect, even at close range. Indeed, satellites of the Milky Way can be fainter than the night sky itself. More recent surveys, e.g. Müller and Jerjen (2020) still count fewer satellite galaxies than expected from simulations.

- The 'too big to fail' problem (Boylan-Kolchin et al., 2011), highlights that the Milky Way has too few large detectable satellites. There should be approximately 6 objects with circular velocities greater than $30\ \mathrm{kms}^{-1}$, when none are detected. This either means that these satellites do not exist or star formation has been suppressed in them.

All of these problems can be alleviated by the suppression of gas inflow onto galaxies or ejection of gas directly from galaxies, flattening their stellar and dark matter profiles, thereby reducing their stellar mass and hence their detectability. Reionisation is known to have an impact on the mass accretion of low mass galaxies, e.g. Iliev et al. (2007) found that reionisation is self-regulating in that as reionisation advanced less gas was available for star formation and thus the progress of reionisation was slowed.

One of the big questions surrounding reionisation is what causes it (D'Aloisio et al., 2015; Chardin et al., 2017; Parsa et al., 2018). Some potential sources are quasars, low mass dwarf galaxies, or larger, highly star forming galaxies. A focus of galaxy simulations has been to compute the escape fraction, f_{esc}, from galaxies. Most of the UV photons produced by the galaxy do not escape the relatively dense gas of the galaxy. Indeed, the photons may even struggle to escape the stellar birth clouds themselves, given that the bulk of UV photons are produced by short-lived giant stars. Simulating reionisation is an inherently multiscale problem, requiring both high resolution of the ISM around the sources of the radiation, and of the larger scale structure of the Universe itself. The value obtained for f_{esc} can have extreme implications for the types of objects that can trigger reionisation, its onset and duration. Simulations indicate that it is predominately galaxies that drive reionisation rather than quasars (Trebitsch et al., 2020). This is in part due to the steep decline in the quasar number density at high redshift(e.g. Kulkarni et al., 2019).

Most of the gas accreted by a galaxy at high redshift arrives via the cold mode in filaments (Kereš et al., 2005). It is thus important to understand the influence of reionisation on this gas and to assess its importance relative to shock heating. Ocvirk et al. (2016b) studied the gas of a single filament and found it to be shock heated to 10^5 K, a factor of 10 higher than that caused by reionisation (Haardt and Madau, 2012; Bolton et al., 2012; Puchwein et al., 2018).

In this chapter, I will use the SPHINX suite of cosmological radiation hydrodynamics simulations (Rosdahl et al., 2018) to study the effect of reionisation on filaments and dwarf galaxy formation. This work led to a publication (Katz et al., 2019). In Section 5.2 I will describe the SPHINX simulation set up and analysis routines. In section 5.3 I compare the impact of reionisation on cosmic filaments and the galaxies that they feed. The chapter concludes in section 5.4.

5.2 Methods

5.2.1 The SPHINX simulation suite

The SPHINX suite are a series of simulations studying reionisation (Rosdahl et al., 2018) using RAMSES -RT (Rosdahl et al., 2013). The challenge faced by cosmological simulation is to have a volume large enough volume to overcome cosmic variance while having high enough resolution to capture small scale physics. In order to minimise the effect of cosmic variance, Iliev et al. (2014) suggests a cube of sidelength 200 cMpc. This is typically not even achieved by hydrodynamic simulations which do not model radiative transfer. For example HORIZON-AGN, ILLUSTRIS TNG and SIMBA are all hydrodynamical simulations of cosmological volumes of only 100 cMpc on a side. Alongside a large box size, in order to resolve the ionising fronts of radiation, parsec resolution is required (Kimm and Cen, 2014; Xu et al., 2016). Many radiative transfer simulations have attempted to either capture the large scales while barely resolving galaxies e.g. Ocvirk et al. (2016a, 2018), or to capture the small scales with radiative transfer zoom simulations, which give the detailed reionisation history of a small group of galaxies without capturing the large scale changes. In either case reionisation is not captured self-consistently.

5.2.2 Choosing Initial Conditions

In order to obtain a set of 'average' initial conditions and minimise the effect of cosmic variance, 60 pure DM simulations, each with 256^3 particles in a box of sidelength 5 cMpc were run using the initial conditions from MUSIC (Hahn and Abel, 2013). Cosmological parameters were chosen to be consistent with Planck Collaboration et al. (2016): $\Omega_\Lambda = 0.6825$, $\Omega_m = 0.3175$, $\Omega_b = 0.049$, $h = H_0/(100 kms^{-1}Mpc^{-1}) = 0.6711$ and $\sigma_8 = 0.83$. Each realisation had a random seed. The initial conditions which generated the most average mass function amongst this set of simulations was chosen as the initial conditions for the SPHINX simulation suite (in practice the $M_{\rm vir}^{1.5}$ was used as this was found to correlate more strongly with luminosity). This volume should be more representative of the Universe

as a whole despite being far below the homogeneity scale with a cubic volume of only 5 cMpc on a side. The absence of extremely large but rare galaxies could have a large impact on the local reionisation history and as a result the findings from this chapter may not apply in such environments.

5.2.3 Numerical Set Up

Here I describe the details of the RAMSES-RT implementation used for the SPHINX . The hydrodynamics is solved with the HLLC Riemann solver (Toro et al., 1994). An adiabatic index $\gamma = 5/3$ is used which is appropriate for an ideal monatomic gas. A first order method is employed for radiation advection using M1 closure for the Eddington tensor (Levermore, 1984) and the Global-Lax-Friedrich flux function for constructing the inter-cell radiation field. Cooling is calculated by interpolating the cooling tables of CLOUDY (Ferland et al., 1998) for temperatures above 10^4 K. Hydrogen and helium mass fractions are set to X = 0.76 and Y =0.24, while the gas is given an initial metallicity of $Z_{\rm init} = 6.4\times10^{-6} = 3.2\times10^{-4} Z_\odot$ (assuming a Solar metal mass fraction of $Z_\odot = 0.02$ throughout this work). While unphysical, this small amount of metals is added to allow the gas to cool below 10^4 K, using the rates computed by Rosen and Bregman (1995). The metallicity floor is a way to compensate for the fact that the simulation does not have sufficient resolution to capture the formation of molecular hydrogen. With the metallicity floor we ensure that the first stars form at redshift $z \sim 15$. To minimise the computational expense of a high resolution radiative transfer simulation, the variable speed of light approximation (VSLA) is used (Katz et al., 2017). AGN are expected to become relevant for reionisation in galaxies larger than the ones studied in this set of simulations Trebitsch et al. (2017); Mitchell et al. (2018). As a result AGN physics is not included in these runs, though we hope to include its effects in later SPHINX simulations.

The two simulations considered in this chapter are identical in initial conditions and physical models except that the radiation field is disabled in the non-reionised run (NOIO run) and enabled in the REIO run. This allows the direct comparison of the effect of radiation on the evolution of the filaments and the galaxies that reside within them.

5.2.4 Structure Extraction

The filaments of the SPHINX simulations were extracted using the dark matter particle distribution, with persistences from 5σ to 10σ, and every half σ in between. The 5σ skeleton is produced by subtracting the 5.5σ skeleton, leaving only segments with persistences between 5σ and 5.5σ. As discussed in previous chapters, this is a proxy for how well defined a

filament is, with lower persistences generally corresponding to lower mass filaments. Due to the impact of reionisation on the gas filaments it is important that the DM skeleton is used in order to have a comparable set of filaments for the two simulations. Any segments within a halo were removed by ensuring that the gas density of the simulation cell it resides in has a density below 130 times the mean density. Filament profiles were extracted as described in Chapter 3 on 1024^3 cell cubes out to 90 cells away in the radial direction perpendicular to the length of the filament.

Halos were identified using the ADAPTAHOP algorithm, with a minimum number of DM particles of 300, giving a minimum halo mass of $6.4 \times 10^6 \mathrm{M}_\odot h^{-1}$. Only isolated halos (more than 6 virial radii from the nearest neighbour, following Okamoto et al. (2008)) are considered. Stellar and baryonic masses are attributed by counting all material within a halo's virial radius, with the centre defined as the most dense point within the halo. Gas inflow and outflow are measured in a spherical shell at the virial radius with thickness $\pm 5\%$ of R_{vir}.

5.3 Results

5.3.1 Global Effects of Reionisation

We now seek to understand the impact of reionisation on the properties of dwarf galaxies embedded in cosmic filaments. From a visual inspection of the two simulations it is already apparent from Fig. 5.1 that the lowest mass filaments at $z = 6$ are drastically affected by the radiation field. With reionisation enabled (right panel) lower mass filaments are no longer visible, and even the larger, more well defined filaments appear to be more radially extended. In both simulations (NOIO run , REIO run) the gas is shock heated upon accretion and the gas is allowed to cool. The difference is that the REIO run is continually heated by the external radiation field and so cooling of the filament gas is less efficient, maintaining and growing the size of the accretion shock. It is important to note that in both simulations the dark matter itself is almost scale free, with the index of the power spectrum $n_s = 0.96$ Planck Collaboration et al. (2018). This means that zooming in on any particular structure will statistically look identical to any structure at larger scales. This is exactly what is seen in Fig. 5.1, with filaments splitting into progressively smaller filamentary structures. The scale invariance is broken by the gas once the local sound speed becomes greater than $\sqrt{2}\sigma$ as discussed in Chapters 3 and 4.

Comparing the left (NOIO run) panel with the middle (DM) panel of Fig. 5.1, the baryons can be seen to closely trace the dark matter density distribution. The intergalactic gas in this version of the simulation cools with the adiabatic expansion of the Universe

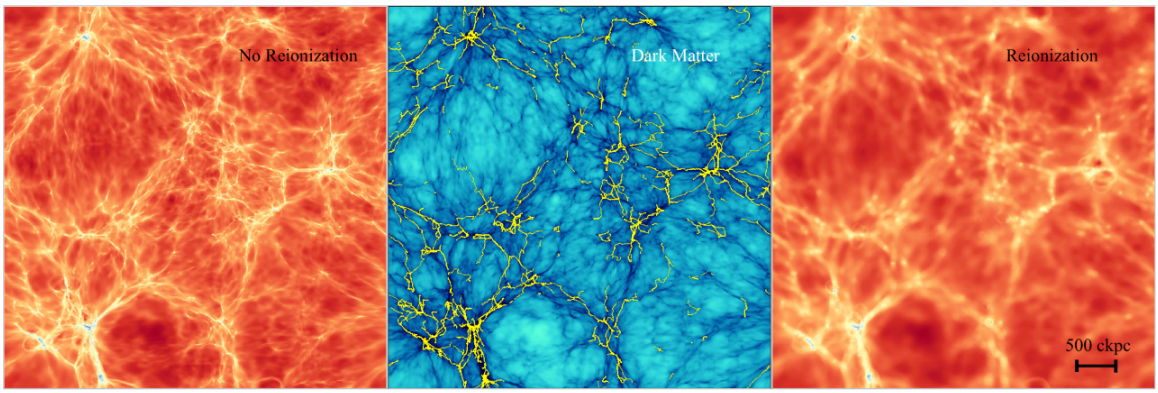

Figure 5.1: The effect of reionisation on the filaments of the Universe *left* panel shows the projection of the entire SPHINX volume without radiative transfer at $z = 6$. On the *right* the same volume is shown with radiative transfer enabled. The small scale filaments are visibly washed out in this view of the simulation. In the *centre* the corresponding DM field is shown, overplotted with the filaments in *yellow* that have persistence $\sigma > 6$ found by DISPERSE . The slice is 500 ckpc in all panels. The gas filaments maintain the scale invariance seen in the DM when radiative transfer is turned off. In the *right* panel all filaments are affected, and are puffed up by comparison. The lowest mass filaments are virtually erased.

and hence has very little pressure support to prevent collapse onto a filament. In fact, the theory put forward in Chapter 3 (Section 3.4.1) suggests that these filaments should be significantly narrower than the DM filaments due to the reduced sound speed relative to velocity dispersion.

The *right* panel of Fig.5.1 shows the run with radiation(REIO run) and thus a very different state for the IGM. It is already apparent that at $z = 6$ the number of gas filaments is far reduced compared to the non-reionised simulation. The increased heating from the radiation fields of the young galaxies allows the gas to resist the potentials of smaller DM filaments, completely washing out their structure in this projected view, while even the highest mass filaments, which generally connect higher mass nodes of the cosmic web, show the same pattern of widening. Any galaxy residing within the cosmic web should be strongly affected by the suppression of its gas supply from cold mode accretion. Further, this affect should be amplified for galaxies residing in lower mass filaments. This impact will be explored in the next sections.

5.3.2 Effect of Reionisation on Filament Profiles

Median filament profiles for the NOIO and REIO runs are shown in Fig. 5.2. Before the onset of reionisation at $z = 9$ the two simulations are nearly identical, diverging as

the simulations progress. In the case of the underlying DM distribution the effect is minimal showing that the large scale structure of the Universe is not significantly impacted by reionisation. However, turning to the baryonic component, the central density is suppressed. This is made more obvious by looking at the ratio of the baryonic density to the DM. For the non-reionised simulation the ratio stays close to the universal fraction, particularly at scales above 10 kpc. There is some deviation from the universal fraction at small scales however, and the sign of this deviation depends on the persistence, or mass of the filament. At high masses this is likely due to the density enhancement reducing the cooling time and hence pressure support. Lower mass filaments still have some pressure support, as they cool adiabatically after decoupling from the CMB, slightly reducing the baryonic density with respect to the DM field.

In the REIO run however, this effect is amplified with a significant reduction below the universal baryon fraction. The central suppression is greatest in the lowest persistence filaments at $7 \leq z \leq 9$, but by $z = 6$ there is no obvious trend with persistence. This suggests that the lower mass filaments are ionised first. While matter is prevented from falling into the centre of a filament itself, it is still attracted to the filament, resulting in a density enhancement with respect to the DM at around 5kpc. Pressure from the heating of the gas prevents accretion into the filament core.

Turning to the ionisation fractions in rows 4 and 5 (the NOIO run is omitted) the filaments are seen to be ionised from the outside. The denser filament core is protected, to a certain extent, but cannot stop the conversion of HI into HII. Again the low persistence filaments are ionised before their larger mass counterparts. By $z = 6$ all filaments, regardless of persistence are fully ionised.

In order to identify how and where filaments are being impacted by reionisation the sample is classified according to the distance, d, of each filament segment from the nearest halo as follows:

- $d < 3r_v$ for "feeding" filaments
- $3r_v < d < 6r_v$, for "proximity" filaments
- $d > 6r_v$ for "isolated" filaments

Any bin which contains fewer than 20,000 segments was discarded to avoid the impact of small number statistics. Note that d is the shortest distance of the segment from a halo, not the distance along the filament. Measuring distance to the filament was used as this parameter is more relevant to the radiation flux experienced by the filament. The filament can partially shield itself from radiation emitted from a galaxy within the filament.

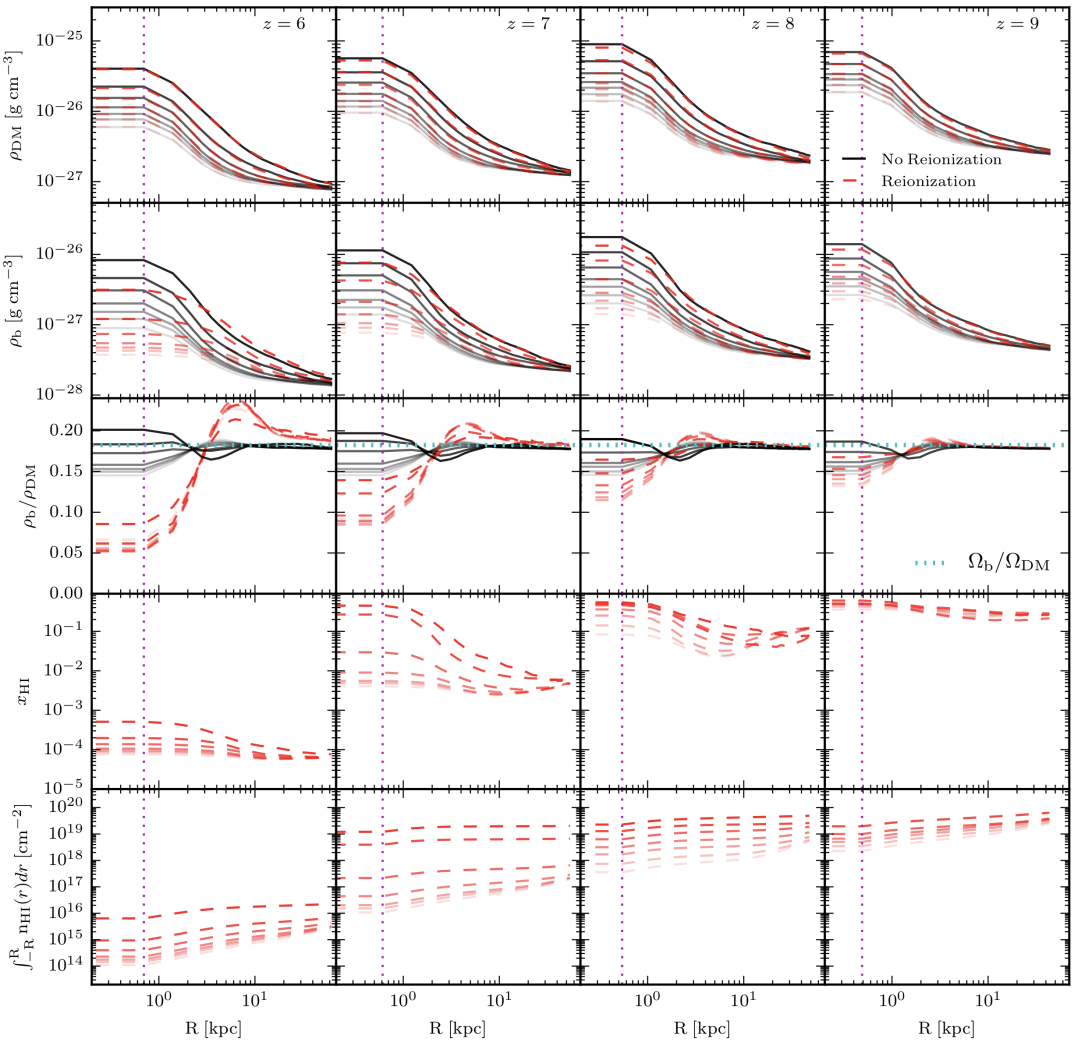

Figure 5.2: The median filament profiles for the two simulations, *red* is with reionisation, *black* is without, across cosmic time. The dashed *purple* line is the minimum resolution the filaments are extracted at. Each line represents a 0.5σ increase in persistence from faint to bold, starting at 5σ. The rows in descending order are DM density, baryonic density, baryon to DM ratio, HI fraction and HI column density. The DM reveals a scale invariant profile, which is also reflected in the gas in the absence of reionisation. Filaments can have their relative baryon content reduced by as much as 80%, with the lowest density filaments being affected first.

As found in Chapter 3, Fig. 3.13 shows that the filaments closer to the galaxies have higher densities than those further away. Initially, before the onset of reionisation the filaments of different persistences have only a small variation in gas density. The variation in density seen in the $z = 9$ column of Fig. 5.2 is driven entirely by the distance to the halo. As reionisation progresses the profiles are separated by their persistence, as the deeper potentials of persistent filaments are more successful at containing the gas as they get heated and increase their cooling rate. It is also notable that the DM density profiles are rescaled versions of the same underlying profile, as suggested by the underlying scale invariant power spectrum of the Universe, and makes it easier to quantify deviations from this scale free behaviour in the gas.

Comparing the profiles of the two simulations in Fig. 5.3, the central density is seen to be reduced by 20% even before $z = 9$, due to the cooling of the IGM in NOIO run contracting the filaments. By $z = 6$ the core density of the isolated filaments are reduced by 80%. The separation of the filaments according to persistence is inverted with respect to previous plots, with more persistent structures undergoing more suppression. These denser structures are also more likely to house higher mass halos which are better able to ionise the filaments. The feeding filaments are in fact more suppressed than proximity filaments as a result of being closer to the source of the ionising radiation. This, in addition to the widening action of the radiative feedback should greatly impact the efficiency of accretion from the cold streams. The accretion shock has expanded from 2 kpc to 8 kpc from the far right, $z = 9$ panel of Fig. 5.3 to $z = 6$ on the far left. From the results of Chapter 3 concerning the scaling of the truncation radius, the truncation radius should be at 4 kpc by $z = 6$. This highlights the difference caused by inhomogeneous reionisation in the SPHINX simulation compared to the uniform UV background used in the NUT .

Since our interest in filamentary accretion fundamentally stems from their influence on galaxies themselves, the properties of the simulated halos are now explored in Fig. 5.4. For each halo, the outflow and inflow rates were calculated at the virial radius. The halos were binned according to virial mass with bins of width $\Delta \log_{10}(M_{\rm vir}/M_{\odot}) = 0.2$ for $20 \geq z \geq 6$. The greatest difference between the two simulations can be seen for halo masses below $10^8 M_{\odot}$. In the non-reionised case the accretion rate follows the scaling with mass described in Neistein et al. (2006); Dekel et al. (2009) $\dot{M} = M^{1.15}(1+z)^{2.25}$. At fixed mass, the inflow rate is reduced as the Universe expands and the mean density falls. For the reionised run this also occurs down to $z = 12$, but, as the simulation progresses, the lower mass halos have their accretion rates reduced by over an order of magnitude below the non-reionised run. We may attribute this reduction to the reduced efficiency of accretion onto filaments and onwards to the galaxies accreting from these cold streams as the lowest mass

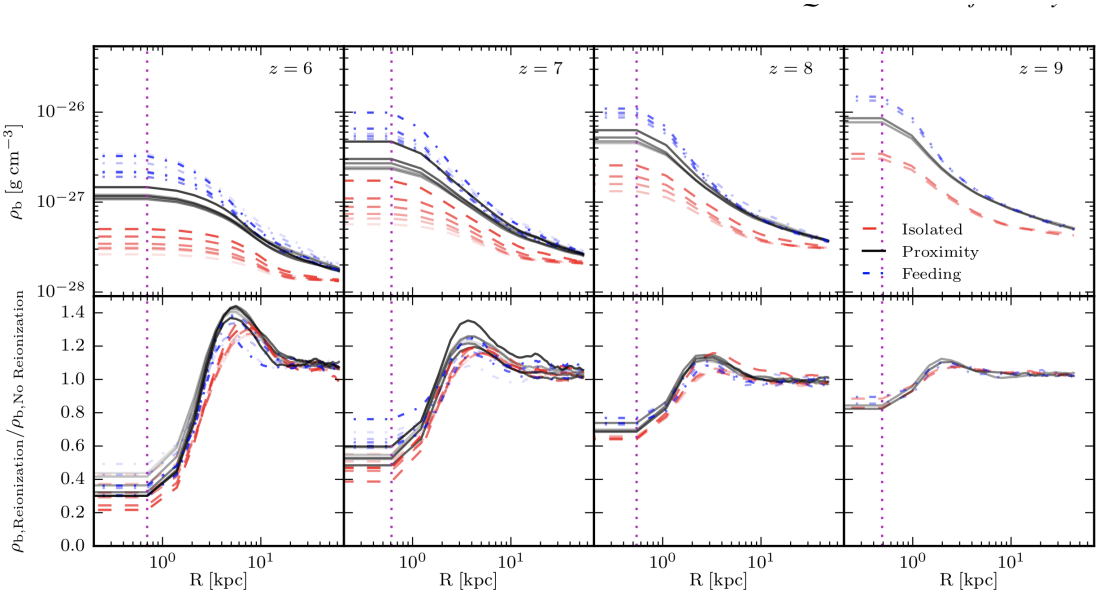

Figure 5.3: Filaments profiles binned according to distance to the nearest halo. Isolated, proximity and feeding filaments (as defined in the main text) are shown in *red*, *black* and *blue* for the reionised run. The lower row shows the ratio between the baryonic profiles of the two simulations. By the end of reionisation at $z = 6$, isolated filaments see a median reduction of 80% in the central density. Despite the fiercer radiation field experienced by the feeding filaments, their enhanced densities has a protective effect.

halos, residing in the low persistence filaments are most strongly affected, while the larger halos are virtually unaffected by the radiative action. Due to the non-linear nature of galaxy evolution the accretion rate is more diverse for the reionised version of the simulation.

Similarly, the distribution of outflowing gas rates also has this larger dispersion. At $z = 6$ the lowest mass halos in the reionisation run show increased outflow rates compared to the NOIO run . This seems to be due to the lowest mass galaxies forming stars later in the REIO run. In simulations stellar particles have a minimum mass, preventing star formation until sufficient mass has gathered in a single cell to trigger conversion into a star particle. The outflow is therefore driven entirely by radiation from external sources boiling gas off the young dwarf galaxies. The uptick in outflow rates at $z = 6$ is likely triggered by the first supernovae in these galaxies, but is not a physical effect. The final column shows the ratio of inflow to outflow rates. If this ratio is above 1, the galaxy grows. This is seen in all galaxies in the non-reionised run. However at $z = 10$ the first galaxies in the REIO run exit this regime. As the REIO run progresses more halos stop growing, up to $10^8 M_\odot$ by $z = 6$. Comparing with the NOIO run shown in the bottom row, no suppression of the inflow occurs, and as such no quenching ever occurs.

The inflow and outflow rates as well as the evolution of the galaxies is dependant on

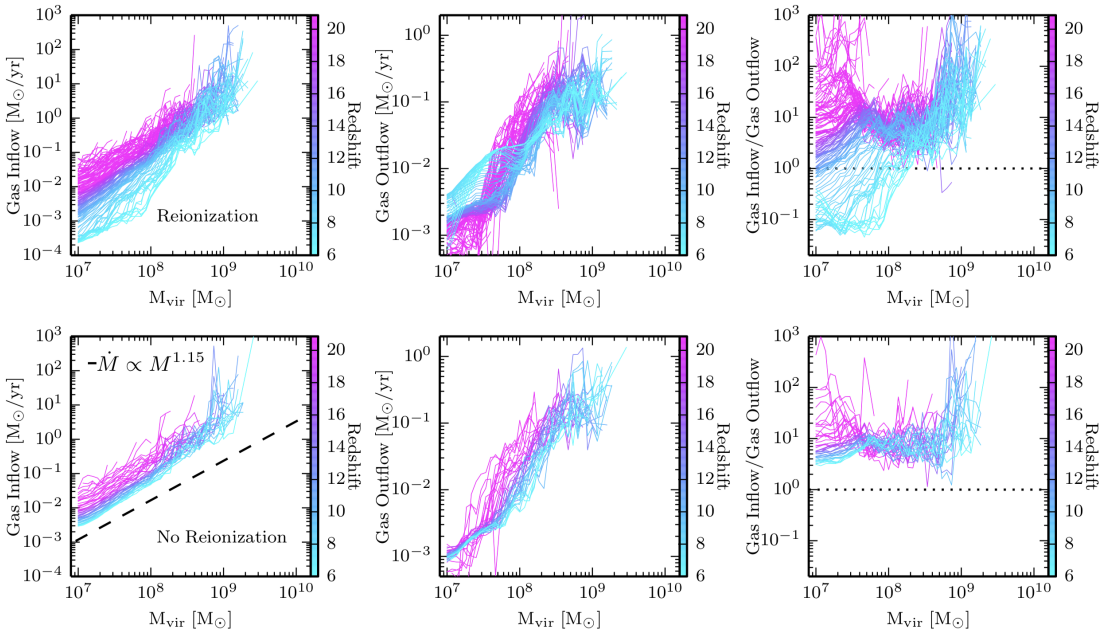

Figure 5.4: Running median inflow (*left*), outflow (*centre*) rates and ratios (*right*) for isolated halos as a function of virial mass in bins of $\Delta\log_{10}(M_{\rm vir}/M_\odot) = 0.2$), shown only if that bin contains more than 10 halos. Merging systems have been removed to isolate the effect of filamentary gas accretion. The *top* row represents the reionisation run and the bottom row the represents the no reionisation run. The dotted horizontal line in the rightmost panels indicate a ratio of one. Halos that have a ratio below one are losing gas either due to supernovae or radiation feedback for the REIO run. Inflow rates are not affected for galaxies with virial masses above $10^{8.5}M_\odot$. Below this mass, and after reionisation, inflow rates are significantly reduced. The radiation serves to increase the variation in gas outflow rates, and particularly enhances it for the lowest mass galaxies, driven by photoevaporation. The result of this is that galaxies with virial masses below $10^8 M_\odot$ after reionisation experience a net loss in mass, driven primarily through the throttling of the accretion rate while continuing to lose mass.

the competing influences of reionisation and stellar feedback. In order to isolate the effects of reionisation, we use a subsample of galaxies which host no stellar particles at $z = 6$. The mass bins are defined by the virial mass at $z = 6$: $\mathrm{M_{vir}}/\mathrm{M_\odot} < 3 \times 10^7$, $3 \times 10^7 < \mathrm{M_{vir}}/\mathrm{M_\odot} < 7 \times 10^8$, $7 \times 10^8 < \mathrm{M_{vir}}/\mathrm{M_\odot} < 10^8$ and $10^8 < \mathrm{M_{vir}}/\mathrm{M_\odot}$, containing 1979, 553, 84 and 65 objects respectively.

We characterise the environment of the galaxy by degrading the simulation to level 6, splitting it into 64^3 cells with $\Delta x = 78$ ckpc. The environment of a galaxy is defined by the closest 27 cells. Reionisation is defined as the first time the environment is 90% ionised.

Considering the gas inflow rates in Fig. 5.5, reionisation causes a rapid drop by a median value of two orders of magnitude for the two lowest mass bins, though the lower mass halos show not only a more rapid drop, but also a large scatter in the gas inflow rates. Halos that are reionised earlier show a slower rate of inflow rate suppression. The filaments feeding the galaxies grow less dense as time progresses, making them more susceptible to the radiation field, and causing them to be unable to channel gas onto the halos. This, coupled with an enhancement in the strength of the UV background as the simulation progresses will suppress the rate of accretion more rapidly in environments that reionise at later redshifts. This is expected until $z \approx 4$ from observations (Calverley et al., 2011; Wyithe and Bolton, 2011). The higher mass bins show little suppression in their accretion rates, although like the lower mass bins they again have a large scatter in inflow rates. There is no difference in the median accretion rates for (top panels) halos reionised at different redshifts, probably as a result of them being fed by more resilient filaments.

In the absence of stellar feedback, photoevaporation of the halos is driving outflows alone. For the two lower mass bins the lowest mass halos exhibit higher outflow rates if they reionise later, again due to the growing strength of the radiation field. Secondly, as the halos grow and the mean density of the Universe falls, the gas at the edge of the halo also falls in density, becoming more susceptible to photoevaporation. Interestingly, the outflow rates peak at 200 Myr, before falling again. This is likely due to most of the susceptible gas being previously ablated. Higher mass halos do not show this suppression, likely because the reduction in accretion rate is less severe or does not happen. The reservoir of available gas for expulsion is therefore not used up.

In the 3rd row of Fig. 5.5 the ratio of baryonic to expected baryonic mass is plotted, where the expected baryonic mass assumes that the galaxy accretes the universal baryon fraction. Across all mass bins this ratio falls after reionisation. The lower the mass, the greater the suppression, with the largest halo bin showing virtually no suppression. In the lowest mass bin, the median lines end at $z = 6$, revealing that the halos which reionised at z=6 have a greater baryon mass fraction by half an order of magnitude than those that

reionised much earlier, which has severe implications for the shape of the dwarf galaxy mass function. The baryonic mass is an integrated quantity and is as a result very sensitive to changes in the inflow and outflow rates of the halos. The lowest two mass bins reveal a loss of baryonic mass post reionisation, while halos in the two higher mass bins are still capable of accreting material.

We now turn to the thermal history of the environment of the filaments. The temperature of the IGM in the vicinity of the galaxies is shown in Fig. 5.6. By plotting the temperature against time since the local reionisation, thermal histories between late and early reionised regions can be compared, which reveals that environments that are reionised later are systematically heated to higher temperatures, again driven by the fiercer UV background generated by the end of reionisation. The filament environments are shown to be extremely cool (below 10^4 K) before reionisation, cooled adiabatically by the expansion of the Universe, before rapidly heating at reionisation. This shows that, despite thermal shocks occurring as gas is accreted by filaments, this alone is unable to maintain a high temperature in the IGM. The local radiation field is responsible for heating the IGM to high temperatures. Post reionisation however, the gas is once again able to cool, reaching temperatures similar to the virial temperatures of the smallest halos, indicating that accretion could restart once again. However this is not seen in the accretion rates in Fig. 5.5. This is likely an issue with volume averaging the environment around the cells. The shock temperature of filaments are lower than the virial temperatures of halos, and particularly for the lower persistence filaments, cannot capture the reionised gas. This prevents the funnelling of gas onto the lower mass halos.

In Fig. 5.7 a high mass galaxy from a 10 Mpc SPHINX simulation is shown. This reveals that accretion may efficiently continue to feed high mass galaxies even within the hot halo of a galaxy, provided the filament is able to maintain a cool core. There are also some lower mass filaments which are visibly disturbed and disrupted by the hot gas. Indeed, it must be the case that filaments can continue to feed high mass galaxies even without the hot halo of a galaxy as the radiation field must eventually approximate the Haardt and Madau (1996) UV background and these cosmological filaments are observed at lower redshift in simulations using the Haardt and Madau (1996) UV background in Chapters 3 and 4 of this thesis.

5.4 Conclusions and Discussion

In this chapter we used the SPHINX simulations, a suite of high resolution radiation hydrodynamic cosmological simulations that aim to self consistently capture reionisation on the

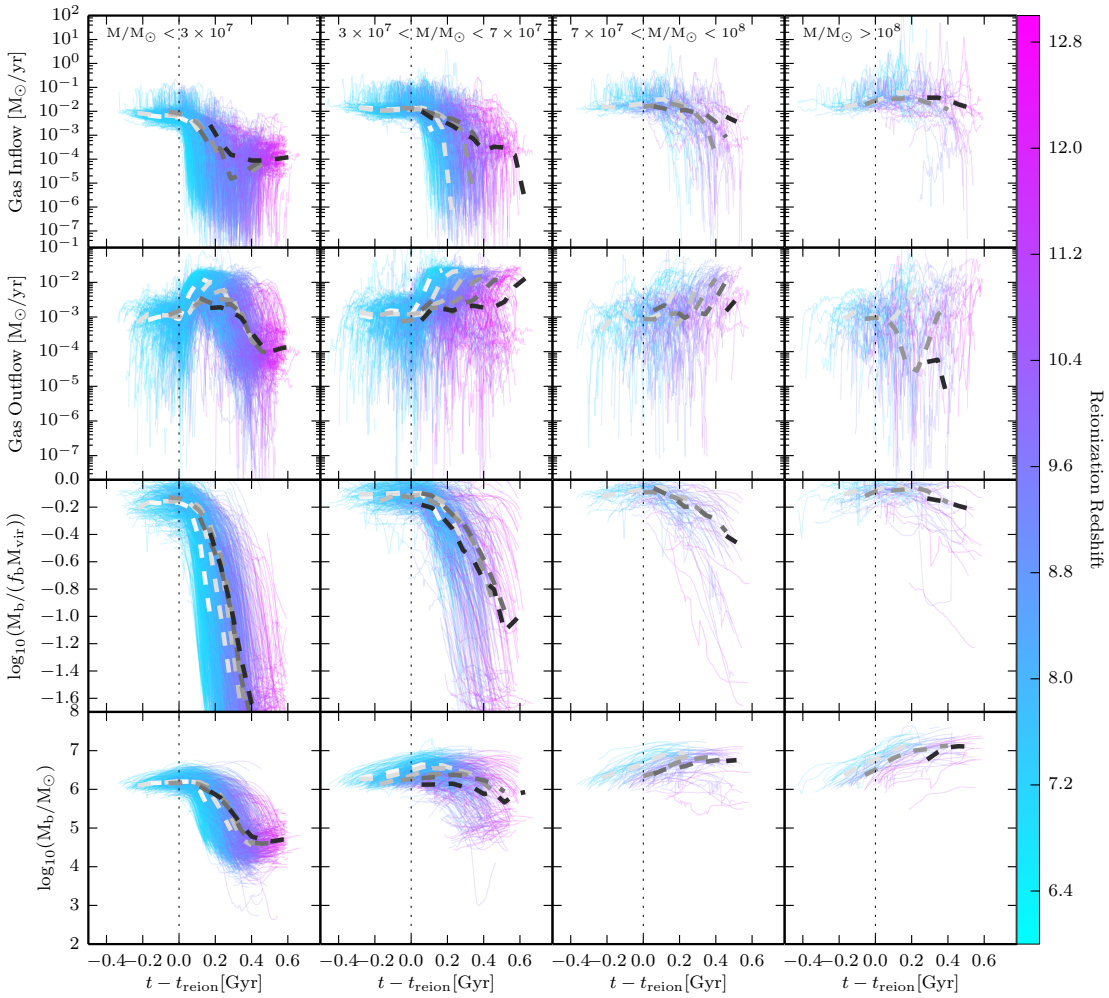

Figure 5.5: Plotting the inflow (*1st row*), outflow (*2nd* row), baryonic to expected baryonic mass (*3rd* row) and baryonic mass (*last* row) against time since reionisation, coloured according to the reionisation redshift. Dashed lines represent median values for galaxies binned according to reionisation redshift, with lighter indicating a later reionisation. Each column represents halos in a certain mass range. Reionisation is demarcated by the *dotted vertical* line. Once the local environment of a galaxy is reionised, the gas inflow is reduced if the mass of the object is below $7 \times 10^7 M_\odot$. This is accompanied with an enhancement of the rate of outflow (temporary in the lowest mass bin), resulting in mass loss or at the very least a slowing in the accretion rate. For masses above $7 \times 10^7 M_\odot$ there is no visible reduction. Note that these galaxies are highly unusual in that they have not yet formed star particles by $z = 6$, and are as such heated entirely by reionisation.

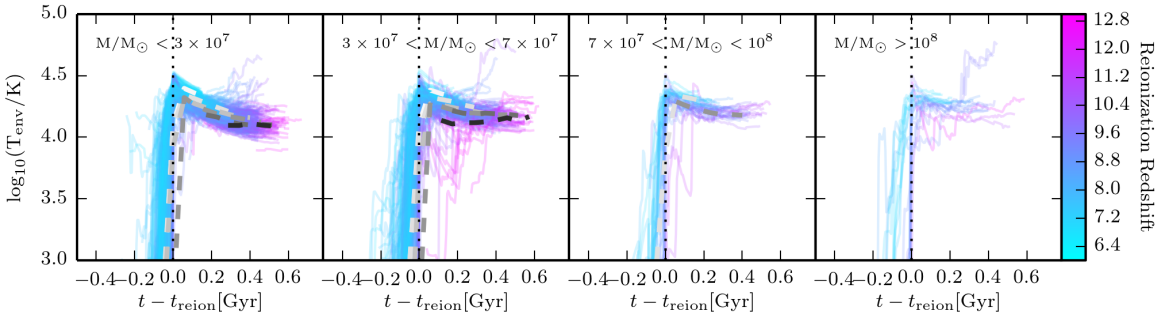

Figure 5.6: The temperature of the galactic environments, binned according to their halo mass for 'isolated' star free galaxies. Regardless of the local reionisation redshift, shown by the colour of the line, the environments show a rapid transition to a hot environment. The median evolution of environments with similar reionisation redshifts are shown as dashed lines, with lighter lines reionising later. The *dotted vertical* line demarcates the time of reionisation.

large scales of the Universe, and the back reaction this has on the systems residing within the simulated volume.

The main results from this chapter were as follows:

- Reionisation is able to heat the IGM filaments to the point where the gas no longer sees the shallow potential well of the lower mass filaments. While the DM is unaffected by this, the gas density of the filaments can be reduced by 60-80% by $z = 6$.
- "Feeding" filaments closer to galaxies are ionised first, with the effect propagating to more distant filaments later on.
- Filaments with shock temperatures higher than the post-reionisation IGM gas temperature continue to accrete efficiently and feed high mass galaxies.
- Halos with $M_{vir} \lesssim 10^8 M_\odot$ have their gas accretion rates reduced by an order of magnitude by reionisation. Gas outflow rates for $M_{vir} \lesssim 3 \times 10^7 M_\odot$ are enhanced due to photoevaporation. The reduction in inflow is greater than the increase in photoevaporation and thus starvation is more important in quenching the star formation in low mass halos in the early Universe.

The SPHINX simulation helps to alleviate the tensions in the 'too big to fail' and 'missing dwarfs' problems by suppressing the accretion of gas onto low mass halos post reionisation. This also generates a population of low mass, low metallicity objects which agree with observations (e.g. Okamoto et al., 2012; Brown et al., 2012) and suggest the quenching by reionisation for these objects. The core-cusp problem is not alleviated however as this

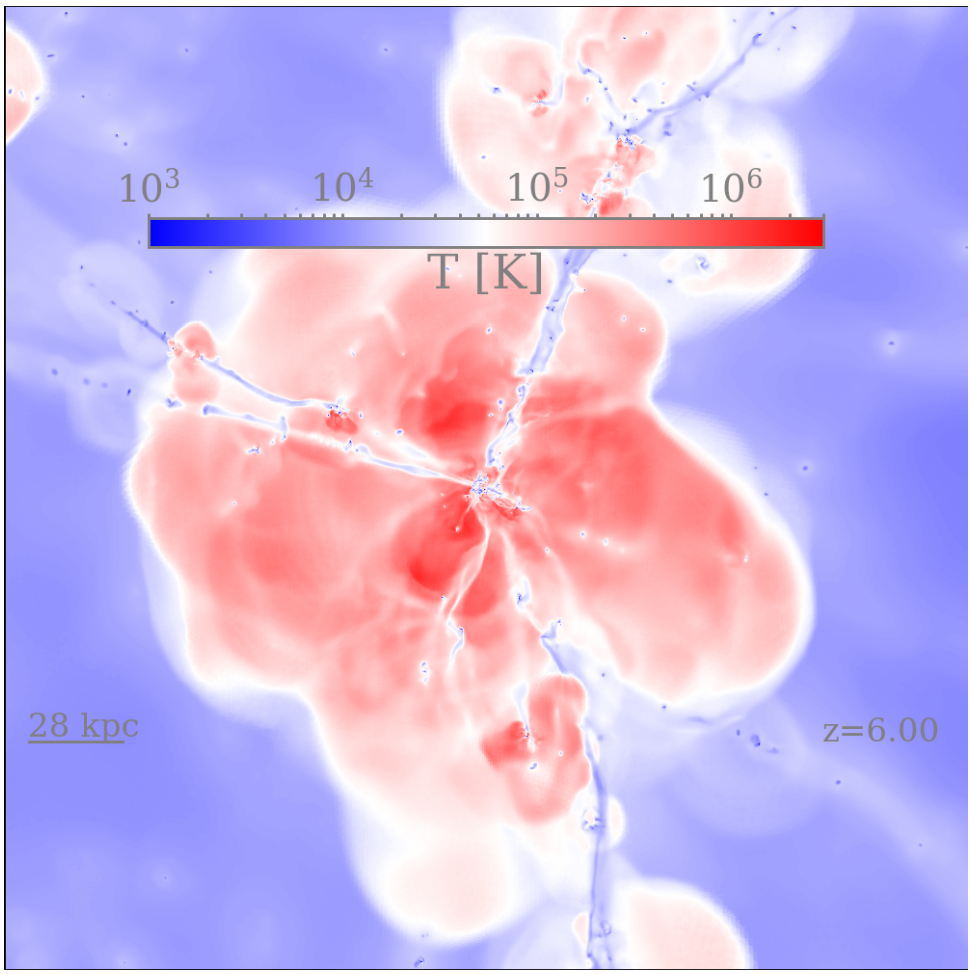

Figure 5.7: A thin slice through the temperature field of a large galaxy in the SPHINX 10 Mpc volume. Clearly visible is the hot bubble generated by supernovae, surrounded by the colder IGM only heated by the radiation field. Threading the bubble are cold filaments, which are still capable of feeding the central galaxy efficiently.

is primarily resolved through increased outflows (e.g. Teyssier et al., 2013) rather than reduced inflows.

Chapter 6

Conclusions and Further Work

Accretion onto galaxies via cosmological filaments and cold mode accretion is extremely important in determining the star formation history and morphology of galaxies at high redshift (e.g. Kereš et al., 2005; Dekel and Birnboim, 2006; Pichon et al., 2011). These filaments provide a direct connection between a growing disk and the larger scales of the cosmic web. Unfortunately these structures have proved to be elusive. Their low density, low metallicity and only being prevalent at high redshift makes observation difficult other than in extreme environments, e.g. lit up by a powerful nearby AGN (e.g. Cantalupo et al., 2014), or a chance alignment of filaments with more distant quasars (e.g. Ho et al., 2017). Indeed, most observational results are in fact indirect, relying on the detection of extended disks (e.g. Martin et al., 2019), arguments on metal content of galaxies (van den Bergh, 1962; Schmidt, 1963) or gas depletion timescales (e.g. Genzel et al., 2006). In spite of these problems, cosmological filaments are ubiquitous to simulations (e.g. Kereš et al., 2005; Nelson et al., 2013; Tillson et al., 2015; Katz et al., 2019) and are thus an excellent way to inform future observations. Prior to this thesis, most studies on filaments focused on idealised simulations (e.g. Mandelker et al., 2016, amongst others), or used large scale cosmological simulations to study the influence of filaments on galaxies (Danovich et al., 2012; Cen, 2014) without considering the nature of the streams themselves. Yet others focus on the larger scale cosmic web, acting through the tidal influence on the galaxies that reside within the filamentary network (e.g. Laigle et al., 2015). There had yet to be a study of the nature of the filaments that feed galaxies themselves, in terms of their profiles and the influence of these streams on the galaxies they feed.

In Chapter 3 I start to address this problem by designing a scheme to measure the properties of the filaments of a single Milky Way-like galaxy, in the hope of extending this to a larger set of galaxies in later chapters. I find that the filaments in this simulation can be fit with a combined filament and wall profile. These profiles can be derived from the equations of hydrostatic equilibrium in 1 or 2 dimensions under the assumption of isothermality. While it

is clear that the filaments themselves are pressure supported either thermally (or by dispersion in the case of DM) rather than rotationally supported, it is not clear that isothermality itself holds as an assumption. This is due to the temperature and velocity dispersion of the DM evolving over the course of the simulation, which is not expected under isothermality. Regardless, the isothermal model predicts a characteristic filament scale, the core radius. I find that this scales similarly to the radius of the galaxy with redshift. A second characteristic scale, the truncation radius, develops due to the shock heating of gas and shell crossing of DM, traced by vorticity, velocity dispersion and the thermal shock itself. Beyond this scale the isothermal model is expected to have broken down. The truncation radius scales similarly to the virial radius for the DM, while the gas truncation radius catches up with the DM by approximately $z = 3.5$ for this particular filament.

Our simulations also establish that filaments need to be resolved with a minimum of ~ 10 ckpc for a Milky Way sized halo. This might have important consequences for the angular momentum content of the gas transported to the galaxy. Still higher resolution will be required to capture the filaments around dwarf galaxies, though these are far more vulnerable to photoionisation and so probably do not need be resolved in detail beyond $z = 6$. This was explored in Chapter 5. I also performed the analysis on the same simulation with stellar feedback, in preparation for Chapter 4. While the mass brought by the inflowing filament gas is affected to a level of $\sim$20-30 percent as a result of stellar feedback from the central galaxy, a further reduction is likely to occur as the filament enters the virial radius. I plan to tackle this issue using tracer particles in the near future. The NUT suite allows the efficient exploration of various subgrid prescriptions as many versions of the NUT simulation have already been completed. This will allow me to test the effect of different physical processes on the filaments. The interaction of the filament with galactic winds and the virialised halo hot atmosphere is expected to be a function of the halo mass, and therefore our results need to be extended to a larger sample.

The study of a single galaxy cannot possibly hope to represent the diversity of galaxies that we observe in our night sky. To try to address this imbalance (at least partly), Chapter 4 explores the filaments of a few tens of galaxies with masses between $10^{10}\mathrm{M}_{\odot}$ and $10^{12.6}\mathrm{M}_{\odot}$. The impact on the galaxies connecting to filaments of different widths, lengths temperatures is explored. In this chapter I find that filaments of the NEW HORIZON simulation are similar in nature to those in the NUT suite, which is highly suggestive that the profiles are generic and universal. As well as the shape, the core densities and temperatures scales similarly between the two simulations. High mass galaxies, which typically reside in higher mass halos are typically fed by higher density filaments. However, this effect does not tend to persist. The final mass (in this case $z = 0.7$) of the halo is not beholden to the properties

of the filaments that feed the galaxy at much higher redshifts. Around $z = 2$, however, it can be seen that galaxies with higher star formation rates, stellar masses and formation efficiencies tend to form in cooler filaments. These structures are more conducive to efficient accretion of gas onto galaxies, fuelling the star formation rates up to $z = 0.7$.
Comparing to the NUT suite, the filament core radii and truncation radii scale very similarly, however, it should be noted that the ~ 2.5 orders of magnitude variation in mass only yields a factor of 10 variation in virial and galactic radii. It is therefore difficult to draw any meaningful conclusions on the comparison of the scaling of the size of the filaments and galaxies. It remains to be seen whether these scalings are similar to those obtained from the NUT suite far outside this mass range. This will be partly addressed in future by analysing the filaments at lower redshifts which allows higher mass objects time to form. Studying a larger simulation containing rarer, higher mass objects would also be helpful in this endeavour.
I also studied the distribution of stellar and halo masses, galaxy formation efficiency and specific star formation rates. These distributions are affected by whether or not the galaxy is considered part of a filament, with filaments typically hosting the largest galaxies, and maintaining higher star formation rates for longer. This also gives way to suppression of the very highest star formation rates at later times. Counter to this however, the average properties of the galaxies (of those that I considered during the course of this thesis) are not significantly impacted, regardless of filament inclusion/exclusion or the local density.
While the filaments maintain a cold core as in the NUT suite, the difference in temperature between the filamentary accretion shock and the core filament temperature reduces towards $z = 2$. In contrast to the idealised filaments explored by Mandelker et al. (2016, 2018a,b); Padnos et al. (2018); Aung et al. (2019), where the filament DM backbone is not modelled, the gravity of these structures act to reduce the effects of the Kelvin Helmholtz instability, as well as the influence of feedback. This is particularly apparent in the case of radiative feedback explored in Chapter 5 where the lowest mass filaments are are seen to be affected first. This is due to the sound speeds of the gas exceeding the local filament escape velocity, $\sqrt{2}\sigma$. Eventually, the heating of the gas does begin the process of the dilution of all gas filaments, though these effects are only just beginning at $z = 2$. This is entirely analogous to the process identified in Dekel and Birnboim (2006) whereby the dilution of mean density of the Universe and growing size of the the halos in the Universe leads to increasing cooling times. This represents an end to the dominance of cold mode accretion as the main method of gas accretion. Similarly to the hot halos of modern ellipticals, the filaments themselves fill with hot gas, and become ineffective at transporting cold gas to the galaxies they attempt to feed.

Finally, to summarise Chapter 5 we used the SPHINX simulations and the techniques developed for Chapters 3 and 4 to study the impact of reionisation on galaxies through their influence on the filaments that feed them. At these high redshifts, the cold mode of accretion dominates the flow of gas onto the young galaxies. Suppression of the flow of this gas could explain some peculiarities on low abundance of dwarf galaxies compared to the expected numbers from ΛCDM (e.g. Mateo, 1998) as well as the apparent truncation of their star formation histories around reionisation (e.g. Okamoto et al., 2012). The suppression of flow rates by an order of magnitude is seen for galaxies with halos of $\mathrm{M_{vir}} \lesssim 10^8 \mathrm{M_\odot}$. We can see that the cause of this is reionisation by comparing with a simulation in which reionisation does not occur.

One of the most important aspects of this thesis is not the results which have so far been extracted from the NEW HORIZON simulation, the SPHINX suite or the NUT suite. It is the set of the techniques and frameworks that were designed in order to allow these measurements to be made. I have developed the tools to take the raw skeleton output of DISPERSE from the density field and the galaxy catalogue and to use this to extract the main filaments from the simulation. Not only does this allow the exploration of much larger datasets as in the NEW HORIZON simulation, but also the impact of various forms of feedback on the filaments. This could yield interesting constraints on feedback processes by the back reaction onto the accretion and star formation rate of the feeding galaxy. It could also inform the design of future observational surveys of filaments. The techniques developed over the course of this thesis become particularly powerful when combined with concepts such as tracer particles which allow the gas to be followed directly.

6.1 Further Work and Future Directions

In Chapter 4 I performed the analysis of filament profiles down to $z = 2$, however I have produced skeletons down to $z = 0.7$, which was as far as the NEW HORIZON simulation had been run when I was performing the analysis for this chapter. In the end skeletons at 16 snapshots were finished in time for the thesis between $z = 6$ and $z = 2$. I hope to extend this analysis down to $z = 0$ in the future. An interesting transition occurs as the filaments evaporate around $z = 1$. The beginnings of this transition can be seen at $z = 2$ in the gas temperature profiles of Fig. 4.25. At $z = 2$ The filament still has enhanced cooling in the core at smaller radii than the accretion shock, but it will not be long until the filament begins to completely evaporate. This should have a profound effect on the gas supplies of galaxies being fed by these filaments, reminiscent of the high redshift quenching due to reionisation seen in Chapter 5.

There are a number of other avenues of enquiry which I have not explored yet. I did not have time to look at the effect of the distance to a galaxy on the properties of the filament. This was briefly explored in Chapter 3, but not in a statistical context. Additionally, the impact of accretion onto the filaments themselves on the truncation radius has yet to be explored. This was briefly looked at in Chapter 3, however, the simple model based on Adhikari et al. (2014) was found to be unsuitable when computed naïvely on the DM profile. It is possible that more careful accounting for the filament substructure will yield a closer match to the expected scaling with accretion rate. Another thing I did not have time to address as part of the thesis was the actual accretion of gas onto the galaxy via the cold mode within the virial radius. This is arguably the most important phase of cold mode accretion since this is where the gas joins the galaxy and becomes available for star formation and transfers angular momentum to the galactic disk. I have already rerun the NUT simulation with no feedback using the Monte Carlo tracer particles implemented by Cadiou et al. (2019). These particles stochastically follow the gas flow. With sufficient numbers of tracer particles (in this case I used 300 million), we can follow the filaments from large scales, across the virial radius to galaxies. More specifically I can use the DISPERSE algorithm to identify the filament and then follow particles that are within a truncation radius of the filament as they flows towards the galaxy. I can identify exactly where the filament gas is being shocked, both as it accretes onto the filament and as it falls onto the galaxy and study how long this gas takes to be incorporated into the stellar population. Beyond this I hope to rerun the tracer particle simulation with feedback in order to explore the interaction of inflows with outflows. I would also like to explore the effect of the density enhancement of filaments measured around $z = 8$ in Chapter 3 which these two simulations, with feedback and no feedback and tracers, will be ideal for studying.

z	DM			gas		
	r_0 (kpc)	r_T (kpc)	r_ω (kpc)	r_0 (kpc)	r_T (kpc)	r_ω (kpc)
3.26	10.31 ± 4.41	36.90 ± 5.36	35.11 ± 8.25	7.92 ± 3.77	–	–
3.35	10.96 ± 4.81	33.82 ± 6.43	33.82 ± 8.34	12.14 ± 7.02	–	–
3.44	10.71 ± 4.77	34.33 ± 5.42	34.05 ± 7.36	8.64 ± 3.95	–	–
3.53	16.01 ± 10.50	34.80 ± 12.75	38.96 ± 17.90	7.22 ± 4.23	–	–
3.60	11.20 ± 5.17	36.80 ± 12.47	35.69 ± 14.22	8.02 ± 7.38	–	–
3.65	11.86 ± 4.88	30.58 ± 3.67	31.68 ± 5.53	8.04 ± 3.75	–	–
3.82	10.45 ± 4.37	28.99 ± 3.93	30.51 ± 7.28	5.89 ± 2.79	–	–
3.96	10.28 ± 4.59	27.86 ± 4.01	24.48 ± 7.15	5.10 ± 2.29	–	–
4.00	7.33 ± 4.43	27.23 ± 4.84	22.41 ± 6.05	5.13 ± 2.28	–	–
4.02	9.36 ± 4.30	26.48 ± 4.34	24.21 ± 7.01	4.94 ± 2.34	–	–
4.56	8.61 ± 5.60	23.13 ± 4.57	23.13 ± 5.06	4.21 ± 2.10	–	–
5.45	3.37 ± 1.96	14.37 ± 3.83	12.99 ± 3.13	2.70 ± 1.55	–	–
5.67	2.13 ± 1.33	11.59 ± 2.57	11.66 ± 2.60	2.78 ± 1.50	–	–
6.99	1.80 ± 1.13	9.20 ± 2.69	9.20 ± 2.58	2.79 ± 1.51	–	–
8.09	1.58 ± 1.00	7.08 ± 2.19	6.30 ± 1.91	2.43 ± 1.49	–	–

Table 1: Redshift evolution of the filament core radius derived from density (r_0) and truncation radii derived from temperature (r_T) and vorticity (r_ω) as fitted from the density, temperature and vorticity fields extracted from the *feedback* run. See Section 3.4.2 for details. Note the absence of data for the radii derived from vorticity and temperature, due to the destructive impact of feedback on these fields.

.1 Appendix

In Table 1 (*feedback* run) and Table 2 (*no feedback* run) we present the redshift evolution of the filament radius, as fitted from the density, temperature and vorticity field.

z	DM			gas		
	r_0 (kpc)	r_T (kpc)	r_ω (kpc)	r_0 (kpc)	r_T (kpc)	r_ω (kpc)
3.35	15.37 ± 6.66	32.94 ± 3.47	39.35 ± 8.38	9.29 ± 4.13	27.24 ± 6.07	23.02 ± 6.79
3.44	10.54 ± 4.48	31.56 ± 3.94	33.91 ± 4.23	9.82 ± 3.92	26.27 ± 6.21	25.01 ± 10.41
3.60	10.48 ± 4.22	33.82 ± 5.91	35.41 ± 6.45	7.66 ± 2.73	25.65 ± 5.04	17.65 ± 5.60
3.65	11.20 ± 3.62	33.62 ± 5.44	32.90 ± 5.04	7.34 ± 2.70	27.63 ± 6.28	18.68 ± 5.01
3.82	11.44 ± 4.59	28.83 ± 3.84	31.92 ± 4.66	6.18 ± 2.19	22.20 ± 6.36	16.29 ± 5.86
3.94	8.64 ± 3.89	27.12 ± 5.14	29.77 ± 6.11	4.27 ± 1.38	20.44 ± 4.52	14.95 ± 4.81
4.00	8.39 ± 3.82	28.57 ± 6.47	25.87 ± 4.48	5.04 ± 1.96	18.58 ± 3.96	21.70 ± 6.62
4.13	7.88 ± 3.64	26.57 ± 7.79	24.43 ± 5.05	3.96 ± 1.53	17.70 ± 4.12	14.48 ± 4.63
4.55	7.34 ± 3.50	20.28 ± 4.04	22.82 ± 5.57	4.45 ± 1.72	13.84 ± 2.64	13.33 ± 3.18
5.06	3.95 ± 2.27	17.14 ± 3.05	19.84 ± 3.55	3.68 ± 0.85	10.04 ± 2.34	10.13 ± 3.03
5.45	3.37 ± 1.53	14.75 ± 2.99	16.31 ± 3.37	2.96 ± 1.23	7.80 ± 2.13	6.89 ± 1.73
5.66	2.74 ± 1.74	11.27 ± 2.52	15.32 ± 4.32	2.99 ± 1.39	7.48 ± 2.22	$.23 \pm 1.45$
7.00	1.75 ± 0.75	9.19 ± 2.58	10.33 ± 1.76	1.77 ± 0.79	3.79 ± 0.49	4.46 ± 0.66
8.09	1.59 ± 1.00	6.28 ± 1.48	8.18 ± 1.82	1.58 ± 0.74	3.78 ± 0.56	3.96 ± 0.58

Table 2: Redshift evolution of the filament core radius derived from density (r_0) and truncation radii derived from temperature (r_T) and vorticity (r_ω) as fitted from the density, temperature and vorticity fields extracted from the *no-feedback* run. See Section 3.4.2 for details.

z	DM			gas		
	$\log_{10}(\rho_0/\mathrm{M}_\odot\mathrm{pc}^{-3})$	$\log_{10}(\rho_1/\mathrm{M}_\odot\mathrm{pc}^{-3})$	r_1(kpc)	$\log_{10}(\rho_0/\mathrm{M}_\odot\mathrm{pc}^{-3})$	$\log_{10}(\rho_1/\mathrm{M}_\odot\mathrm{pc}^{-3})$	r_1(kpc)
3.26	-3.88 ± 0.46	-4.44 ± 0.41	8.45 ± 3.67	-4.69 ± 0.42	-5.02 ± 0.47	13.82 ± 6.81
3.35	-4.01 ± 0.46	-4.50 ± 0.46	9.08 ± 3.92	-4.82 ± 0.50	-5.16 ± 0.45	8.63 ± 3.50
3.44	-3.98 ± 0.42	-4.31 ± 0.44	8.38 ± 3.16	-4.65 ± 0.45	-5.01 ± 1.20	9.18 ± 3.34
3.53	-4.11 ± 0.59	-4.45 ± 0.51	8.16 ± 3.60	-4.78 ± 0.69	-5.10 ± 0.48	7.50 ± 2.78
3.60	-3.99 ± 0.56	-4.43 ± 0.53	5.86 ± 2.65	-4.46 ± 0.86	-4.92 ± 0.56	9.09 ± 3.67
3.65	-3.93 ± 0.43	-4.38 ± 0.55	8.80 ± 3.92	-4.63 ± 0.41	-5.17 ± 0.41	7.95 ± 3.16
3.82	-3.88 ± 0.42	-4.25 ± 0.62	7.69 ± 2.97	-4.53 ± 0.39	-5.02 ± 0.42	8.13 ± 3.18
3.96	-3.84 ± 0.41	-4.39 ± 0.42	9.47 ± 5.03	-4.48 ± 0.42	-4.86 ± 1.07	8.26 ± 2.98
4.00	-3.81 ± 0.44	-4.18 ± 0.62	7.69 ± 4.16	-4.48 ± 0.43	-4.97 ± 0.44	10.04 ± 6.40
4.02	-3.83 ± 0.41	-4.43 ± 1.03	7.88 ± 3.06	-4.45 ± 0.43	-4.81 ± 0.53	9.23 ± 3.70
4.56	-3.65 ± 0.44	-4.38 ± 1.17	6.59 ± 2.84	-4.36 ± 0.41	-4.84 ± 0.42	7.48 ± 2.75
5.45	-3.44 ± 0.40	-4.18 ± 1.17	6.53 ± 5.57	-4.11 ± 0.49	-4.79 ± 0.39	6.03 ± 2.49
5.67	-3.46 ± 0.44	-4.24 ± 1.30	5.77 ± 2.38	-4.19 ± 0.50	-4.76 ± 0.37	6.18 ± 2.40
6.99	-3.20 ± 0.49	-4.02 ± 1.23	3.74 ± 1.39	-3.99 ± 0.46	-4.65 ± 0.36	6.01 ± 2.38
8.09	-3.10 ± 0.57	-3.72 ± 0.42	3.36 ± 1.49	-3.87 ± 0.57	-4.72 ± 0.26	4.20 ± 1.66

Table 3: Redshift evolution of the model fitted density as extracted from the *feedback* run. See Section 3.4.2 for details.

z	DM		gas	
	$\log_{10}(\rho_0/\mathrm{M}_\odot\mathrm{pc}^{-3})$	$\log_{10}(\rho_1/\mathrm{M}_\odot\mathrm{pc}^{-3})$	$r_1(\mathrm{kpc})$	$\log_{10}(\rho_0/\mathrm{M}_\odot\mathrm{pc}^{-3})$	$\log_{10}(\rho_1/\mathrm{M}_\odot\mathrm{pc}^{-3})$	$r_1(\mathrm{kpc})$
3.35	-3.92 ± 0.46	-4.34 ± 0.46	7.66 ± 3.15	-4.60 ± 0.34	-5.16 ± 0.36	12.36 ± 5.49
3.44	-3.96 ± 0.39	-4.47 ± 0.40	9.30 ± 3.62	-4.48 ± 0.64	-5.03 ± 1.01	16.32 ± 7.66
3.60	-3.89 ± 0.42	-4.27 ± 0.44	7.89 ± 3.20	-4.59 ± 1.15	-5.10 ± 0.38	8.69 ± 3.13
3.65	-3.87 ± 0.42	-4.40 ± 0.43	8.13 ± 3.00	-4.50 ± 0.38	-5.14 ± 0.38	7.82 ± 2.65
3.82	-3.88 ± 0.41	-4.21 ± 0.48	8.05 ± 3.00	-4.48 ± 0.41	-5.09 ± 0.37	8.82 ± 3.02
3.94	-3.69 ± 0.47	-4.34 ± 0.41	7.95 ± 3.42	-4.02 ± 0.64	-4.79 ± 1.19	7.68 ± 2.81
4.00	-3.67 ± 0.49	-4.29 ± 0.45	6.79 ± 2.80	-4.37 ± 0.45	-4.96 ± 0.39	7.70 ± 3.00
4.13	-3.64 ± 0.44	-4.36 ± 1.10	6.89 ± 2.75	-3.65 ± 1.85	-4.89 ± 0.37	6.76 ± 2.78
4.55	-3.65 ± 0.48	-4.18 ± 0.41	6.89 ± 2.97	-4.28 ± 0.45	-4.84 ± 0.36	7.17 ± 2.76
5.06	-3.42 ± 0.45	-4.27 ± 1.20	6.06 ± 2.80	-3.59 ± 2.00	-4.72 ± 0.36	6.27 ± 2.39
5.45	-3.50 ± 0.42	-3.90 ± 0.61	6.00 ± 2.55	-4.07 ± 0.42	-4.50 ± 1.30	5.92 ± 2.14
5.66	-3.46 ± 0.43	-4.25 ± 1.25	9.00 ± 4.78	-3.95 ± 0.56	-4.76 ± 0.44	5.47 ± 2.06
7.00	-3.26 ± 0.45	-4.04 ± 1.20	6.43 ± 4.50	-3.95 ± 0.53	-4.93 ± 0.07	6.39 ± 4.89
8.09	-3.16 ± 0.46	-3.81 ± 1.22	6.07 ± 3.69	-3.82 ± 0.57	-4.50 ± 0.36	4.53 ± 1.72

Table 4: Redshift evolution of the model fitted density as extracted from the *no-feedback* run. See Section 3.4.2 for details.

Bibliography

Adhikari, S., Dalal, N., and Chamberlain, R. T. (2014). Splashback in accreting dark matter halos. , 2014(11):019.

Agertz, O., Moore, B., Stadel, J., Potter, D., Miniati, F., Read, J., Mayer, L., Gawryszczak, A., Kravtsov, A., Nordlund, Å., Pearce, F., Quilis, V., Rudd, D., Springel, V., Stone, J., Tasker, E., Teyssier, R., Wadsley, J., and Walder, R. (2007). Fundamental differences between SPH and grid methods. , 380(3):963–978.

Allen, S. W., Schmidt, R. W., and Fabian, A. C. (2002). Cosmological constraints from the X-ray gas mass fraction in relaxed lensing clusters observed with Chandra. , 334(2):L11–L15.

Alpaslan, M., Robotham, A. S. G., Driver, S., Norberg, P., Baldry, I., Bauer, A. E., Bland -Hawthorn, J., Brown, M., Cluver, M., Colless, M., Foster, C., Hopkins, A., Van Kampen, E., Kelvin, L., Lara-Lopez, M. A., Liske, J., Lopez-Sanchez, A. R., Loveday, J., McNaught-Roberts, T., Merson, A., and Pimbblet, K. (2014). Galaxy And Mass Assembly (GAMA): the large-scale structure of galaxies and comparison to mock universes. , 438(1):177–194.

Aragón-Calvo, M. A., Jones, B. J. T., van de Weygaert, R., and van der Hulst, J. M. (2007a). The multiscale morphology filter: identifying and extracting spatial patterns in the galaxy distribution. , 474(1):315–338.

Aragon-Calvo, M. A., van de Weygaert, R., Araya-Melo, P. A., Platen, E., and Szalay, A. S. (2010). Unfolding the hierarchy of voids. , 404(1):L89–L93.

Aragón-Calvo, M. A., van de Weygaert, R., Jones, B. J. T., and van der Hulst, J. M. (2007b). Spin Alignment of Dark Matter Halos in Filaments and Walls. , 655:L5–L8.

Aragon-Calvo, M. A. and Yang, L. F. (2014). The hierarchical nature of the spin alignment of dark matter haloes in filaments. , 440:L46–L50.

Arrigoni Battaia, F., Prochaska, J. X., Hennawi, J. F., Obreja, A., Buck, T., Cantalupo, S., Dutton, A. A., and Macciò, A. V. (2018). Inspiraling halo accretion mapped in Ly α emission around a z $\sim$ 3 quasar. , 473(3):3907–3940.

Aubert, D., Pichon, C., and Colombi, S. (2004). The origin and implications of dark matter anisotropic cosmic infall on $_*$ haloes. , 352(2):376–398.

Aubert, D. and Teyssier, R. (2008). A radiative transfer scheme for cosmological reionization based on a local Eddington tensor. , 387(1):295–307.

Audouze, J. and Silk, J. (1995). The First Generation of Stars: First Steps toward Chemical Evolution of Galaxies. , 451:L49.

Aung, H., Mandelker, N., Nagai, D., Dekel, A., and Birnboim, Y. (2019). Kelvin-Helmholtz instability in self-gravitating streams. , 490(1):181–201.

Bahcall, J. N. and Salpeter, E. E. (1965). On the Interaction of Radiation from Distant Sources with the Intervening Medium. , 142:1677–1680.

Baldry, I. K., Alpaslan, M., Bauer, A. E., Bland -Hawthorn, J., Brough, S., Cluver, M. E., Croom, S. M., Davies, L. J. M., Driver, S. P., Gunawardhana, M. L. P., Holwerda, B. W., Hopkins, A. M., Kelvin, L. S., Liske, J., López-Sánchez, Á. R., Loveday, J., Norberg, P., Peacock, J., Robotham, A. S. G., and Taylor, E. N. (2014). Galaxy And Mass Assembly (GAMA): AUTOZ spectral redshift measurements, confidence and errors. , 441(3):2440–2451.

Baldry, I. K., Balogh, M. L., Bower, R., Glazebrook, K., and Nichol, R. C. (2004). Color bimodality: Implications for galaxy evolution. In Allen, R. E., Nanopoulos, D. V., and Pope, C. N., editors, The New Cosmology: Conference on Strings and Cosmology, volume 743 of American Institute of Physics Conference Series, pages 106–119.

Balogh, M. L., Baldry, I. K., Nichol, R., Miller, C., Bower, R., and Glazebrook, K. (2004). The Bimodal Galaxy Color Distribution: Dependence on Luminosity and Environment. , 615(2):L101–L104.

Barnes, J. and Hut, P. (1986). A hierarchical O(N log N) force-calculation algorithm. , 324(6096):446–449.

Beckmann, R. S., Devriendt, J., Slyz, A., Peirani, S., Richardson, M. L. A., Dubois, Y., Pichon, C., Chisari, N. E., Kaviraj, S., Laigle, C., and Volonteri, M. (2017). Cosmic evolution of stellar quenching by AGN feedback: clues from the Horizon-AGN simulation. , 472(1):949–965.

Beckmann, R. S., Slyz, A., and Devriendt, J. (2018). Bondi or not Bondi: the impact of resolution on accretion and drag force modelling for supermassive black holes. , 478(1):995–1016.

Behroozi, P. S., Wechsler, R. H., and Conroy, C. (2013). The Average Star Formation Histories of Galaxies in Dark Matter Halos from z = 0-8. , 770(1):57.

Berlok, T. and Pfrommer, C. (2019a). On the Kelvin-Helmholtz instability with smooth initial conditions - linear theory and simulations. , 485(1):908–923.

Berlok, T. and Pfrommer, C. (2019b). The impact of magnetic fields on cold streams feeding galaxies. , 489(3):3368–3384.

Bi, H. and Davidsen, A. F. (1997). Evolution of Structure in the Intergalactic Medium and the Nature of the Lyα Forest. , 479(2):523–542.

Bigiel, F., Leroy, A. K., Walter, F., Brinks, E., de Blok, W. J. G., Kramer, C., Rix, H. W., Schruba, A., Schuster, K.-F., Usero, A., and Wiesemeyer, H. W. (2011). A Constant Molecular Gas Depletion Time in Nearby Disk Galaxies. , 730:L13.

Birnboim, Y. and Dekel, A. (2003). Virial shocks in galactic haloes? , 345:349–364.

Blondin, J. M., Wright, E. B., Borkowski, K. J., and Reynolds, S. P. (1998). Transition to the Radiative Phase in Supernova Remnants. , 500(1):342–354.

Bolton, J. S., Becker, G. D., Raskutti, S., Wyithe, J. S. B., Haehnelt, M. G., and Sargent, W. L. W. (2012). Improved measurements of the intergalactic medium temperature around quasars: possible evidence for the initial stages of He II reionization at z 6. , 419(4):2880–2892.

Bond, J. R., Kofman, L., and Pogosyan, D. (1996). How filaments of galaxies are woven into the cosmic web. , 380:603–606.

Bondi, H. and Hoyle, F. (1944). On the mechanism of accretion by stars. , 104:273.

Borisova, E., Cantalupo, S., Lilly, S. J., Marino, R. A., Gallego, S. G., Bacon, R., Blaizot, J., Bouché, N., Brinchmann, J., Carollo, C. M., Caruana, J., Finley, H., Herenz, E. C., Richard, J., Schaye, J., Straka, L. A., Turner, M. L., Urrutia, T., Verhamme, A., and Wisotzki, L. (2016). Ubiquitous Giant Lyα Nebulae around the Brightest Quasars at z 3.5 Revealed with MUSE. , 831(1):39.

Bouché, N., Finley, H., Schroetter, I., Murphy, M. T., Richter, P., Bacon, R., Contini, T., Richard, J., Wendt, M., Kamann, S., Epinat, B., Cantalupo, S., Straka, L. A., Schaye, J., Martin, C. L., Péroux, C., Wisotzki, L., Soto, K., Lilly, S., Carollo, C. M., Brinchmann, J., and Kollatschny, W. (2016). Possible Signatures of a Cold-flow Disk from MUSE Using a z $\sim$ 1 Galaxy-Quasar Pair toward SDSS J1422-0001. , 820(2):121.

Bouché, N., Murphy, M. T., Kacprzak, G. G., Péroux, C., Contini, T., Martin, C. L., and Dessauges-Zavadsky, M. (2013). Signatures of Cool Gas Fueling a Star-Forming Galaxy at Redshift 2.3. Science, 341(6141):50–53.

Bournaud, F., Combes, F., Jog, C. J., and Puerari, I. (2005). Lopsided spiral galaxies: evidence for gas accretion. , 438(2):507–520.

Boylan-Kolchin, M., Bullock, J. S., and Kaplinghat, M. (2011). Too big to fail? The puzzling darkness of massive Milky Way subhaloes. , 415(1):L40–L44.

Brooks, A. M., Governato, F., Quinn, T., Brook, C. B., and Wadsley, J. (2009). The Role of Cold Flows in the Assembly of Galaxy Disks. , 694(1):396–410.

Brown, T. M., Tumlinson, J., Geha, M., Kirby, E. N., VandenBerg, D. A., Muñoz, R. R., Kalirai, J. S., Simon, J. D., Avila, R. J., Guhathakurta, P., Renzini, A., and Ferguson, H. C. (2012). The Primeval Populations of the Ultra-faint Dwarf Galaxies. , 753(1):L21.

Bryan, G. L., Norman, M. L., O'Shea, B. W., Abel, T., Wise, J. H., Turk, M. J., Reynolds, D. R., Collins, D. C., Wang, P., Skillman, S. W., Smith, B., Harkness, R. P., Bordner, J., Kim, J.-h., Kuhlen, M., Xu, H., Goldbaum, N., Hummels, C., Kritsuk, A. G., Tasker, E., Skory, S., Simpson, C. M., Hahn, O., Oishi, J. S., So, G. C., Zhao, F., Cen, R., Li, Y., and Enzo Collaboration (2014). ENZO: An Adaptive Mesh Refinement Code for Astrophysics. , 211(2):19.

Cadiou, C., Dubois, Y., and Pichon, C. (2019). Accurate tracer particles of baryon dynamics in the adaptive mesh refinement code Ramses. , 621:A96.

Calverley, A. P., Becker, G. D., Haehnelt, M. G., and Bolton, J. S. (2011). Measurements of the ultraviolet background at 4.6 ¡ z ¡ 6.4 using the quasar proximity effect. , 412(4):2543–2562.

Cantalupo, S., Arrigoni-Battaia, F., Prochaska, J. X., Hennawi, J. F., and Madau, P. (2014). A cosmic web filament revealed in Lyman-α emission around a luminous high-redshift quasar. , 506:63–66.

Casuso, E. and Beckman, J. E. (2004). The K-dwarf problem and the time-dependence of gaseous accretion to the Galactic disc. , 419:181–190.

Cautun, M., van de Weygaert, R., and Jones, B. J. T. (2013). NEXUS: tracing the cosmic web connection. , 429(2):1286–1308.

Cautun, M., van de Weygaert, R., Jones, B. J. T., and Frenk, C. S. (2014). Evolution of the cosmic web. , 441(4):2923–2973.

Cen, R. (2014). Evolution of Cold Streams and the Emergence of the Hubble Sequence. , 789(1):L21.

Cen, R., Miralda-Escudé, J., Ostriker, J. P., and Rauch, M. (1994). Gravitational Collapse of Small-Scale Structure as the Origin of the Lyman-Alpha Forest. , 437:L9.

Ceverino, D., Dekel, A., and Bournaud, F. (2010). High-redshift clumpy discs and bulges in cosmological simulations. , 404(4):2151–2169.

Ceverino, D. and Klypin, A. (2009). The Role of Stellar Feedback in the Formation of Galaxies. , 695(1):292–309.

Chabanier, S., Bournaud, F., Dubois, Y., Codis, S., Chapon, D., Elbaz, D., Pichon, C., Bressand, O., Devriendt, J., Gavazzi, R., Kraljic, K., Kimm, T., Laigle, C., Lekien, J.-B., Martin, G., Palanque-Delabrouille, N., Peirani, S., Piserchia, P.-F., Slyz, A., Trebitsch, M., and Yèche, C. (2020). Formation of compact galaxies in the Extreme-Horizon simulation. arXiv e-prints, page arXiv:2007.04624.

Chabrier, G. (2003). Galactic Stellar and Substellar Initial Mass Function. , 115(809):763–795.

Chardin, J., Puchwein, E., and Haehnelt, M. G. (2017). Large-scale opacity fluctuations in the Lyα forest: evidence for QSOs dominating the ionizing UV background at z $\sim$ 5.5-6? , 465(3):3429–3445.

Charlton, J. C. and Churchill, C. W. (1998). The Kinematic Composition of Mg II Absorbers. , 499(1):181–197.

Chen, Y.-C., Ho, S., Blazek, J., He, S., Mandelbaum, R., Melchior, P., and Singh, S. (2019). Detecting galaxy-filament alignments in the Sloan Digital Sky Survey III. , 485(2):2492–2504.

Chevalier, R. A. (1974). The Evolution of Supernova Remnants. Spherically Symmetric Models. , 188:501–516.

Cioffi, D. F., McKee, C. F., and Bertschinger, E. (1988). Dynamics of Radiative Supernova Remnants. , 334:252.

Codis, S., Pichon, C., Devriendt, J., Slyz, A., Pogosyan, D., Dubois, Y., and Sousbie, T. (2012). Connecting the cosmic web to the spin of dark haloes: implications for galaxy formation. Monthly Notices of the Royal Astronomical Society, 427(4):3320–3336.

Codis, S., Pichon, C., and Pogosyan, D. (2015). Spin alignments within the cosmic web: a theory of constrained tidal torques near filaments. Monthly Notices of the Royal Astronomical Society, 452(4):3369–3393.

Codis, S., Pogosyan, D., and Pichon, C. (2018a). On the connectivity of the cosmic web: theory and implications for cosmology and galaxy formation. , 479(1):973–993.

Codis, S., Pogosyan, D., and Pichon, C. (2018b). On the connectivity of the cosmic web: theory and implications for cosmology and galaxy formation. ArXiv e-prints.

Colberg, J. M., Krughoff, K. S., and Connolly, A. J. (2005). Intercluster filaments in a ΛCDM Universe. , 359:272–282.

Cornuault, N., Lehnert, M. D., Boulanger, F., and Guillard, P. (2018). Are cosmological gas accretion streams multiphase and turbulent? , 610:A75.

Courant, R., Friedrichs, K., and Lewy, H. (1928). Über die partiellen Differenzengleichungen der mathematischen Physik. Mathematische Annalen, 100:32–74.

Croton, D. J., Springel, V., White, S. D. M., De Lucia, G., Frenk, C. S., Gao, L., Jenkins, A., Kauffmann, G., Navarro, J. F., and Yoshida, N. (2006). The many lives of active galactic nuclei: cooling flows, black holes and the luminosities and colours of galaxies. , 365(1):11–28.

D'Aloisio, A., McQuinn, M., and Trac, H. (2015). Large Opacity Variations in the High-redshift Lyα Forest: The Signature of Relic Temperature Fluctuations from Patchy Reionization. , 813(2):L38.

Danovich, M., Dekel, A., Hahn, O., and Teyssier, R. (2012). Coplanar streams, pancakes and angular-momentum exchange in high-z disc galaxies. , 422:1732–1749.

Davé, R., Anglés-Alcázar, D., Narayanan, D., Li, Q., Rafieferantsoa, M. H., and Appleby, S. (2019). SIMBA: Cosmological simulations with black hole growth and feedback. , 486(2):2827–2849.

Davé, R., Thompson, R., and Hopkins, P. F. (2016). MUFASA: galaxy formation simulations with meshless hydrodynamics. , 462(3):3265–3284.

Davidge, T. J., McConnachie, A. W., Fardal, M. A., Fliri, J., Valls-Gabaud, D., Chapman, S. C., Lewis, G. F., and Rich, R. M. (2012). THE RECENT STELLAR ARCHEOLOGY OF m31—THE NEAREST RED DISK GALAXY. The Astrophysical Journal, 751(1):74.

Davis, M., Huchra, J., Latham, D. W., and Tonry, J. (1982). A survey of galaxy redshifts. II - The large scale space distribution. , 253:423–445.

de Lapparent, V., Geller, M. J., and Huchra, J. P. (1986). A slice of the universe. , 302:L1–L5.

Dekel, A. and Birnboim, Y. (2006). Galaxy bimodality due to cold flows and shock heating. , 368:2–20.

Dekel, A., Birnboim, Y., Engel, G., Freundlich, J., Goerdt, T., Mumcuoglu, M., Neistein, E., Pichon, C., Teyssier, R., and Zinger, E. (2009). Cold streams in early massive hot haloes as the main mode of galaxy formation. , 457:451–454.

Dekel, A. and Silk, J. (1986). The Origin of Dwarf Galaxies, Cold Dark Matter, and Biased Galaxy Formation. , 303:39.

Diemer, B. and Kravtsov, A. V. (2014). Dependence of the Outer Density Profiles of Halos on Their Mass Accretion Rate. , 789(1):1.

Dijkstra, E. W. (1959). A note on two problems in connexion with graphs. Numerische Mathematik, 1(1):269–271.

Dijkstra, M. and Loeb, A. (2009). Lyα blobs as an observational signature of cold accretion streams into galaxies. , 400(2):1109–1120.

Dolag, K., Meneghetti, M., Moscardini, L., Rasia, E., and Bonaldi, A. (2006). Simulating the physical properties of dark matter and gas inside the cosmic web. , 370:656–672.

Doroshkevich, A. G. (1970). The space structure of perturbations and the origin of rotation of galaxies in the theory of fluctuation. Astrofizika, 6:581–600.

Dubois, Y., Beckmann, R., Bournaud, F., Choi, H., Devriendt, J., Jackson, R., Kaviraj, S., Kimm, T., Kraljic, K., Laigle, C., Martin, G., Park, M.-J., Peirani, S., Pichon, C., Volonteri, M., and Yi, S. K. (2020). Introducing the NewHorizon simulation: galaxy properties with resolved internal dynamics across cosmic time. arXiv e-prints, page arXiv:2009.10578.

Dubois, Y., Pichon, C., Devriendt, J., Silk, J., Haehnelt, M., Kimm, T., and Slyz, A. (2013). Blowing cold flows away: the impact of early AGN activity on the formation of a brightest cluster galaxy progenitor. , 428(4):2885–2900.

Dubois, Y., Pichon, C., Welker, C., Le Borgne, D., Devriendt, J., Laigle, C., Codis, S., Pogosyan, D., Arnouts, S., Benabed, K., Bertin, E., Blaizot, J., Bouchet, F., Cardoso, J.-F., Colombi, S., de Lapparent, V., Desjacques, V., Gavazzi, R., Kassin, S., Kimm, T., McCracken, H., Milliard, B., Peirani, S., Prunet, S., Rouberol, S., Silk, J., Slyz, A., Sousbie, T., Teyssier, R., Tresse, L., Treyer, M., Vibert, D., and Volonteri, M. (2014a). Dancing in the dark: galactic properties trace spin swings along the cosmic web. , 444:1453–1468.

Dubois, Y. and Teyssier, R. (2008). On the onset of galactic winds in quiescent star forming galaxies. , 477(1):79–94.

Dubois, Y., Volonteri, M., Silk, J., Devriendt, J., and Slyz, A. (2014b). Black hole evolution - II. Spinning black holes in a supernova-driven turbulent interstellar medium. , 440(3):2333–2346.

Dunkley, J., Komatsu, E., Nolta, M. R., Spergel, D. N., Larson, D., Hinshaw, G., Page, L., Bennett, C. L., Gold, B., Jarosik, N., Weiland, J. L., Halpern, M., Hill, R. S., Kogut, A., Limon, M., Meyer, S. S., Tucker, G. S., Wollack, E., and Wright, E. L. (2009). Five-Year Wilkinson Microwave Anisotropy Probe Observations: Likelihoods and Parameters from the WMAP Data. , 180:306–329.

Efstathiou, G. (1992). Suppressing the formation of dwarf galaxies via photoionization. , 256(2):43P–47P.

Eisenstein, D. J. and Hut, P. (1998). HOP: A New Group-Finding Algorithm for N-Body Simulations. , 498(1):137–142.

El-Badry, K., Quataert, E., Wetzel, A., Hopkins, P. F., Weisz, D. R., Chan, T. K., Fitts, A., Boylan-Kolchin, M., Kereš, D., Faucher-Giguère, C.-A., and Garrison-Kimmel, S. (2018). Gas kinematics, morphology and angular momentum in the FIRE simulations. , 473(2):1930–1955.

Elias, L. M., Genel, S., Sternberg, A., Devriendt, J., Slyz, A., Visbal, E., and Bouché, N. (2020). Detecting the cosmic web: Lyα emission from simulated filaments at z = 3. , 494(4):5439–5448.

Elmegreen, D. M., Elmegreen, B. G., Ravindranath, S., and Coe, D. A. (2007). Resolved Galaxies in the Hubble Ultra Deep Field: Star Formation in Disks at High Redshift. , 658(2):763–777.

Erdoğdu, P., Lahav, O., Zaroubi, S., Efstathiou, G., Moody, S., Peacock, J. A., Colless, M., Baldry, I. K., Baugh, C. M., Bland-Hawthorn, J., Bridges, T., Cannon, R., Cole, S., Collins, C., Couch, W., Dalton, G., De Propris, R., Driver, S. P., Ellis, R. S., Frenk, C. S., Glazebrook, K., Jackson, C., Lewis, I., Lumsden, S., Maddox, S., Madgwick, D., Norberg, P., Peterson, B. A., Sutherland, W., and Taylor, K. (2004). The 2dF Galaxy Redshift Survey: Wiener reconstruction of the cosmic web. , 352(3):939–960.

Falck, B. and Neyrinck, M. C. (2015). The persistent percolation of single-stream voids. , 450(3):3239–3253.

Falck, B. L., Neyrinck, M. C., and Szalay, A. S. (2012). ORIGAMI: Delineating Halos Using Phase-space Folds. , 754(2):126.

Faucher-Giguère, C.-A. and Kereš, D. (2011). The small covering factor of cold accretion streams. , 412(1):L118–L122.

Federrath, C. and Klessen, R. S. (2012). The Star Formation Rate of Turbulent Magnetized Clouds: Comparing Theory, Simulations, and Observations. , 761(2):156.

Ferland, G. J., Korista, K. T., Verner, D. A., Ferguson, J. W., Kingdon, J. B., and Verner, E. M. (1998). CLOUDY 90: Numerical Simulation of Plasmas and Their Spectra. , 110(749):761–778.

Ferrarese, L. and Merritt, D. (2000). A Fundamental Relation between Supermassive Black Holes and Their Host Galaxies. , 539(1):L9–L12.

Forero-Romero, J. E., Hoffman, Y., Gottlöber, S., Klypin, A., and Yepes, G. (2009). A dynamical classification of the cosmic web. , 396(3):1815–1824.

Förster Schreiber, N. M., Genzel, R., Bouché, N., Cresci, G., Davies, R., Buschkamp, P., Shapiro, K., Tacconi, L. J., Hicks, E. K. S., Genel, S., Shapley, A. E., Erb, D. K., Steidel, C. C., Lutz, D., Eisenhauer, F., Gillessen, S., Sternberg, A., Renzini, A., Cimatti, A., Daddi, E., Kurk, J., Lilly, S., Kong, X., Lehnert, M. D., Nesvadba, N., Verma, A., McCracken, H., Arimoto, N., Mignoli, M., and Onodera, M. (2009). The SINS Survey: SINFONI Integral Field Spectroscopy of z ~2 Star-forming Galaxies. , 706(2):1364–1428.

Förster Schreiber, N. M., Genzel, R., Lehnert, M. D., Bouché, N., Verma, A., Erb, D. K., Shapley, A. E., Steidel, C. C., Davies, R., Lutz, D., Nesvadba, N., Tacconi, L. J., Eisenhauer, F., Abuter, R., Gilbert, A., Gillessen, S., and Sternberg, A. (2006). SINFONI Integral Field Spectroscopy of z ~2 UV-selected Galaxies: Rotation Curves and Dynamical Evolution. , 645(2):1062–1075.

Fraternali, F. and Binney, J. J. (2008). Accretion of gas on to nearby spiral galaxies. , 386(2):935–944.

Fraternali, F., Marasco, A., Armillotta, L., and Marinacci, F. (2015). Galactic hail: the origin of the high-velocity cloud complex C. , 447:L70–L74.

French, D. M. and Wakker, B. P. (2020). Evidence for a Rotational Component in the Circumgalactic Medium of Nearby Galaxies. , 897(2):151.

Freundlich, J., Jog, C. J., and Combes, F. (2014). Local stability of a gravitating filament: a dispersion relation. , 564:A7.

Fryxell, B., Olson, K., Ricker, P., Timmes, F. X., Zingale, M., Lamb, D. Q., MacNeice, P., Rosner, R., Truran, J. W., and Tufo, H. (2000). FLASH: An Adaptive Mesh Hydrodynamics Code for Modeling Astrophysical Thermonuclear Flashes. , 131(1):273–334.

Fumagalli, M., Mackenzie, R., Trayford, J., Theuns, T., Cantalupo, S., Christensen, L., Fynbo, J. P. U., Møller, P., O'Meara, J., Prochaska, J. X., Rafelski, M., and Shanks, T. (2017). Witnessing galaxy assembly in an extended z≈3 structure. , 471(3):3686–3698.

Fumagalli, M., Prochaska, J. X., Kasen, D., Dekel, A., Ceverino, D., and Primack, J. R. (2011). Absorption-line systems in simulated galaxies fed by cold streams. , 418(3):1796–1821.

Gallego, S. G., Cantalupo, S., Lilly, S., Marino, R. A., Pezzulli, G., Schaye, J., Wisotzki, L., Bacon, R., Inami, H., Akhlaghi, M., Tacchella, S., Richard, J., Bouche, N., Steinmetz, M., and Carollo, M. (2017). Stacking the Cosmic Web in Fluorescent Lyman alpha Emission with MUSE. ArXiv e-prints.

Ganeshaiah Veena, P., Cautun, M., van de Weygaert, R., Tempel, E., Jones, B. J. T., Rieder, S., and Frenk, C. S. (2018). The Cosmic Ballet: spin and shape alignments of haloes in the cosmic web. , 481:414–438.

Gardner, J. P., Mather, J. C., Clampin, M., Doyon, R., Greenhouse, M. A., Hammel, H. B., Hutchings, J. B., Jakobsen, P., Lilly, S. J., Long, K. S., Lunine, J. I., McCaughrean, M. J., Mountain, M., Nella, J., Rieke, G. H., Rieke, M. J., Rix, H.-W., Smith, E. P., Sonneborn, G., Stiavelli, M., Stockman, H. S., Windhorst, R. A., and Wright, G. S. (2006). The James Webb Space Telescope. , 123(4):485–606.

Geller, M. J. and Huchra, J. P. (1989). Mapping the Universe. Science, 246(4932):897–903.

Genzel, R., Burkert, A., Bouché, N., Cresci, G., Förster Schreiber, N. M., Shapley, A., Shapiro, K., Tacconi, L. J., Buschkamp, P., Cimatti, A., Daddi, E., Davies, R., Eisenhauer, F., Erb, D. K., Genel, S., Gerhard, O., Hicks, E., Lutz, D., Naab, T., Ott, T., Rabien, S., Renzini, A., Steidel, C. C., Sternberg, A., and Lilly, S. J. (2008). From Rings to Bulges: Evidence for Rapid Secular Galaxy Evolution at z ~2 from Integral Field Spectroscopy in the SINS Survey. , 687(1):59–77.

Genzel, R., Tacconi, L. J., Eisenhauer, F., Förster Schreiber, N. M., Cimatti, A., Daddi, E., Bouché, N., Davies, R., Lehnert, M. D., Lutz, D., Nesvadba, N., Verma, A., Abuter, R., Shapiro, K., Sternberg, A., Renzini, A., Kong, X., Arimoto, N., and Mignoli, M. (2006). The rapid formation of a large rotating disk galaxy three billion years after the Big Bang. , 442(7104):786–789.

George, K. (2017). Structural analysis of star-forming blue early-type galaxies. Merger-driven star formation in elliptical galaxies. , 598:A45.

Gheller, C., Vazza, F., Brüggen, M., Alpaslan, M., Holwerda, B. W., Hopkins, A. M., and Liske, J. (2016). Evolution of cosmic filaments and of their galaxy population from MHD cosmological simulations. , 462(1):448–463.

Gheller, C., Vazza, F., Favre, J., and Brüggen, M. (2015). Properties of cosmological filaments extracted from Eulerian simulations. , 453(2):1164–1185.

Giavalisco, M., Vanzella, E., Salimbeni, S., Tripp, T. M., Dickinson, M., Cassata, P., Renzini, A., Guo, Y., Ferguson, H. C., Nonino, M., Cimatti, A., Kurk, J., Mignoli, M., and Tang, Y. (2011). Discovery of Cold, Pristine Gas Possibly Accreting onto an Overdensity of Star-forming Galaxies at Redshift z ˜ 1.6. , 743:95.

Gnedin, N. Y. (2000). Effect of Reionization on Structure Formation in the Universe. , 542(2):535–541.

Goerdt, T. and Ceverino, D. (2015). Inflow velocities of cold flows streaming into massive galaxies at high redshifts. , 450(4):3359–3370.

Goerdt, T., Dekel, A., Sternberg, A., Gnat, O., and Ceverino, D. (2012). Detectability of cold streams into high-redshift galaxies by absorption lines. , 424(3):2292–2315.

González, M., Audit, E., and Huynh, P. (2007). HERACLES: a three-dimensional radiation hydrodynamics code. , 464(2):429–435.

González, R. E. and Padilla, N. D. (2010). Automated detection of filaments in the large-scale structure of the Universe. , 407(3):1449–1463.

Gott, J. Richard, I., Jurić, M., Schlegel, D., Hoyle, F., Vogeley, M., Tegmark, M., Bahcall, N., and Brinkmann, J. (2005). A Map of the Universe. , 624(2):463–484.

Gunn, J. E. and Gott, J. Richard, I. (1972). On the Infall of Matter Into Clusters of Galaxies and Some Effects on Their Evolution. , 176:1.

Guth, A. H. (1981). Inflationary universe: A possible solution to the horizon and flatness problems. , 23(2):347–356.

Haardt, F. and Madau, P. (1996). Radiative Transfer in a Clumpy Universe. II. The Ultraviolet Extragalactic Background. , 461:20.

Haardt, F. and Madau, P. (2012). Radiative Transfer in a Clumpy Universe. IV. New Synthesis Models of the Cosmic UV/X-Ray Background. , 746(2):125.

Hahn, O. and Abel, T. (2013). MUSIC: MUlti-Scale Initial Conditions.

Hahn, O., Carollo, C. M., Porciani, C., and Dekel, A. (2007). The evolution of dark matter halo properties in clusters, filaments, sheets and voids. , 381(1):41–51.

Hanson, D. and Lewis, A. (2009). Estimators for CMB statistical anisotropy. , 80(6):063004.

Harford, A. G. and Hamilton, A. J. S. (2011). Intergalactic filaments as isothermal gas cylinders. , 416(4):2678–2687.

Hernquist, L., Katz, N., Weinberg, D. H., and Miralda-Escudé, J. (1996). The Lyman-Alpha Forest in the Cold Dark Matter Model. , 457:L51.

Ho, S. H. and Martin, C. L. (2019). New Constraints on Models for Circumgalactic Gas Inflow: How Do Galaxies Get Their Gas at Low Redshift? arXiv e-prints, page arXiv:1901.11182.

Ho, S. H., Martin, C. L., Kacprzak, G. G., and Churchill, C. W. (2017). Quasars Probing Galaxies. I. Signatures of Gas Accretion at Redshift Approximately 0.2. , 835(2):267.

Hoeft, M., Yepes, G., Gottlöber, S., and Springel, V. (2006). Dwarf galaxies in voids: suppressing star formation with photoheating. , 371(1):401–414.

Hoffman, Y., Metuki, O., Yepes, G., Gottlöber, S., Forero-Romero, J. E., Libeskind, N. I., and Knebe, A. (2012). A kinematic classification of the cosmic web. , 425(3):2049–2057.

Hopkins, P. F., Narayanan, D., and Murray, N. (2013). The meaning and consequences of star formation criteria in galaxy models with resolved stellar feedback. , 432(4):2647–2653.

Hoyle, F. (1951). The Origin of the Rotations of the Galaxies. In Problems of Cosmical Aerodynamics, page 195.

Hoyle, F. and Lyttleton, R. A. (1939). The effect of interstellar matter on climatic variation. Proceedings of the Cambridge Philosophical Society, 35(3):405.

Hubble, E. P. (1926). Extragalactic nebulae. , 64:321–369.

Hummel, J. A., Pawlik, A. H., Milosavljević, M., and Bromm, V. (2012). The Source Density and Observability of Pair-instability Supernovae from the First Stars. , 755(1):72.

Hummels, C. B. and Bryan, G. L. (2012). Adaptive Mesh Refinement Simulations of Galaxy Formation: Exploring Numerical and Physical Parameters. , 749(2):140.

Hwang, H. S., Geller, M. J., Park, C., Fabricant, D. G., Kurtz, M. J., Rines, K. J., Kim, J., Diaferio, A., Zahid, H. J., Berlind, P., Calkins, M., Tokarz, S., and Moran, S. (2016). HectoMAP and Horizon Run 4: Dense Structures and Voids in the Real and Simulated Universe. , 818(2):173.

Iliev, I. T., Mellema, G., Ahn, K., Shapiro, P. R., Mao, Y., and Pen, U.-L. (2014). Simulating cosmic reionization: how large a volume is large enough? , 439(1):725–743.

Iliev, I. T., Mellema, G., Shapiro, P. R., and Pen, U.-L. (2007). Self-regulated reionization. , 376(2):534–548.

Jeans, J. H. (1915). On the theory of star-streaming and the structure of the universe. , 76:70–84.

Jian, H.-Y., Lin, L., and Chiueh, T. (2012). Environmental Dependence of the Galaxy Merger Rate in a ΛCDM Universe. , 754(1):26.

Kacprzak, G. G., Churchill, C. W., Ceverino, D., Steidel, C. C., Klypin, A., and Murphy, M. T. (2010). Halo Gas and Galaxy Disk Kinematics Derived from Observations and ΛCDM Simulations of Mg II Absorption-selected Galaxies at Intermediate Redshift. , 711(2):533–558.

Kacprzak, G. G., Churchill, C. W., and Nielsen, N. M. (2012). Tracing Outflows and Accretion: A Bimodal Azimuthal Dependence of Mg II Absorption. , 760:L7.

Kang, X. and Wang, P. (2015). The Accretion of Dark Matter Subhalos within the Cosmic Web: Primordial Anisotropic Distribution and its Universality. , 813(1):6.

Kassin, S. A., Weiner, B. J., Faber, S. M., Gardner, J. P., Willmer, C. N. A., Coil, A. L., Cooper, M. C., Devriendt, J., Dutton, A. A., Guhathakurta, P., Koo, D. C., Metevier, A. J., Noeske, K. G., and Primack, J. R. (2012). The Epoch of Disk Settling: z ~1 to Now. , 758(2):106.

Katz, H., Kimm, T., Sijacki, D., and Haehnelt, M. G. (2017). Interpreting ALMA observations of the ISM during the epoch of reionization. , 468(4):4831–4861.

Katz, H., Ramsoy, M., Rosdahl, J., Kimm, T., Blaizot, J., Haehnelt, M. G., Michel-Dansac, L., Garel, T., Laigle, C., and Devriendt, J. (2019). How to Quench a Dwarf Galaxy: The Impact of Inhomogeneous Reionization on Dwarf Galaxies and Cosmic Filaments. arXiv e-prints, page arXiv:1905.11414.

Katz, N. (1992). Dissipational galaxy formation. II - Effects of star formation. , 391:502–517.

Katz, N., Keres, D., Dave, R., Weinberg, D. H., Rosenberg, J., and Putman, M. (2003). How do galaxies get their gas? Astrophysics and Space Science Library, 281:185–192.

Kauffmann, G., Heckman, T. M., Tremonti, C., Brinchmann, J., Charlot, S., White, S. D. M., Ridgway, S. E., Brinkmann, J., Fukugita, M., Hall, P. B., Ivezić, Ž., Richards, G. T., and Schneider, D. P. (2003). The host galaxies of active galactic nuclei. , 346(4):1055–1077.

Kaviraj, S., Laigle, C., Kimm, T., Devriendt, J. E. G., Dubois, Y., Pichon, C., Slyz, A., Chisari, E., and Peirani, S. (2017). The Horizon-AGN simulation: evolution of galaxy properties over cosmic time. , 467(4):4739–4752.

Kay, S. T., Thomas, P. A., and Theuns, T. (2003). The impact of galaxy formation on X-ray groups. , 343(2):608–618.

Kennicutt, Robert C., J. (1998). The Global Schmidt Law in Star-forming Galaxies. , 498(2):541–552.

Keres, D. (2009). Galaxy Buildup by Gas Accretion. In American Astronomical Society Meeting Abstracts #213, volume 213 of American Astronomical Society Meeting Abstracts, page 313.06.

Kereš, D., Katz, N., Weinberg, D. H., and Davé, R. (2005). How do galaxies get their gas? , 363:2–28.

Kereš, D. and Hernquist, L. (2009). Seeding the Formation of Cold Gaseous Clouds in Milky Way-Size Halos. , 700(1):L1–L5.

Khandai, N., Di Matteo, T., Croft, R., Wilkins, S., Feng, Y., Tucker, E., DeGraf, C., and Liu, M.-S. (2015). The MassiveBlack-II simulation: the evolution of haloes and galaxies to z $\sim$ 0. , 450(2):1349–1374.

Kikuta, S., Matsuda, Y., Cen, R., Steidel, C. C., Yagi, M., Hayashino, T., Imanishi, M., Komiyama, Y., Momose, R., and Saito, T. (2019). Lyα view around a z = 2.84 hyperluminous QSO at a node of the cosmic web. , 71(3):L2.

Kimm, T. and Cen, R. (2014). Escape Fraction of Ionizing Photons during Reionization: Effects due to Supernova Feedback and Runaway OB Stars. , 788(2):121.

Kimm, T., Cen, R., Devriendt, J., Dubois, Y., and Slyz, A. (2015). Towards simulating star formation in turbulent high-z galaxies with mechanical supernova feedback. , 451:2900–2921.

Kimm, T., Devriendt, J., Slyz, A., Pichon, C., Kassin, S. A., and Dubois, Y. (2011a). The angular momentum of baryons and dark matter halos revisited. ArXiv e-prints.

Kimm, T., Devriendt, J., Slyz, A., Pichon, C., Kassin, S. A., and Dubois, Y. (2011b). The angular momentum of baryons and dark matter halos revisited. ArXiv e-prints.

Kimm, T., Haehnelt, M., Blaizot, J., Katz, H., Michel-Dansac, L., Garel, T., Rosdahl, J., and Teyssier, R. (2018). Impact of Lyman alpha pressure on metal-poor dwarf galaxies. , 475(4):4617–4635.

Kitaura, F.-S. and Angulo, R. E. (2012). Linearization with cosmological perturbation theory. , 425(4):2443–2454.

Klar, J. S. and Mücket, J. P. (2012). Filaments and sheets of the warm-hot intergalactic medium. , 423:304–319.

Klessen, R. S. and Hennebelle, P. (2010). Accretion-driven turbulence as universal process: galaxies, molecular clouds, and protostellar disks. , 520:A17.

Klypin, A., Kravtsov, A. V., Valenzuela, O., and Prada, F. (1999). Where Are the Missing Galactic Satellites? , 522(1):82–92.

Knebe, A., Knollmann, S. R., Muldrew, S. I., Pearce, F. R., Aragon-Calvo, M. A., Ascasibar, Y., Behroozi, P. S., Ceverino, D., Colombi, S., Diemand, J., Dolag, K., Falck, B. L., Fasel, P., Gardner, J., Gottlöber, S., Hsu, C.-H., Iannuzzi, F., Klypin, A., Lukić, Z., Maciejewski, M., McBride, C., Neyrinck, M. C., Planelles, S., Potter, D., Quilis, V., Rasera, Y., Read, J. I., Ricker, P. M., Roy, F., Springel, V., Stadel, J., Stinson, G., Sutter, P. M., Turchaninov, V., Tweed, D., Yepes, G., and Zemp, M. (2011). Haloes gone MAD: The Halo-Finder Comparison Project. , 415(3):2293–2318.

Komatsu, E., Smith, K. M., Dunkley, J., Bennett, C. L., Gold, B., Hinshaw, G., Jarosik, N., Larson, D., Nolta, M. R., Page, L., Spergel, D. N., Halpern, M., Hill, R. S., Kogut, A., Limon, M., Meyer, S. S., Odegard, N., Tucker, G. S., Weiland, J. L., Wollack, E., and Wright, E. L. (2011). Seven-year Wilkinson Microwave Anisotropy Probe (WMAP) Observations: Cosmological Interpretation. , 192(2):18.

Kraljic, K., Pichon, C., Dubois, Y., Codis, S., Cadiou, C., Devriendt, J., Musso, M., Welker, C., Arnouts, S., Hwang, H. S., Laigle, C., Peirani, S., Slyz, A., Treyer, M., and Vibert, D. (2019). Galaxies flowing in the oriented saddle frame of the cosmic web. , 483(3):3227–3254.

Kravtsov, A. V., Klypin, A. A., and Khokhlov, A. M. (1997). Adaptive Refinement Tree: A New High-Resolution N-Body Code for Cosmological Simulations. , 111(1):73–94.

Kriek, M., van Dokkum, P. G., Franx, M., Illingworth, G. D., and Magee, D. K. (2009). The Hubble Sequence Beyond z = 2 for Massive Galaxies: Contrasting Large Star-forming and Compact Quiescent Galaxies. , 705(1):L71–L75.

Krolewski, A., Ho, S., Chen, Y.-C., Chan, P. F., Tenneti, A., Bizyaev, D., and Kraljic, K. (2019). Alignment between filaments and galaxy spins from the MaNGA integral-field survey. arXiv e-prints, page arXiv:1902.09797.

Krumholz, M. R. and McKee, C. F. (2005). A General Theory of Turbulence-regulated Star Formation, from Spirals to Ultraluminous Infrared Galaxies. , 630(1):250–268.

Krumholz, M. R. and Tan, J. C. (2007). Slow Star Formation in Dense Gas: Evidence and Implications. , 654(1):304–315.

Kulkarni, G., Worseck, G., and Hennawi, J. F. (2019). Evolution of the AGN UV luminosity function from redshift 7.5. , 488(1):1035–1065.

Labbé, I., Rudnick, G., Franx, M., Daddi, E., van Dokkum, P. G., Förster Schreiber, N. M., Kuijken, K., Moorwood, A., Rix, H.-W., Röttgering, H., Trujillo, I., van der Wel, A., van der Werf, P., and van Starkenburg, L. (2003). Large Disklike Galaxies at High Redshift. , 591(2):L95–L98.

Laigle, C., Pichon, C., Codis, S., Dubois, Y. le Borgne, D., Pogosyan, D., Devriendt, J., Peirani, S., Prunet, S., Rouberol, S., Slyz, A., and Sousbie, T. (2015). Swirling around filaments: are large-scale structure vortices spinning up dark halos? MNRAS, 446:2744–2759.

Larson, R. B. (1972). Infall of Matter in Galaxies. , 236(5340):21–23.

Laureijs, R., Amiaux, J., Arduini, S., Augueres, J. L., Brinchmann, J., Cole, R., Cropper, M., Dabin, C., Duvet, L., Ealet, A., Garilli, B., Gondoin, P., Guzzo, L., Hoar, J., Hoekstra, H., Holmes, R., Kitching, T., Maciaszek, T., Mellier, Y., Pasian, F., Percival,

W., Rhodes, J., Saavedra Criado, G., Sauvage, M., Scaramella, R., Valenziano, L., Warren, S., Bender, R., Castander, F., Cimatti, A., Le Fèvre, O., Kurki-Suonio, H., Levi, M., Lilje, P., Meylan, G., Nichol, R., Pedersen, K., Popa, V., Rebolo Lopez, R., Rix, H. W., Rottgering, H., Zeilinger, W., Grupp, F., Hudelot, P., Massey, R., Meneghetti, M., Miller, L., Paltani, S., Paulin-Henriksson, S., Pires, S., Saxton, C., Schrabback, T., Seidel, G., Walsh, J., Aghanim, N., Amendola, L., Bartlett, J., Baccigalupi, C., Beaulieu, J. P., Benabed, K., Cuby, J. G., Elbaz, D., Fosalba, P., Gavazzi, G., Helmi, A., Hook, I., Irwin, M., Kneib, J. P., Kunz, M., Mannucci, F., Moscardini, L., Tao, C., Teyssier, R., Weller, J., Zamorani, G., Zapatero Osorio, M. R., Boulade, O., Foumond, J. J., Di Giorgio, A., Guttridge, P., James, A., Kemp, M., Martignac, J., Spencer, A., Walton, D., Blümchen, T., Bonoli, C., Bortoletto, F., Cerna, C., Corcione, L., Fabron, C., Jahnke, K., Ligori, S., Madrid, F., Martin, L., Morgante, G., Pamplona, T., Prieto, E., Riva, M., Toledo, R., Trifoglio, M., Zerbi, F., Abdalla, F., Douspis, M., Grenet, C., Borgani, S., Bouwens, R., Courbin, F., Delouis, J. M., Dubath, P., Fontana, A., Frailis, M., Grazian, A., Koppenhöfer, J., Mansutti, O., Melchior, M., Mignoli, M., Mohr, J., Neissner, C., Noddle, K., Poncet, M., Scodeggio, M., Serrano, S., Shane, N., Starck, J. L., Surace, C., Taylor, A., Verdoes-Kleijn, G., Vuerli, C., Williams, O. R., Zacchei, A., Altieri, B., Escudero Sanz, I., Kohley, R., Oosterbroek, T., Astier, P., Bacon, D., Bardelli, S., Baugh, C., Bellagamba, F., Benoist, C., Bianchi, D., Biviano, A., Branchini, E., Carbone, C., Cardone, V., Clements, D., Colombi, S., Conselice, C., Cresci, G., Deacon, N., Dunlop, J., Fedeli, C., Fontanot, F., Franzetti, P., Giocoli, C., Garcia-Bellido, J., Gow, J., Heavens, A., Hewett, P., Heymans, C., Holland, A., Huang, Z., Ilbert, O., Joachimi, B., Jennins, E., Kerins, E., Kiessling, A., Kirk, D., Kotak, R., Krause, O., Lahav, O., van Leeuwen, F., Lesgourgues, J., Lombardi, M., Magliocchetti, M., Maguire, K., Majerotto, E., Maoli, R., Marulli, F., Maurogordato, S., McCracken, H., McLure, R., Melchiorri, A., Merson, A., Moresco, M., Nonino, M., Norberg, P., Peacock, J., Pello, R., Penny, M., Pettorino, V., Di Porto, C., Pozzetti, L., Quercellini, C., Radovich, M., Rassat, A., Roche, N., Ronayette, S., Rossetti, E., Sartoris, B., Schneider, P., Semboloni, E., Serjeant, S., Simpson, F., Skordis, C., Smadja, G., Smartt, S., Spano, P., Spiro, S., Sullivan, M., Tilquin, A., Trotta, R., Verde, L., Wang, Y., Williger, G., Zhao, G., Zoubian, J., and Zucca, E. (2011). Euclid Definition Study Report. arXiv e-prints, page arXiv:1110.3193.

Leclercq, F., Bacon, R., Wisotzki, L., Mitchell, P., Garel, T., Verhamme, A., Blaizot, J., Hashimoto, T., Herenz, E. C., Conseil, S., Cantalupo, S., Inami, H., Contini, T., Richard, J., Maseda, M., Schaye, J., Marino, R. A., Akhlaghi, M., Brinchmann, J., and Carollo, M. (2017). The MUSE Hubble Ultra Deep Field Survey. VIII. Extended Lyman-α haloes around high-z star-forming galaxies. , 608:A8.

Leclercq, F., Lavaux, G., Jasche, J., and Wand elt, B. (2016). Comparing cosmic web classifiers using information theory. , 2016(8):027.

Lee, K.-G., Bailey, S., Bartsch, L. E., Carithers, W., Dawson, K. S., Kirkby, D., Lundgren, B., Margala, D., Palanque-Delabrouille, N., Pieri, M. M., Schlegel, D. J., Weinberg, D. H., Yèche, C., Aubourg, É., Bautista, J., Bizyaev, D., Blomqvist, M., Bolton, A. S., Borde, A., Brewington, H., Busca, N. G., Croft, R. A. C., Delubac, T., Ebelke, G., Eisenstein, D. J., Font-Ribera, A., Ge, J., Hamilton, J.-C., Hennawi, J. F., Ho, S., Honscheid, K., Le Goff, J.-M., Malanushenko, E., Malanushenko, V., Miralda-Escudé, J., Myers, A. D., Noterdaeme, P., Oravetz, D., Pan, K., Pâris, I., Petitjean, P., Rich, J., Rollinde, E., Ross, N. P., Rossi, G., Schneider, D. P., Simmons, A., Snedden, S., Slosar, A., Spergel, D. N., Suzuki, N., Viel, M., and Weaver, B. A. (2013). The BOSS Lyα Forest Sample from SDSS Data Release 9. , 145(3):69.

Leitherer, C., Schaerer, D., Goldader, J. D., Delgado, R. M. G., Robert, C., Kune, D. F., de Mello, D. F., Devost, D., and Heckman, T. M. (1999). Starburst99: Synthesis Models for Galaxies with Active Star Formation. , 123(1):3–40.

Leroy, A. K., Walter, F., Sandstrom, K., Schruba, A., Munoz-Mateos, J.-C., Bigiel, F., Bolatto, A., Brinks, E., de Blok, W. J. G., Meidt, S., Rix, H.-W., Rosolowsky, E., Schinnerer, E., Schuster, K.-F., and Usero, A. (2013). Molecular Gas and Star Formation in nearby Disk Galaxies. , 146:19.

Levermore, C. D. (1984). Relating Eddington factors to flux limiters. , 31(2):149–160.

Libeskind, N. I., van de Weygaert, R., Cautun, M., Falck, B., Tempel, E., Abel, T., Alpaslan, M., Aragón-Calvo, M. A., Forero-Romero, J. E., Gonzalez, R., Gottlöber, S., Hahn, O., Hellwing, W. A., Hoffman, Y., Jones, B. J. T., Kitaura, F., Knebe, A., Manti, S., Neyrinck, M., Nuza, S. E., Padilla, N., Platen, E., Ramachandra, N., Robotham, A., Saar, E., Shand arin, S., Steinmetz, M., Stoica, R. S., Sousbie, T., and Yepes, G. (2018). Tracing the cosmic web. , 473(1):1195–1217.

Loeb, A. and Zaldarriaga, M. (2005). Small-scale power spectrum of cold dark matter. , 71(10):103520.

Mac Low, M.-M. and Klessen, R. S. (2004). Control of star formation by supersonic turbulence. Reviews of Modern Physics, 76(1):125–194.

MacArthur, L. A., Courteau, S., Bell, E., and Holtzman, J. A. (2004). Structure of Disk-dominated Galaxies. II. Color Gradients and Stellar Population Models. , 152(2):175–199.

Madau, P. and Dickinson, M. (2014). Cosmic Star Formation History. Ann. Rev. Astron. Astrophys., 52:415–486.

Magorrian, J., Tremaine, S., Richstone, D., Bender, R., Bower, G., Dressler, A., Faber, S. M., Gebhardt, K., Green, R., Grillmair, C., Kormendy, J., and Lauer, T. (1998). The Demography of Massive Dark Objects in Galaxy Centers. , 115(6):2285–2305.

Mandelker, N., Nagai, D., Aung, H., Dekel, A., Padnos, D., and Birnboim, Y. (2019). Instability of supersonic cold streams feeding Galaxies - III. Kelvin-Helmholtz instability in three dimensions. , 484:1100–1132.

Mandelker, N., Padnos, D., Dekel, A., Birnboim, Y., Burkert, A., Krumholz, M. R., and Steinberg, E. (2016). Instability of supersonic cold streams feeding galaxies - I. Linear Kelvin-Helmholtz instability with body modes. , 463:3921–3947.

Mandelker, N., van Dokkum, P. G., Brodie, J. P., van den Bosch, F. C., and Ceverino, D. (2018a). Cold Filamentary Accretion and the Formation of Metal-poor Globular Clusters and Halo Stars. , 861(2):148.

Mandelker, N., van Dokkum, P. G., Brodie, J. P., van den Bosch, F. C., and Ceverino, D. (2018b). Cold Filamentary Accretion and the Formation of Metal-poor Globular Clusters and Halo Stars. , 861:148.

Martin, C. L., Ho, S. H., Kacprzak, G. G., and Churchill, C. W. (2019). Kinematics of Circumgalactic Gas: Feeding Galaxies and Feedback. , 878(2):84.

Martin, D., Matuszewski, M., Morrissey, P., Neill, J., Moore, A., Steidel, C., and Trainor, R. (2016). A newly forming cold flow protogalactic disk, a signature of cold accretion from the cosmic web. The Astrophysical Journal Letters, 824(1):L5.

Martin, D. C., Chang, D., Matuszewski, M., Morrissey, P., Rahman, S., Moore, A., and Steidel, C. C. (2014a). Intergalactic Medium Emission Observations with the Cosmic Web Imager. I. The Circum-QSO Medium of QSO 1549+19, and Evidence for a Filamentary Gas Inflow. , 786(2):106.

Martin, D. C., Chang, D., Matuszewski, M., Morrissey, P., Rahman, S., Moore, A., Steidel, C. C., and Matsuda, Y. (2014b). Intergalactic Medium Emission Observations with the Cosmic Web Imager. II. Discovery of Extended, Kinematically Linked Emission around SSA22 Lyα Blob 2. , 786(2):107.

Martin, G., Kaviraj, S., Devriendt, J. E. G., Dubois, Y., and Pichon, C. (2018). The role of mergers in driving morphological transformation over cosmic time. , 480(2):2266–2283.

Mateo, M. L. (1998). Dwarf Galaxies of the Local Group. , 36:435–506.

Mather, J. C., Cheng, E. S., Eplee, R. E., J., Isaacman, R. B., Meyer, S. S., Shafer, R. A., Weiss, R., Wright, E. L., Bennett, C. L., Boggess, N. W., Dwek, E., Gulkis, S., Hauser, M. G., Janssen, M., Kelsall, T., Lubin, P. M., Moseley, S. H., J., Murdock, T. L., Silverberg, R. F., Smoot, G. F., and Wilkinson, D. T. (1990). A Preliminary Measurement of the Cosmic Microwave Background Spectrum by the Cosmic Background Explorer (COBE) Satellite. , 354:L37.

Matsuda, Y., Yamada, T., Hayashino, T., Yamauchi, R., and Nakamura, Y. (2006). A Keck/DEIMOS Spectroscopy of Lyα Blobs at Redshift z = 3.1. , 640(2):L123–L126.

Matsuda, Y., Yamada, T., Hayashino, T., Yamauchi, R., Nakamura, Y., Morimoto, N., Ouchi, M., Ono, Y., Kousai, K., Nakamura, E., Horie, M., Fujii, T., Umemura, M., and Mori, M. (2011). The Subaru Lyα blob survey: a sample of 100-kpc Lyα blobs at z = 3. , 410(1):L13–L17.

McQuinn, M. (2012). Constraints on X-ray emissions from the reionization era. , 426(2):1349–1360.

Melso, N., Bryan, G. L., and Li, M. (2019). Simulating Gas Inflow at the Disk-Halo Interface. , 872(1):47.

Mihalas, D. and Mihalas, B. W. (1984). Foundations of radiation hydrodynamics.

Miralda-Escudé, J. and Rees, M. J. (1994). Reionization and thermal evolution of a photoionized intergalactic medium. , 266:343–352.

Mitchell, P. D., Blaizot, J., Devriendt, J., Kimm, T., Michel-Dansac, L., Rosdahl, J., and Slyz, A. (2018). Gas flows in the circumgalactic medium around simulated high-redshift galaxies. , 474(4):4279–4301.

Moore, B. (1994). Evidence against dissipation-less dark matter from observations of galaxy haloes. , 370(6491):629–631.

Moore, B., Ghigna, S., Governato, F., Lake, G., Quinn, T., Stadel, J., and Tozzi, P. (1999). Dark Matter Substructure within Galactic Halos. , 524(1):L19–L22.

Muñoz-Cuartas, J. C., Macciò, A. V., Gottlöber, S., and Dutton, A. A. (2011). The redshift evolution of Λ cold dark matter halo parameters: concentration, spin and shape. , 411:584–594.

Müller, O. and Jerjen, H. (2020). The abundance of dwarf galaxies around low-mass giants in the Local Volume. arXiv e-prints, page arXiv:2008.08954.

Naab, T., Johansson, P. H., Ostriker, J. P., and Efstathiou, G. (2007). Formation of Early-Type Galaxies from Cosmological Initial Conditions. , 658(2):710–720.

Naab, T. and Ostriker, J. P. (2017). Theoretical Challenges in Galaxy Formation. , 55(1):59–109.

Navarro, J. F. and White, S. D. M. (1993). Simulations of Dissipative Galaxy Formation in Hierarchically Clustering Universes - Part One - Tests of the Code. , 265:271.

Neistein, E., van den Bosch, F. C., and Dekel, A. (2006). Natural downsizing in hierarchical galaxy formation. , 372:933–948.

Nelson, D., Pillepich, A., Springel, V., Pakmor, R., Weinberger, R., Genel, S., Torrey, P., Vogelsberger, M., Marinacci, F., and Hernquist, L. (2019). First Results from the TNG50 Simulation: Galactic outflows driven by supernovae and black hole feedback. arXiv e-prints.

Nelson, D., Springel, V., Pillepich, A., Rodriguez-Gomez, V., Torrey, P., Genel, S., Vogelsberger, M., Pakmor, R., Marinacci, F., Weinberger, R., Kelley, L., Lovell, M., Diemer, B., and Hernquist, L. (2018). The IllustrisTNG Simulations: Public Data Release. arXiv e-prints, page arXiv:1812.05609.

Nelson, D., Vogelsberger, M., Genel, S., Sijacki, D., Kereš, D., Springel, V., and Hernquist, L. (2013). Moving mesh cosmology: tracing cosmological gas accretion. , 429(4):3353–3370.

Noh, Y. and McQuinn, M. (2014). A physical understanding of how reionization suppresses accretion on to dwarf haloes. , 444(1):503–514.

Novikov, D., Colombi, S., and Doré, O. (2006). Skeleton as a probe of the cosmic web: the two-dimensional case. , 366(4):1201–1216.

Ocvirk, P., Aubert, D., Sorce, J. G., Shapiro, P. R., Deparis, N., Dawoodbhoy, T., Lewis, J., Teyssier, R., Yepes, G., Gottlöber, S., Ahn, K., Iliev, I. T., and Hoffman, Y. (2018). Cosmic Dawn II (CoDa II): a new radiation-hydrodynamics simulation of the self-consistent coupling of galaxy formation and reionization. ArXiv e-prints, page arXiv:1811.11192.

Ocvirk, P., Gillet, N., Shapiro, P. R., Aubert, D., Iliev, I. T., Teyssier, R., Yepes, G., Choi, J.-H., Sullivan, D., Knebe, A., Gottlöber, S., D'Aloisio, A., Park, H., Hoffman, Y., and Stranex, T. (2016a). Cosmic Dawn (CoDa): the First Radiation-Hydrodynamics Simulation of Reionization and Galaxy Formation in the Local Universe. , 463:1462–1485.

Ocvirk, P., Gillet, N., Shapiro, P. R., Aubert, D., Iliev, I. T., Teyssier, R., Yepes, G., Choi, J.-H., Sullivan, D., Knebe, A., Gottlöber, S., D'Aloisio, A., Park, H., Hoffman, Y., and Stranex, T. (2016b). Cosmic Dawn (CoDa): the First Radiation-Hydrodynamics Simulation of Reionization and Galaxy Formation in the Local Universe. , 463:1462–1485.

Ocvirk, P., Pichon, C., and Teyssier, R. (2008a). Bimodal gas accretion in the Horizon-MareNostrum galaxy formation simulation. , 390:1326–1338.

Ocvirk, P., Pichon, C., and Teyssier, R. (2008b). Bimodal gas accretion in the Horizon-MareNostrum galaxy formation simulation. , 390:1326–1338.

Oh, S.-H., Hunter, D. A., Brinks, E., Elmegreen, B. G., Schruba, A., Walter, F., Rupen, M. P., Young, L. M., Simpson, C. E., Johnson, M. C., Herrmann, K. A., Ficut-Vicas, D., Cigan, P., Heesen, V., Ashley, T., and Zhang, H.-X. (2015). High-resolution Mass Models of Dwarf Galaxies from LITTLE THINGS. , 149(6):180.

Okamoto, S., Arimoto, N., Yamada, Y., and Onodera, M. (2012). Stellar Populations and Structural Properties of Ultra Faint Dwarf Galaxies, Canes Venatici I, Boötes I, Canes Venatici II, and Leo IV. , 744(2):96.

Okamoto, T., Gao, L., and Theuns, T. (2008). Mass loss of galaxies due to an ultraviolet background. , 390(3):920–928.

Oort, J. H. (1970). The formation of galaxies and the origin of the high-velocity hydrogen. , 7:381.

Oppenheimer, B. D. (2018). Deviations from hydrostatic equilibrium in the circumgalactic medium: spinning hot haloes and accelerating flows. , 480(3):2963–2975.

Ostriker, J. (1964). The Equilibrium of Polytropic and Isothermal Cylinders. , 140:1056.

Padnos, D., Mandelker, N., Birnboim, Y., Dekel, A., Krumholz, M. R., and Steinberg, E. (2018). Instability of supersonic cold streams feeding galaxies-II. Non-linear evolution of surface and body modes of Kelvin-Helmholtz instability. , 477:3293–3328.

Padoan, P. and Nordlund, Å. (2011). The Star Formation Rate of Supersonic Magnetohydrodynamic Turbulence. , 730(1):40.

Park, M.-J., Yi, S. K., Dubois, Y., Pichon, C., Kimm, T., Devriendt, J., Choi, H., Volonteri, M., Kaviraj, S., and Peirani, S. (2019). New Horizon: On the origin of the stellar disk and spheroid of field galaxies. arXiv e-prints, page arXiv:1905.02216.

Parsa, S., Dunlop, J. S., and McLure, R. J. (2018). No evidence for a significant AGN contribution to cosmic hydrogen reionization. , 474(3):2904–2923.

Peebles, P. J. E. (1969). Origin of the Angular Momentum of Galaxies. , 155:393.

Penzias, A. A. and Wilson, R. W. (1965). A Measurement of Excess Antenna Temperature at 4080 Mc/s. , 142:419–421.

Petitjean, P., Mueket, J. P., and Kates, R. E. (1995). The Lyα forest at low redshift: tracing the dark matter filaments. , 295:L9–L12.

Pfrommer, C., Pakmor, R., Schaal, K., Simpson, C. M., and Springel, V. (2017). Simulating cosmic ray physics on a moving mesh. , 465(4):4500–4529.

Pichon, C. and Bernardeau, F. (1999). Vorticity generation in large-scale structure caustics. , 343:663–681.

Pichon, C., Pogosyan, D., Kimm, T., Slyz, A., Devriendt, J., and Dubois, Y. (2011). Rigging dark haloes: why is hierarchical galaxy formation consistent with the inside-out build-up of thin discs? MNRAS, 418:24932507.

Pillepich, A., Nelson, D., Springel, V., Pakmor, R., Torrey, P., Weinberger, R., Vogelsberger, M., Marinacci, F., Genel, S., van der Wel, A., and Hernquist, L. (2019). First results from the TNG50 simulation: the evolution of stellar and gaseous discs across cosmic time. , 490(3):3196–3233.

Planck Collaboration, Ade, P. A. R., Aghanim, N., Arnaud, M., Ashdown, M., Atrio-Barandela, F., Aumont, J., Baccigalupi, C., Balbi, A., Banday, A. J., Barreiro, R. B., Battaner, J. G. B. E., Benabed, K., Benoît, A., Bernard, J. P., Bersanelli, M., Bhatia, R., Bikmaev, I., Böhringer, H., Bonaldi, A., Bond, J. R., Borrill, J., Bouchet, F. R., Bourdin, H., Burenin, R., Burigana, C., Cabella, P., Cardoso, J. F., Castex, G., Catalano, A., Cayón, L., Chamballu, A., Chary, R. R., Chiang, L. Y., Chon, G., Christensen, P. R., Clements, D. L., Colafrancesco, S., Colombo, L. P. L., Comis, B., Coulais, A., Crill, B. P., Cuttaia, F., Danese, L., Davis, R. J., de Bernardis, P., de Gasperis, G., de Zotti, G., Delabrouille, J., Démoclès, J., Désert, F. X., Diego, J. M., Dolag, K., Dole, H., Donzelli, S., Doré, O., Dörl, U., Douspis, M., Dupac, X., Efstathiou, G., Enßlin, T. A., Eriksen, H. K., Finelli, F., Flores-Cacho, I., Forni, O., Frailis, M., Franceschi, E., Frommert, M., Ganga, K., Génova-Santos, T., Giard, M., Gilfanov, M., Giraud-Héraud, Y., González-Nuevo, J., Górski, K. M., Gregorio, A., Gruppuso, A., Hansen, F. K., Harrison, D., Hempel, A., Henrot-Versillé, S., Hernández-Monteagudo, C., Herranz, D., Hildebrandt, S. R., Hivon, E., Hobson, M., Holmes, W. A., Hovest, W., Hurier, G., Jaffe, T. R., Jaffe, A. H., Jagemann, T., Jones, W. C., Juvela, M., Khamitov, I., Kisner, T. S., Kneissl, R., Knoche, J., Knox, L., Kunz, M., Kurki-Suonio, H., Lagache, G., Lamarre, J. M., Lasenby, A., Lawrence, C. R., Le Jeune, M., Leonardi, R., Lilje, P. B., Linden-Vørnle, M., López-Caniego, M., Lubin, P. M., Luzzi, G., Macías-Pérez, J. F., Maffei, B., Maino, D., Mand olesi, N., Maris, M., Marleau, F., Marshall, D. J., Martínez-González, E., Masi, S., Massardi, M., Matarrese, S., Matthai, F., Mazzotta, P., Mei, S., Melchiorri, A., Melin, J. B., Mendes, L., Mennella, A., Mitra, S., Miville-Deschènes, M. A., Moneti, A., Montier, L., Morgante, G., Munshi, D., Murphy, J. A., Naselsky, P., Nati, F., Natoli, P., Nørgaard-Nielsen, H. U., Noviello, F., Novikov, D., Novikov, I., Osborne, S., Pajot, F., Paoletti, D., Pasian, F., Patanchon, G., Perdereau, O., Perotto, L., Perrotta, F., Piacentini, F., Piat, M., Pierpaoli, E., Piffaretti, R., Plaszczynski, S., Pointecouteau, E., Polenta, G., Ponthieu, N., Popa, L., Poutanen, T., Pratt, G. W., Prunet, S., Puget, J. L., Rachen, J. P., Rebolo, R., Reinecke, M., Remazeilles, M., Renault, C., Ricciardi, S., Riller, T., Ristorcelli, I., Rocha, G., Roman, M., Rosset, C., Rossetti, M., Rubiño-Martín, J. A., Rusholme, B., Sandri, M., Savini, G., Schaefer, B. M., Scott, D., Smoot, G. F., Starck, J. L., Sudiwala, R., Sunyaev, R., Sutton, D., Suur-Uski, A. S., Sygnet, J. F., Tauber, J. A., Terenzi, L., Toffolatti, L., Tomasi, M., Tristram, M., Tucci, M., Valenziano, L., Van Tent, B., Vielva, P., Villa, F., Vittorio, N., Wade, L. A., Wandelt, B. D., Welikala, N., White, S. D. M., Yvon, D., Zacchei, A., and Zonca, A. (2013). Planck intermediate results. VIII. Filaments between interacting clusters. , 550:A134.

Planck Collaboration, Ade, P. A. R., Aghanim, N., Arnaud, M., Ashdown, M., Aumont, J., Baccigalupi, C., Banday, A. J., Barreiro, R. B., Bartlett, J. G., Bartolo, N., Battaner, E., Battye, R., Benabed, K., Benoît, A., Benoit-Lévy, A., Bernard, J. P., Bersanelli, M., Bielewicz, P., Bock, J. J., Bonaldi, A., Bonavera, L., Bond, J. R., Borrill, J., Bouchet, F. R., Boulanger, F., Bucher, M., Burigana, C., Butler, R. C., Calabrese, E., Cardoso, J. F., Catalano, A., Challinor, A., Chamballu, A., Chary, R. R., Chiang, H. C., Chluba, J., Christensen, P. R., Church, S., Clements, D. L., Colombi, S., Colombo, L. P. L., Combet, C., Coulais, A., Crill, B. P., Curto, A., Cuttaia, F., Danese, L., Davies, R. D., Davis, R. J., de Bernardis, P., de Rosa, A., de Zotti, G., Delabrouille, J., Désert, F. X., Di Valentino, E., Dickinson, C., Diego, J. M., Dolag, K., Dole, H., Donzelli, S., Doré, O., Douspis, M., Ducout, A., Dunkley, J., Dupac, X., Efstathiou, G., Elsner, F., Enßlin, T. A., Eriksen, H. K., Farhang, M., Fergusson, J., Finelli, F., Forni, O., Frailis, M., Fraisse, A. A., Franceschi, E., Frejsel, A., Galeotta, S., Galli, S., Ganga, K., Gauthier, C., Gerbino, M., Ghosh, T., Giard, M., Giraud-Héraud, Y., Giusarma, E., Gjerløw, E., González-Nuevo, J., Górski, K. M., Gratton, S., Gregorio, A., Gruppuso, A., Gudmundsson, J. E., Hamann, J., Hansen, F. K., Hanson, D., Harrison, D. L., Helou, G., Henrot-Versillé, S., Hernández-Monteagudo, C., Herranz, D., Hildebrand t, S. R., Hivon, E., Hobson, M., Holmes, W. A., Hornstrup, A., Hovest, W., Huang, Z., Huffenberger, K. M., Hurier, G., Jaffe, A. H., Jaffe, T. R., Jones, W. C., Juvela, M., Keihänen, E., Keskitalo, R., Kisner, T. S., Kneissl, R., Knoche, J., Knox, L., Kunz, M., Kurki-Suonio, H., Lagache, G., Lähteenmäki, A., Lamarre, J. M., Lasenby, A., Lattanzi, M., Lawrence, C. R., Leahy, J. P., Leonardi, R., Lesgourgues, J., Levrier, F., Lewis, A., Liguori, M., Lilje, P. B., Linden-Vørnle, M., López-Caniego, M., Lubin, P. M., Macías-Pérez, J. F., Maggio, G., Maino, D., Mandolesi, N., Mangilli, A., Marchini, A., Maris, M., Martin, P. G., Martinelli, M., Martínez-González, E., Masi, S., Matarrese, S., McGehee, P., Meinhold, P. R., Melchiorri, A., Melin, J. B., Mendes, L., Mennella, A., Migliaccio, M., Millea, M., Mitra, S., Miville-Deschênes, M. A., Moneti, A., Montier, L., Morgante, G., Mortlock, D., Moss, A., Munshi, D., Murphy, J. A., Naselsky, P., Nati, F., Natoli, P., Netterfield, C. B., Nørgaard-Nielsen, H. U., Noviello, F., Novikov, D., Novikov, I., Oxborrow, C. A., Paci, F., Pagano, L., Pajot, F., Paladini, R., Paoletti, D., Partridge, B., Pasian, F., Patanchon, G., Pearson, T. J., Perdereau, O., Perotto, L., Perrotta, F., Pettorino, V., Piacentini, F., Piat, M., Pierpaoli, E., Pietrobon, D., Plaszczynski, S., Pointecouteau, E., Polenta, G., Popa, L., Pratt, G. W., Prézeau, G., Prunet, S., Puget, J. L., Rachen, J. P., Reach, W. T., Rebolo, R., Reinecke, M., Remazeilles, M., Renault, C., Renzi, A., Ristorcelli, I., Rocha, G., Rosset, C., Rossetti, M., Roudier, G., Rouillé d'Orfeuil, B., Rowan-Robinson, M., Rubiño-Martín, J. A., Rusholme, B., Said, N., Salvatelli, V., Salvati, L., Sandri, M.,

Santos, D., Savelainen, M., Savini, G., Scott, D., Seiffert, M. D., Serra, P., Shellard, E. P. S., Spencer, L. D., Spinelli, M., Stolyarov, V., Stompor, R., Sudiwala, R., Sunyaev, R., Sutton, D., Suur-Uski, A. S., Sygnet, J. F., Tauber, J. A., Terenzi, L., Toffolatti, L., Tomasi, M., Tristram, M., Trombetti, T., Tucci, M., Tuovinen, J., Türler, M., Umana, G., Valenziano, L., Valiviita, J., Van Tent, F., Vielva, P., Villa, F., Wade, L. A., Wandelt, B. D., Wehus, I. K., White, M., White, S. D. M., Wilkinson, A., Yvon, D., Zacchei, A., and Zonca, A. (2016). Planck 2015 results. XIII. Cosmological parameters. , 594:A13.

Planck Collaboration, Aghanim, N., Akrami, Y., Ashdown, M., Aumont, J., Baccigalupi, C., Ballardini, M., Banday, A. J., Barreiro, R. B., Bartolo, N., Basak, S., Battye, R., Benabed, K., Bernard, J. P., Bersanelli, M., Bielewicz, P., Bock, J. J., Bond, J. R., Borrill, J., Bouchet, F. R., Boulanger, F., Bucher, M., Burigana, C., Butler, R. C., Calabrese, E., Cardoso, J. F., Carron, J., Challinor, A., Chiang, H. C., Chluba, J., Colombo, L. P. L., Combet, C., Contreras, D., Crill, B. P., Cuttaia, F., de Bernardis, P., de Zotti, G., Delabrouille, J., Delouis, J. M., Di Valentino, E., Diego, J. M., Doré, O., Douspis, M., Ducout, A., Dupac, X., Dusini, S., Efstathiou, G., Elsner, F., Enßlin, T. A., Eriksen, H. K., Fantaye, Y., Farhang, M., Fergusson, J., Fernandez-Cobos, R., Finelli, F., Forastieri, F., Frailis, M., Fraisse, A. A., Franceschi, E., Frolov, A., Galeotta, S., Galli, S., Ganga, K., Génova-Santos, R. T., Gerbino, M., Ghosh, T., González-Nuevo, J., Górski, K. M., Gratton, S., Gruppuso, A., Gudmundsson, J. E., Hamann, J., Handley, W., Hansen, F. K., Herranz, D., Hildebrandt, S. R., Hivon, E., Huang, Z., Jaffe, A. H., Jones, W. C., Karakci, A., Keihänen, E., Keskitalo, R., Kiiveri, K., Kim, J., Kisner, T. S., Knox, L., Krachmalnicoff, N., Kunz, M., Kurki-Suonio, H., Lagache, G., Lamarre, J. M., Lasenby, A., Lattanzi, M., Lawrence, C. R., Le Jeune, M., Lemos, P., Lesgourgues, J., Levrier, F., Lewis, A., Liguori, M., Lilje, P. B., Lilley, M., Lindholm, V., López-Caniego, M., Lubin, P. M., Ma, Y. Z., Macías-Pérez, J. F., Maggio, G., Maino, D., Mandolesi, N., Mangilli, A., Marcos-Caballero, A., Maris, M., Martin, P. G., Martinelli, M., Martínez-González, E., Matarrese, S., Mauri, N., McEwen, J. D., Meinhold, P. R., Melchiorri, A., Mennella, A., Migliaccio, M., Millea, M., Mitra, S., Miville-Deschênes, M. A., Molinari, D., Montier, L., Morgante, G., Moss, A., Natoli, P., Nørgaard-Nielsen, H. U., Pagano, L., Paoletti, D., Partridge, B., Patanchon, G., Peiris, H. V., Perrotta, F., Pettorino, V., Piacentini, F., Polastri, L., Polenta, G., Puget, J. L., Rachen, J. P., Reinecke, M., Remazeilles, M., Renzi, A., Rocha, G., Rosset, C., Roudier, G., Rubiño-Martín, J. A., Ruiz-Granados, B., Salvati, L., Sandri, M., Savelainen, M., Scott, D., Shellard, E. P. S., Sirignano, C., Sirri, G., Spencer, L. D., Sunyaev, R., Suur-Uski, A. S., Tauber, J. A., Tavagnacco, D., Tenti, M., Toffolatti, L., Tomasi, M., Trombetti, T., Valenziano, L., Valiviita, J., Van Tent, B., Vibert, L., Vielva, P., Villa, F., Vittorio, N., Wand elt, B. D., Wehus, I. K., White, M., White,

S. D. M., Zacchei, A., and Zonca, A. (2018). Planck 2018 results. VI. Cosmological parameters. arXiv e-prints, page arXiv:1807.06209.

Pogosyan, D., Bond, J. R., Kofman, L., and Wadsley, J. (1998). Cosmic Web: Origin and Observables. In Colombi, S., Mellier, Y., and Raban, B., editors, Wide Field Surveys in Cosmology, page 61.

Poudel, A., Heinämäki, P., Tempel, E., Einasto, M., Lietzen, H., and Nurmi, P. (2017). The effect of cosmic web filaments on the properties of groups and their central galaxies. , 597:A86.

Powell, L. C., Slyz, A., and Devriendt, J. (2011). The impact of supernova-driven winds on stream-fed protogalaxies. , 414:3671–3689.

Power, C., Navarro, J. F., Jenkins, A., Frenk, C. S., White, S. D. M., Springel, V., Stadel, J., and Quinn, T. (2003). The inner structure of ΛCDM haloes - I. A numerical convergence study. , 338(1):14–34.

Prescott, M. K. M., Martin, C. L., and Dey, A. (2015). Spatially Resolved Gas Kinematics within a Lyα Nebula: Evidence for Large-scale Rotation. , 799:62.

Press, W. H. and Rybicki, G. B. (1993). Properties of High-Redshift Lyman-Alpha Clouds. II. Statistical Properties of the Clouds. , 418:585.

Press, W. H., Rybicki, G. B., and Schneider, D. P. (1993). Properties of High-Redshift Lyman-Alpha Clouds. I. Statistical Analysis of the Schneider-Schmidt-Gunn Quasars. , 414:64.

Press, W. H. and Schechter, P. (1974). Formation of Galaxies and Clusters of Galaxies by Self-Similar Gravitational Condensation. , 187:425–438.

Prochaska, J. X., Lau, M. W., and Hennawi, J. F. (2014). Quasars Probing Quasars. VII. The Pinnacle of the Cool Circumgalactic Medium Surrounds Massive z ~2 Galaxies. , 796(2):140.

Prunet, S., Pichon, C., Aubert, D., Pogosyan, D., Teyssier, R., and Gottloeber, S. (2008). Initial Conditions For Large Cosmological Simulations. , 178(2):179–188.

Puchwein, E., Haardt, F., Haehnelt, M. G., and Madau, P. (2018). Consistent modelling of the meta-galactic UV background and the thermal/ionization history of the intergalactic medium. ArXiv e-prints.

Puchwein, E. and Springel, V. (2013). Shaping the galaxy stellar mass function with supernova- and AGN-driven winds. , 428(4):2966–2979.

Rahman, N., Bolatto, A. D., Xue, R., Wong, T., Leroy, A. K., Walter, F., Bigiel, F., Rosolowsky, E., Fisher, D. B., Vogel, S. N., Blitz, L., West, A. A., and Ott, J. (2012). CARMA SURVEY TOWARD INFRARED-BRIGHT NEARBY GALAXIES (STING). II. MOLECULAR GAS STAR FORMATION LAW AND DEPLETION TIME ACROSS THE BLUE SEQUENCE. The Astrophysical Journal, 745(2):183.

Rahmani, H., Péroux, C., Augustin, R., Husemann, B., Kacprzak, G. G., Kulkarni, V., Milliard, B., Møller, P., Pettini, M., Straka, L., Vernet, J., and York, D. G. (2018). Observational signatures of a warped disk associated with cold-flow accretion. , 474(1):254–270.

Ramachandra, N. S. and Shandarin, S. F. (2017). Topology and geometry of the dark matter web: A multi-stream view. , 467(2):1748–1762.

Rasera, Y. and Teyssier, R. (2006). The history of the baryon budget. Cosmic logistics in a hierarchical universe. , 445(1):1–27.

Renaud, F., Bournaud, F., Emsellem, E., Elmegreen, B., Teyssier, R., Alves, J., Chapon, D., Combes, F., Dekel, A., Gabor, J., Hennebelle, P., and Kraljic, K. (2013). A sub-parsec resolution simulation of the Milky Way: global structure of the interstellar medium and properties of molecular clouds. , 436(2):1836–1851.

Ribaudo, J., Lehner, N., Howk, J. C., Werk, J. K., Tripp, T. M., Prochaska, J. X., Meiring, J. D., and Tumlinson, J. (2011). Evidence for Cold Accretion: Primitive Gas Flowing onto a Galaxy at z ˜ 0.274. , 743:207.

Rosdahl, J. and Blaizot, J. (2012). Extended Lyα emission from cold accretion streams. , 423:344–366.

Rosdahl, J., Blaizot, J., Aubert, D., Stranex, T., and Teyssier, R. (2013). RAMSES-RT: radiation hydrodynamics in the cosmological context. , 436(3):2188–2231.

Rosdahl, J., Katz, H., Blaizot, J., Kimm, T., Michel-Dansac, L., Garel, T., Haehnelt, M., Ocvirk, P., and Teyssier, R. (2018). The SPHINX cosmological simulations of the first billion years: the impact of binary stars on reionization. , 479(1):994–1016.

Rosen, A. and Bregman, J. N. (1995). Global Models of the Interstellar Medium in Disk Galaxies. , 440:634.

Rubin, V. C. and Ford, W. Kent, J. (1971). Radial Velocities and Line Strengths of Emission Lines across the Nuclear Disk of M31. , 170:25.

Schaap, W. E. (2007). DTFE: the Delaunay Tessellation Field Estimator. PhD thesis, Kapteyn Astronomical Institute ¡EMAIL¿w_schaap@live.nl¡/EMAIL¿.

Schaap, W. E. and van de Weygaert, R. (2000). Continuous fields and discrete samples: reconstruction through Delaunay tessellations. , 363:L29–L32.

Schaerer, D. (2002). On the properties of massive Population III stars and metal-free stellar populations. , 382:28–42.

Schaye, J., Crain, R. A., Bower, R. G., Furlong, M., Schaller, M., Theuns, T., Dalla Vecchia, C., Frenk, C. S., McCarthy, I. G., Helly, J. C., Jenkins, A., Rosas-Guevara, Y. M., White, S. D. M., Baes, M., Booth, C. M., Camps, P., Navarro, J. F., Qu, Y., Rahmati, A., Sawala, T., Thomas, P. A., and Trayford, J. (2015). The EAGLE project: simulating the evolution and assembly of galaxies and their environments. , 446:521–554.

Schmidt, M. (1959). The Rate of Star Formation. , 129:243.

Schmidt, M. (1963). The Rate of Star Formation. II. The Rate of Formation of Stars of Different Mass. , 137:758.

Schramm, D. N. and Turner, M. S. (1998). Big-bang nucleosynthesis enters the precision era. Rev. Mod. Phys., 70:303–318.

Sharma, H., Zerbe, N., Lohmann, S., Kayser, K., Hellwich, O., and Hufnagl, P. (2015). A review of graph-based methods for image analysis in digital histopathology. The Diagnostic Pathology Journal, 1.

Silk, J. (1968). Cosmic Black-Body Radiation and Galaxy Formation. , 151:459.

Simons, R. C., Kassin, S. A., Weiner, B. J., Faber, S. M., Trump, J. R., Heckman, T. M., Koo, D. C., Pacifici, C., Primack, J. R., Snyder, G. F., and de la Vega, A. (2017). z 2: An Epoch of Disk Assembly. , 843(1):46.

Somerville, R. S. and Primack, J. R. (1999). Semi-analytic modelling of galaxy formation: the local Universe. , 310(4):1087–1110.

Sousbie, T. (2011). The persistent cosmic web and its filamentary structure - I. Theory and implementation. , 414:350–383.

Sousbie, T., Pichon, C., Colombi, S., Novikov, D., and Pogosyan, D. (2008). The 3D skeleton: tracing the filamentary structure of the Universe. , 383(4):1655–1670.

Spitzer, L. (1978). Physical Processes in the Interstellar Medium. New York.

Springel, V. (2005). The cosmological simulation code GADGET-2. , 364(4):1105–1134.

Springel, V. (2010). E pur si muove: Galilean-invariant cosmological hydrodynamical simulations on a moving mesh. , 401(2):791–851.

Springel, V., Frenk, C. S., and White, S. D. M. (2006). The large-scale structure of the Universe. , 440(7088):1137–1144.

Springel, V., White, S. D. M., Jenkins, A., Frenk, C. S., Yoshida, N., Gao, L., Navarro, J., Thacker, R., Croton, D., Helly, J., Peacock, J. A., Cole, S., Thomas, P., Couchman, H., Evrard, A., Colberg, J., and Pearce, F. (2005). Simulations of the formation, evolution and clustering of galaxies and quasars. , 435(7042):629–636.

Stark, D. P., Swinbank, A. M., Ellis, R. S., Dye, S., Smail, I. R., and Richard, J. (2008). The formation and assembly of a typical star-forming galaxy at redshift z~3. , 455(7214):775–777.

Steidel, C. C., Adelberger, K. L., Shapley, A. E., Pettini, M., Dickinson, M., and Giavalisco, M. (2000). Lyα Imaging of a Proto-Cluster Region at ¡z¿=3.09. , 532(1):170–182.

Steidel, C. C., Kollmeier, J. A., Shapley, A. E., Churchill, C. W., Dickinson, M., and Pettini, M. (2002). The Kinematic Connection between absorbing Gas toward QSOs and Galaxies at Intermediate Redshift. , 570(2):526–542.

Stewart, K. R., Brooks, A. M., Bullock, J. S., Maller, A. H., Diemand, J., Wadsley, J., and Moustakas, L. A. (2013). Angular Momentum Acquisition in Galaxy Halos. , 769(1):74.

Stewart, K. R., Kaufmann, T., Bullock, J. S., Barton, E. J., Maller, A. H., Diemand, J., and Wadsley, J. (2011). Orbiting Circumgalactic Gas as a Signature of Cosmological Accretion. , 738(1):39.

Stewart, K. R., Maller, A. H., Oñorbe, J., Bullock, J. S., Joung, M. R., Devriendt, J., Ceverino, D., Kereš, D., Hopkins, P. F., and Faucher-Giguère, C.-A. (2017). High Angular Momentum Halo Gas: A Feedback and Code-independent Prediction of LCDM. , 843:47.

Stodólkiewicz, J. S. (1963). On the Gravitational Instability of Some Magneto-Hydrodynamical Systems of Astrophysical Interest. Part III. , 13:30–54.

Stone, J. M., Gardiner, T. A., Teuben, P., Hawley, J. F., and Simon, J. B. (2008). Athena: A New Code for Astrophysical MHD. , 178(1):137–177.

Strateva, I., Ivezić, Ž., Knapp, G. R., Narayanan, V. K., Strauss, M. A., Gunn, J. E., Lupton, R. H., Schlegel, D., Bahcall, N. A., Brinkmann, J., Brunner, R. J., Budavári, T., Csabai, I., Castander, F. J., Doi, M., Fukugita, M., Győry, Z., Hamabe, M., Hennessy, G., Ichikawa, T., Kunszt, P. Z., Lamb, D. Q., McKay, T. A., Okamura, S., Racusin, J., Sekiguchi, M., Schneider, D. P., Shimasaku, K., and York, D. (2001). Color Separation of Galaxy Types in the Sloan Digital Sky Survey Imaging Data. , 122(4):1861–1874.

Sutherland, R. S. and Dopita, M. A. (1993). Cooling functions for low-density astrophysical plasmas. , 88:253–327.

Tamai, R. and Spyromilio, J. (2014). European Extremely Large Telescope: progress report. In Ground-based and Airborne Telescopes V, volume 9145 of Society of Photo-Optical Instrumentation Engineers (SPIE) Conference Series, page 91451E.

Tempel, E. and Libeskind, N. I. (2013). , 775:L42.

Tempel, E., Libeskind, N. I., Hoffman, Y., Liivamägi, L. J., and Tamm, A. (2014). Orientation of cosmic web filaments with respect to the underlying velocity field. Monthly Notices of the Royal Astronomical Society: Letters, 437(1):L11–L15.

Tempel, E., Stoica, R. S., Kipper, R., and Saar, E. (2016). Bisous model-Detecting filamentary patterns in point processes. Astronomy and Computing, 16:17–25.

Teyssier, R. (2002). Cosmological hydrodynamics with adaptive mesh refinement. A new high resolution code called RAMSES. , 385:337–364.

Teyssier, R., Pontzen, A., Dubois, Y., and Read, J. I. (2013). Cusp-core transformations in dwarf galaxies: observational predictions. , 429(4):3068–3078.

Thornton, K., Gaudlitz, M., Janka, H. T., and Steinmetz, M. (1998). Energy Input and Mass Redistribution by Supernovae in the Interstellar Medium. , 500(1):95–119.

Tillson, H., Devriendt, J., Slyz, A., Miller, L., and Pichon, C. (2015). Angular momentum transfer to a milky way disc at high redshift. MNRAS, 449:4363–4379.

Toro, E. F., Spruce, M., and Speares, W. (1994). Restoration of the contact surface in the HLL-Riemann solver. Shock Waves, 4(1):25–34.

Trebitsch, M., Blaizot, J., Rosdahl, J., Devriendt, J., and Slyz, A. (2017). Effect Of Feedback On The Escape Of Ionizing Radiation From High-Z Galaxies. In Galaxy Evolution Across Time, page 49.

Trebitsch, M., Dubois, Y., Volonteri, M., Pfister, H., Cadiou, C., Katz, H., Rosdahl, J., Kimm, T., Pichon, C., Beckmann, R. S., Devriendt, J., and Slyz, A. (2020). The Obelisk simulation: galaxies contribute more than AGN to HI reionization of protoclusters. arXiv e-prints, page arXiv:2002.04045.

Trowland, H. E., Lewis, G. F., and Bland-Hawthorn, J. (2013). The Cosmic History of the Spin of Dark Matter Halos within the Large-scale Structure. , 762(2):72.

Tweed, D., Devriendt, J., Blaizot, J., Colombi, S., and Slyz, A. (2009). Building merger trees from cosmological N-body simulations. Towards improving galaxy formation models using subhaloes. , 506(2):647–660.

Umehata, H., Fumagalli, M., Smail, I., Matsuda, Y., Swinbank, A. M., Cantalupo, S., Sykes, C., Ivison, R. J., Steidel, C. C., Shapley, A. E., Vernet, J., Yamada, T., Tamura, Y., Kubo, M., Nakanishi, K., Kajisawa, M., Hatsukade, B., and Kohno, K. (2019). Gas filaments of the cosmic web located around active galaxies in a protocluster. Science, 366(6461):97–100.

van de Voort, F., Schaye, J., Altay, G., and Theuns, T. (2012). Cold accretion flows and the nature of high column density H I absorption at redshift 3. , 421(4):2809–2819.

van de Voort, F., Schaye, J., Booth, C. M., Haas, M. R., and Dalla Vecchia, C. (2011). The rates and modes of gas accretion on to galaxies and their gaseous haloes. , 414(3):2458–2478.

van den Bergh, S. (1962). The frequency of stars with different metal abundances. , 67:486–490.

Vietri, M., Ferrara, A., and Miniati, F. (1997). The Survival of Interstellar Clouds against Kelvin-Helmholtz Instabilities. , 483(1):262–273.

Vogelsberger, M., Genel, S., Springel, V., Torrey, P., Sijacki, D., Xu, D., Snyder, G., Nelson, D., and Hernquist, L. (2014). Introducing the Illustris Project: simulating the coevolution of dark and visible matter in the Universe. , 444:1518–1547.

Vogelsberger, M., Sijacki, D., Kereš, D., Springel, V., and Hernquist, L. (2012). Moving mesh cosmology: numerical techniques and global statistics. , 425(4):3024–3057.

Wadsley, J. W., Stadel, J., and Quinn, T. (2004). Gasoline: a flexible, parallel implementation of TreeSPH. , 9(2):137–158.

Wang, P. and Kang, X. (2017). A general explanation on the correlation of dark matter halo spin with the large-scale environment. , 468(1):L123–L127.

Wang, P. and Kang, X. (2018). The build up of the correlation between halo spin and the large-scale structure. , 473(2):1562–1569.

Welker, C., Devriendt, J., Dubois, Y., Pichon, C., and Peirani, S. (2014). Mergers drive spin swings along the cosmic web. , 445:L46–L50.

Werner, N., Finoguenov, A., Kaastra, J. S., Simionescu, A., Dietrich, J. P., Vink, J., and Böhringer, H. (2008). Detection of hot gas in the filament connecting the clusters of galaxies Abell 222 and Abell 223. , 482(3):L29–L33.

Wetzel, A. R. and Nagai, D. (2015). The Physical Nature of the Cosmic Accretion of Baryons and Dark Matter into Halos and Their Galaxies. , 808(1):40.

White, S. D. M. (1984). Angular momentum growth in protogalaxies. , 286:38–41.

White, S. D. M. and Rees, M. J. (1978). Core condensation in heavy halos - A two-stage theory for galaxy formation and clustering. , 183:341–358.

Woods, R. M., Wadsley, J., Couchman, H. M. P., Stinson, H. M. P., and Shen, S. (2014). The role of cold flows and reservoirs in galaxy formation with strong feedback. MNRAS, 442:732–740.

Woolf, V. M. and West, A. A. (2012). The M dwarf problem in the Galaxy. , 422(2):1489–1494.

Wyithe, J. S. B. and Bolton, J. S. (2011). Near-zone sizes and the rest-frame extreme ultraviolet spectral index of the highest redshift quasars. , 412(3):1926–1936.

Xu, H., Wise, J. H., Norman, M. L., Ahn, K., and O'Shea, B. W. (2016). Galaxy Properties and UV Escape Fractions during the Epoch of Reionization: Results from the Renaissance Simulations. , 833(1):84.

Zabl, J., Bouché, N. F., Schroetter, I., Wendt, M., Finley, H., Schaye, J., Conseil, S., Contini, T., Marino, R. A., Mitchell, P., Muzahid, S., Pezzulli, G., and Wisotzki, L. (2019). MusE GAs FLOw and Wind (MEGAFLOW) II. A study of gas accretion around z $\approx$ 1 star-forming galaxies with background quasars *. , page 388.

Zel'Dovich, Y. B. (1970). Reprint of 1970A&A.....5...84Z. Gravitational instability: an approximate theory for large density perturbations. , 500:13–18.

Zwicky, F. (1937). On the Masses of Nebulae and of Clusters of Nebulae. , 86:217.